REFERENCE ONLY

UNIVERSITY OF LONDON THESIS

Degree PhD Year 2005 Name of Author PATTCHANO, H.M.J.

Spectroscopic Studies to establish Relationships between Structure, Bonding and Reactivity in Selected Inorganic Species

A thesis submitted for the Degree of

Doctor of Philosophy

In the faculty of Science of the University of London

By

Helen Margaret Inskip Pritchard

Department of Chemistry
University College
University of London

July 2005

ProQuest LLC
789 East Eisenhower Parkway
P.O. Box 1346
Ann Arbor, MI 48106-1346

Abstract

This thesis explores the influence of molecular and electronic structure on the reactivity of some small inorganic complexes, beginning with a review of the nature and properties of metal-hydrogen and metal-carbon bonds of early transition metals and of their importance in catalysis.

A series of cationic niobium methyl complexes, $[Tp^{Me2}NbMe(L)(MeC{\equiv}CMe)][BAr^{f}_{4}]$ (L = OEt_2, THF, $O^{i}Pr_2$, PMe_2Ph and PEt_3) was synthesised and characterised by NMR spectroscopy. Small-scale reactions at low temperatures resulted in the formation of a highly unstable cation, which was stabilised by co-ordination with a series of small electron donor ligands (L). Low temperature NMR studies were used to characterise the resulting air- and temperature- sensitive complexes in solution. One adduct (L = OEt_2) was isolated in the solid state and its structure, determined by X-ray crystallography, accorded with the interpretation of its NMR spectrum. The influence of L on the reactivity and stability of the complexes was explored, with preferred co-ordination demonstrated through ligand exchange reactions. Initial catalytic assays established a level of activity warranting further investigation.

A high quality crystal of $[(Bz_3Ti)_2O]$ was sujected to an experimental charge density study, assisted by an 'Atoms in Molecules' (AIM) theory analysis. This yielded insights into the charge distribution at the Ti and O centres demonstrating the presence of 'ligand induced charge concentration' (LICC). Density functional theory (DFT) calculations were carried out on $[(Bz_3Ti)_2O]$ producing theoretical charge densities in excellent agreement with the experimental results. X-ray crystallography studies were conducted on the intermediates in the synthesis of $MeTi(NMe_2)_3$, $BrTi(NMe_2)_3$ and the novel complex $[\{Ti(NMe_2)_2O\}_2Ti_3(NMe_2)_6OBr_2]$. IR and NMR spectroscopies were used to explore the nature of the Ti–Me moiety in $MeTi(O^{i}Pr)_3$; no α-agostic interactions were discovered.

Variable energy photoelectron spectroscopy has been used for an in-depth study of the electronic structure, including core electrons, of some small, tetrahedral inorganic compounds. The bonding in the industrially used catalyst $MeReO_3$ was studied through the variation of the valence electron band intensities over a wide range of photon energies. Investigation of the electronic structure at the metal centres of the series of metalloborohydrates $Zr(BH_4)_4$, $Hf(BH_4)_4$ and $U(BH_4)_4$ was carried out in a similar manner. Calculation of relative partial photoionisation cross-sections and derived branching ratios along with observation of features such as shape and giant resonance gave insight into the relative ligand and metal contributions to the orbitals. The core electrons and absorption edges of the complexes were also studied. Experimental results showed good correlation with density functional theory calculations.

For my boys, Max and Daniel.

Acknowledgments

There are many people who contributed to the success of this piece of work.

Firstly I would like to thank my supervisors for their support and encouragement: Associate Prof. Sean McGrady especially, with his many ideas throughout my time at King's College and for all his help from afar, and Prof. Robin Clark at UCL for taking me on in my final year. Profs Jenny Green and Michel Etienne have provided inspiration and valuable practical help in their subject areas and along with my mentor Dr. Andrea Sella have provided encouragement and enthusiasm throughout the final stages. My thanks must also go to Profs Jenny and Malcolm Green for giving me an enduring love of Chemistry.

The McGrady group has been a haven of fun and laughter in the face of black gunge. My thanks to Emanuel for his jokes; Nick for hosting a wonderful Christmas meal, his tales of mis-adventure and, with Gemma, restorative lunches; Gemma for always seeing the lighter side of life; Paul for coffee, jazz and the f*-up of the month awards; Aled for pizzas in Trieste and his good music taste, and honorary member Alison for all the laughter and gossip. My thanks go to all in Equipe E for making me so welcome and to Richard, Dina, Christina, Rob and Lizzie for making the transition to UCL a happy one.

The technical support I've received has been excellent. At King's I must thank Jon Cobb for outstanding NMR support; as well as Pete; Roger; Alan; Fitz; Malcolm; Callum; Joe and Jane for all they have done. At UCL Steve, Dave, Joe, John and Crosby have all gone beyond my hopes and expectations to help the doomed. In Trieste Monica, Marcello, Roberto and all of the Gas Phase team gave incredible levels of support, especially at 2 am. Bruno and Francis at the LCC-Toulouse went out of their way to help with my X-ray and NMR studies. I must also thank Wolfgang Scherer and Dmitry Shorokhov in München for conducting the charge density studies.

To the many commuters who, over the past months, have made the journey to and from work possible: Daniel and I thank you for your help, tolerance, seats, and smiles.

For funding I thank: EPSRC, the Marie Curie Institute and Max.
For everything else I thank my family.

Table of Contents

List of Figures

Chapter 1

Chapter 2

Chapter 3

Chapter 4

Chapter 5

Chapter 6

List of Tables

Chapter 1

Chapter 2

Chapter 3

Chapter 5

Chapter 6

List of Complexes

(1) - $[Tp^{Me2}NbMe_2(MeCCMe)]$

(2) - $[Tp^{Me2}NbMe(OEt_2)(MeCCMe)][BAr^f_4]$

(3) - $[H(OEt_2)_2][BAr^f_4]$

(4) - $[Tp^{Me2}NbMe(OC_4D_8)(MeCCMe)][BAr^f_4]$

(5) - $[Tp^{Me2}NbMe(O^iPr_2)(MeCCMe)][BAr^f_4]$

(6a) - $[Tp^{Me2}NbMe(PMe_2Ph)(MeCCMe)][BAr^f_4]$

(6b) - $[Tp^{Me2}NbMe(PEt_3)(MeCCMe)][BAr^f_4]$

(7) - $[Tp^{Me2}TaMe(OEt_2)(MeCCPh)][BAr^f_4]$

(8) - $[(Bz_3)Ti]_2O$

(9) - $BrTi(NMe_2)_3$

(10) - $[\{Ti(NMe_2)_3O\}_2Ti_3(NMe_2)_6OBr_2]$

(11) - $[Ti_3(\mu_3\text{-}O)(\mu_3\text{-}Cl)(\mu\text{-}Cl)_3(Me_2Si(N^tBu)_2)_3]$

(12) - $[Ti_3(\mu_3\text{-}O)(\mu_3\text{-}Cl)(\mu\text{-}OCH_2CMe_3)_3(OCH_2CMe_3)_6]$

(13) - $[Ti_3(\mu\text{-}O^iPr)_3(\mu_3\text{-}O)(\mu_3\text{-}F)(O^iPr)_6]$

(14) - $MeTi(NMe_2)_3$

(15) - $MeTi(O^iPr)_3$

(16) - $[(NC_6H_3{}^iPr_2\text{-}2,6)_2MoMe_2]$

Abbreviations

ε	Bond ellipticity
$\nabla\rho(r)$	Gradient vector field of $\rho(r)$
$\rho(r)$	Electron density distribution
1D	One dimensional
2c-2e	2 centre – 2 electron
2D	Two dimensional
3c-2e	3 centre – 2 electron
ADF	Amsterdam Density Functional
AIM	Atoms in molecules
AO	Atomic orbitals
Ar^f	3,5-difluoromethylbenzene
ARPES	Angle Resolved Photoelectron Spectrometer
b	Bonding
BCA	Beam condensing accessory
BCC	Bonding charge concentration
BCP	Bond critical point
BNFL	British Nuclear Fuels Limited
BP	Bond path
Bz	Benzyl
ca	Circa
CA	Cossee-Arlman
CC	Charge concentration
CCD	Charge-coupled devices
COSY	Correlation spectroscopy
CP	Critical point
Cp	Cyclopentadiene
Cp'	Methylcyclopentadiene
Cp*	Pentamethylcyclopentadiene
CSD	Cambridge structural database
d	Day
d	Doublet
DCM	Dichloromethane
DFT	Density functional theory
DME	1,2-dimethoxyethane
dmpe	1,2-bis(dimethylphosphino)ethane
Et	Ethyl
esd	Experimental standard deviation
FWHH	Full-width, half-height

h	Hour
HOMO	Highest occupied molecular orbitals
I_0	Incident photon flux
IPR	Isotopic perturbation of resonance
^{i}Pr	Isopropoxyl
IR	Infra-red
LCGTO-DF	Linear combination of gaussian type orbitals – density functional
LCAO-HFS	Linear combination of atomic orbials – Hartree-Fock-Slater
LICC	Ligand induced charge concentration
l/mm	Lines per millimetre
LOCC	Ligand opposed charge concentration
LUMO	Lowest unoccupied molecular orbitals
m	Multiplet
Me	Methyl
MGR	Modified Green-Rooney
min	Minute
MO	Molecular orbital
nb	Non-bonding
NBCC	Non-bonding charge concentration
NMR	Nuclear magnetic resonance
PES	Photoelectron spectroscopy
Ph	Phenyl
ppm	Parts per million
pz	3,5-dimethyl-1-pyrazolyl group
RCP	Ring critical point
RPPICS	Relative partial photoionisation cross section
s	Singlet
SCK	Super Coster-Kronig
SW	Scattered wave
tacn	triazacyclononane
Tf	Triflic group
THF	Tetrahydrofuran
TM	Transition metal
Tp^{Me2}	Hydrotris(3,5-dimethylpyrazolyl)borate
VEPES	Variable energy photoelectron spectroscopy
VSEPR	Valence shell electron pair repulsion
VUV	Vacuum ultra violet
ZORA	Zero order relativistic approximation
zpe	Zero point energy

Part of the work described in this thesis has been published:

Elusive Niobium Alkyl Cations Related to Ethylene Polymerisation; H. M. Pritchard, M. Etienne, L. Vendier, G. S. McGrady, Organometallics 2004, 23, 1203-1206

Electronic Structure of ReO_3Me by Variable Photon Energy Photoelectron Spectroscopy, Absorption Spectroscopy and Density Functional Calcuations; M. de Simone, M. Coreno, J. C. Green, G. S. McGrady, H. M. Pritchard, Inorg. Chem 2003, 42, 1908-1918

Electronic Structure of $M(BH_4)_4$, M = Zr, Hf, and U, by Variable Photon-Energy Photoelectron Spectroscopy and Density Functional Calculations
J. C. Green, M. de Simone, M. Coreno, A. Jones, H. M. I. Pritchard, G. S. McGrady, Inorg. Chem. 2005, ASAP Article, DOI: 10.1021/ic050370u

"When you know a thing, to hold that you know it; and when you do not know a thing, to allow that you do not know it – this is knowledge."

Confucius

Chapter 1

Introduction

This thesis is concerned with the study of organotransition metal chemistry and that of transition metal hydrides through the application of physical techniques. These areas of inorganic chemistry have developed rapidly in the past few decades, particularly because of their application in catalysis,[1] their use as reagents in organic synthesis[2] and through a desire to have a greater understanding of their involvement in biological processes.[3] The aim of this introduction is to review the nature and properties of metal-carbon and metal-hydrogen bonds in early transition metal complexes, their importance in catalysis and the influences on their structures.

1.1 Overview

Organometallic complexes are defined as compounds containing at least one metal-carbon bond, with their synthesis stretching back nearly two and a half centuries. From the preparation of $[(CH_3)_2As]_2O$ in 'Cadet's fuming liquid' in 1760, the field has expanded at a great rate. The synthesis of Zeise's Salt, $K[PtCl_3(\eta^2\text{-}C_2H_4)]\cdot H_2O$, was followed by the preparation of a range of organometallic complexes, such as $HgMe_2$, $PbEt_4$ and $[Pt(CO)Cl_2]$.[4]

The beginning of the last century saw the expansion of synthesis to σ-bonded organometallic compounds, with the first transition metal hydride complex, $[H_2Fe(CO)_4]$, prepared by Hieber in 1931.[5] The existence of this Fe–H bond was not widely acknowledged until much later with the discovery of hydrides such as Cp_2ReH and $K_2[ReH_9]$.[6] There was also extensive research into the catalytic properties of organometallic complexes, resulting in large-scale industrial processes such as hydroformylation and Ziegler-Natta catalysis for the polymerisation of olefins.[7] The discovery that the co-ordinatively unsaturated complex $[RhCl(PPh_3)_3]$ will hydrogenate alkenes at ambient temperature and pressure[8] focussed attention on the nature and influence of the ancillary ligands on the reactive metal centre. The enormous economic impact of catalysis is illustrated by the comparison of the total GNP of Canada in 2002 (875 billion US$) and that generated in the USA by catalysis alone (~891 billion US$).[9]

Today research continues apace for a more thorough understanding of the nature and intimate details of catalytic processes. Central to this is an understanding of the nature of the M–C and M–H bonds in different chemical environments and their participation in C–H activation processes.

1.2 Bonding Modes

Transition metals display a wide variety of bonding modes with organic ligands. The main types can be grouped as:

- σ-donor, including η^1 and η^2 σ-donors and agostic bonding
- σ -donor / π-acceptor
- π-donor
- Bridging

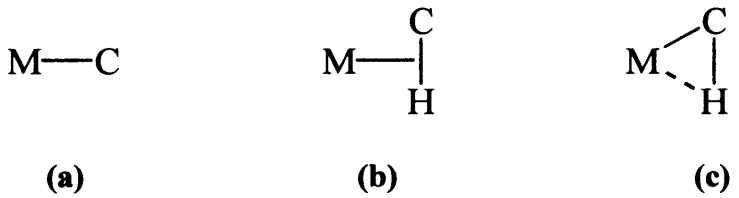

Figure 1.1: σ-bonding modes: (a) classical, (b) η^2 type and (c) agostic.

When considering transition metal alkyl complexes however, some bonding modes are more prevalent than others. That which is of most interest in this Thesis is the σ-donor bond. For formal d^0 species, when the metal is regarded as an ion, a σ-donor ligand is considered to be a two electron donor, with classical σ-donors forming a 2 centre–2 electron (2c-2e) bond by donating a pair of electrons to an empty orbital on the metal centre and occupying one co-ordination site.

Other σ-donor complexes of a more non-classical nature have 3 centre–2 electron (3c-2e) bonds and include η^2 σ-complexes such as η^2-alkyl and dihydrogen complexes *e.g.* $[W(CO)_3(P^iPr_3)_2(\eta^2\text{-}H_2)]$, those with agostic bonding *e.g.* $[EtTiCl_3(dmpe)]$, silane complexes *e.g.* $[Cp'Mn(CO)_2(\eta^2\text{-}HSiHPh_2)]$ and borohydride complexes *e.g.* $[Al(BH_4)_3]$. η^2 σ-complexes with d^0 metal centres have not as yet been isolated as they have, in rare cases, for other transition metals as intermediates in oxidative addition.[10] Although it is proposed that η^2-alkyl complexes could be very short-lived intermediates in some reactions, it is unlikely that such η^2 C–H donation to d^0 transition metal centres will

ever be observed, as such complexes would have very short lifetimes without the increased stabilisation of partial π back-donation into the empty C–H σ^* orbital. It is this absence of non-bonding *d*-electrons for π back-donation that makes study of formally d^0 species a useful starting point for the investigation of other factors that influence the relationships between structure, bonding, and reactivity. The special case of the non-classical 3c-2e bonded tetrahydroborate, or borohydride ion, BH_4^-, is discussed in Section 1.2.3 below.

The agostic C–H bond has widely recognised for over 20 years[11] and is particularly important as it represents an 'arrested' C–H activation process. Finding molecules that display this interaction in the ground state provides opportunities to study the influences upon the bonding and increase our understanding of the interrelationship between C–H, M–H and M–C bonds, which in turn may be used to improve the understanding and development of catalysts. The agostic bond is a 3c-2e entity and is intimately related to the M–C bond. This relationship is especially important in light of the proposal by Scherer and McGrady that in d^0 complexes agostic bonding is more a result of hyperconjugative delocalisation of the M–C bonding electrons than of C–H→M electron donation.[12] In this interpretation, the same pair of electrons that form the M–C bond is also responsible for the M···H–C bonding.

As discussed in more detail in Chapter 3, the presence of agostic interactions in molecules may be established in a number of ways, frequently in combination:

- NMR spectroscopy[13] *e.g.* $[Tp^{Me2}NbCl(sec\text{-}Bu)(MeCCMe)]$[14]
- IR spectroscopy *e.g* $[EtTiCl_3(dmpe)]$[15]
- Neutron and X-ray diffraction *e.g.* $[MeTiCl_3(dmpe)]$, $[(THF)_4Eu\{(\mu\text{-}H)_2BC_8H_{14}\}_2]$[16]
- Charge density studies *e.g.* $[EtTiCl_3]$[17]

1.2 .1 The M–C Bond

Most main-group M–C bonds are σ bonds, with π interactions being less common. The transition metals, with their accessible *d*-orbitals, can have σ, π or both types of interaction with their organic ligands and there is a growing field of carbene complexes stabilised through hyperconjugation.[18] Back-donation of *d* electrons from the metal to the ligand can also take place when an empty *p*-π orbital is available, strengthening the M–C bond, but either increasing or decreasing the overall strength of bonding within the molecule.

(a)

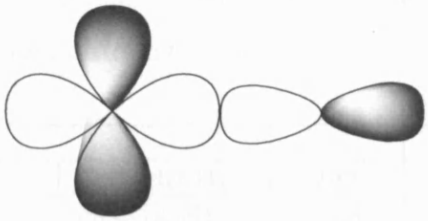

(b)

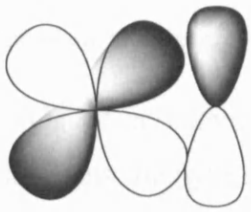

Figure 1.2: (a) *d-p* σ-interaction, (b) *d-p* π-interaction.

With alkyl groups having a relatively low electronegativity (2.67 cf. 3.54 for Cl),[19] M–C bonds are intrinsically weaker than those formed between the metal and other main-group elements. The strength of the M–C bond varies widely within a specific group. For main-group metals the bond becomes weaker descending through the group, as illustrated by comparison of the M–C stretching frequency force constants for the tetramethyl derivatives of Group 14; Table 1.1.[4]

M	Si	Ge	Sn	Pb
k(M–C) Ncm^{-1}	2.93	2.72	2.25	1.90

Table 1.1: M–C stretching force constants for Group 14 MMe_4 compounds.

Molecular orbital (MO) theory considers chemical bonding to arise from the overlap of atomic orbitals (AOs); significant interaction occurs when the metal and ligand orbitals are of similar energies and their symmetries are compatible. Quantum chemical calculations can provide an accurate assessment of the overlap of AO wavefunctions and the energy and composition of the resultant MOs. The best overlap with the carbon

2*s*/2*p* AOs will be achieved with the smaller, lighter main-group metals, as the valence AOs of heavier elements are more diffuse, reducing the overlap and weakening the bond.

However, the opposite trend occurs for transition metal–carbon bonds, where the n*s* and (n-1)*d*-orbitals are the valence AOs. Once again, the degree of orbital diffuseness increases going down the group. However, this plays out differently in terms of a bonding match to the valence orbitals of carbon: the 3*d* orbitals, being strongly contracted, have a smaller overlap than the 4*d* and 5*d* orbitals. The bond dissociation enthalpies given in Table 1.2 demonstrate this trend.

M		Ti	Zr	Hf
D(M–C) kJmol^{-1}	$Cp^*_2M(CH_3)_2$	281	284	306
	$M(CH_2CMe_3)_4$	198	249	266

Table 1.2: M–C bond dissociation energies for Group 4 metal alkyls.[20]

The energies of the 2*s*/2*p* AOs of a carbon atom are affected by its effective electronegativity, which in turn affects the hybridisation of the 2*s* and 2*p* orbitals in the bonds formed at carbon. The larger the C 2*s* orbital contribution to the valence orbital, the greater the exposure of the electrons to nuclear attraction; therefore the electrons are less readily polarised and the resulting MO is lower in energy. This is ostensibly the reason why C–H bonds with more *s*-orbital character react faster than those with greater *p*-orbital character in σ-bond metathesis.[21] Experimental measurement of MO energies may be conducted using photoelectron spectroscopy. Using a variable-energy light source, this technique can also enable study of the delocalisation of an AO into a number of MOs, which can be modelled through calculations to provide insights into the reactivity of molecules, as shown in the latter chapters of this Thesis.

Thermodynamic stability and kinetic inertness are the two factors governing the overall stability of molecules. The lifetime of a compound depends upon its kinetic stability with respect to decomposition pathways to a more thermodynamically stable compound. For example, both $SnMe_4$ and $SnEt_4$ are thermodynamically unstable molecules, but whereas $SnEt_4$ decomposes readily, $SnMe_4$ is a commercially available reagent. This kinetic control is frequently exploited by working at low temperatures. One influence on kinetic stability is the availability of additional co-ordination sites that may be involved in a decomposition pathway. The steric bulk of other ligands, *e.g.* Cp or PPh_3, may

block the availability of this site. Alternatively, a neutral electron-donating ligand, such as an ether or phosphine, may occupy the site.

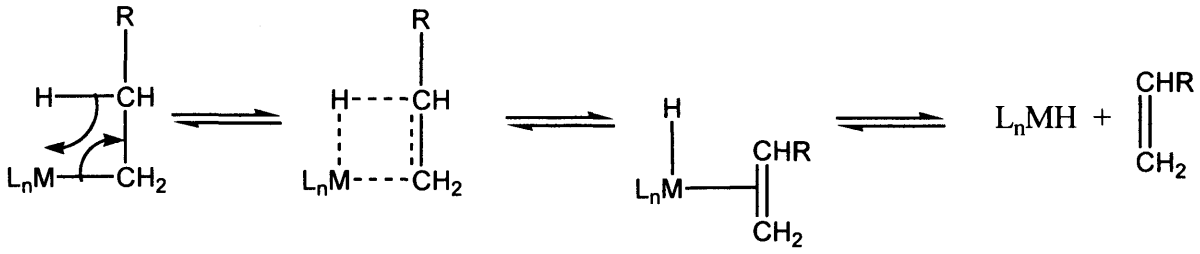

Figure 1.3: β-elimination pathway.

Most organometallic compounds are thermodynamically unstable towards oxidation and many are also unstable to hydrolysis. In other words, it is not necessarily the weakness of an M–C bond causes its reactivity; rather it is a combination of low-lying vacant or non-bonding orbitals and a high degree of M–C bond polarity that contribute to the high reactivity and inherent instability observed in organo-transition metal complexes. These factors lead to a number of possible decomposition pathways, such as β-elimination (Figure 1.3), reductive elimination and α-elimination, which have been harnessed to create the major industrial processes involving catalysis of olefin chemistry. For example, the β-elimination decomposition pathway is employed by Wilkinson's Catalyst [$(Ph_3P)_3RhCl$] and other modern catalysts for the hydrogenation of alkenes.[7]

1.2.2 The M–H Bond

All M–H bonds are polar to some degree, ranging from the strongly ionic *e.g.* KH to the more covalent; *e.g.* AlH_3. Transition metal hydride complexes also exhibit a wide variation in the degree of polarity in the M–H bond and in this Thesis it is their bonding that is of interest. After the 1931 report of the first transition metal hydride complex, $[H_2Fe(CO)_4]$, it was the studies on Cp_2ReH, discovered in 1955[22] that opened the door to the investigation of the nature of the M–H bond in organometallic chemistry. With limited potential for π bonding, most bonds are σ only in character, except in η^2-dihydrogen complexes experiencing $M \rightarrow \sigma^*$ back donation, but this does not limit the richness of chemistry observed. Despite the electronic simplicity of hydrogen – or indeed because of it – many hundreds of metal hydride complexes with a wide variety of bonding modes are now known. Transition metal hydrides exhibit a wide range of

bonding types, spanning a whole spectrum of hydride and hydrogen-bonding types, including:

- Terminal, including di-, tri- and poly-hydrides such as $[W(PPh_3)_2H_6]$,[23]
- Bridging, *e.g.* the bent anion $[(CO)_5Cr–H–Cr(CO)_5]^-$,[24]
- η^2-dihydrogen, *e.g.* $[W(\eta^2\text{-}H_2)(CO)_3(P^iPr_3)_2]$, [25]
- Non-classical proton-hydride hydrogen bonding, M–H···H–X, *e.g.* Re–H···H–N, as found in $ReH_5(PPh_3)_3$.Indole,[26]
- Borohydride complexes such as $[(PPh_3)(phen)Cu(\eta^2\text{-}BH_4)]$,[27]
- Interstitial, *e.g.* $[Co_6H(CO)_{15}]^-$, with a single hydrogen atom embedded within a cluster of metal atoms.[28]

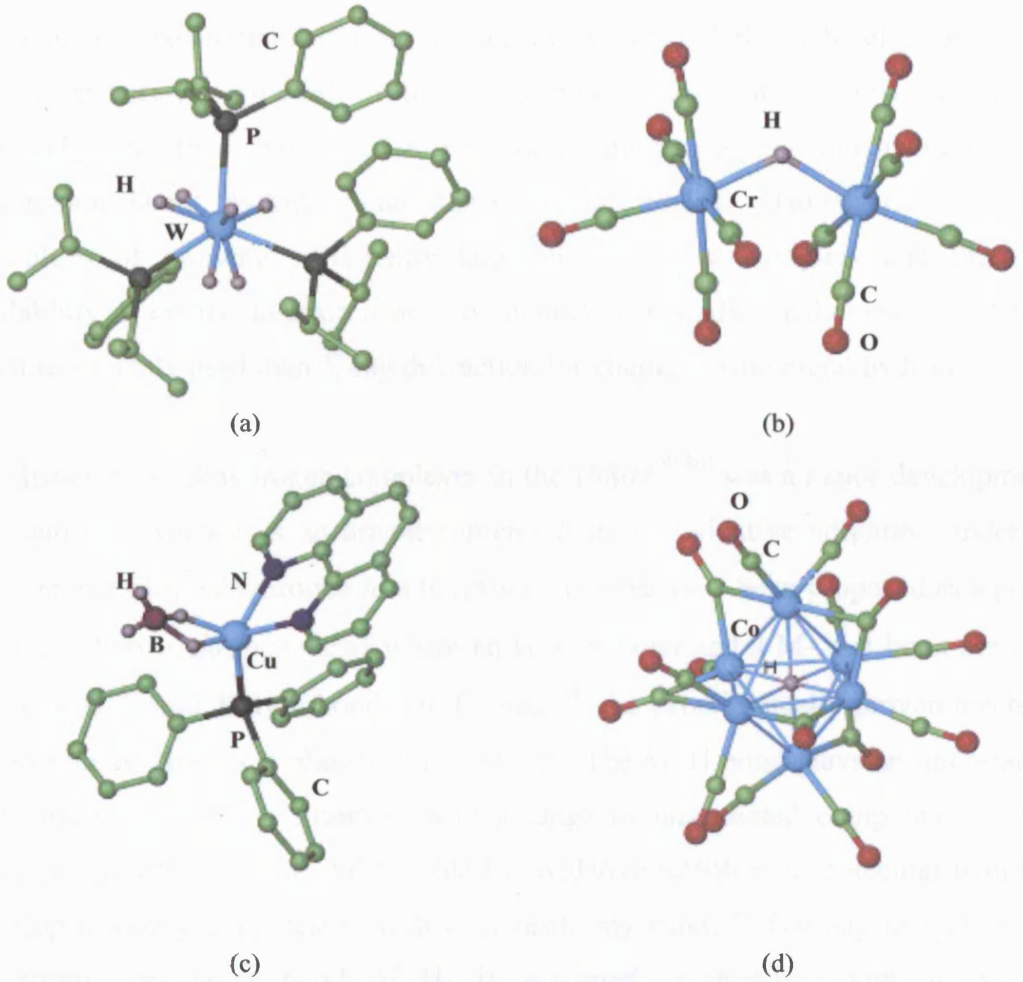

Figure 1.4: Examples of hydride bonding modes in transition metal complexes: molecular structures of (a) $[(Ph^iPr_2P)_3WH_6]$, (b) $[(CO)_5W\text{-}H\text{-}W(CO)_5]^-$, (c) $[(PPh_3)(phen)Cu(\mu^2\text{-}BH_4)]$ and (d) $[(Co_6H(CO)_{15}]^-$ as determined by neutron diffraction.

As with organometallic complexes, many of the transition metal hydride complexes that have been isolated are thermodynamically unstable, but kinetically stable under dry, oxygen-free conditions. With a characteristic chemical shift to high field, frequently in the region of 0 - –30 ppm (although Group 4 d^0 hydrides generally occur in the 0-10 ppm region), ^{1}H NMR spectroscopy is a key tool for their identification. However, many hydride systems are fluxional on the NMR timescale (~10^{-2} s), and a variety of methods need to be employed to fully characterise such complexes. With a timescale of ~10^{-12} s, the M–H stretching vibrations in the 1500 - 2300 cm^{-1} region of IR spectra are an additional and important method of characterisation of the different bonding modes. By contrast, characterisation of metal hydrides by X-ray diffraction presents problems due to the low electron density around the hydride compared to that associated with the metal centre, and the absence of core electron density at H. It is therefore less common to obtain clear positional data from this technique, particularly as the electron density is not symmetrically disposed in the M–H bond. In contrast, neutron diffraction accurately identifies the position of atomic nuclei, giving much more reliable information about hydride bond distances and angles. However, the technical difficulties of growing sufficiently large crystals of a complex, and the limited availability of intense neutron beams to conduct such studies make neutron diffraction much less widely used than X-ray diffraction for characterising metal hydrides.

The discovery of dihydrogen complexes in the 1980s[29;30] was a major development, as they can be regarded as an arrested intermediate of oxidative addition. Indeed, the involvement of η^2-dihydrogen in a transition-state has now been proposed as a possible intermediate σ-bond metathesis where an H–H σ bond and a M–X σ bond are broken and new M–H and X–H σ bonds are formed.[31] An experimentally proven mechanism of this type of process is shown in Figure 1.5. The M–H bond plays an important rôle in catalysis, undergoing insertion with a range of unsaturated compounds, with the formation of a transition metal hydride by oxidative addition of molecular hydrogen a key step in catalytic processes such as hydroformylation.[7] Gaining insight into how the strong, non-polar bond of H_2 is activated is therefore vital to increased understanding of catalytic processes. It is interesting to note that in some instances, the H_2 complex exists in equilibrium with the dihydride tautomer,[29;32] providing opportunities to study this fundamental change in bonding mode.

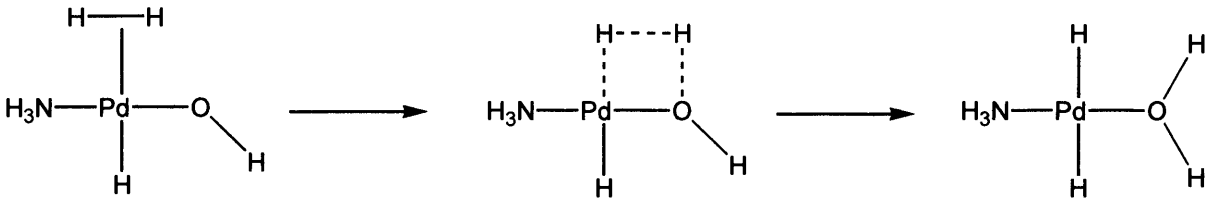

Figure 1.5: An example of polar σ-bond-type metathesis.[31]

1.2.3 Borohydride Complexes

Transition metal borohydride complexes have been the focus of considerable attention over recent decades, not only because of their practical use in synthesis and catalysis, but also because they represent a unique and interesting type of transition metal complex.[33] The borohydride ion, BH_4^-, is isoelectronic with CH_4. This lends it further interest, as some of its transition metal complexes may be considered as prototype structures for saturated hydrocarbon activation. It forms both ionic and covalent bonds with main-group metals *e.g.* $LiBH_4$, $[Al(BH_4)_3]$, reacting by ligand displacement to form covalently-bonded transition metal complexes via 3c-2e B–H–M bonds. $[Al(BH_4)_3]$ was the first covalent borohydride complex to be identified and the first to demonstrate the now familiar characteristic of fluxionality in ^1H NMR spectroscopy, with all 12 hydrides appearing to be equivalent. This problem still besets ^1H NMR spectroscopic studies of borohydride complexes at ambient temperatures, with the group appearing as a quartet broadened through coupling with the quadrupolar ^{11}B nucleus ($I = {}^3/_2$, 81.2% abundance). Low temperature NMR studies are affected by thermal decoupling caused by the ^{10}B ($I = 3$) and ^{11}B nuclei.[34] However, the slow exchange limit may occasionally be reached by irradiating the B nucleus to remove the coupling, as was shown for the complex $[Mo(CO)_4(BH_4)]^-$.[33]

The BH_4^- ion is usually co-ordinated to transition metal atoms through a variable number of bridging hydrogen atoms, commonly with monohapto (η^1), dihapto (η^2), and trihapto (η^3) bonding modes, as in Figure 1.6.

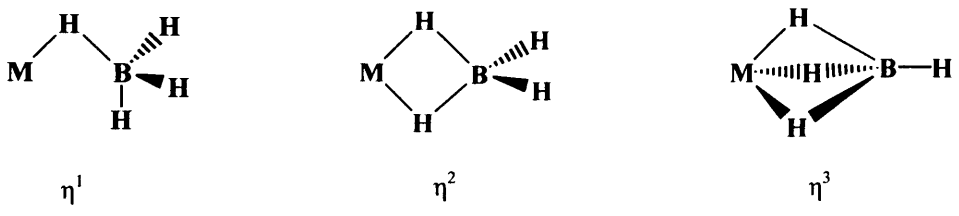

Figure 1.6: Examples of the bonding modes of the borohydride ion, BH_4^-.

Examples of each type include: $[Cu(\eta^1\text{-}BH_4)(PMePh_2)_3]$,[35] $[(Cy_3P)_2OsH_3(\eta^2\text{-}BH_4)]$[36;37] and $[Hf(\eta^3\text{-}BH_4)_4]$.[38] In addition to these η^1, η^2 and η^3 modes, examples of bridging modes $\mu(\eta^2{:}\eta^2)$, $\mu(\eta^3)$, and $\mu(\eta^4)$ are also known,[39] and in fact the solid-state structure of $U(BH_4)_4$ has been shown to include a '14 co-ordinate' uranium centre surrounded by two $\eta^3\text{-}BH_4$ and 4 $\mu(\eta^2{:}\eta^2)\text{-}BH_4$ groups. The hapticity of BH_4^- is influenced both by the steric requirements of the co-ligands; *e.g.* $PMePh_2$ is less demanding than PPh_3, and by the size of the central metal atom *e.g.* Zr can accommodate simultaneous ligation by 12 H atoms. The different coordination modes of the BH_4^- ligand in some transition metal borohydride complexes, and particularly mono-borohydride species, can be easily understood according to the 18-electron rule, when each co-ordinating B–H bond is regarded as a formal 2-electron donor to the metal centre. This model results from MO analyses of borohydride complexes, with the η^1, η^2 and η^3 modes being considered $2e^-$, $4e^-$ and $6e^-$ donors through the donation of their σ-bonding electron pair. For some complexes, such as $[M(\eta^3\text{-}BH_4)_4]$ (M = Zr, Y, Hf) and $[Tp^{Me2}Cd(\eta^2\text{-}BH_4)]$,[40] the 2-electron donation model cannot be simply applied, since it results in a formal count of 24 and 20 valence electrons respectively. Such high electron counts usually imply a high degree of ionic nature. A consideration of the $[M(\eta^3\text{-}BH_4)_4]$ species and their unusual electron counts is given in Chapter 6. A detailed analysis by Xu and Lin demonstrates that both ionic and electronic effects play important roles in the stereochemistry of these borohydride complexes:[41] the ionic effects work so as to maximise the co-ordination number, whilst the electronic effects influence the orientation of ligands.

1.3 Catalysis

Catalysis is essential to life, with our bodies containing many biological catalysts. Reactions that are thermodynamically favourable, but involve an unfavourable or inaccessible transition state, require the help of a catalyst. In general a catalyst acts by bringing the two reactants together at a distance and angle at which the reaction can occur. In some cases the presence of a catalyst simply increases the rate of a reaction, but in many other instances it activates an otherwise inert substrate. Activation affects the chemical nature of an internal bond in one of the reactants, generally weakening it to facilitate reaction. For metal-containing catalysts (**M**), their ability to provide a lower energy, alternative reaction pathways arise through the complexation of the substrates, illustrated in Figure 1.7. Not only does this bring the reactants close together in a

favourable orientation for an extended period, but in the case of organic molecules, the interaction with the metal centre activates the molecule, facilitating nucleophilic attack at the co-ordinated carbon atom.

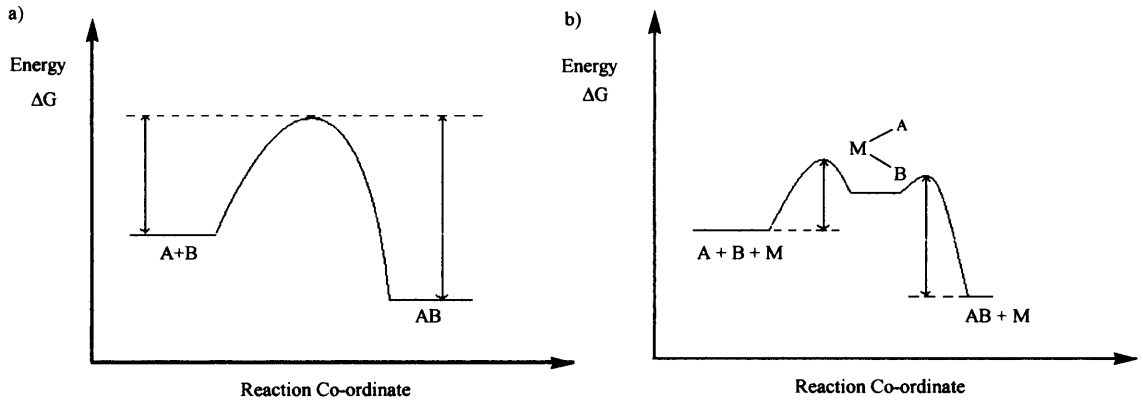

Figure 1.7: A representation of the energetics of a catalytic pathway.

The large HOMO–LUMO energy gap of the C–H bond gives a typical bond energy of 90-100 kcal mol^{-1},[21] so ways of reducing the energy needed to break it are very important. The enabling of α or β elimination pathways or addition or insertion of functional groups through co-ordination to a metal centre motivates the investigation of factors affecting M–C and M–H bonds. It is the key interrelationship of the M–H, M–C and C–H bonds that gives the petrochemical industry access to a wider range of applications for the alkenes and alkanes they extract from the earth. Industry exploits the flexibility of organotransition metal chemistry to make processes economically viable in terms of reaction conditions and evolved product. A number of olefin-based processes, including oxidation, polymerisation, hydrogenation and hydroformylation, all rely on transition metal catalysts.

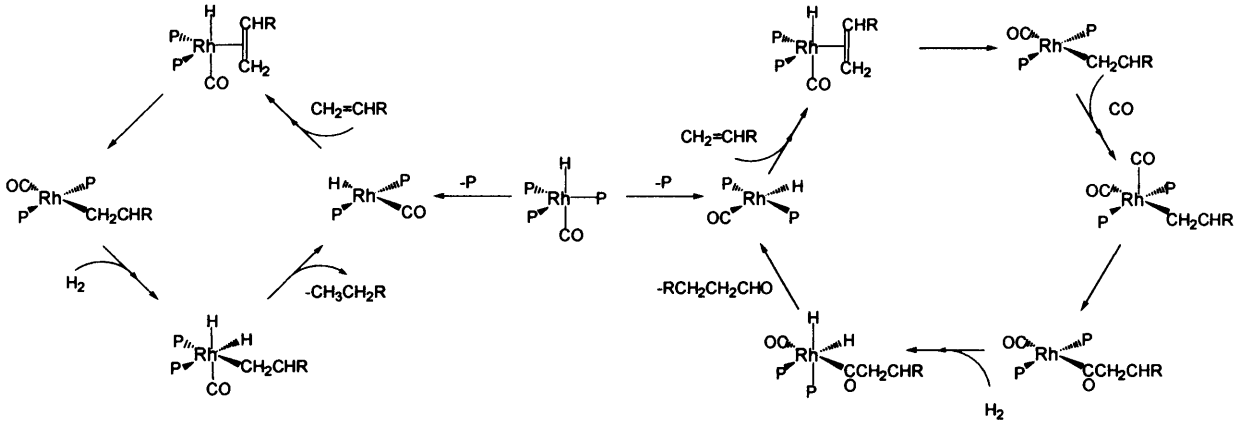

Figure 1.8: Cycles showing the stages in catalysis of alkene hydrogenation (left) and hydroformylation (right) by $[(PPh_3)_3(CO)RhH]$. In each case, PPh_3 is represented as P.

In some cases there are ways of influencing and even controlling the nature of the product, so different catalysts can be used with the same starting material to produce different chemical or stereochemical products *e.g.* avoid atactic and produce syndio- and/or iso-tactic polymers. This enhanced selectivity reduces waste or the length of the refining process. A detailed understanding of the precise nature of the catalyst and its intermediates in such polymerisations is crucial to improved catalyst design and process development.

Well-defined single site molecular catalyst systems, often based on Group 4 metals, have now moved from the lab to commercial application, but their extraordinarily high activities often preclude detailed study of the key transition states of the insertion process. Isolation of Group 4 metal d^0 alkyl cations as active intermediates in some mechanistic steps has made them a crucial synthetic target.

1.4 Structure and Bonding in d^0 Transition Metal (TM) Compounds

The stability of a complex, strength of the TM–C bond and the structure of the molecule are influenced by a number of factors, which in turn affect the reactivity; viz:

- σ bonding
- π bonding
- ligand effects
- core polarisation

It is the interpretation of the interplay of these key influences that gives rise to the various bonding models. The Valence Shell Electron-Pair Repulsion (VSEPR) model is widely used for structural predictions and is an effective tool for many simple main-group molecules, but has only limited success with the heavier *p*-block element and transition metal complexes. A good example of the limitations of VSEPR theory is given by the different structures of $TaMe_5$, $SbMe_5$ and $SbPh_5$. Although the covalent radii of these three metals are of similar size,[42] their pentamethyl compounds have differing structures: $TaMe_5$ has been found to adopt a C_{4v}, square pyramid structure while $SbMe_5$ displays the trigonal bipyramid structure predicted by VSEPR.[43] $SbPh_5$ however, also adopts a C_{4v} structure demonstrating the influence of ligand repulsion on the adopted structure and highlighting the inadequacies of the VSEPR model for heavy metal complexes.[44] The number of 'non-VSEPR' structures now known demonstrates

the simplicity of the model, which whilst making it user-friendly, ignores several important aspects. One of these is the assumption that the electron core of the central atom is spherical and therefore does not influence the conformation of the complex. For open-shell transition metal compounds, where the *d* orbitals are only partially filled, the electron core is better regarded as an ellipsoid.[45] The degree and direction in which the electron core of the transition metals is polarised is an important structural factor, one that can be investigated by charge density studies. The model also takes no account of the ligand field splitting, a key factor in the structure adopted by open-shell molecules or unexpected multiple bonding; *e.g.* the planarity of silylamines such as $[Me_2NSiMe_3]$.

There seems, as yet, to be no consensus on the weighting of each of these factors or which model is the most useful to predict structures. Calculations and experimental data can be effectively used and interpreted to increase our understanding of the complex nature of molecular structure.

π bonding

Although π bonding does not occur directly in the alkyl M–C bond, its effect is worth noting as other ligands considered in this project do have π interactions with a d^0 metal centre. When ligand electrons and an empty orbital on the metal centre each have π symmetry their overlap leads to a certain degree of π bonding, the extent of which can be investigated by photoelectron spectroscopy. It has long been considered that π bonding to a metal centre results in the VSEPR-predicted structure; however this is not always the case, *e.g.* the strongly bent $[MoO_2]^+$ moiety found in many heteroleptic molybdenyl complexes. Kaupp proposes that π donors be placed in either the 'strong' or 'weak' donor category, each having an opposite effect on the bond angle.[46] Generally however, the effect on structure of these orbital overlap considerations is not uniform and no predictive model has been put forward.

Ligand effects

Steric and electrostatic repulsions are chemically intuitive aspects of molecule stereochemistry and generally increase with higher co-ordination numbers, although their impact depends upon both the nature of the metal centre and the ligands present.

The second order Jahn-Teller effect is a distortion of the structure of a molecule resulting from the mixing of the HOMO and LUMO in a higher symmetry structure. The distortion also leads to the destabilisation of some lower-lying filled orbitals: hence it is the overall energetics which dictate the extent of any distortion observed. The HOMO-LUMO gap depends upon bond polarity, widening as the polarity increases, thus a high degree of polarity prevents the mixing of the orbitals and the accompanying reduction in molecular symmetry. Conversely, a more covalent bond with a relatively electropositive ligand raises the energy of the HOMO, making the molecule more prone to a distorted structure. In this case, the resultant HOMO is more stable, with the stabilisation afforded inversely dependent upon the HOMO-LUMO gap.[47] For example: $[Zr(CH_3)_6]^{2-}$,[48] and $[Ta(CH_3)_6]^{-}$,[49] have been shown experimentally and $[TiH_6]^{2-}$ through calculation,[50] to prefer a regular trigonal prism structure, rather than an octahedral one, whilst $[W(CH_3)_6]$[51] and $[Mo(CH_3)_6]$[52] are distorted even further from O_h symmetry.[46] The 1990 report by Haaland et al.[51] of the non-octahedral structure of the simple, d^0 complex $[W(CH_3)_6]$ in the gas phase was confirmed by X-ray diffraction studies.[53] Interestingly, these studies also reported the d^1 complex $ReMe_6$ to be a regular trigonal prism. Theoretical studies have also confirmed the distorted structure of $[W(CH_3)_6]$ as the most energetically favoured.[47]

d orbital participation in σ bonding

The availability of the empty *d* orbitals of d^0 transition metal complexes contrasts with the *p* block elements, which, except in some specialised (but controversial) cases of hypervalence,[54;55] have filled *d* orbitals lying contracted and unavailable for ligand interaction. The *d* orbital availability at accessible energies in transition metal chemistry gives an opportunity for increased orbital overlap and therefore stronger bonding interactions in σ bonding. Landis et al.[56;57] have conducted a number of elegant calculations using a molecular mechanics approach to investigate the effect of *sd* hybridisation of the metal atomic orbitals. Maximising this overlap can result in distortion from regular to irregular molecular symmetries, with energy minima occurring at different bond angles, depending on the extent of sd^n hybridisation. Extended-Hückel-type calculations have also shown that the lowering of symmetry allows for increased *d* orbital participation[47] as illustrated in Figure 1.9.

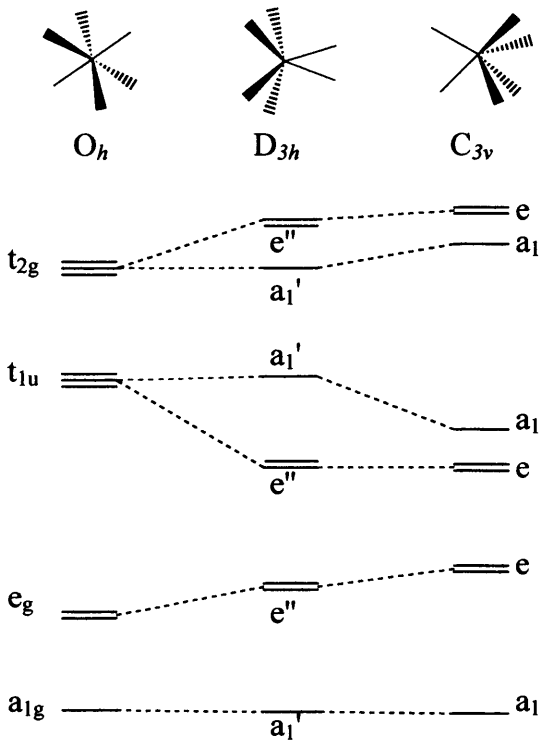

Figure 1.9: Molecular orbital correlation diagram for d^0 MMe_6 complexes.[58]

Core polarisation

Pioneering work by Gillespie and Bader has shown experimentally that the outer electron cores of heavy atoms, including the *d* block elements, show local charge concentrations.[59] Charge density studies on the hypothetical molecule CaF_2, which is predicted to have a quasi-linear structure, show local charge concentrations in the electronic core of the Ca atom,[60] similar to those modelled for the Cr core of $Cr(O_2)F_2$,[61] which adopts a distorted tetrahedral structure. They proposed that the electron core is susceptible to polarisation by the electron pairs in the valence shell, with core polarisation dependent on the bond polarity: the more polar the bond, the lower the core polarisation effect, as the electron density is further removed from the core. The areas of core polarisation, termed ligand-opposed charge concentrations (LOCCs) are thought to influence structure in a similar manner to lone and bonding electron pairs, in that they compete for space around the metal centre. It has been suggested that this influence diminishes on increasing the formal oxidation state of the metal centre, when other influences rise to prominence.[46] The impact of the phenomenon on the structures adopted by d^0 alkyl complexes is real, but the interpretation of its origin still open to debate. More recently it has been reported that these LOCCs are not part of the core, but a natural result of sd^n orbitals,[62] as illustrated below.

Main group orbitals:

n*s* n*p* *sp* hybrids

These point in one direction, with only a small lobe at the rear.

Transition metal orbitals:

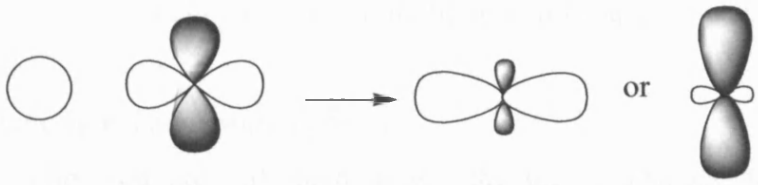

n*s* (n-1)*d* *sd* hybirds

These point both ways along one axis.

When a TM–C bond is formed from a *sd* hybrid there is a 'charge concentration', shown below as the shade lobe, which is ligand opposed by definition:

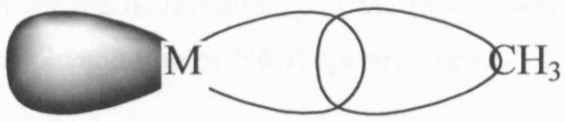

sd sp^3

The four key influences on structure discussed above cannot be considered in isolation from one another, but rather it is their interdependence and relative importance in each chemical situation that determines the structure adopted.[i]

1.5 Aims of the Project

The overall aim of this project was to gain a better understanding of the influence of bonding and structure on the reactivity of some small inorganic molecules. With their involvement in a wide range of industrial processes, it was the nature of M–C and M–H bonds that were of particular interest: how their reactivity is affected by structural and chemical factors. We have employed a variety of physical methods to study the electronic and physical structure of the compounds, complementing and expanding previous work, in solution and in the solid and gaseous phases.

Our original aims were threefold:

1. Our first area of interest was the highly reactive transition states involved in homogeneous catalysis. We aimed to prepare Group 5 analogues of Group 4 systems in order to facilitate the isolation of a cation of sufficient stability for study. We particularly hoped to be able to look at the strength of co-ordination of a range of electron-donor ligands at the metal centre and investigate the steric influence of the ancillary ligands. As the conditions for homogeneous catalysis make solution analysis essential for the understanding of the mechanism involved we planned to study these systems in solution by NMR spectroscopy.

2. We also aimed to study a series of methyltitanium compounds to investigate the influence of the basicity of the ligands on the nature of the M–C bond. We hoped to collect structural details of the complexes by electron diffraction, charge density analysis and X-ray crystallography, with the reactivity of the complexes studied by infra-red spectroscopy at low temperatures in an argon matrix.

3. Our final area of interest was the electronic structure of simple small molecules. By exploiting the advantages of synchrotron radiation we hoped to use photoelectron and absorption spectroscopy to probe the electronic structure of both the outer valence and core electrons for the d^0 compounds $MeReO_3$, $Zr(BH_4)_4$, $Hf(BH_4)_4$ and $U(BH_4)_4$. Molecular orbital energies and properties can be directly determined experimentally and we aimed to determine their nature of through the interpretation of the spectral data in conjunction with DFT calculations, thus enabling comparison of structure and reactivity within a series.

Chapter 2

Structural and Chemical Studies of some Niobium Alkyl Cations

The work in this Chapter focuses on the structural aspects influencing the reactivity of the metal centre. The aim of this project was to isolate, characterise and explore the chemistry of a proposed intermediate of the polymerisation of ethene; the alkyl cation $[Tp^{Me2}NbMe(MeCCR)L]^+$.

2.1 Introduction

Group 4 metals form highly efficient, industrially important, catalytic complexes.[63] The generation, identification and isolation of d^0 alkyl cations of the Group 4 metals has confirmed that they are key intermediates in the polymerisation of olefins.[64;65] Detailed thermodynamic and kinetic studies of alkene binding, ion pairing, migratory insertion (i.e. chain growth) and β-H and β-alkyl eliminations (i.e. chain transfer and chain termination) have been carried out on discrete, highly reactive cationic alkyl complexes of these and related materials.[66] A combination of these efforts at the molecular level has resulted in considerable improvements in catalyst design and ultimately to process development. However, investigations of the alkyl cations have been hampered by the instability of the catalysts, with one of the seminal advances in this field being the discovery that alkyl cations of the Group 4 metallocene complexes could indeed be generated and stabilised.[67]

A typical example is the 14 electron, strong Lewis acid $[Cp_2ZrMe]^+$ shown in Figure 2.1. Not only is it highly electrophilic, but it also has a vacant site for co-ordination by an electron-rich species such as an alkene. Initial investigations involved creation of the cation by abstraction of a methyl group from $[Cp_2ZrMe_2]$ and its stabilisation by a neutral Lewis base such as THF in the presence of a large non-coordinating anion such as $[BPh_4]^-$.[68] As expected for such a charged species, X-ray studies showed the cation to have a Zr–CH_3 bond of 2.256 Å; 0.02 Å shorter than in the neutral complex. Further work in non-Lewis base solvents employed large, loosely co-ordinating anions, such as $[(C_2B_9H_{11})_2M]^-$ (where M = Fe, Co, Ni) which readily dissociate to allow polymerisation to occur.[69;70]

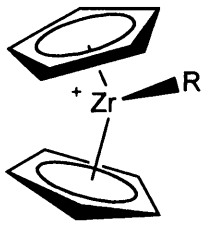

Figure 2.1: Structure of the $[Cp_2ZrCH_3]^+$ cation.

Although simple vanadium compounds are used industrially for ethene/propene copolymerisation,[71] polymerisation of olefins with complexes of the heavier Group 5 metals (Nb, Ta) has received considerably less attention.[72;73] With a range of stable oxidation states, these metals offer an opportunity to study in more depth the influence of charge, electron count and other variables on the various steps of the polymerisation process. These complexes may also be more tolerant to functional groups than the oxophilic species derived from Group 4 metals: their use as selective catalysts may then parallel mechanistic insights. Group 5 systems have produced creditable performances in terms of product polydispersity,[74] if not in terms of catalyst activity. In some instances Group 5 catalysts have been shown to have reactivity comparable to that of Group 4 congeners, such as in the recently described trimerisation of ethene to 1-hexene, catalysed by $[Me_2TaCl_3]$,[75] also catalysed by $[\{\eta^5\text{-}C_5H_3R\text{–(bridge)–}Ar\}TiCl_3]$ complexes activated with MAO.[76] However, in general their reactivity is significantly lower than that of Group 4 complexes, which is advantageous when attempting to isolate transient species.

2.2 Group 5 Metal Catalysts

Most attempts to develop active Group 5 catalysts have been inspired by isoelectronic, isolobal or isostructural relationships with known Group 4 metal complexes. Thus, complexes based on cyclopentadienyl (mono and bis),[77] amidinate,[78] imido,[79;80] borollide,[81] tribenzylidenemethane,[82] amidopyridine,[83] tris(pyrazolyl)borate[84] and diene[85;86] ligands – or combinations thereof – have all been explored. However, simple alkyl cations, or related ion pairs or base adducts, that also polymerise ethene or higher olefins have rarely been characterised for heavier Group 5 metals.[83;87] Consequently, associated mechanistic studies are extremely rare and no information is available concerning the details of the polymerisation process.

The use of amido ligands can provide a stable, sterically inhibited environment for the metal centre, which may prove useful in future catalyst design for selectivity of olefin functional groups. The characterisation of a catalytically active niobium-centred zwitterion[83] through the partial abstraction of the metal-methyl group by $B(C_6H_5)_3$ from a diamido alkyne niobium alkyl complex demonstrates this potential.

2.2.1 The Tp Ligand: A Cp Analogue

The tris(pyrazolyl)borato ligand, Tp, is often considered to be electronically equivalent to Cp, but is more sterically controlling.[88] This is in part due to a larger cone angle of 236°[89] cf. 125°.[90] Shown in Figure 2.2, Tp is a tri-dentate ligand, occupying half of an octahedral co-ordination sphere. Not only does it possess three-fold symmetry, but has clefts or wedges above the other octahedral co-ordination sites, which heavily influence the stereochemistry at the metal centre of a complex.

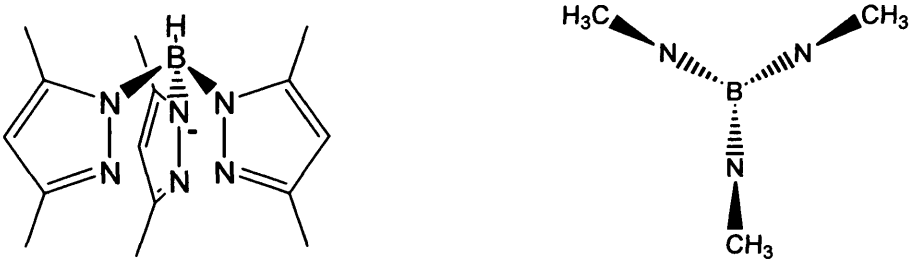

(a) (b)

Figure 2.2: The Tp^{Me2} ligand (a) side on and (b) from above.

As with Cp, Tp can be adapted to give a series of ligands of increased bulk or differing basisity. $[Tp^RNbMe_2(PhC{\equiv}CMe)]/[B(C_6F_5)_3]$ (Tp^R = Tp, Tp^{Me2}, $Tp^{Me2,4\text{-}Cl}$) polymerises ethene at differing rates depending on the substituents on the Tp^R.[84] In this case it was shown that the electrophilicity of the ligand did not influence the polymerisation activity as significantly as the increased steric bulk. For Tp^R = Tp and $Tp^{Me2,4\text{-}Cl}$ the electron density at the metal is almost identical, however the activity is markedly different. Also, the activity levels for Tp^R = Tp^{Me2} and $Tp^{Me2,4\text{-}Cl}$ are only slightly different despite the higher electron donating nature of Tp^{Me2}. The higher rate recorded for Tp vs. Tp^{Me2} and $Tp^{Me2,4\text{-}Cl}$ highlights the increased ease of feedstock association and dissociation of the polymer due to a lower steric hindrance at the metal centre. This is presumed to be responsible for the shorter lifetime of this species, leading to reaction inhibition caused by the formation of an association product. Several Group 4 catalysts degrade by the

formation of dimers.[64] The versatility of the Tp moiety makes it ideal for use when exploring a series of complexes. Tp^{Me2} has been used in this project, chosen for its size and electron donating potential; further exploration of the systems described below could exploit the wider Tp family.

2.2.2 Alkyne Complexes

Many Group 5 half-sandwich imido complexes are known, with interest derived from their isolobal relationship to the Group 4 metallocenes. Gibson et al.[91-93] have reported widely on the structural and chemical similarities of the Nb and Ta complexes to the Group 4 metallocenes. A catalytically active tantalum derivative [Cp*Ta(=N-Si^{t}Bu$_3$)Cl$_2$]/MAO system has been characterised,[94] and illustrates the suitability of the imido ligand as a Cp equivalent for Group 5 complexes. Alkynes acting as 4-electron donors are similar to the imido ligands,[95] and when used with the Tp ligand family adopt a vertical geometry.[96] With one end of the alkyne locked into a cleft and two free co-ordination sites, this structurally mimics the Group 4 metallocenes and, as discussed earlier, these Group 5 complexes have been shown to be catalytically active. As for Tp, the alkyne can be functionalised to provide ligands of different size and basicity.

2.2.3 α-Hydrogen Agostic Interactions

Some of the Group 5 cationic complexes based on the metallocene model include $[Cp_2TaMe_2]^+$, stabilised with a large non-coordinating anion, and the reactive zwitterion $[Cp_2TaMe(CH_2B(C_6H_5)_3)]$ reported by Piers et al. stabilised instead through an α-agostic interaction with the bridging methylene.[97] α-hydrogen agostic interactions, illustrated in Figure 2.3, restrict rotation within a molecule, increasing the rigidity of a structure. It is proposed that where present in catalysis, the α-agostic interaction lowers the activation barrier to olefin insertion through the electronic stabilisation of the charged metal centre.[98] The associated rigidity dictates the orientation of the polymer chain, thus influencing the tacticity of the polymer produced.

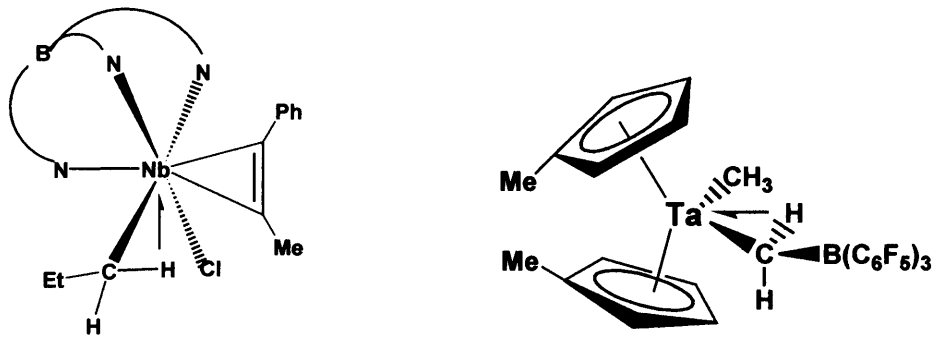

(a) (b)

Figure 2.3: α-agostic interaction in (a) [Tp^{Me2}Nb(Cl)(Et)(PhC≡CMe)] and (b) [$(C_5H_4Me)_2TaMe(CH_2B(C_6F_5)_3)$].

The complex [Tp^{Me2}Nb(Cl)(CH_2CH_3)(PhC≡CR)] (R = Me, Et) exhibits an unusual preference for α- over β-agostic ethyl interaction.[99] Moreover, this complex undergoes reversible migratory insertion/β-alkyl elimination,[100] a major chain transfer step in Ziegler-Natta catalysis.[101;102] The analogous isopropyl complex demonstrates an equilibrium between α- and β-agostic forms,[103] each of which has one methyl arm trapped within the Tp^{Me2} cleft, as shown in Figure 2.4. The energetics of the systems have been measured experimentally and calculated (for R = H) to show the steric effects of Tp^{Me2} on the structures adopted.[14] It is the presence of the methyl groups at the 3-position, influencing the alkyl orientation, that dictates α- or β-agostic bonding.

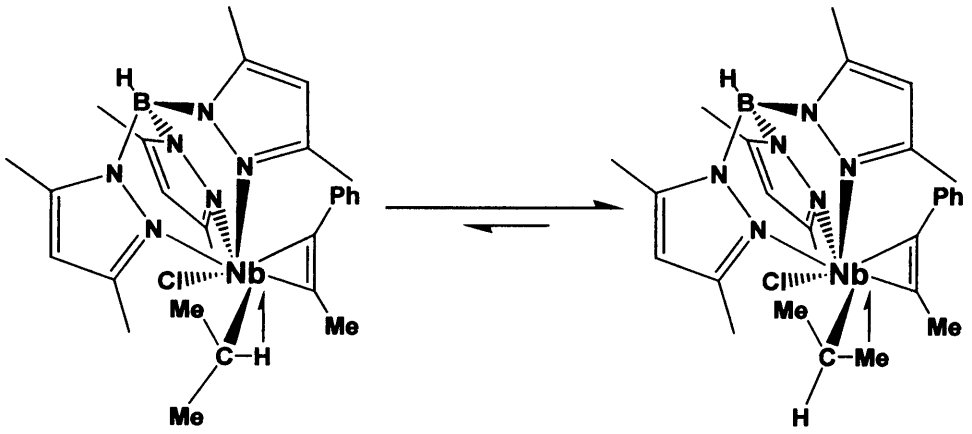

Figure 2.4: Equilibrium between alpha and beta agostic interactions in [Tp^{Me2}Nb(Cl)(^{i}Pr)(PhC≡CMe)].

2.3 Aims of This Research

The aim of this project was the synthesis and characterisation of the alkyl cations $[Tp^{Me2}NbMe(RCCMe)(L)]^+$ (L = ether, alkene, alkyne, phosphine, R = Me, Ph), putative intermediates, or models of the intermediates, in the catalysis of ethene

polymerisation. We hoped to focus on the influence of the steric and electronic effects of the ligands on the reactivity of the cationic metal centre. We expected the species to be highly reactive and planned to characterise the compounds by low temperature NMR spectroscopy and, if possible, X-ray diffraction.

Previous attempts by Etienne and co-workers to observe the putative intermediate ion pair $[Tp^{Me2}Nb^{+}Me(PhC{\equiv}CMe)(\mu\text{-}Me)B^{-}(C_6F_5)_3]$ of the catalytically active system described earlier involved *in situ* NMR tube reactions at low temperatures in various solvents (d_8-toluene, d_2-DCM). These experiments were frustrated by extensive decomposition, possibly through electrophilic cleavage of the B–N bond of Tp^{Me2}; a well known phenomenon in Tp*-based chemistry.[104]

Only a few examples of such cationic models can be found in the literature. It has been shown that triflic acid, HOTf, protonates the dimethyl complex $[Cp^{*}TaMe_2(\eta^4\text{-isoprene})]$ to yield the structurally characterised $[Cp^{*}TaMe(OTf)(\eta^4\text{-isoprene})]$ with a covalent Ta–OTf bond. However this complex only serves as a very crude model for a base-stabilised cation.[105] Pioneering work on the Group 4 systems employed $[HNMe_2Ph][BPh_4]$ as the combined proton donor and, Lewis acid-based, non-nucleophilic, non-coordinating anion source.[64;65] However, Etienne et al. had previously shown this acid not to protonate $[Tp^{Me2}NbMe_2(PhCCMe)]$. An alternative, stronger acid $[H(OEt_2)_2][BAr^{f}_4]$ (Ar^{f}_4 = 3,5-$C_6H_3(CF_3)_2$)[106] has been extensively used to generate labile ether adducts of late transition metal alkyl complexes,[107] including Tp*-containing complexes.[108] Reactions of this acid with early transition metal alkyl complexes have not often been reported, although half-sandwich cationic chromium alkyls which polymerise olefins have been generated via this route.[109]

Preliminary NMR tube based reactions by Etienne et al. with $[Tp^{Me2}TaMe_2(PhCCMe)]$ resulted in a complex NMR spectrum. Full assignment was not possible at that time, but the ^1H spectrum showed the expected alteration of symmetry from C_s to C_1 as evidenced by the Tp^{Me2} C–*H* signals in the 5-6 ppm window changing from a 2:1 to 1:1:1 pattern. In order to remove some of the complexity, it was decided to focus on the symmetric but-2-yne ligand rather than PhC≡CMe in this project.

$[Tp^{Me2}NbMe_2(MeCCMe)]$ **(1)**, previously synthesised and characterised by Teuma,[110] was therefore an ideal starting point for this project. The advantage of this system over the known, catalytically active systems discussed above is its spectroscopic symmetry. No studies have as yet been conducted, but the degree of similarity of this complex to those demonstrating α–agostic interactions[14;100] provided an added potential for stabilisation of any cation synthesised, increasing the chance of its isolation.

2.4 Synthesis and Studies of $[Tp^{Me2}NbMe(OEt_2)(MeCCMe)][BAr^f_4]$ (2)

2.4.1 Preparation of $[Tp^{Me2}NbMe_2(MeCCMe)]$ (1)

The complex $[Tp^{Me2}NbMe_2(MeCCMe)]$ **(1)** was prepared in a four-step reaction. $NbCl_5$ was reduced by tributyltin hydride in DME at –78 °C to $NbCl_3$.dme, in 88% yield, following the literature method.[111] The ligands were then introduced sequentially to a solution of this purple, air-sensitive compound to give $[Tp^{Me2}NbCl_2(MeCCMe)]$ as described by Etienne et al.[112] Firstly $[NbCl_3.dme(CH_3C{\equiv}CCH_3)]$ was obtained by stirring $[NbCl_3.dme]$ overnight with but-2-yne in DCM, filtering through celite and evaporating to dryness. A solution of KTp^{Me2} in THF was then added and stirred for 6 h, resulting in a plum coloured solution. After extraction and purification $[Tp^{Me2}NbCl_2(MeCCMe)]$ was isolated as a purple solid. The final step followed a similar procedure to that used previously by Etienne et al.,[110;112] with an excess of MeLi added dropwise to a solution of $[Tp^{Me2}NbCl_2(MeCCMe)]$ in toluene at –20 °C. The reaction mixture stirred for 30 min at –78 °C and a further 30 min at room temperature; monitoring by NMR ensured completion. Yellow crystalline $[Tp^{Me2}NbMe_2(MeCCMe)]$ was isolated in a yield of 86%.

2.4.2 Synthesis and Characterisation of $[Tp^{Me2}NbMe(OEt_2)(MeCCMe)][BAr^f_4]$ (2)

The orange complex $[Tp^{Me2}NbMe(OEt_2)(MeCCMe)][BAr^f_4]$ **(2)** was initially prepared on a small scale (0.05 mmol) to establish optimal conditions. It was assumed that the complex would be highly reactive and thus both air- and temperature-sensitive – and indeed it is.

$$[Tp^{Me2}NbMe_2(CH_3CCCH_3)] + [H(OEt_2)_2][BAr^f_4] \xrightarrow[\text{at -80°C warming to -60°C}]{\text{DCM}} [Tp^{Me2}NbMe(OEt_2)(CH_3CCCH_3)][BAr^f_4] + CH_4 + OEt_2 \qquad [2.1]$$

Protonation of the yellow dimethyl complex [$Tp^{Me2}NbMe_2(MeCCMe)$] **(1)** with 1 equivalent of $[H(OEt_2)_2][BAr^f_4]$ **(3)** at –80 °C was achieved by the addition of pre-cooled d_2-DCM to a mixture of the two powders in an NMR tube equipped with a Teflon valve. Complex **1** quickly dissolved to form a yellow solution; as the acid **3** dissolved, the solution became bright orange. The evolution of gas, identified as methane (^1H δ 0.17), was observed after 2-3 min as the reaction progressed. The product was found to be unstable in solution above 0 °C after several min; and after 3 d at –35 °C. No associated colour change was noted. Use of an excess of acid, **3,** did not result in sequential protonation of the methyl groups, but the stability of **2** did appear to be adversely effected.

Complex **2** was characterised by ^1H and ^{13}C NMR at –80 °C, shown in Figure 2.5. This was the most suitable of all characterisation techniques as the reaction vessel could be placed directly into the NMR spectrometer, reducing the opportunities for decomposition by eliminating the need to manipulate the reaction mixture. Other advantages of this procedure include: the facile control of sample temperature; small-scale sample preparation; maintenance of inert conditions and reaction monitoring.

The identification of **2** was achieved through the interpretation and assignment of the ^1H and ^{13}C spectra, based on the predicted outcome of the reaction. Essential to this was an indication of asymmetry at the metal centre and the unambiguous identification of co-ordinated diethyl ether. The ^1H spectral window at 5.5-6.5 ppm shows features corresponding to the Tp^{Me2} C–*H*s at the 4-point of the pyrozolyl group (also butene from decomposition and d_2-DCM) and is diagnostic of any alteration in symmetry at the metal centre. The starting material, **1**, has a plane of symmetry arising from the locked vertical position of the but-2-yne within the Tp^{Me2} cleft, and its ^1H-NMR spectrum shows Tp^{Me2} C–*H* peaks in a 1:2 ratio. The replacement of one CH_3 group breaks this symmetry leading to a 1:1:1 ratio, illustrated in Figure 2.5(a). It is this region in particular that enables the identification of the number of products and their relative proportions. In addition, rather than the 1:1:2:2 ratio of the six Tp^{Me2} methyl groups observed for **1**, the observation of six separate resonances in the ^1H and ^{13}C spectra for **2** testifies to the absence of a plane of symmetry.

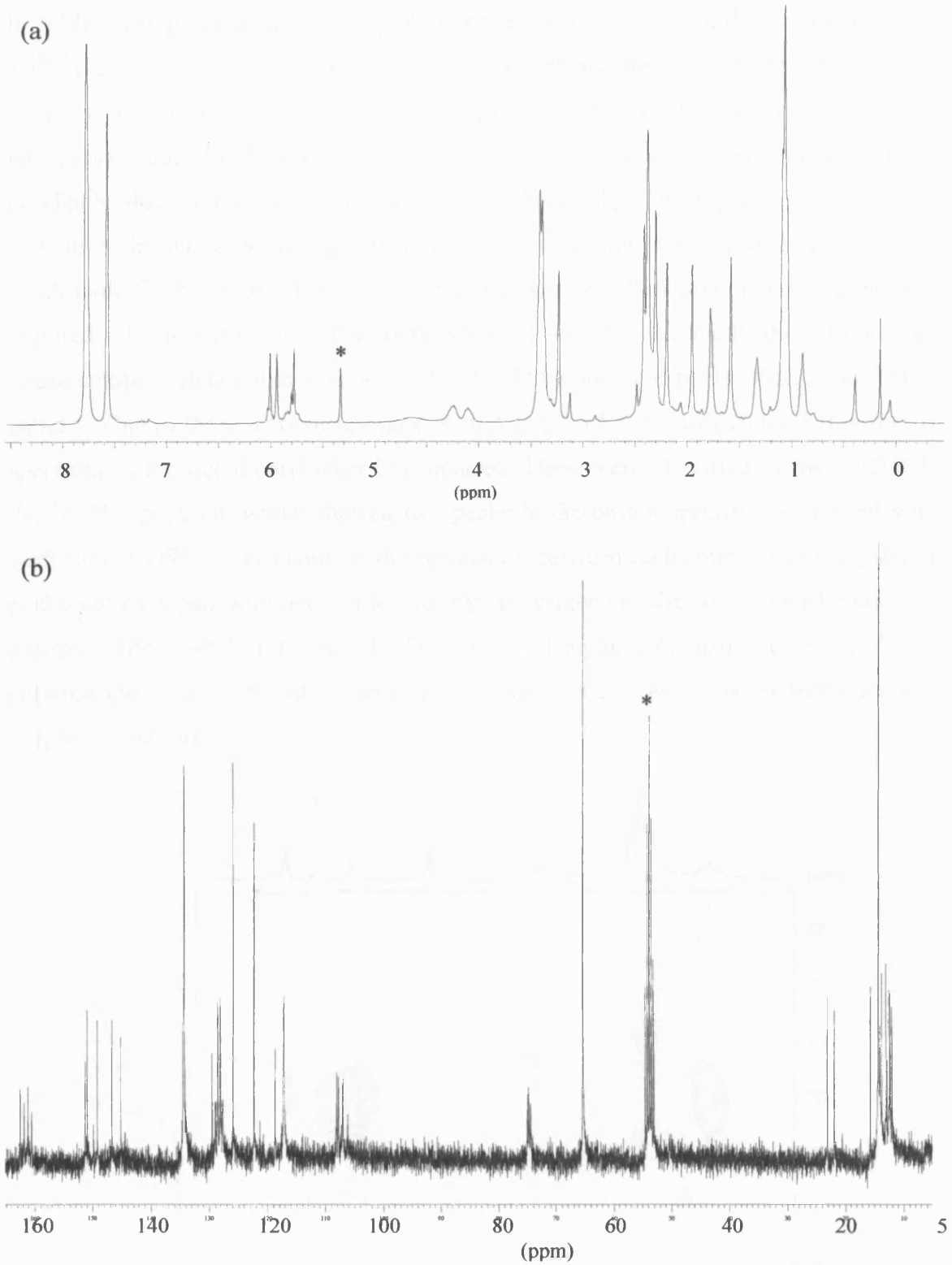

Figure 2.5: NMR spectra of the reaction mixture: $[Tp^{Me2}NbMe_2(MeCCMe)]$ and $[H(OEt_2)_2][BAr^f{}_4]$ at –80 °C in CD_2Cl_2. (a) Full 300 MHz ^1H NMR spectrum, and (b) 75 MHz ^{13}C NMR spectrum in the 175-5 ppm range. * indicates solvent peak.

With the loss of either methyl group being equally probable, and the formation of a chiral metal centre, two enantiomeric products are expected, but are not distinguishable

by NMR. The predicted positioning of the ether, with one arm in and one arm out of the Tp^{Me2} cleft, gives rise to two possible CH_2 chemical environments and the multiplets at 4.24 and 4.11 ppm were provisionally assigned to these two methylene groups. The integration values for these peaks appeared to be too low, although these values may be unreliable due to the proximity of the very broad $Tp^{Me2}B$-*H* peak. The lack of resolution in the expected quartets, even allowing for the broadening from the quadrupole ^{93}Nb centre (I = 9/2), indicated that an alternative interpretation was required. Considering the ether to be static at –60 °C, the methylene protons are diastereotopic. Hence four sets of signals should be observed in ^1H NMR in an AMX_3 pattern. One of these pairs of resonances, at 3.4 and 3.5 ppm, was concealed in the ^1H spectrum by the free diethyl ether CH_2 quartet. These were identified by the ^1J HMQC ^{13}C-^1H 2D spectrum, which showed two peaks in the proton spectrum associated with each *C*H_2. COSY studies confirm the correlation between each couplet in these pairs of peaks and each pair with one of the two triplets assigned as the co-ordinated ether CH_3 groups. The HMQC (^2J) ^{13}C-^1H 2D spectrum (Figure 2.6) also shows correlation between the peaks assigned to the ether *C*H_2 and C*H*$_3$, as would be expected for this proposed structure.

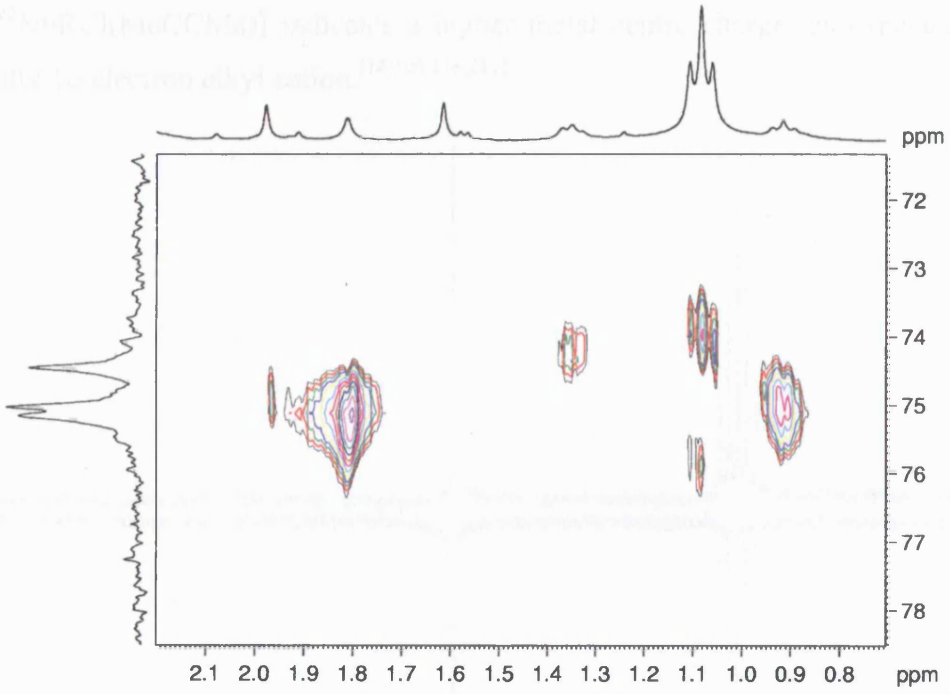

Figure 2.6: HMQC (^2J) ^{13}C-^1H 2D spectrum in the methylene proton range of $[Tp^{Me2}NbMe(OEt_2)(MeCCMe)][BAr^f_4]$ (**2**).

Peaks corresponding to the uncoordinated $[BAr^f_4]^-$ anion are present in both ^1H and ^{13}C spectra, but the loss of the acid $H(OEt_2)^+$ peak at 10.87 ppm clearly indicates its

consumption in the reaction. The reduction of the Nb–CH_3 peak to an integral value of 3H supports the proposal that the gas evolved in the reaction is CH_4. The anticipated positive charge at Nb will increase deshielding of the methyl group, causing a shift towards low field. This is particularly notable in the ^{13}C spectrum where the Nb–CH_3 is observed at 75.0 ppm, vs. 52.5 ppm in **1**. Identification of the Nb–CH_3 peak was achieved through the use of the ^{13}C DEPT spectrum, shown in Figure 2.7, distinguishing the co-ordinated ether CH_2 peaks by inversion. The ^{13}C-^{1}H 2D spectrum shows a cross-peak indicating the Nb–CH_3 peak is that at 1.80 ppm. The change in the Nb–CH_3 chemical shift of the product from the dimethyl moiety (0.36 ppm) reveals the change in the electronic nature of the metal centre is as anticipated. The ^{1}H-coupled ^{13}C spectrum gave a coupling constant of $^{1}J_{C\text{-}H}$ = 121 Hz, comparable to that for [Tp^{Me2}NbMe$_2$(MeCCMe)], and typical of an sp^3-hybridized Me group.[113] It was noted that no α-agostic interaction could be inferred from the data, nor did migratory insertion of the 4e$^-$ alkyne into the Nb–Me occur at –20 °C.[114] The quaternary carbons observed at 254.8 and 245.8 ppm (–60 °C) confirm the continued presence of the alkyne ligand as a 4e$^-$ donor, a 2e$^-$ donor alkyne group being expected in the range between δ 179 – 169.[115] The alkyne signals' lower-field shift in the ^{13}C spectrum vs. neutral [Tp^{Me2}NbRCl(MeCCMe)] indicates a higher metal centre charge, as expected for the formally 16 electron alkyl cation.[14;100;116;117]

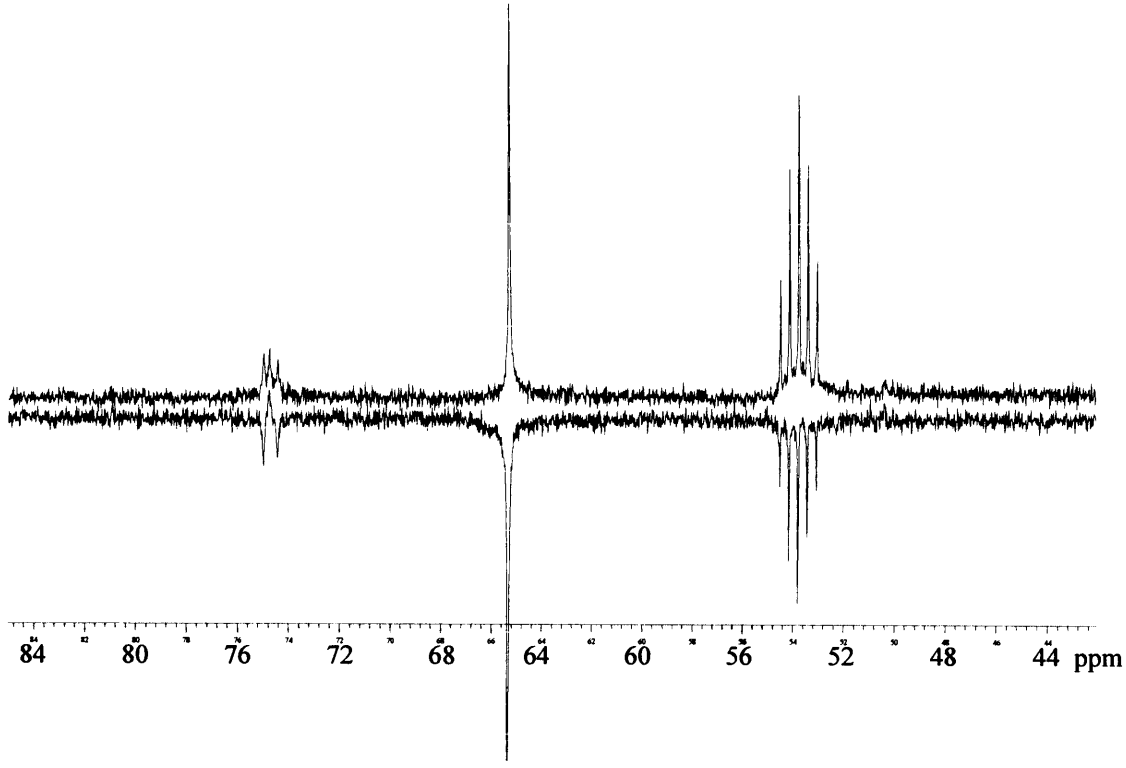

Figure 2.7: ^{13}C NMR (top) and ^{13}C DEPT (bottom) spectra of [Tp^{Me2}NbMe(OEt$_2$)(MeCCMe)][BAr$^f_4$] (**2**).

Although the NMR spectra indicated a high percentage of conversion, no definitive yield can be reported, as attempts to isolate **2** from solution were largely unsuccessful. Pumping the solution to dryness yielded only a mixture of decomposition products.

A larger scale reaction (0.24 mmol) was carried out under similar conditions in DCM, and again the yellow solution turned orange. External condensation of moisture onto the walls of the reaction flask precluded the observation of gas evolution. The solution volume was reduced and the remainder left overnight at –35 °C. No crystallisation occurred. Pumping a small amount of the solution to dryness to add deuterated solvent resulted in an orange oil showing a variety of unidentified products by NMR. A larger scale reaction in d_2-DCM, to monitor the reaction by NMR, was not undertaken as no reliable method for isolating **2** could be found.

The elemental analysis of **2** under anaerobic conditions produced the results shown in Table 2.1. The poor correlation between theoretical and experimental values is likely due to the analysis being conducted at room temperature and, or more probably, product decomposition on work-up.

Element	Theoretical %	Experimental % (run 1)	Experimental % (run 2)
C	47.58	36.58	37.03
H	3.78	1.98	1.80
N	5.95	3.35	3.32

Table 2.1: Elemental analysis results for $[Tp^{Me2}NbMe(OEt_2)(MeCCMe)][BAr^f_4]$ (**2**).

2.4.3 X-Ray Structure of $[Tp^{Me2}NbMe(OEt_2)(MeCCMe)][BAr^f_4]$ (2)

Many attempts at crystallisation of **2** were performed. A DCM solution was layered with diethyl ether and left for 3 weeks at –35 °C; concentrated DCM solutions were slowly cooled from –20 °C to –80 °C and left for over 2 weeks and further solutions were prepared at –40 °C, allowed to stand for 2 h at –10 °C and left to crystallise at –35 °C. Microcrystals were observed after 12 h in the most concentrated solution at –80 °C, but in an insufficient quantity to isolate. They redissolved after 10 d without increasing in size or number. Three successful crystallisations occurred under similar circumstances. A d_2-DCM solution was placed at –60 °C in the NMR spectrometer

without spinning for over 6 h and kept overnight at a low, stable temperature. In two cases this was during an overnight NMR experiment and in the third case the sample had been transferred in an ethanol/liquid N_2 bath at the same temperature to a –35 °C freezer. Each time orange block crystals resulted. It is possible that only fresh, concentrated solutions yield crystals due to the gradual appearance of decomposition products; a stationary sample is undoubtedly an important factor in the successful crystallisation.

The proposed structure of **2** was confirmed by two separate X-ray diffraction studies of the orange block crystals; initially conducted at 180 K and subsequently at 120 K. Use of the lower temperature was employed in an attempt to reduce atomic vibrations. In both cases the space group was found to be $P\bar{1}$, a centrosymmetric space group, reflecting the expected 1:1 enantiomer distribution. The structure shows that the ligands adopt a distorted octahedral conformation around the metal centre, with the tridentate Tp^{Me2} maintaining its 3-fold symmetry, capping the complex and each of the three remaining ligands occupying one octahedral co-ordination site in a *fac* arrangement. The structure clearly shows the entrapment of one arm of the co-ordinated diethyl ether within the Tp^{Me2} cavity, depicted in Figure 2.8.

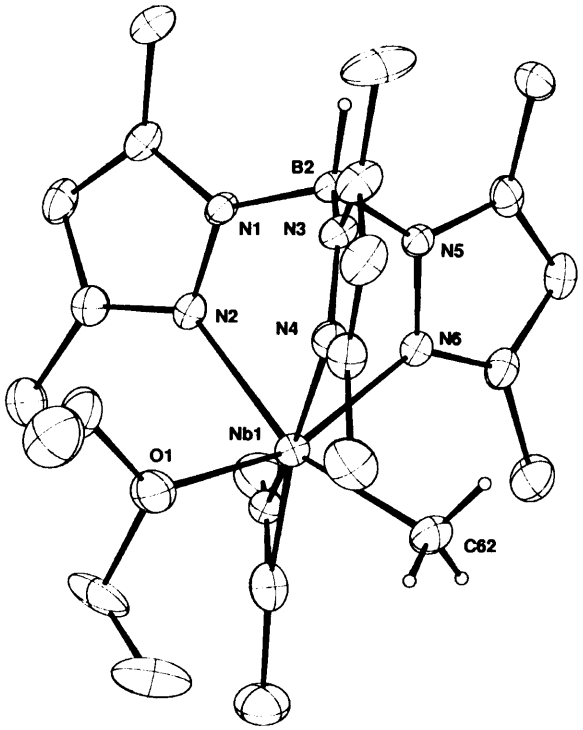

Figure 2.8: Structure of the cation portion of $[Tp^{Me2}NbMe(OEt_2)(MeCCMe)][BAr^f_4]$ (**2**) as determined by X-ray diffraction. The counterion and most hydrogen atoms are omitted for clarity; ellipsoids are drawn at the 30% probability level.

Disorder was found in the free ethyl arm of the diethyl ether, away from the Tp^{Me2}, and in the CF_3 groups of the $[BAr^f_4]^-$ anion, resulting in an R-value of 0.0531. The Nb–C bond (2.182(7) Å) lies at the shorter end of the range of Nb–C bond lengths observed in the series of neutral [TpNbCl(alkyl)(RCCMe)] complexes,[118] and is slightly shorter than that in complex **1** (Nb–C = 2.210(4), 2.213(4) Å),[110] in accord with the higher electrophilicity of the metal centre in the cation. In the ionic complex $[Cp_2TaMe_2][(C_6F_5)_3Al(\mu\text{-}Me)Al(C_6F_5)_3]$, the Ta–C bond lengths are comparable at 2.188(3) and 2.166(3) Å,[87] as would be expected given the similarity of the Nb and Ta centres and the effects of the lanthanide contraction in this region of the Periodic Table. Neutral $[L_2NbMe(PhC{\equiv}CSiMe_3)]$ (L = 6-methyl-2-trimethylsilylamido-pyridine) has a Nb–C bond length of 2.195(13) Å, whereas in the ion pair $[L_2Nb(PhC{\equiv}CSiMe_3)(\mu\text{-}Me)][B(C_6F_5)_3]$ it is significantly elongated to 2.611(5) Å[83] owing to the bridging nature of the methyl group.

The Tp^{Me2} ligand plays its characteristic directing role: one of the ethyl arms of the OEt_2 ligand sits in the cleft between two pyrazole rings, with the other (disordered) one pointing away from the pendant Me groups of Tp^{Me2}. The Nb–OEt_2 and Nb–C bond lengths are almost identical, with no Nb–O shortening apparent from the probable involvement of Nb–O π–bonding.[67] The presence of this π–bonding is evidenced by the planar nature of the Nb–O and O–C bonds.

The alkyne also sits within a Tp^{Me2} cleft; the bent nature of the alkyne ligand confirms it still to be a $4e^-$ donor. A C20–C21 bond length of 1.23(1) Å indicates preservation of the triple bond. Even allowing for our somewhat large esd, this is slightly shorter than the C–C bonds in the more electron rich, neutral species listed in Table 2.2: $[Tp^{Me2}NbCl_2(PhCCMe)]$, complex **1**, $[Tp^{Me2}NbCl(CH_2SiMe_3)(PhCCMe)]$ and $[Tp^{Me2}Nb(CO)(EtCN)(PhCCMe)]$. This latter complex also has longer Nb–C (alkyne) distances than those in **2**; again a combination of a neutral metal centre and the presence of strongly donating ligands. In $4e^-$ alkyne complexes in particular, definitive assignment of an oxidation state to the metal is a matter of some conjecture. The bond distances in **2** indicate that the alkyne is partially oxidised, so the niobium centre should not be regarded as Nb(V) (d^0).[118]

Unequal Nb–C (alkyne) bond lengths are observed for all the complexes listed in Table 2.2; with the asymmetry observed in **2** being at the more extreme end. These were observed in both crystal structure determinations, so are not due to experimental error. This asymmetry appears to be electronic in origin, as it does not depend upon the bulk of the alkyne substituents, and the shorter bond Nb–C(21) lies within the cleft. Evidence to support this lies in the Tp^{Me2} bonding: although the Nb–Tp^{Me2}N distances in **2** are not dissimilar, Nb–N(4) is 0.07 Å shorter than Nb–N(1) and 0.04 Å shorter than Nb–N(6). With N(1) lying trans to the alkyne, it suggests that the greater trans influence of the alkyne ligand destabilises the Nb–N(1) bond.

Complex	C–C (Å)	Nb–C (Å)	Nb–C (Å)
$[Tp^{Me2}Nb(CO)(EtCN)(PhCCMe)]$ [115;119]	1.307(3)	2.121(2)	2.169(2)
$[L_2Nb(PhC{\equiv}CSiMe_3)(\mu\text{-}Me)][B(C_6F_5)_3]$ [83]	1.313(6)	2.081(4)	2.117(4)
$[Tp^{Me2}NbCl(CH_2SiMe_3)(PhCCMe).Et_2O]$ [100]	1.305(5)	2.065(3)	2.078(3)
$[Tp^{Me2}NbCl_2(PhCCMe)]$ [96]	1.31(1)	2.050	2.093
complex **1** (unpublished data)	1.311(6)	2.048(4)	2.054(5)
complex **2** (this work)	1.234(10)	2.047(7)	2.104(8)

Table 2.2: Comparative bond lengths for the alkyne moiety in selected complexes.

2.5 Chemical Studies of the $[Tp^{Me2}NbMe(L)(MeCCMe)]^+$ System

Investigations were carried out into the steric and electronic effects of different electron donor ligands on the complex. Substitution of the diethyl ether in the reaction by other ethers or by more strongly electron donating phosphines give a preliminary overview of the stability requirements of the cationic metal centre. A summary is presented in Scheme 2.1.

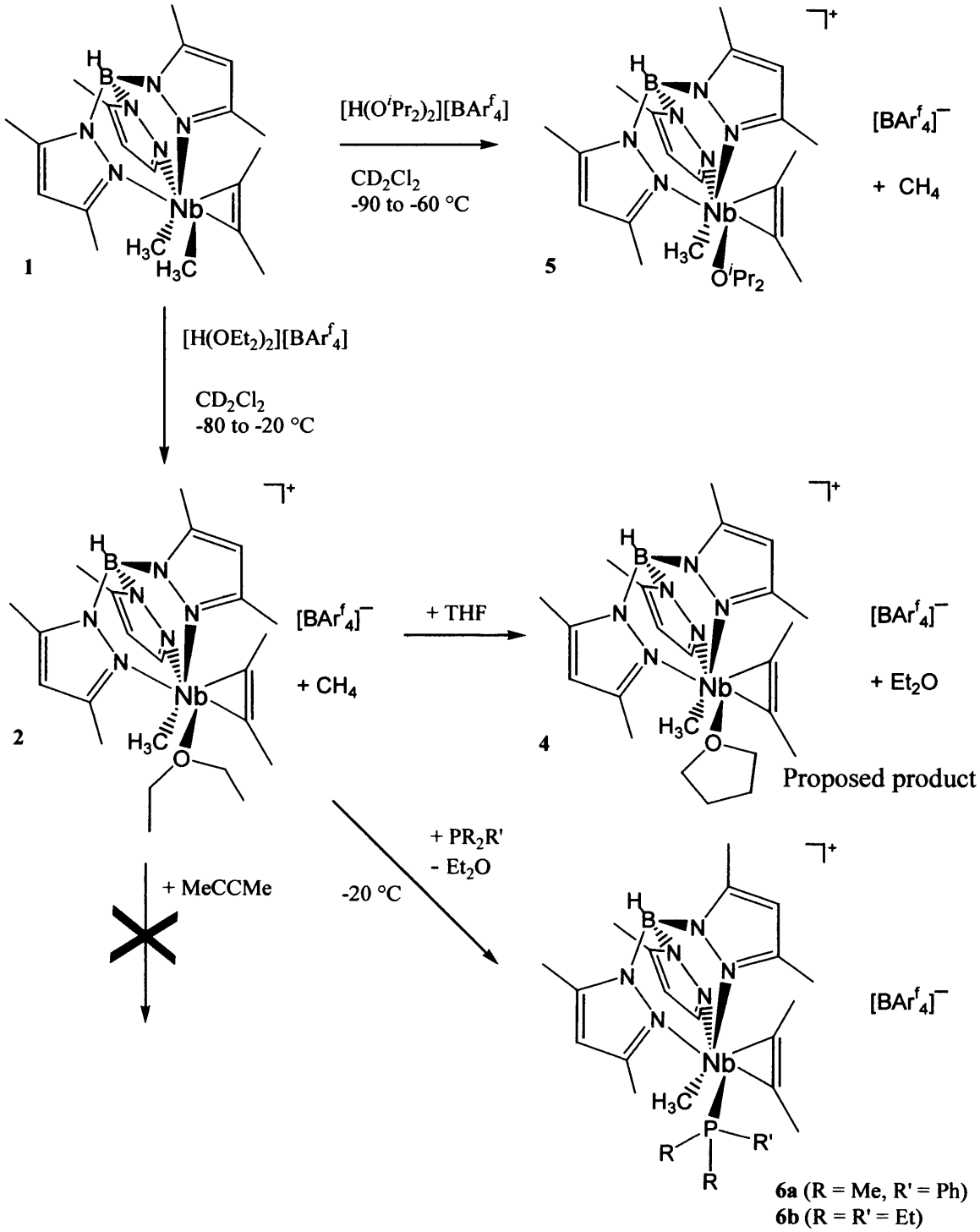

Scheme 2.1: Summary of the reactions conducted and the resulting complexes observed.

2.5.1 Reaction in the Presence of Other Ethers

Reaction of [$Tp^{Me2}NbMe_2(MeCCMe)$] (1) and [$H(OEt_2)_2$][BAr^f_4] (3) in d_8-THF

This reaction was conducted in a similar manner as for the formation of **2** (described earlier) using d_8-THF in place of d_2-DCM. The solution once again changed from yellow to orange, accompanied by effervescence. NMR studies conducted at –60 °C revealed the formation of a mixture of two products: one was identified as **2**; and the other (**4**) is tentatively assigned as the d_8-THF adduct. On standing overnight at –35 °C, the intensity of the peaks arising from **2** decreased in relation to those from **4**, indicative of a gradual ligand exchange, with the labile diethyl ether being displaced by the more polar electron donor. These observations suggest that the second product is [$Tp^{Me2}NbMe(OC_4D_8)(MeCCMe)$][$BAr^f_4$]. Studies conducted at –20 °C showed a clear major product in the ^1H NMR spectrum after only 30 min, as depicted in Figure 2.9. Integration of the 2.4-2.5 ppm region indicates it contains 12 protons (4 methyl peaks), but once again no Nb–Me resonance was observed in the ^{13}C NMR spectrum (Figure 2.10) to permit unambiguous assignment. The failure to observe co-ordinated THF in the ^1H NMR spectrum is to be expected, with the combination of a low percentage of co-ordination and ^1H in the solvent. However, the absence of a signal corresponding to the Nb–Me moiety in the ^{13}C NMR spectra leaves some questions as to the nature of **4**.

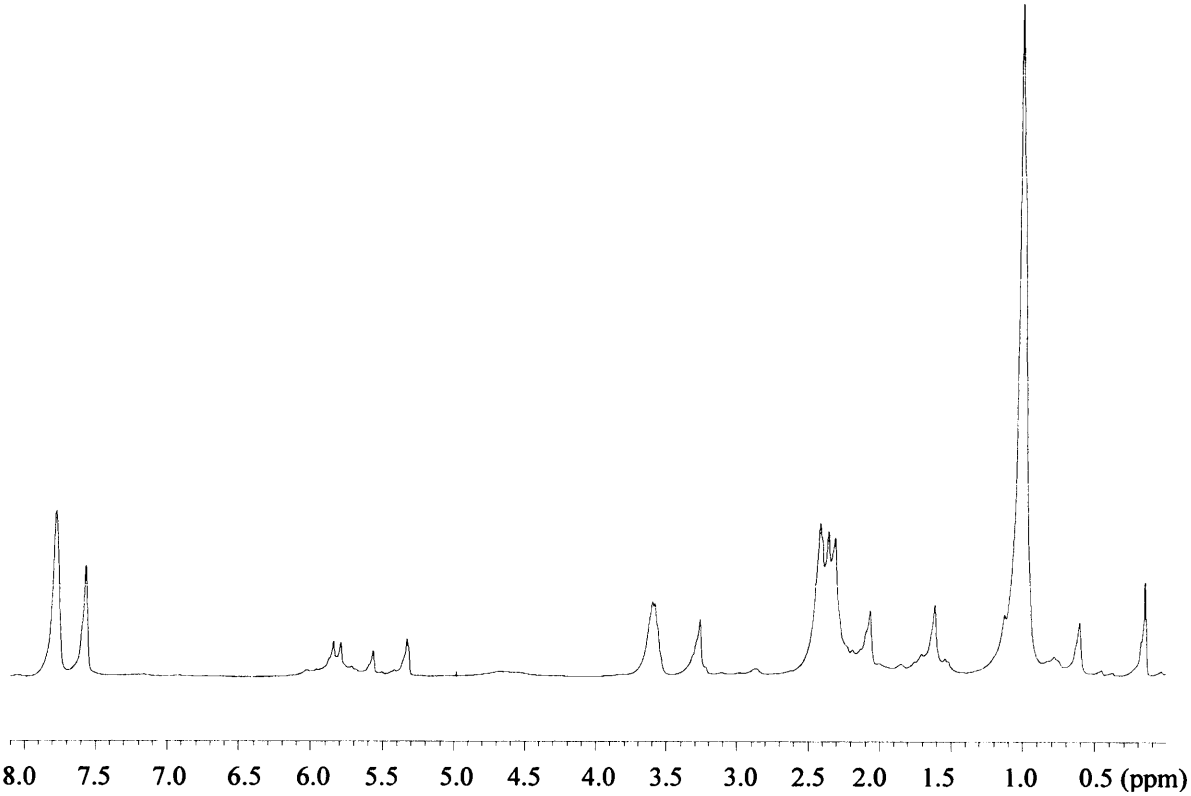

Fig 2.9: ^1H-NMR spectrum of the reaction between [$Tp^{Me2}NbMe_2(MeCCMe)$] (**1**) and [$H(OEt_2)_2$][BAr^f_4] (**3**) in d_8-THF at –20 °C (8-0 ppm range).

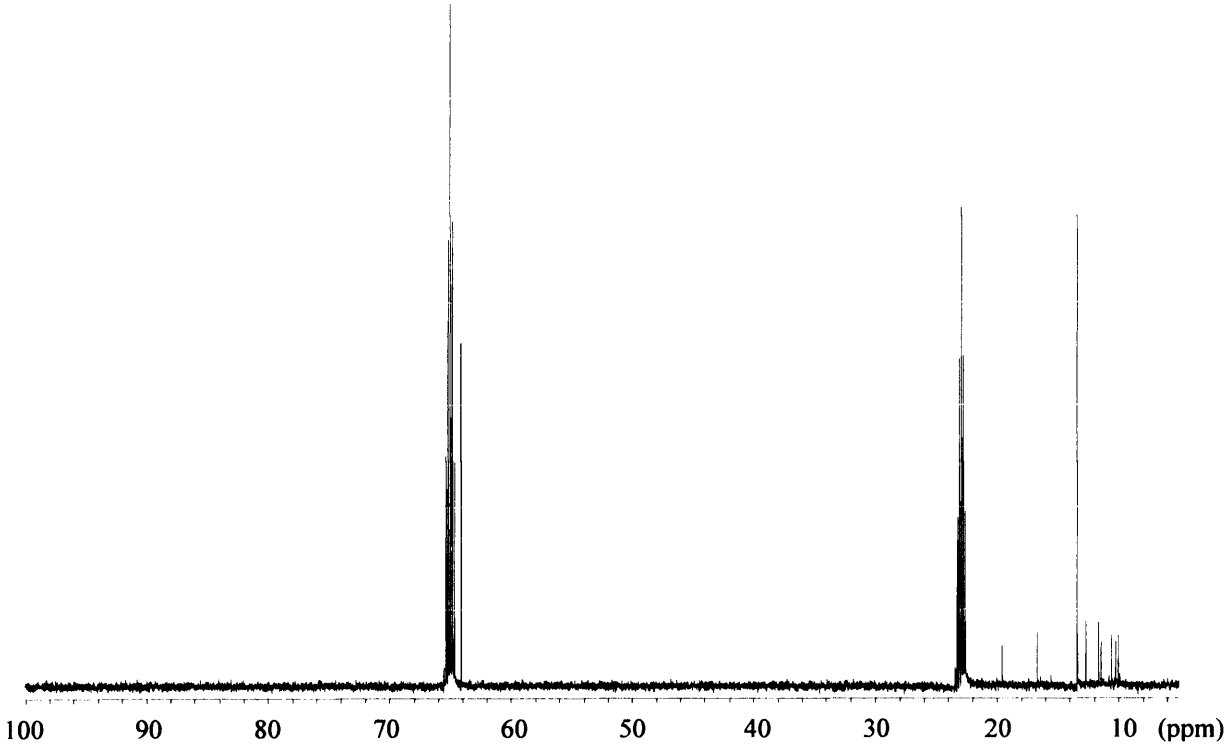

Figure 2.10: ^{13}C NMR spectrum of the reaction between [$Tp^{Me2}NbMe_2$(MeCCMe)] (**1**) and [$H(OEt_2)_2$][BAr^f_4] (**3**) in d_8-THF (100-5 ppm range).

On dissolving the acid **3** separately in d_8-THF prior to addition to **1**, a much reduced initial ratio of diethyl ether adduct was observed, and the main peaks in the spectra obtained corresponded to those noted for **4** in earlier experiments. Again no Nb–Me moiety was positively identified, even with using ^1H–^{13}C correlation spectroscopy.

Attempts to isolate an h_8-THF adduct by conducting the reaction in a protic solvent and pumping to near-dryness before addition of deuterated solvent only resulted in decomposition or solvent-dominated spectra. Deuterium NMR spectra of reactions in d_8-THF with the solvent being replaced by protonated THF gave similarly poor spectra.

It is possible that the THF undergoes ring opening in the presence of the acid – a strong electrophile – giving rise to a neutral Nb–$OCH_2CH_2CH_2CH_3$ adduct. This complex would be able to undergo an additional reaction to lose the second Nb–Me group. Indeed the chemical shifts of the Me*C*≡*C*Me at ~ 40 ppm higher field than observed for the other adducts and **1** indicates further investigation is required. Future experiments to establish the exact nature of **4** could also involve the addition of a phosphine to **4** to investigate if ligand exchange occurs. If so, and if the Nb-CH_3 becomes visible, it can be concluded that product **4** is [Tp^{Me2}NbMe(THF)(MeCCMe)][BAr^f_4].

Reaction of [$Tp^{Me2}NbMe_2(MeCCMe)$] (1) with [$H(^iPr_2O)_2$][BAr^f_4]

Initially, **1** and [$H(^iPr_2O)_2$][BAr^f_4] were reacted in a similar manner to that for the formation of **2**, as described above. Once again, the solution was seen to change from yellow to orange with the evolution of gas, but NMR spectra showed a mixture of decomposition products. In order to establish whether this arose from the thermal sensitivity of the product formed in this reaction, the method was altered.

Complex **1** and [$H(^iPr_2O)_2$][BAr^f_4] were placed in separate NMR tubes at –50 °C. Pre-cooled d_2-DCM was added to each; and once all solids had dissolved the temperature was lowered to –90 °C. Again, **1** quickly dissolved to form a yellow solution. This was added via cannula to the [$H(^iPr_2O)_2$][BAr^f_4] solution, which had solidified at the reduced temperature. Placing the two-phase NMR sample directly into a pre-cooled probe of an NMR spectrometer at –80 °C allowed the reaction to be monitored as the solution of **3** melted and the initial product (**5**) was generated. The gradual mixing of the two materials and formation of **5** took place over a period of 5 min, with the reaction moving to completion over 30 min as the remaining acid dissolved. The product was found to be unstable in solution at –35 °C after a number of minutes and was unstable at –60 °C after less than 1 h. On standing at room temperature the solution gradually darkens to a deep red colour. This instability is attributed to the steric bulk of the diisopropyl ether; it readily dissociates from the crowded coordination sphere of niobium, and in the absence of a suitable donor ligand the co-ordinatively unsaturated cation $[Tp^{Me2}NbMe(MeC{\equiv}CMe)]^+$ decomposes.

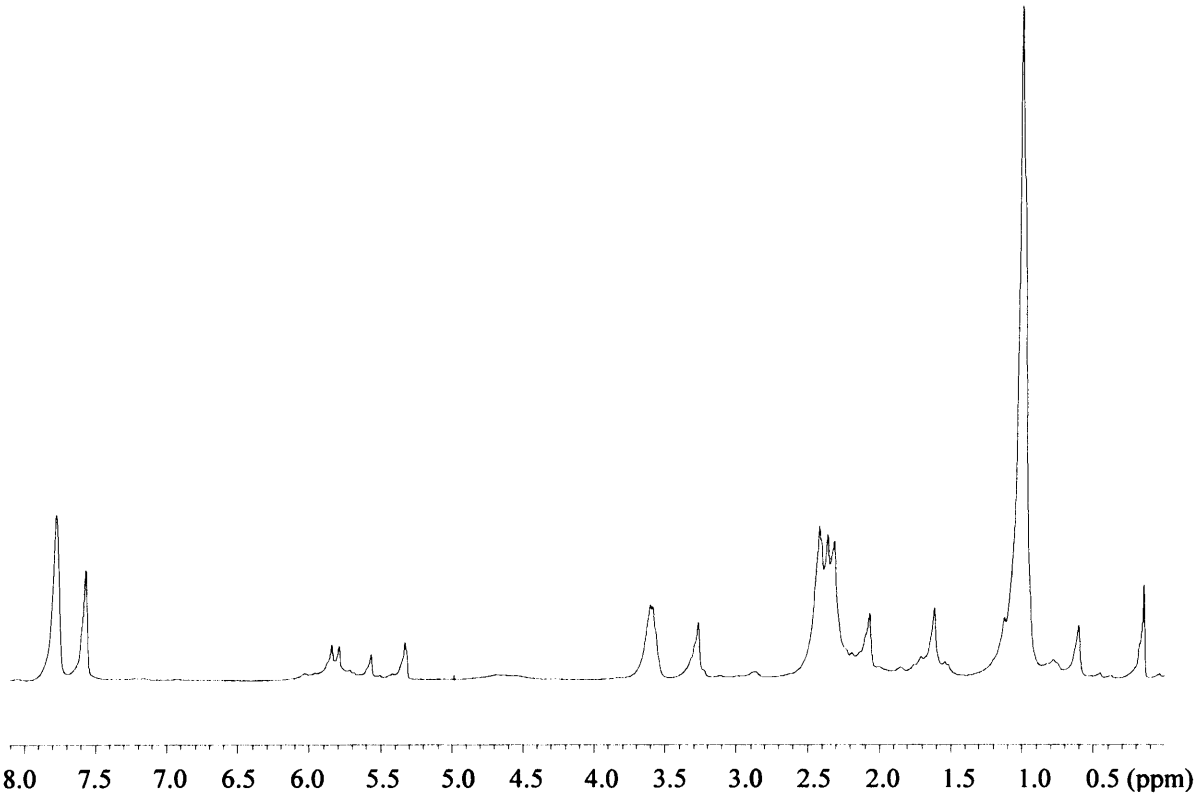

Figure 2.11: ^{1}H NMR spectrum of the complex formed by reaction of $[Tp^{Me2}NbMe_2(MeCCMe)]$ (**1**) with $[H(^{i}Pr_2O)_2][BAr^{f}_4]$ in DCM at –80 °C.

The ^{1}H NMR spectrum recorded at –80 °C in Figure 2.11 revealed the characteristic 1:1:1 ratio of the Tp^{Me2} protons at 5.85, 5.80 and 5.57 ppm confirming that a reaction had occurred. The free ether C–H (3.61 ppm) and C–Me (0.98 ppm) peaks indicate that the acid solution melted, but no co-ordinated ether was observed. Of the nine CH_3 peaks expected (six Tp^{Me2} 3,5 C–CH_3, two butyne ≡C–CH_3, one Nb–CH_3) only four have been unambiguously assigned through ^{1}H-^{13}C 2D NMR. The line broadening caused by the low temperature affects all the peaks, prevented the identification of the Nb–CH_3 peak by broadening due to the quadrupolar niobium nucleus. The 2D correlation spectrum did not show sufficient intensity for this peak to be assigned in the ^{1}H spectrum. The ^{13}C spectrum has been fully assigned, confirming the generation of the $[Tp^{Me2}NbMe(MeCCMe)]^{+}$ cationic species, again with no observable ether co-ordination. Key features are similar to those of **2** with, a ^{13}C signal at δ 70.5 (q, $^{1}J_{CH}$ = 121 Hz), appearing as the Nb–Me signature.

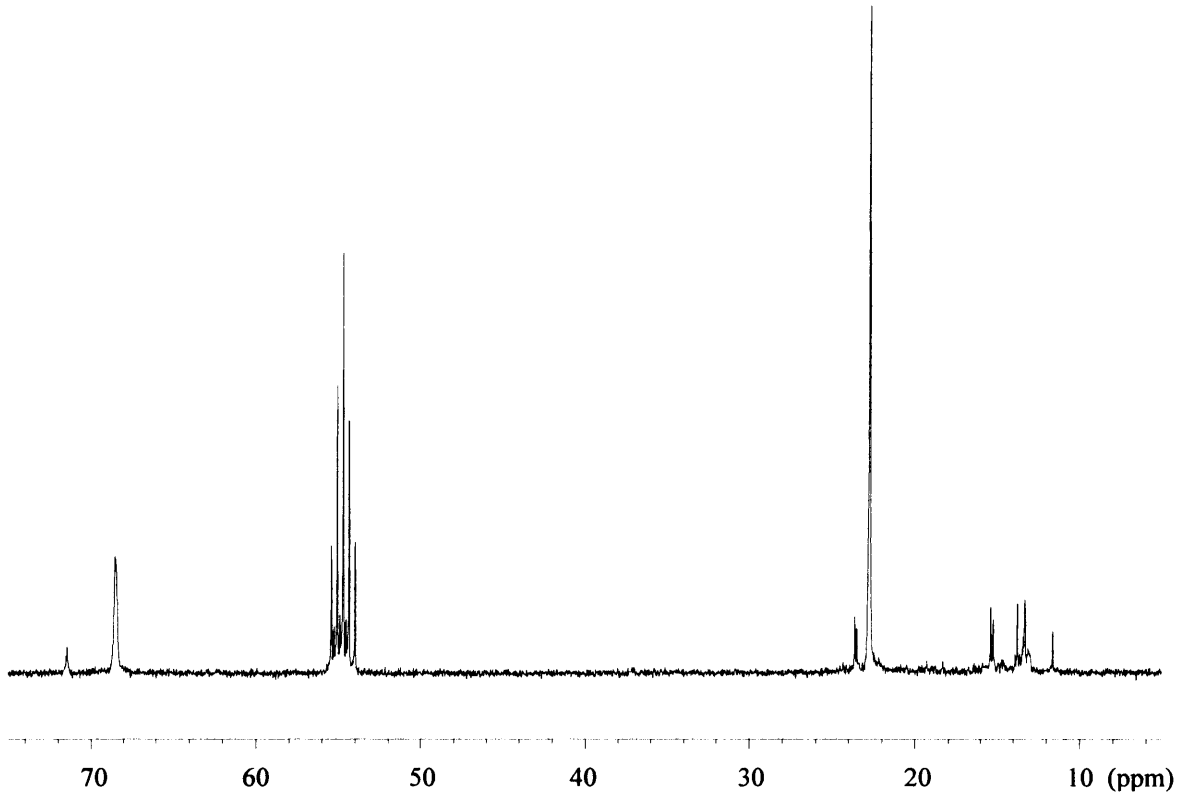

Figure 2.12: ^{13}C NMR spectrum of the complex formed by reaction of $[Tp^{Me2}NbMe_2(MeCCMe)]$ (**1**) with $[H(^iPr_2O)_2][BAr^f_4]$ (75-5 ppm) at –80 °C.

The ancillary ligands are observed at comparable chemical shifts to those of **2**, confirming their retention and indicating a similar chemical environment. A trace impurity or decomposition product is seen at 36.3 ppm, which is also observed in some spectra of reactions with phosphines. It is proposed that the lack of observable co-ordinated ether arises from the rapid association/dissociation of the weakly co-ordinated ether.

2.5.2 Investigation into the Influence of Stronger Electron Donors

With their stronger Lewis basicity than ethers, phosphines and alkynes make stronger electron donors, so reactions were conducted to investigate the proclivity of phosphines to co-ordinate to our cationic niobium centre. It was proposed that complexation with better electron donors would result in a more stable cation, reflected by an increased thermal stability of the products. This was employed to test if the cation $[Tp^{Me2}NbMe(O^iPr_2)(MeCCMe)]^+$ was really present in the reaction between **1** and **3**. PMe_2Ph was added to the reaction mixture in an attempt to co-ordinate it to the charged metal centre and stabilise the complex. As the Tp^{Me2}–*H* region of the ^1H NMR spectrum did not show peaks in a ratio of 1:1:1, we infer that decomposition of the

cation occurred before ligand exchange. This tallies with our observation in the catalytic trials described in Section 2.6.

On reaction of **1** with **3** in the presence of a phosphine, there are two possible routes for protonation of the Nb-bound methyl, illustrated in Scheme 2.2, which our experiments allowed us to investigate. Initial protonation of the phosphine by **3** may result in a much slower methyl abstraction from the metal centre. In this case, only the phosphine adduct would be expected to form as the proximity of the phosphine would render this the kinetic product, and its stronger donor properties would ensure that it was also the thermodynamically favoured product. However, if methyl protonation is kinetically favoured we would expect to see the formation of **2** followed by subsequent substitution to give phosphine adducts.

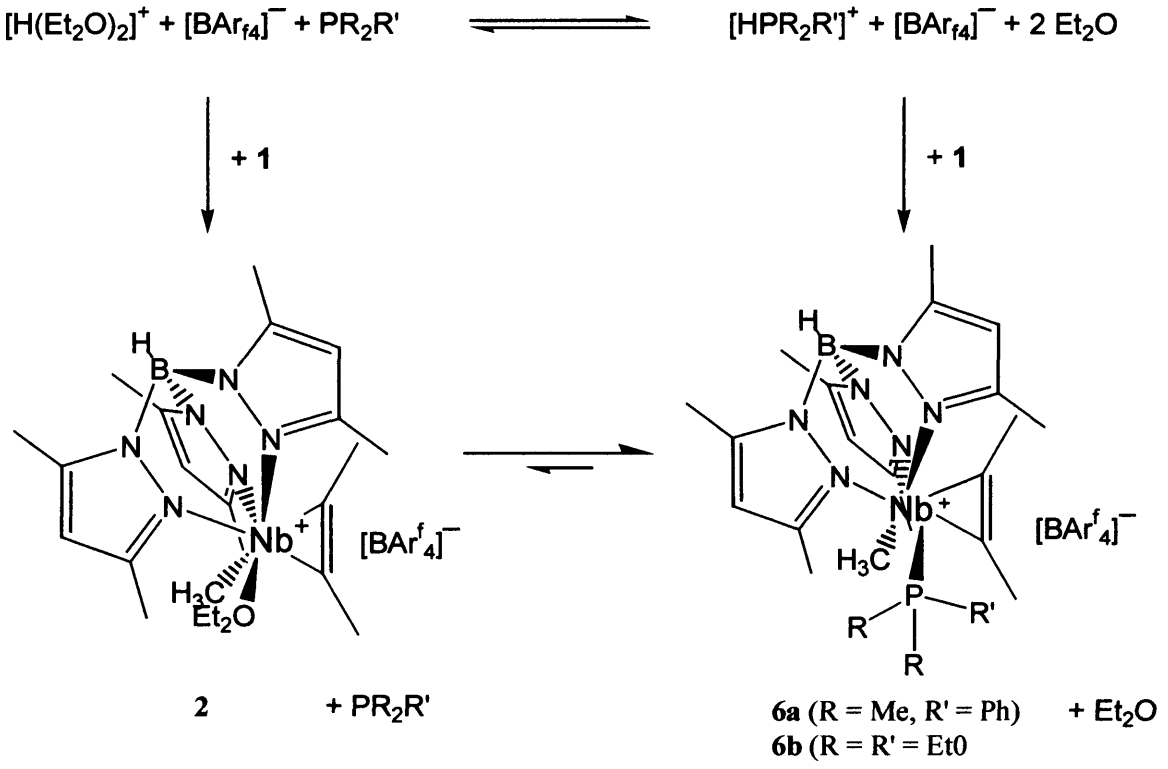

Scheme 2.2: Alternative reaction routes for the formation of **6a** and **6b**.

From the experiments described below, it appears that in each case initial protonation occurs at the phosphine, which then reacts with **1** to form the phosphine adduct with no substantial competition from the diethyl ether.

Reaction of $[Tp^{Me2}NbMe_2(MeCCMe)]$ (1), $[H(Et_2O)_2][BAr^f_4]$ (3) and PMe_2Ph

In the presence of excess dimethylphenylphospine, the diethyl ether ligand of **2** is quantitatively replaced between –60 and –20 °C over 18 h to give $[Tp^{Me2}NbMe(PMe_2Ph)(MeCCMe)][BAr^f_4]$ (**6a**), characterised by NMR spectroscopy at –60 °C. The ^1H NMR spectra are shown in Figure 2.13 below. This reaction was also conducted using a 'one-pot' route, similar to that for the formation of **2**. A cooled solution of **1** with an excess of PMe_2Ph was added to a solution of acid **3** at –80 °C, and the reaction was monitored by NMR spectroscopy at –40 °C over a number of hours. After 3 h a mixture of **1**, the PMe_2Ph adduct and the diethyl adduct **2** was observed. After storing at –35 °C for 48 h, the solution had changed from yellow to deep red, and its NMR spectrum indicated the reaction had gone to completion; as predicted, no exchange between the co-ordinated phosphine and the diethyl ether took place. Solutions of **6a** are stable for 24 h below –20 °C, with gradual decomposition occurring over the course of a week.

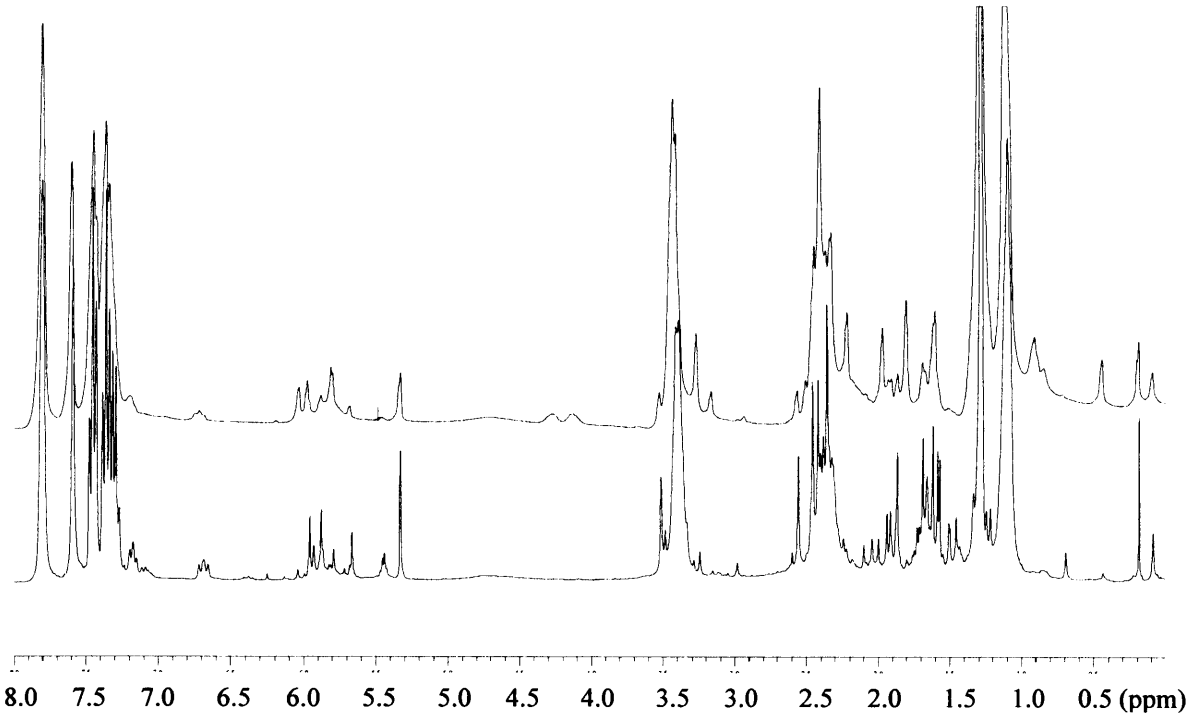

Figure 2.13: ^1H NMR spectra of the complex formed by reaction of $[Tp^{Me2}NbMe(Et_2O)(MeCCMe)][BAr^f_4]$ (**2**) and PMe_2Ph at –60 °C after 10 min (top) and 18 h (bottom).

Prominent resonances in the ^{1}H and ^{13}C NMR spectra of **6a**, at δ 1.68 and 95.1 (q, $^{1}J_{CH}$ = 122 Hz), respectively are assigned to the Nb–Me moiety, which shows no apparent coupling with the phosphorus of the phosphine ligand (^{31}P-NMR δ -1.75). The diastereotopic phosphine methyl groups appear at δ 1.93 and 1.25 in the ^{1}H NMR spectrum.

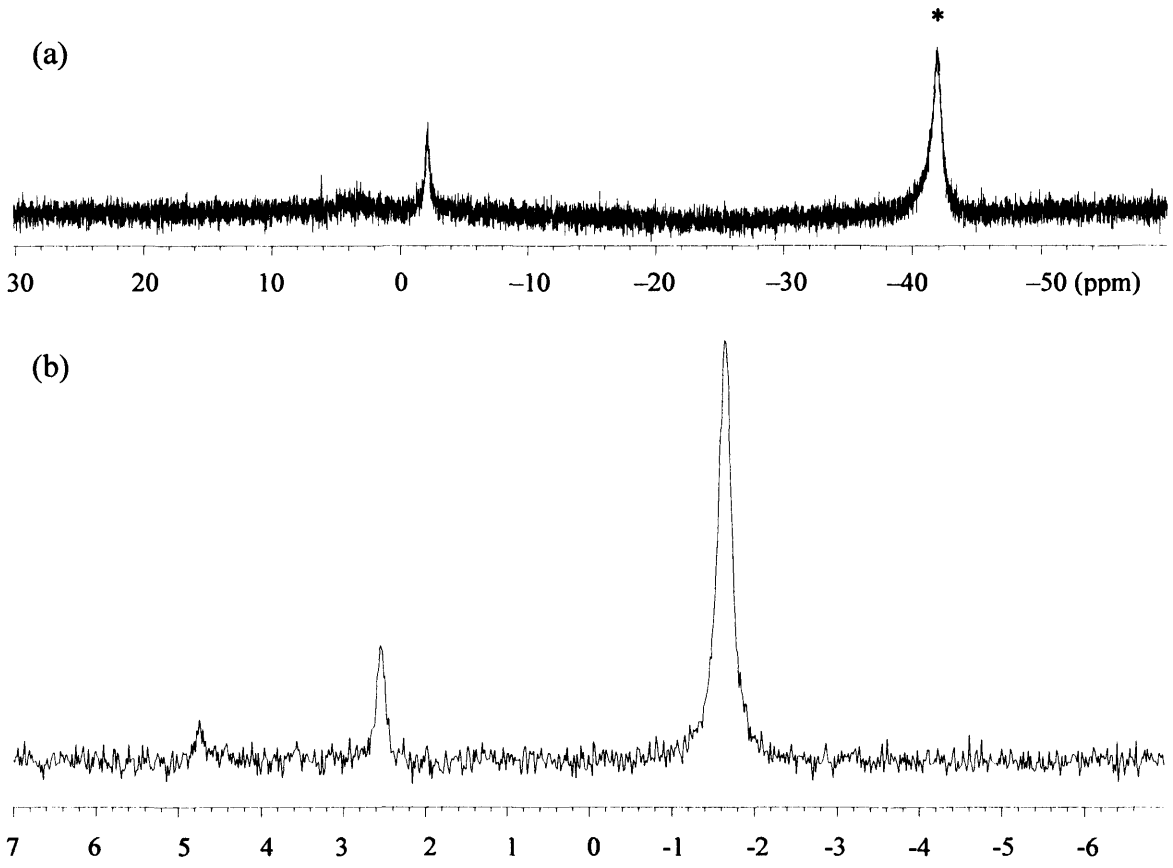

Figure 2.14: Decoupled ^{31}P NMR spectrum of the complex formed by reaction of $[Tp^{Me2}NbMe(Et_2O)(MeCCMe)][BAr^{f}_{4}]$ (**2**) and PMe_2Ph at –60 °C after 48 h
(a) over the range 75 - 5 ppm and (b) expanded around 0 between 7 and –7 ppm. * indicates free PMe_2Ph

The asymmetric phosphine has a preferred orientation in the crowded co-ordination sphere of the cation centre. This is not necessarily that of the initial product, as this kinetic isomer involves the protonation of the Nb-Me group. A clear preference for one orientation on formation of **6a** is seen in both ^{31}P and ^{1}H NMR spectra. A small quantity of a second and a tiny amount of a third isomer were present after 12 h, but these did not increase on warming or leaving for longer. The phosphine appears to be too hindered by the phenyl ring to rotate around the Nb–P bond, leaving dissociation and reassociation the only route to isomerisation. The increased stability of **6a** (both thermal and temoral) relative to the ether adducts demonstrates the more strongly

bonding nature of the phosphine. Although we would not expect it to dissociate readily, the gradual isomerisation indicates that it is sufficiently labile for the formation of a thermodynamic product to be possible. From this it is concluded that the initial isomer is also the most sterically favoured, with the other isomers forming as the phosphine dissociates, rotates and associates. The isomer distribution is dictated by the probability of the phenyl ring being in a favourable orientation to the other ligands at the metal centre at the moment of association. During protonation the phosphine is likely to approach the methyl group from below the Tp^{Me2} ligand, with the phenyl group pointing away from the metal centre. As methane exits the co-ordination sphere and the phosphine bonds to niobium, the phenyl group will be trapped in the cleft of Tp^{Me2}. When this dissociates and rotates so a methyl group is in the cleft, the orientation of the phenyl group will inhibit reassociation more effectively when closer to the alkyne than the methyl. The chiral niobium metal centre gives rise to two diastereoisomers and therefore six separate Tp^{Me2} methyl peaks are expected in the 5.5-6.5 ppm region of the ^1H NMR spectra. However, these were not observed, suggesting the difference in chemical shift is insufficient for them to be distinguished under the reaction conditions.

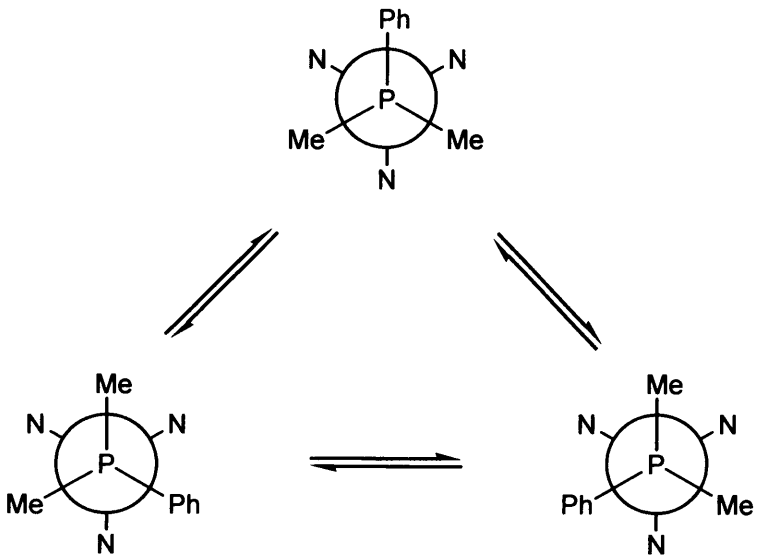

Scheme 2.3: Schematic representation of the possible rotamers of $[Tp^{Me2}NbMe(PMe_2Ph)(MeCCMe)][BAr^f_4]$ (**6a**).

Reaction of $[Tp^{Me2}NbMe_2(MeCCMe)]$ (1), $[H(Et_2O)_2][BAr^f_4]$ (3) and PEt_3

The more basic phosphine PEt_3 was employed in the same manner as PMe_2Ph, with the intention both to simplify the spectra and to investigate the effects of ligand basicity and cone angle. When the reaction was carried out using the 'one-pot' method, the formation of a different phosphine species, presumed to be $[HPEt_3]^+$, was observed, but no subsequent reaction with **1** occurred, even on leaving the reaction mixture for 2 d at –35 °C. This suggests the basicity of the Nb–Me moiety is intermediate between that of PMe_2Ph and PEt_3.

Reaction of **2** with an excess of PEt_3 at –40 °C resulted in the gradual replacement of Et_2O with PEt_3 and the formation of $[Tp^{Me2}NbMe(PEt_3)(MeCCMe)][BAr^f_4]$ (**6b**) over 12 h. Qualitatively, the nature of the phosphine does not appear to influence the rate of reaction and no significant increase in the rate of decomposition through reaction with the excess PEt_3 was observed. The Nb–Me resonances at δ 1.7 (^{1}H) and 94.7 (^{13}C) are comparable with those of **6b** and show a degree broadening due to the phosphine ligand (^{31}P-NMR δ 15.3).

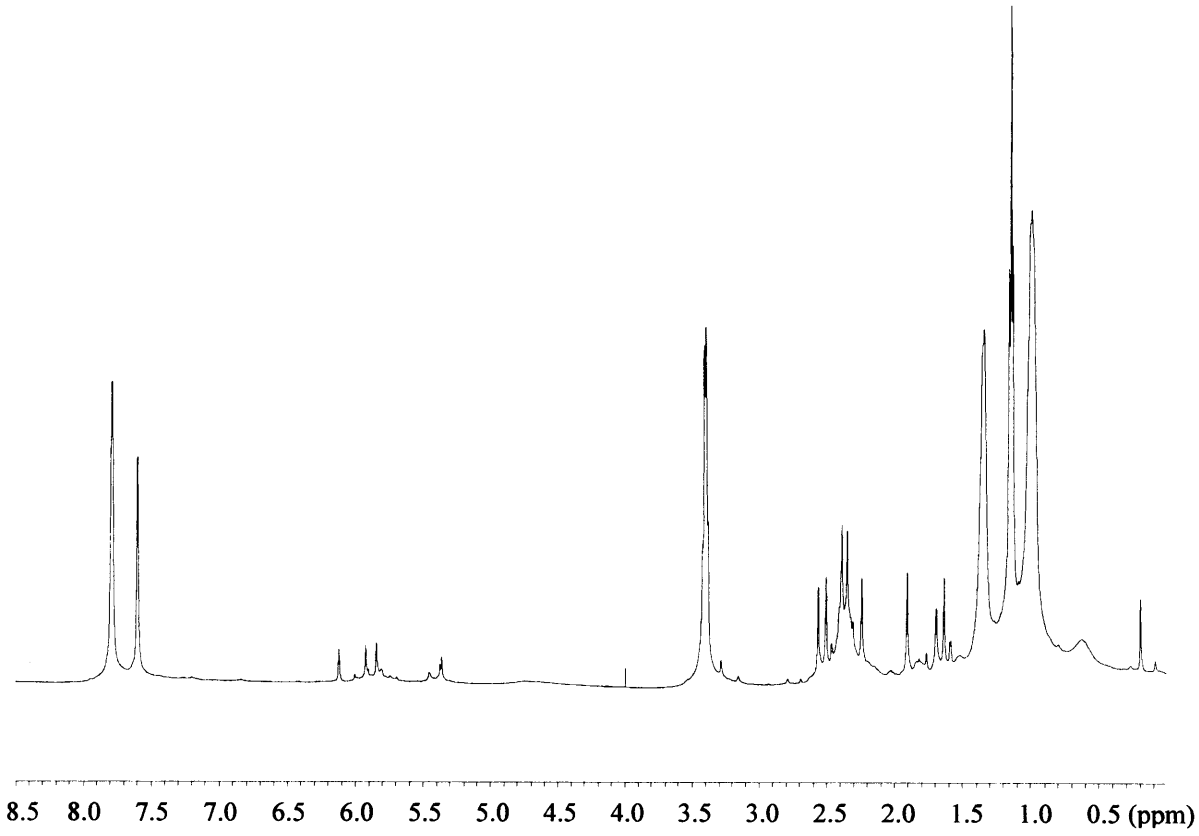

Figure 2.15: ^{1}H NMR spectrum of the complex formed by reaction of $[Tp^{Me2}NbMe(Et_2O)(MeCCMe)][BAr^f_4]$ (**2**) and PEt_3 at –60 °C after 12 h.

Reaction of $[Tp^{Me2}NbMe_2(MeCCMe)]$ (1) and $[H(OEt_2)_2][BAr^f_4]$ (3) in the presence of MeCCMe

Reports of nitrile adducts of the type $[Tp^{Me2}Nb(CO)(PhCCMe)(RCN)]$[115] show it is sterically possible to have two linear η^2-ligands in addition to a small η^1-ligand at the metal centre of a hydridotris(3.5-dimethylpyrazolyl)niobium complex. But-2-yne can also act as an η^2, $2e^-$, donor, or as a variable electron donor between 2 and 4, and if present in excess is expected to substitute into complex **2** in place of the diethyl ether. Isolation of $[Tp^{Me2}NbMe(MeCCMe)_2][BAr^f_4]$ is expected to give valuable insights into the nature of the cation as a catalytic intermediate, as either its structure or reactivity (viz. migratory insertion) could be probed.

In our initial experiments, but-2-yne was added via a microsyringe to a pre-prepared sample of complex **2** at –60 °C. NMR spectroscopic studies showed repeated decomposition of **2**, and on examination of the samples a black, viscous layer was observed to have formed on the surface of the orange solution. Closer examination of the layer revealed some white gelatinous material. The darkening of the solution tallied with a decrease in the free alkyne peak in the ^1H NMR spectrum and a gradual increase in other, unassigned peaks. Repeating the experiment using $[H(O^iPr_2)_2][BAr^f_4]$, with the alkyne added at –80 °C, resulted in the immediate formation of a brown and viscous layer in the upper portion of the sample. Within 10 min the whole sample had changed colour and consistency and a small amount of a white solid was observed.

These observations could result from reaction of the alkyne with the cation, or with any excess acid. In order to resolve this, a further experiment was conducted to eliminate the possibility of acid-catalysed decomposition. $[Tp^{Me2}NbMe_2(MeCCMe)]$ (**1**) was reacted in stoichiometric excess with $[H(OEt_2)_2][BAr^f_4]$ in d_2-DCM at –60 °C. A colour change to orange, accompanied by evolution of gas was noted. The sample was left for 2 h at –20 °C and then overnight at –35 °C to ensure complete reaction of the acid present; this was confirmed by NMR spectroscopy. The but-2-yne was cooled and 10 μl added via a microsyringe. The surface of the solution immediately turned to a brown gel, preventing the solution underneath from moving on inversion of the sample tube. Upon cleaning it was found that the brown gel again contained a plug of a white, flexible, solid.

The observation of the white solid, which is presumed to be polymerised but-2-yne, demonstrates either the potential of the cationic niobium complex as a catalytic system or the alkyne is very sensitive to traces of acid. Establishing the nature of the reaction deserves further investigation. Preliminary results from the reaction in the presence of $[H(O^iPr_2)_2][BAr^f_4]$ indicate that the high concentration of but-2-yne from the neat liquid feedstock allows polymerisation to compete effectively with decomposition, unlike the reaction of **5** with PMe_2Ph.

2.6 Catalytic Trials with Ethene

In order to explore the catalytic potential of **2**, a small series of trials were conducted to test its ability to catalyse the polymerisation of ethene. A 3 ml DCM solution containing 0.01 mmol of **2** was prepared in a specialist catalysis flask equipped with a stirrer bar at –30 °C. The flask was connected via a Teflon screw fitting to a metal manifold T-piece providing access to both vacuum and ethene gas. The dinitrogen atmosphere was replaced with 2 bar pressure of ethene. The solution was stirred vigorously at a constant temperature for 30 min. No colour change was noted for the pale yellow/orange solution over this time, but on raising the temperature to 0 °C for a further hour, the solution became cloudy and the colour less intense. After warming to 25°C, the solution was stirred for 80 min, during which time it became more cloudy and changed colour to a brown/orange. On leaving to settle, a small amount of white precipitate, assumed to be polyethene, separated out on the surface, but its isolation and analysis proved impossible.

This procedure was repeated at –80 °C using $[H(O^iPr_2)_2][BAr^f_4]$ under ethene with a slight excess of **1**, to ensure all the acid was consumed. No change was noted after 1h, so the solution was allowed to gradually warm to room temperature and stirred overnight. On leaving this mixture to settle a small amount of white precipitate was noted floating on the surface, but again this was insufficient to isolate and analyse. A control reaction using $[Tp^{Me2}NbMe_2(MeCCMe)]$ alone at room temperature did not result in any colour change or precipitate.

The presence of a small quantity of white solid indicates that some polymerisation of ethene did occur. The low yield and temperatures at which it appeared suggests that polymerisation occurs during decomposition of the cation. The results of catalytic trials

of $[Cp_2ZrR(THF)][BPh_4]$ (R = CH_3, CH_2Ph)[68;120] lead us to expect the presence of a co-ordinating Lewis base would cause a lowering of catalytic activity from that of the naked cation – had we been able to produce it – but not so drastically as observed. Complete inhibition of catalytic activity in $[Cp_2Zr(MeCN)(THF)][BPh_4]$ by MeCN,[120] demonstrates the requirement of a labile Lewis base (i.e. generation of a co-ordinatively unsaturated $14e^-$ zirconium cation) for catalysis to proceed. We would therefore not expect to see any catalytic reactivity with phosphine adducts.

Our low yields seem surprising given the activities reported for the $[Tp^*NbMe_2(PhCCMe)]/[B(C_6F_5)_3]$ system;[84] however the method of activation by methyl abstraction has been previously shown to be critical in other Group 5 systems.[94] Within this system, it is unclear why the cation of **5**, formed by complexation with the diisopropyl ether, did not show as much catalytic potential as **2**. In light of the behaviour of similar Group 4 complexes[121] we expect a vacant co-ordination site to be required for ethene co-ordination prior to migratory insertion and chain growth. The ready availability of a free co-ordination site from the (assumed) rapid dissociation of the diisopropyl ether would therefore be expected to promote, rather than hinder, polymerisation catalysis. However, steric inhibition of co-ordination site by the more bulky ether may prevent the ethene entering the co-ordination sphere before decomposition occurs. These intriguing preliminary results demand more rigorous and repeated follow-up experiments to investigate the catalytic properties of this system before conclusions can be drawn.

2.7 Comparison of $[Tp^{Me2}NbMe(OEt_2)(MeCCMe)][BAr^f_4]$ (2) with $[Tp^{Me2}TaMe(OEt_2)(MeCCPh)][BAr^f_4]$ (7)

$[Tp^{Me2}TaMe(OEt_2)(MeCCPh)][BAr^f_4]$ (**7**) was prepared in a similar manner as **2**, reacting a 1:1 ratio of $[Tp^{Me2}TaMe_2(MeCCPh)]$ with $[H(Et_2O)_2][BAr^f_4]$ at –60 °C in pre-cooled d_2-DCM. The solution turned bright orange with the evolution of gas over 10 min, with the product characterised by NMR spectroscopy. Unfortunately all attempts at crystallisation, by cooling the sample to –80°C for 2 weeks, resulted only in microcrystals unsuited for X-ray diffraction.

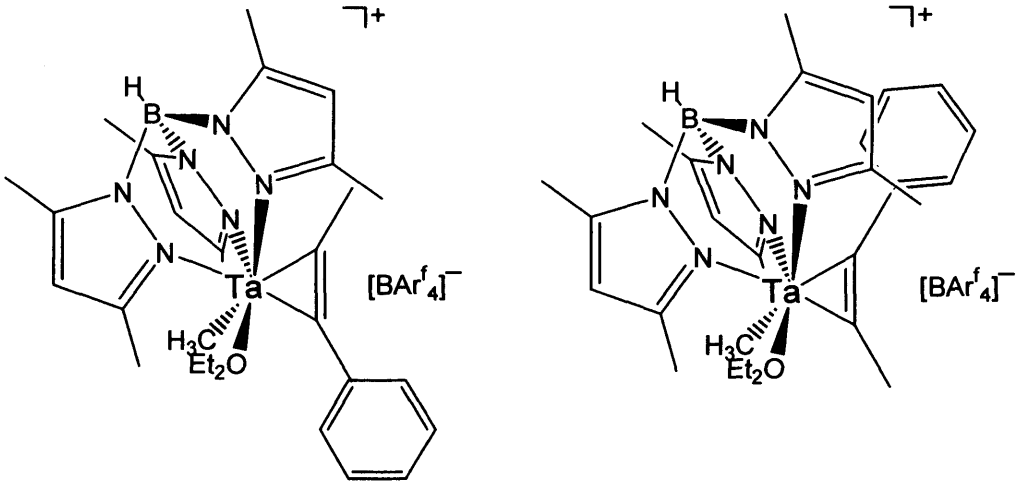

Figure 2.16: Expected products from the reaction of $[Tp^{Me2}TaMe_2(MeCCPh)]$ and $[H(OEt_2)_2][BAr^f_4]$.

The asymmetry of the alkyne ligand allows two possible isomers (Figure 2.16). Initial experiments carried out by Etienne and co-workers show complex spectra, which were difficult to assign despite some qualitative indications of the formation of a Ta–CH_3 cation. Following the characterisation of **2**, it has been possible to revisit the reaction and characterise the main product isolated at –60 °C.

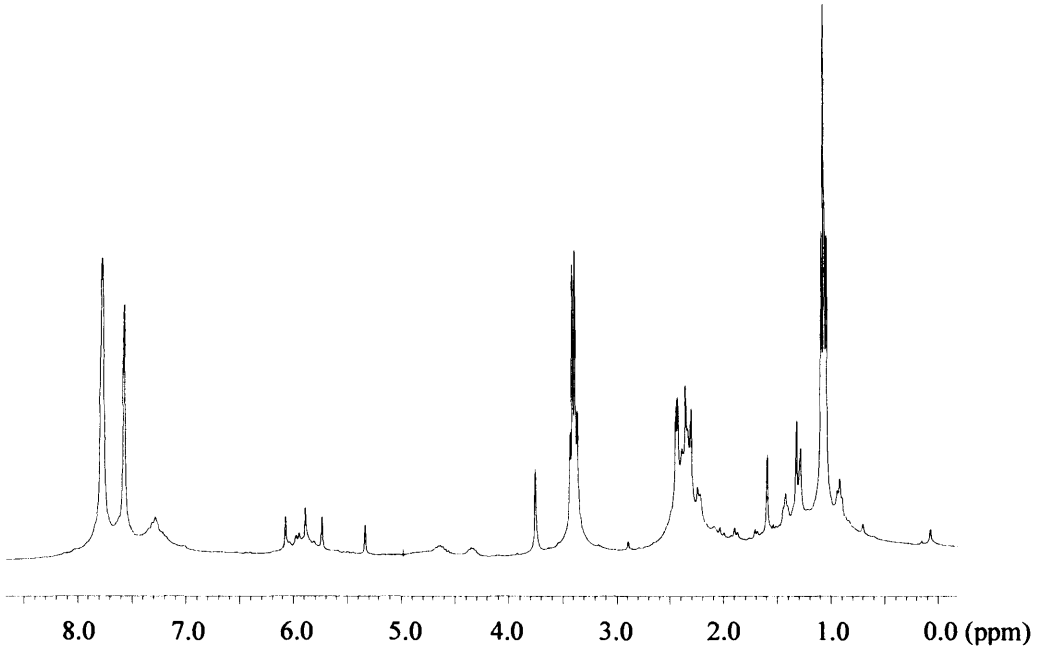

Figure 2.17: ^{1}H NMR spectrum of $[Tp^{Me2}TaMe(OEt_2)(MeCCPh)][BAr^f_4]$ (7) in d_2-DCM at –60 °C.

Prominent features of the ^{1}H NMR (Figure 2.17) are the three 1H and six 3H Tp^{Me2} signals, and the diastereotopic methylene protons of the co-ordinated diethyl ether. The most notable feature is the Ta–CH_3 peak in the ^{13}C NMR spectrum. As with complex **2**, the chemical shift of the metal-methyl group has moved considerably downfield from the dimethyl position, indicating a reduction in electron shielding at the nucleus, and

corresponding to the proposed positive charge at the metal centre. That these shifts are smaller for the tantalum analogue reflects the more diffuse nature of the third row transition metal *d*-orbitals.

		+O^{i}Pr$_2$	+OEt$_2$	+PEt$_3$	+PPhMe$_2$	Ta+OEt$_2$
M–CH$_3$	^{13}C	70.5	74.9	94.7	95.1	66.4
	^{1}H	2.1-2.5	1.80	1.70	1.68	1.29

Table 2.3: Summary of M–CH$_3$ chemical shifts observed for [Tp^{Me2}NbMe(L)(MeCCMe)]$^+$ complexes.

2.8 Conclusions

Chapter 2 presents a rare series of novel alkyl cation complexes of niobium, [Tp^{Me2}NbMe(L)(MeCCMe)][BAr$^f_4$] (L = OEt$_2$, O^{i}Pr$_2$, THF, PMe$_2$Ph, PEt$_3$), related to the active species in ethene polymerisation. The cations are both air- and temperature-sensitive, with stabilisation of the cation achieved by the unique electronic and steric properties of the Tp^{Me2} and 4e$^-$ alkyne ligands, in tandem with the non-coordinating properties of the [BAr$^f_4$]$^-$ anion. The extent of this stabilisation depends upon the properties of the ligand L, with stronger electron donors providing greater stability.

The novel complex [Tp^{Me2}NbMe(OEt$_2$)(MeCCMe)][BAr$^f_4$] (**2**) has been synthesised and characterised by NMR spectroscopy and X-ray diffraction. The reactivity of this complex has been explored, with the labile nature of the diethyl ether ligand demonstrated through substitution by the phosphines PPhMe$_2$ and PEt$_3$. The reaction of but-2-yne with [Tp^{Me2}NbMe(OEt$_2$)(MeCCMe)][BAr$^f_4$] (**2**) does not lead to the formation of [Tp^{Me2}NbMe(MeCCMe)$_2$][BAr$^f_4$]. Although initial results do not support the anticipated ability of the cation to polymerise ethene, its reaction with but-2-yne indicates a degree of activity.

[Tp^{Me2}NbMe(O^{i}Pr$_2$)(MeCCMe)][BAr$^f_4$] (**5**) and [Tp^{Me2}TaMe(OEt$_2$)(MeCCPh)][BAr$^f_4$] (**7**) have also been characterised by NMR spectroscopy. Complex **5** demonstrated a significantly lower degree of stability than its diethyl ether counterpart.

Chapter 3

Studies of some d^0 Titanium Complexes

The work reported in this Chapter examines the influence exerted on the structure of the Ti–R moiety by the other ligands co-ordinated to the d^0 metal centre. The focus was on the electronic effects of electron donation and core polarisation, rather than on the steric effects examined in Chapter 2. The programme aimed to investigate the nature of Ti–C–H interactions in a series of small, 4-co-ordinate Ti complexes of the type $RTiL_3$, where L has differing electron donating abilities (L = CH_2Ph, NMe_2, O^iPr). Despite a range of problems encountered in this work, which prevented clear elucidation of the influence of L, some interesting results were obtained through application of a range of structural and spectroscopic techniques.

3.1 Introduction

Molecules adopt their observed conformations through a balance in the interactions that influence their physical structure. The competition between these steric and electronic factors for d^0 transition metal centres was outlined in Chapter 1. Agostic bonding is one of the physical manifestations of this equilibrium, and $EtTiCl_3$ is a classic example of a molecule finely balanced on the cusp between two structures. The co-ordination complex $[EtTiCl_3(dmpe)]$ exhibits a β-agostic interaction, whereas the more electron-deficient, co-ordinatively unsaturated parent compound $EtTiCl_3$ shows no such interaction.[58]

3.1.1 Agostic Bonding

Reports of ligand deformation suggesting a weak interaction between a C–H moiety of a ligand and its transition metal centre date back to the 1960's.[122;123] Following anomalies observed by Trofimenko[124;125] in $[\{Et_2B(pz)_2\}\{\eta^3\text{-}CH_2C(Ph)CH_2\}(CO)_2Mo]$, Cotton et al. proposed a significant interaction between the ethyl β-C–H and the Mo centre.[126] This was demonstrated by a crystal structure determination, which showed a shortened Mo···C distance and an angle implying that the H must lie within 2.2 Å of the Mo centre, as shown in Figure 3.1. Further examples subsequently emerged, and were identified by X-ray or neutron diffraction or by NMR or IR spectroscopic studies.

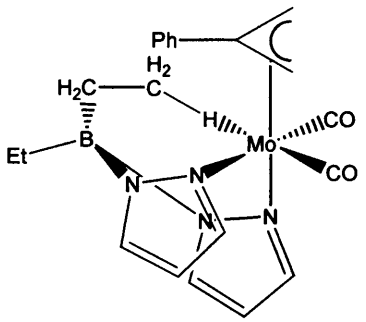

Figure 3.1: β-agostic complex [{$Et_2B(pz)_2$}{η^3-$CH_2C(Ph)CH_2$}$(CO)_2Mo$].

The accumulation of a number of similar species in the literature led Brookhart and Green in 1983 to propose the term 'agostic' to describe the 'various manifestations of covalent interactions between carbon-hydrogen groups and transition metal centres in organometallic compounds';[127] this term is now applied to a wide range of complexes exhibiting this behaviour. A wider phenomenological definition has recently been proposed: agostic interactions are characterised by the distortion of an organometallic moiety which brings an appended C–H bond into close proximity with the metal centre.[12]

3.1.2 Agostic Bonding and Catalytic Pathways

The importance of d^0 Group 4 metal complexes in the polymerisation catalysis of olefins is widely documented.[128;129] They are particularly active Ziegler-Natta catalysts, and as such the key rôle played by the M–R moiety is crucial to a full understanding of their activity. The two main proposed mechanisms for the process are the Cossee-Arlman[130] (CA) and Modified Green-Rooney[127] (MGR) mechanisms, depicted schematically in Figure 3.2.

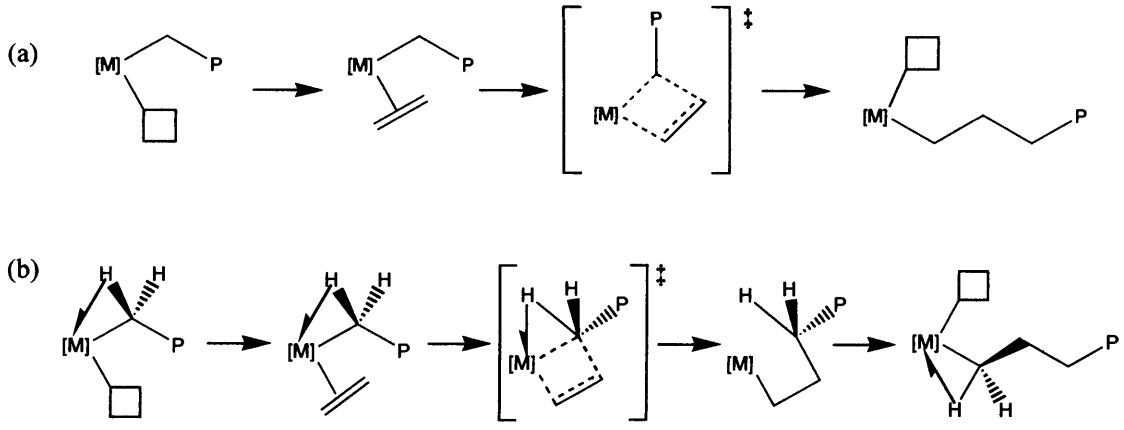

Figure 3.2: Proposed mechanisms for the polymerisation of olefins at a metal centre (a) Cosee-Arlman (b) Modified Green-Rooney.

The key difference in these mechanisms is the interaction in the transition state for olefin insertion between the metal centre and the C–H bond at the α-position. The CA mechanism proposes that chain propagation proceeds via simple migratory insertion into the M–R bond, whereas the MGR mechanism proposes 'α-agostic assistance' from the polymer chain that aids alkene co-ordination and insertion, rather than a full hydride transfer. Brookhart et al.[131] subsequently demonstrated the ethene polymerisation activity of the β-agostic complex $[Cp^*Co(Et)P(OMe)_3]^+$, and proposed that the agostic interaction lowered the activation energy for alkyl migration. A number of researchers have proposed and conducted experiments to establish which mechanism better describes the reaction. Grubbs et al. designed an elegant reaction involving partial deuteration, illustrated in Scheme 3.1.[132]

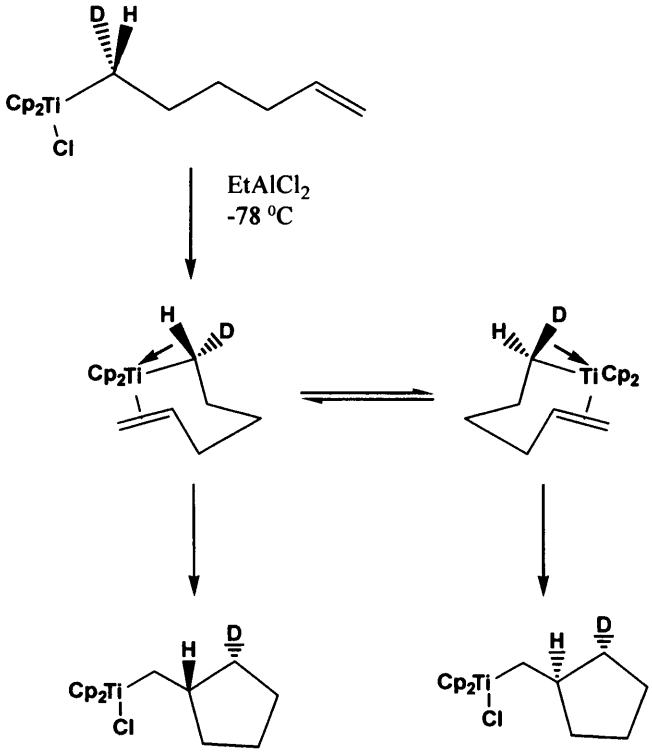

Scheme 3.1: Cyclisation of $[Cp_2TiCl(CHDCH_2CH_2CH_2CHCH_2)]$.

Their aim was to exploit the isotopic preference for the activation of a C–H bond rather than a C–D bond (owing to the lower zero-point energy of the C–D bond) as a stereochemical probe by introducing a deuterium atom on the α-methylene group. The expected ratio of product isotopomers depends on the mechanistic route followed. With the CA mechanism, the observed 1:1 ratio is predicted; however under the MGR mechanism, where an α-agostic interaction is proposed, an unequal product ratio is expected. Although Grubbs' results support the CA mechanism, other experiments and

calculations, notably those by Bercaw[133;134] and Brintzinger,[135] support the MGR mechanism, adding to the continuing mechanistic debate.[128] It is possible – and likely – that the CA mechanism applies to some systems (particularly those with a high energy agostic form of transition state), while the MGR mechanism is adopted by others.

3.1.3 $RTiCl_3$ Molecules and Complexes: A Paradigm of Agostic Bonding

The interesting case of the formally 8-electron molecules $MeTiCl_3$ and $EtTiCl_3$ challenges our intuitive understanding of agostic bonding. Despite early conclusions for $MeTiCl_3$,[136] both $MeTiCl_3$ and its ethyl congener have been shown to exhibit no agostic interactions in the gas phase.[137] However, the more sterically crowded, 12-electron complexes $[MeTiCl_3(dmpe)]$ and $[EtTiCl_3(dmpe)]$ are the classic textbook examples of α- and β- agostic bonding respectively.[137;138]

Gas phase electron diffraction experiments showed $MeTiCl_3$ to have a methyl group with a normal Ti–C–H angle of 109°, whereas in $[MeTiCl_3(dmpe)]$ the Ti–C–H angle measured from neutron diffraction data is 93.7°,[139] demonstrating unambiguously that the methyl group is distorted from a normal tetrahedral structure. X-ray diffraction data for $[EtTiCl_3(dmpe)]$ also show a distorted alkyl moiety, with a Ti–C–C angle of 86°,[140] whilst electron diffraction and theoretical studies of $EtTiCl_3$ both reveal this angle to be normal at 117°.[137]

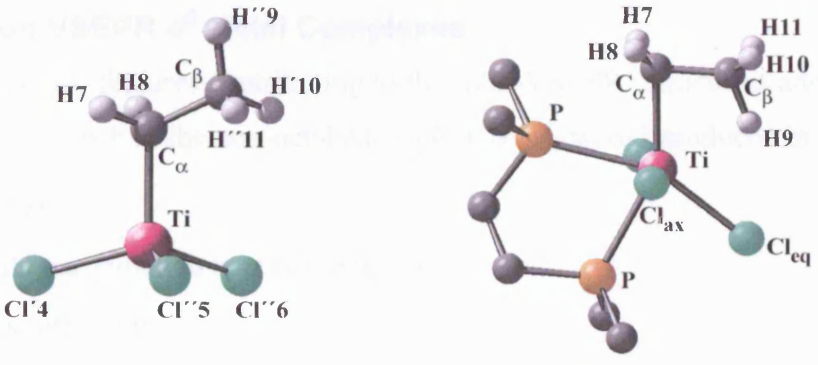

Figure 3.3: The molecular structures of $EtTiCl_3$ and $[EtTiCl_3(dmpe)]$.[12]

Early extended Hückel MO approaches to understanding the nature of the agostic bond focused on the availability of low-lying empty orbitals on the metal centre with the correct orientation for overlap with the C–H bonding orbital, giving rise to a 3c-2e interaction. This approach partly explained the perplexing results described above. An α-agostic interaction of the Me–Ti moiety in the model octahedral system $[MeTiH_5]^{2-}$ is favoured, owing to its stabilising effect on the σ_{Ti-C} HOMO. Interaction of the C–H

bonding orbital with the d_{xz} orbital outweighs the destabilisation resulting from the reduced overlap of the σ_{Ti} and the n_{Me} orbitals because the two fragments no longer point towards one another.[139] Extension to the Et–Ti fragment in $[EtTiH_5]^{2-}$ again demonstrated that a deviation away from the octahedral geometry resulted in stabilisation of the HOMO.[141] More recent studies have examined $EtTiCl_3$ and its dmpe adduct,[15;17;137] and have employed, *inter alia*, DFT calculations and charge density studies to give contour maps of the frontier orbitals responsible for this effect.

In their recent review, Scherer and McGrady proposed a modified bonding model that highlights the need not just for an unencumbered Lewis acidic metal centre, but also the 'presence of sites of locally enhanced Lewis acidity...disposed facing the agostic C–H moiety'.[12] This need for directional parity in the formation of an agostic bond is well illustrated by the case of $EtVCl_3$.[17] Here quantum chemical calculations suggest a β–agostic interaction can be expected in the ground state, but not in the more Lewis acidic $[EtVCl_3]^+$ cation. By placing a greater emphasis on the local charge environment of the M···C–H fragment than that of the whole molecule, the model moves away from the traditional view of the interaction as η^2-C–H→M donation. Rather, it views the interaction in terms of hyperconjugative delocalisation of charge from the M–C bond throughout the alkyl ligand.

3.1.4 Non-VSEPR d^0 Metal Complexes

Some of the key features contributing to the 'non-VSEPR' structures adopted by certain d^0 complexes, such as the non-octahedral $[W(CH_3)_6]$, were introduced in Section 1.4:

- Ligand effects
- *d* orbital participation in σ bonding
- Core polarisation

Examples of non-VSEPR d^0 structures include Me_2TiCl_2 and Me_2NbCl_3. These heteroleptic complexes show distortions of the C–M–C and Cl–M–Cl angles in a reversed manner to those predicted by VSEPR theory,[142;143] viz. the bonds to the more electronegative Cl substituents subtend the greater angle at the metal atom. Analogous derivatives of Main Group elements *e.g.* Me_nSiCl_{4-n} behave in an opposite manner in accord with the normal VSEPR rules.[144]

Important work by Bader and Gillespie identified 'core polarisation' using the AIM theory approach, outlined in Section 3.2.2 below.[145;146] Core polarisation is a phenomenon whereby there are accretions of localised charge density or charge concentrations (CCs) in the electron density profile of the central metal atom of complexes. In the case of d^0 metal complexes, it was observed that many of these areas of CC appeared opposite M–L bonds and accordingly they were termed ligand-opposed CCs (LOCCs).[147;148] LOCCs need to be accommodated along with the M–L bond and non-bonding electrons in the space around the central atom, and hence they exert an influence on the overall structure adopted by a complex. As outlined in Section 1.4, Scherer *et al.* proposed the LOCC to be a natural feature of the sd^n bonding process.[12] This reflects the theoretical work reported by Landis *et al.*, who used a simple valance bond model and sd^n hybrid orbitals to rationalise the observed non-VSEPR structures adopted by some σ-bonded d^0 complexes.[57]

Whatever their origin, these LOCCs also have a critical influence on the development or otherwise of another common phenomenon of d^0 TM chemistry, agostic interactions. A greater understanding of LOCCs and the rôle they play in bonding is a key requirement, as is the ability to obtain a thorough understanding and accurate description of their nature.

3.2 Charge Density Studies of [(Bz$_3$Ti)$_2$O] (8)

3.2.1 Preparation of [(Bz$_3$Ti)$_2$O] (8)

The homoleptic compound $TiBz_4$ was our initial target molecule for charge density studies and attempted syntheses were conducted according to the literature.[149;150] However, each preparation resulted instead in the formation of $[Ti(CH_2C_6H_5)_3]_2O$ (**8**), in a similar manner to that reported by Jacot-Guillarmod et. al.[151]

$$TiCl_4 + 4\ ClMgCH_2C_6H_5 \rightarrow Ti(CH_2C_6H_5)_4 + 4\ MgCl_2$$

$$Ti(CH_2C_6H_5)_4 \xrightarrow{Et_2O} [Ti(CH_2C_6H_5)_3]_2O \qquad \textbf{[3.1]}$$

$TiCl_4$ was transferred via a measuring pipette into a pre-purged Schlenk tube and stirred at 0 °C. Diethyl ether was then cautiously added. ClMgBz (freshly prepared from magnesium turnings and BzCl) was added dropwise to the $TiCl_4$ solution, which changed from colourless through green to brick-red. The reaction mixture was stirred for 12 h to ensure complete reaction. The literature preparation indicates that refluxing

$TiBz_4$ in ether causes the formation of **8**, apparently through reaction with the solvent, but we found that prolonged stirring at room temperature is sufficient. The solution was allowed to settle, the supernatant liquid was decanted, and the residue washed with 3 aliquots of diethyl ether, the washings then being combined with the solution. Decomposition of the sample occurred over a few days if it was stored above 4 °C.

The literature preparation did not describe in detail the methods used to isolate the product, so several attempts were made to grow crystals of sufficient size:

- Concentrated diethyl ether solutions stored at –40 °C
- Extraction into toluene and storage at –40 °C
- Extraction into dimethoxyethane and slow evaporation of solvent.
- Extraction into pentane and storage of a concentrated solution at –40 °C
- Use of a 1:1 pentane : diethyl ether solution and storage at –40 °C

All of the crystallisations attempted at –40 °C were conducted both by immediate cooling of the vessel to this temperature and by intermediate cooling to 4 °C for a few days, then to –20 °C for a similar period and finally to –40 °C for an extended time.

Many of the crystallisation attempts resulted in a thick, viscous solution, from which the crystals formed could not be isolated. Repeatable success was achieved by extraction of the product into pentane; the solution became thinner and more manageable. The final two methods yielded sufficiently large crystals of $[(Bz_3Ti)_2O]$ (**8**) for a sample to be transferred to a Pyrex tube, which was sealed under vacuum and sent to the Department of Inorganic Chemistry, TU München, Germany, for X-ray charge density studies by the Scherer group. The structural determination and quantum mechanical calculations for this study were carried out by Dr. Dmitri Shorokhov.

3.2.2 Charge Density Studies

Mapping the electron density between the atoms gives a unique insight into bond structure and charge distribution in a crystal or molecule. Charge density studies involve the analysis of electron density distribution and can be carried out using experimental or calculated electron densities; these are then processed through the application of the Atoms in Molecules (AIM) theory.[152;153] AIM theory interprets the electron density $\rho(\mathbf{r})$ to reveal bonding interactions within a molecule. This theory is not

based on the initial application of empirical models, such as valence bond theory, so is particularly suitable for the investigation of unconventional or 'non-classical' bonding.

Data Collection

Debye identified the basis for experimental charge-density data collection in 1915. He recognised that the technique of electron diffraction was not limited to the high electron density areas of molecules – the nuclei – used to determine crystal structures: 'the experimental study of the scattering of atoms, in particular for light atoms, should get more attention, since along this way it should be possible to determine the arrangement of the electrons in the atoms.'[154]

Key technological advances in X-ray diffraction equipment over the past decade have enabled data to be collected with sufficient resolution for meaningful interpretation; these include:

- Much better low temperature techniques – reducing motion within the crystal and giving more accurate measurement of scattering at high angles
- High intensity X-ray beams from sources such as rotating anodes – giving access to scattering angles $2\theta > 100°$
- Area detectors *e.g.* CCD or image plates – both with high sensitivity and able to collect data from all angles simultaneously, shortening data collection times.

The intensity of X-rays diffracted by a crystal is related to the amplitude of terms called structure factors. Careful processing of an X-ray diffraction pattern yields structure factors, from which the molecular electron density $\rho_{obs}(\mathbf{r})$ can be extracted via an inverse Fourier transformation. In standard X-ray crystallography, the observed molecular electron density $\rho_{obs}(\mathbf{r})$ is interpreted using a refinement model – the independent atom model – based on the spherically averaged, ground-state atomic electron density, giving $\rho_{ref}(\mathbf{r})$. Fitting the data involves minimising the difference in the two values $\Delta\rho(\mathbf{r})$, defined by Equation 3.2. The larger the atom, the more dominant is the core scattering over the valence scattering and hence the better fit the model.

$$\Delta\rho(\mathbf{r}) = \rho_{obs}(\mathbf{r}) - \rho_{ref}(\mathbf{r}) \qquad [3.2]$$

For high resolution X-ray diffraction, the quality of data collected is sufficiently high that improvements to the refinement model giving $\rho_{ref}(\mathbf{r})$ will leave chemically relevant

information, rather than just noise, in $\Delta\rho(\mathbf{r})$. This more complex, multipole model contains factors for valence orbitals from the mixing of the atomic ground states and valence deformations.

AIM Theory – A Brief Overview

AIM theory is used to interpret $\rho(\mathbf{r})$ data either from experiment or quantum chemical calculations. It is the electron density in the areas between the atomic cores that gives insight into bonding modes and the gradient of ρ, the first derivative, $\nabla\rho(\mathbf{r})$, or gradient field vector is calculated. The AIM approach generates a set of directional field vectors representing the routes of steepest ascent up $\rho(\mathbf{r})$. As an example, these vectors are mapped in Figure 3.4(a) for ethene (C_2H_4). Relief maps of electron density show the main concentrations to be at the atomic centres, as would be expected, and a radial fall-off which is less between atoms than around the remainder of each atom. Two-dimensional contour plots, as in Figure 3.4(b), are most commonly used to depict the data.

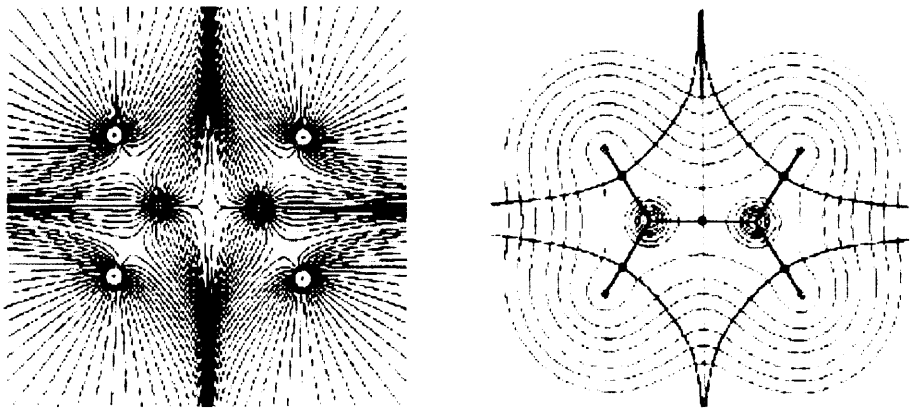

(a) (b)

Figure 3.4: (a) The gradient vector field of the electron density of C_2H_4 in the plane containing the nuclei. (b) Contour plot of C_2H_4 with bond paths and boundaries of atomic basins marked and bond critical points denoted by a dot.

Each atom is regarded as a 'nuclear attractor' for a multitude of gradient paths, which divides the molecule, so each atom is in a unique space of electron density. Where $\nabla\rho(\mathbf{r}) = 0$, a local minimum of $\rho(\mathbf{r})$, critical points occur. When these lie between two atoms, this minimum is termed a bond critical point (BCP), indicating the boundary between the two bonded atoms. Ring critical points (RCP) occur between three or more atoms, and are particularly important in the investigation of η^2-bonded complexes. Each gradient path originates at a minimum and terminates at a maximum. Most

originate away from the molecule (at infinity) and terminate at an atomic nucleus – giving rise to a high number of lines converging on a point named an 'atomic basin'. Some paths are not attracted to the nuclei, but to the bond critical points between the nuclei forming the interatomic surface. When the path originates at a BCP it describes the bond path (BP). Recent studies have challenged this aspect of AIM theory, as critical points have been observed with atomic interaction lines between two anions or other non-bonded atoms.[155] This questioning of the physical meaning of critical points and the paths emanating from them suggests caution and judgement must be used in their interpretation. In this study however, they can continue to be thought of as a molecular Ordinance Survey map, with the critical points as saddle points (local minima). The vectors are then the equivalent of the steepest paths to a mountain top, and the bond paths are the ridges between mountains; the highest electron density linking the atom peaks.

This technique is particularly useful in the study of transition metal hydride systems when used with either DFT calculations or neutron diffraction. Here, the AIM analysis is projected onto the molecular geometry of the molecule obtained from the structural study. A recent example of a transition metal complex investigated this way is the silane σ-bond complex $[MeC_5H_4Mn(CO)_2(\eta^2\text{-}HSiFPh_2)]$.[156] Shown in Figure 3.5(a) is the experimentally derived plot of $\rho(\mathbf{r})$ within the Mn–Si–H plane, illustrating the positions of the BCPs and the RCP. The contour plots of $\rho(\mathbf{r})$ provide little information about the region between the atoms, as the change in electron density is small compared to that of the whole molecule. However, the plot of the calculated gradient field vectors, $\nabla\rho(\mathbf{r})$, Figure 3.5(b), shows these much more clearly along with the interatomic surface.

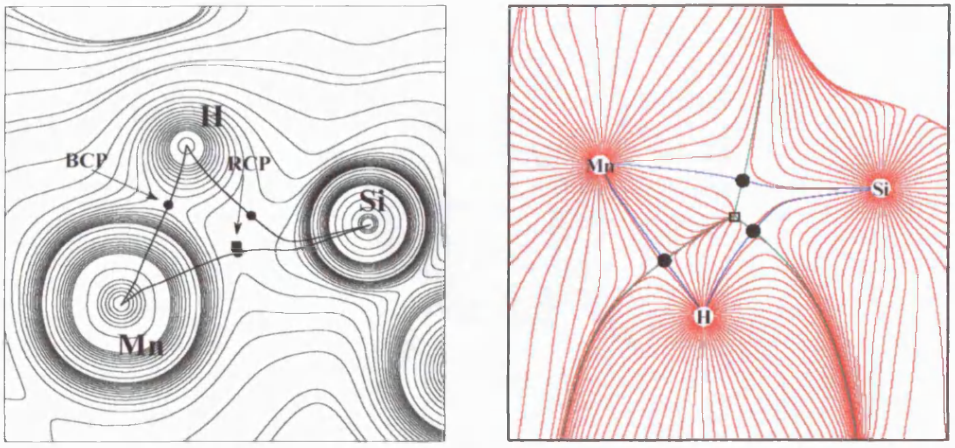

(a) (b)

Figure 3.5: (a) Contour plot of the experimentally derived $\rho(\mathbf{r})$ and (b) Plot of the calculated $\nabla\rho(\mathbf{r})$, for the Mn–Si–H moiety of $[MeC_5H_4Mn(CO)_2(\eta^2\text{-}HSiFPh_2)]$.

The topology of the Laplacian of $\rho(\mathbf{r})$, $\nabla^2\rho(\mathbf{r})$, gives information about localised electron density,[148] acting as a magnifying glass on the relief plot of $\rho(\mathbf{r})$ and showing localised charge concentration $\nabla^2\rho(\mathbf{r}) < 0$ and depletion $\nabla^2\rho(\mathbf{r}) > 0$.[157] In essence, it measures the local curvature of ρ in its three dimensions. In addition to illustrating the shell structure of an atom, plots of this localised charge density or local CC show polarisation or distortion of the electron density at a metal centre and can be used to identify non-bonding pairs and changes within the atomic core *e.g.* in the non-VSEPR structure of the d^0 molecule $Cr(O_2)F_2$.[61] Of particular interest in this work is the distortion in the valence shell of the central metal atom associated with chemical bonding. The correspondence of $\nabla^2\rho(\mathbf{r})$ to localised electron density has been able to provide a physical basis for the VSEPR bonding model.[145] The CCs are best illustrated by envelope maps of the negative Laplacian $L(\mathbf{r})$ of the charge density where $L(\mathbf{r}) = -\nabla^2\rho(\mathbf{r})$, enabling study of the polarisation of the electron core and the valence electrons. These plots are drawn along a single value of $L(\mathbf{r})$, usually corresponding to the valence electron shell, as illustrated by the contour plot of $L(\mathbf{r})$ for the Ti centre of $[EtTiCl_3(dmpe)]$ shown in Figure 3.6. In addition to the expected non-bonding charge concentration (NBCC) at the atomic centre of the d^0 complexes and the bonding charge concentration (BCC) located between bonding atoms, other areas of CC have been located. Those first reported were identified by Gillespie et al.[60] as 'ligand-opposed charge concentrations' (LOCCs), found *trans* to the M–X bonds in the non-linear Group 2 dihalides studied.

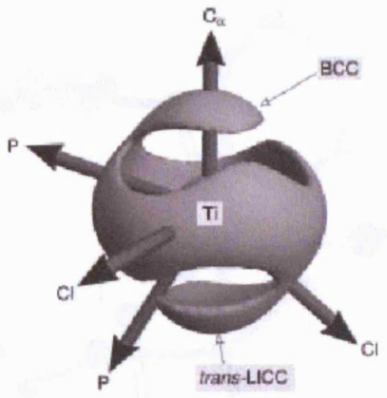

Figure 3.6: Experimental envelope map ($L(\mathbf{r})$ = 160 eÅ^{-5}) showing the ligand-induced polarisation at the Ti atom in [$EtTiCl_3$(dmpe)].[62]

A LOCC may also be regarded as a ligand induced charge concentration in a *trans* position, a term suggested by Scherer, McGrady et al. following their observation of both a LOCC and a CC *cis* to the M–C bond in the model system $[EtCa]^+$.[62] The LOCC is also termed ligand induced CC (LICC); the nomenclature seems appropriate as it implies the CC is a result of the metal-ligand interaction.

3.2.3 Results and Discussion

X-ray diffraction studies of **8** give bond lengths and angles in good agreement with previous studies in the literature.[158] The experimentally determined structure is shown in Figure 3.7. Table 3.1 shows selected structural data for the structures determined experimentally and by DFT calculations (with and without geometrical optimisation) compared with the literature values. It is interesting to note the linearity of the Ti–O–Ti moiety. This is a common feature of μ-oxo bonding where a single bridge is involved *e.g.* in the complex $[\{(Me_3tacn)Ti(NCO)_2\}_2O]$.[159] There are some complexes such as $[Cp^*Ti(SiMe_3)_2]_2O$ and $[Cp^*TiMe_2]_2O_5$ which contain bent μ-oxo bridges.[160] Here the electronic demands are different to the otherwise σ-bonded molecules discussed earlier and the bent structure may be attributed to geometric optimisation, as the π-bonding from the O is no longer necessary for the satisfaction of the Lewis acid Ti centre, which is satisfied by the other ligands present. This is well illustrated by the two different structures of $[Cp^*TiCl_2]_2O$, where the Ti–O–Ti angles are 180° and 116.1°.[161;162]

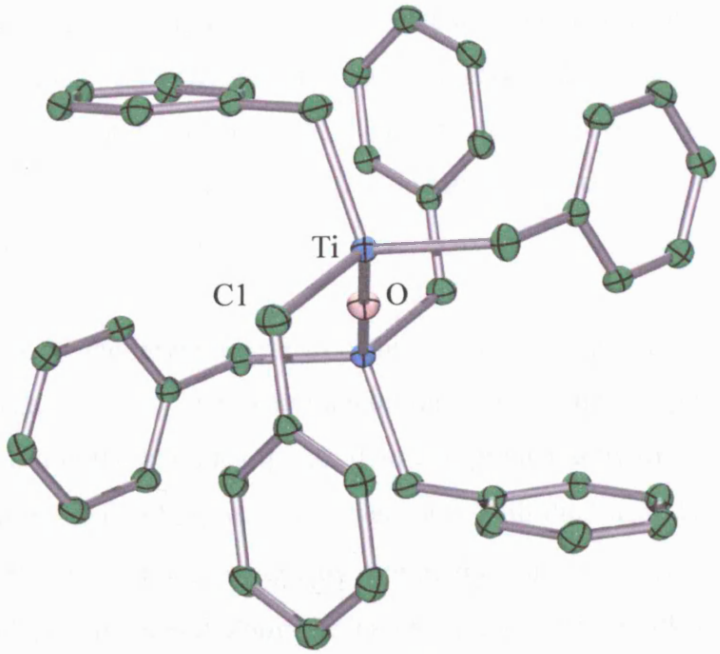

Figure 3.7: ORTEP representation of the molecular structure of $[(Bz_3Ti)_2O]$ (**8**) as determined by high resolution X-ray diffraction.

Unit	Method	Distance (Å)	$\rho(r_c)$ (eÅ^{-3})	$\nabla^2\rho(r_c)$ (eÅ^{-5})	Ellipticity ε
Ti–O	Exp.	1.8009(1)	0.782(5)	19.620(11)	0.01
	Calc.	1.8010	0.969	16.802	0.00
	Opt.	1.8038	0.978	16.836	0.00
	Lit.	1.789(0)			
Ti–C1	Exp.	2.0875(3)	0.672(3)	6.004(3)	0.05
	Calc.	2.0874	0.629	2.763	0.13
	Opt.	2.1060	0.708	2.278	0.02
	Lit.	2.076(9)			
C1–C2	Exp.	1.4806(4)	1.745(16)	-15.117(38)	0.09
	Calc.	1.4809	1.612	-11.824	0.09
	Opt.	1.4909	1.738	-14.360	0.11
	Lit.	1.417(12)			
C1–H1A	Exp.	1.1000	1.534(40)	-12.666(143)	0.04
	Calc.	1.0995	1.760	-19.813	0.07
	Opt.	1.1012	1.750	-19.331	0.05
	Lit.	N/A			

Table 3.1: Selected structural data for $[(Bz_3Ti)_2O]$ (**8**) comparing experimental, calculated and geometrically optimised values to those in the literature.

The charge density studies also show a reasonable fit between the calculated and experimentally determined values, as illustrated by Figure 3.8. Of particular interest is the charge distribution at the d^0 Ti centre. $L(\mathbf{r})$ is just a local measure of charge distribution, with the global charge distribution in all its complexity influencing the

geometry adopted. However, it does allow qualitative comparison with other local areas around a metal centre. The polarisation of the d^0 metal centre influences the degree to which electron delocalisation occurs. At the Ti centre of **8**, the *trans*-LICCs induced by the covalent Ti–C bonds are larger than that induced by the more polar Ti–O bond, indicative of their degree of polarity.

It is interesting to note the larger degree of difference in the experimental and calculated LICCs at the oxygen centre. The experimental data shows the charge concentration to be lower, and therefore the bond less polar, than that predicted by the calculations. This is attributed to partial π-bonding, which also accords with the linear Ti–O–Ti unit. The ellipticity (ε) of the Ti–O bond is zero by symmetry, but the electron density on the oxygen atom is clearly polarised along the Ti–O–Ti axis. This work is part of a wider study still in progress, and the analysis presented here is a preliminary one. The crucial point is that these results, along with other recent ones[12] demonstrate LICCs to be observable not just by calculation, but also from analysis of the experimental molecular charge density. This confirmation of their existence as a real phenomenon warrants further experimental and theoretical investigation to widen their interpretation, enabling comparison with other, similar, molecules.

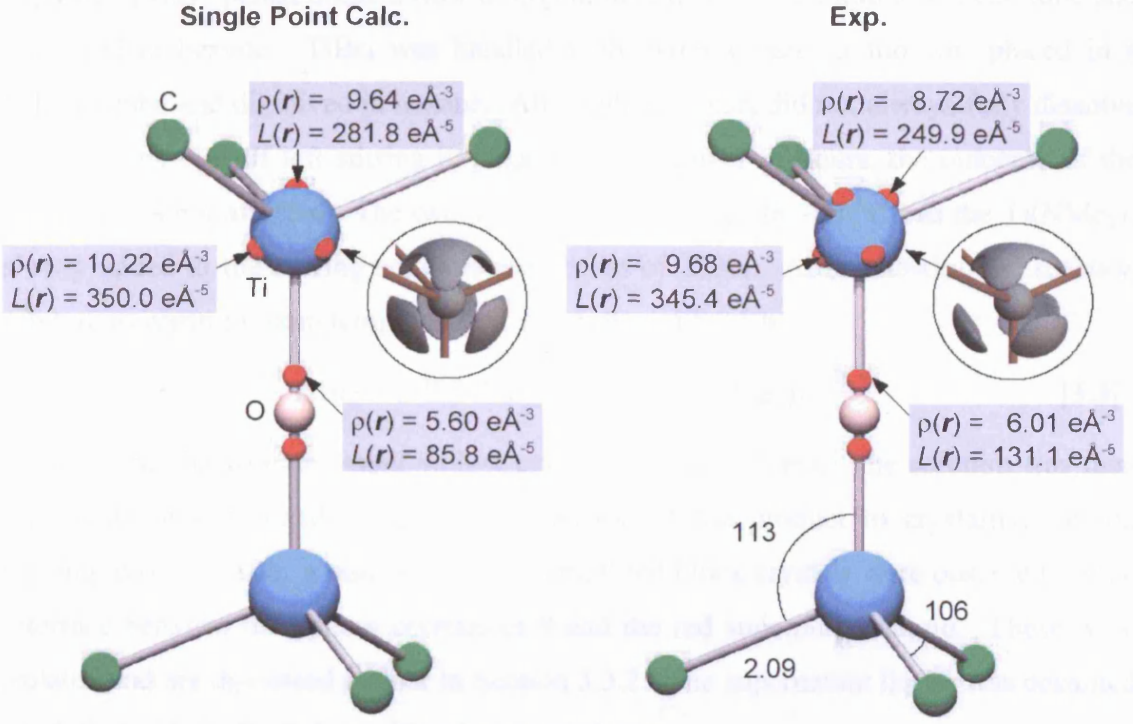

Figure 3.8: Representations of the structure of $[(Bz_3Ti)_2O]$ (**8**) showing the locations of LICCs at the Ti and O atoms.

3.3 Studies of Some (Dimethylamino)titanium Complexes

Bürger and Neese published a number of papers in the 1960s describing a series of compounds of general formula $RTi(NR'_2)_3$.[163-165] These were synthesised by alkylation of the triamidohalide complex, itself prepared by the comproportionation of $Ti(NR'_2)_4$ and TiX_4. The simple molecule $MeTi(NMe_2)_3$ appeared to be an ideal candidate to extend the studies described in Sections 3.1 and 3.2, as it contains a d^0 Ti centre with a potentially agostic methyl ligand, at the same time possessing three π-donor NMe_2 groups. Dr. Dmitri Shorokhov conducted DFT calculations on the molecule, with the predicted propeller structure confirmed as the lowest energy conformer (Appendix 3.2). Naturally, synthesis of the molecule was required before the planned electron diffraction and IR spectroscopic studies could be carried out. This presented severe difficulties which proved to be insurmountable. However, preparation of the intermediate yielded some novel and useful results worthy of comment.

3.3.1 Synthesis and Structual Studies of $BrTi(NMe_2)_3$ (9)

The yellow crystalline intermediate $BrTi(NMe_2)_3$ (**9**) was prepared by the reaction of 1 equivalent of $TiBr_4$ with 3 equivalents of $Ti(NMe_2)_4$, following the method described by Bürger and Neese,[165] and summarised in Equation 3.3. A sealed ampoule containing $Ti(NMe_2)_4$ was opened under a flow of argon, the liquid poured into a Schlenk tube and dissolved in hexane. $TiBr_4$ was handled with extreme care: it too was placed in a Schlenk tube and dissolved in hexane. Although the $TiBr_4$ did not always fully dissolve at this stage, even if left stirring in hexane for a number of hours, the outcome of the reaction was not affected. The two solutions were cooled to –30 °C and the $Ti(NMe_2)_4$ slowly added to the stirring solution/suspension of $TiBr_4$. After allowing the reaction mixture to warm to room temperature it was refluxed for 1 h.

$$TiBr_4 + 3\ Ti(NMe_2)_4 \rightarrow 4\ BrTi(NMe_2)_3 \qquad \textbf{[3.3]}$$

On reducing the volume, small yellow crystals started to form. The solution was then sufficiently concentrated for the major portion of the product to crystallise out on cooling to 0 °C. After a number of days, small red block crystals were observed on the interface between the yellow crystals of **9** and the red supernatant liquid. These were isolated and are discussed further in Section 3.3.2. The supernatant liquor was decanted and left at –30 °C for 4 d, resulting in a second crop.

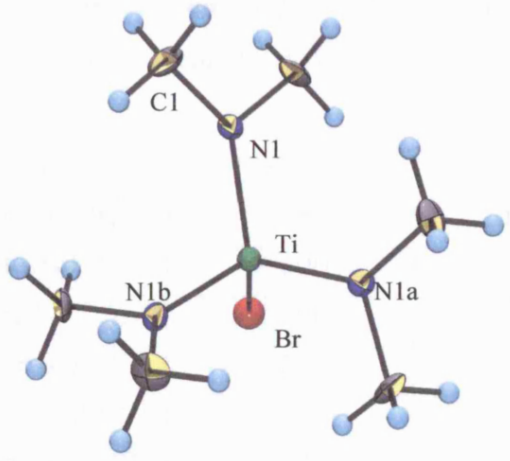

Figure 3.9: Structure of $BrTi(NMe_2)_3$ (**9**) as determined by X-ray diffraction at 120 K.
Selected average bond lengths (in Å): Br-Ti = 2.4718(12), N(1)-Ti(2) = 1.886(7), N(1`)-Ti = 1.870(7)
Selected average bond angles (in degrees): N(1)-Ti-N(1a) = 105.2(2), N(1)-Ti-Br = 113.5(2),
N(1`)-Ti-N(1`a) = 105.1(2), N(1`)-Ti-Br = 113.53(19).

The previously unreported crystal structure of $BrTi(NMe_2)_3$ (**9**) was determined by X-ray diffraction (Figure 3.9). The four co-ordinate titanium atom is the centre of the molecule of C_3 symmetry, which crystallises in the hexagonal space group R3. There is disorder shown in the positioning of the NMe_2 groups, with the three groups of a molecule occupying either the 1 or the 1` position. An interesting feature of the space group is seen in the crystal packing, illustrated in Figure 3.10, with the molecules adopting a uniformly polar orientation.

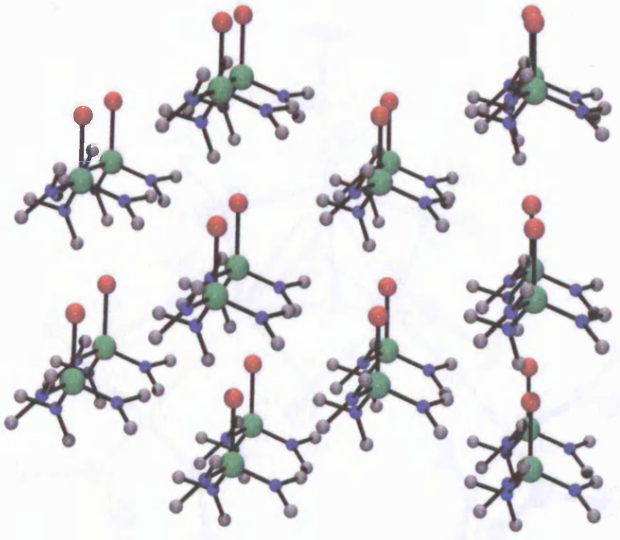

Figure 3.10: Molecular packing in the crystal structure of $BrTi(NMe_2)_3$ (**9**).

The planar nature of the NMe_2 moieties can be clearly seen in Figure 3.10, leading to a propeller-style angling of the groups around the metal centre comparable that predicted by the DFT calculations for $MeTi(NMe_2)_3$. The short Ti–N distance (1.886 Å) coupled

with the planar amine is consistent with $d\pi$–$p\pi$ Ti–N bonding (Table 3.2). The Ti–Br bond length lies around the standard length 2.5 Å

Molecule	Ti–X (Å)	Ti–L (Å)
$BrTi(NMe_2)_3$ (**9**)	2.472	1.886
$ClTi(NMe_2)_3$ [166]	2.300	1.866
$ClTi(NEt_2)_3$ [166]	2.300	1.861
$ClTi(N(SiMe_3)_2)_3$ [167]	2.259	1.940
$ClTi(NMeC_2H_4)_3N$ [168]	2.292	1.923
$ClTi(N(C_6H_{11})_2)_3$ [169]	2.309	1.882

Table 3.2: Comparison of salient structural features of $BrTi(NMe_2)_3$ (**9**) with the corresponding parameters reported for other halo-titanium amides.

3.3.2 Synthesis and Structrual Studies of the Novel Cluster Complex $[\{Ti(NMe_2)_3O\}_2Ti_3(NMe_2)_6OBr_2]$ (10)

Small, red, block crystals were isolated as by-products in the synthesis of $BrTi(NMe_2)_3$ (**9**) described above in Section 3.3.1. Deposited from solutions at low temperature, it was initially thought that they were crystals of $Br_2Ti(NMe_2)_2$, reported to be a red liquid by Bürger and Neese. However, X-ray diffraction studies showed **10** to be much more complex than expected.

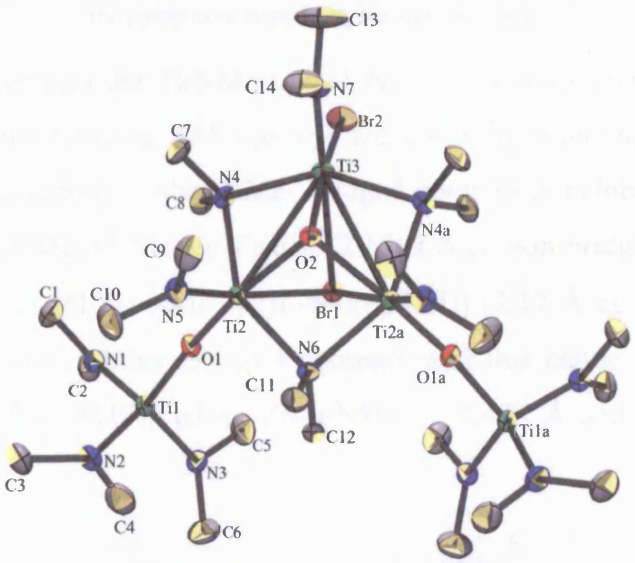

Figure 3.11: X-ray crystal structure of $[\{Ti(NMe_2)_3O\}_2Ti_3(NMe_2)_6OBr_2]$ (**10**) at 130 K.
Selected average bond lengths (in Å): Ti–Ti = 3.0583(8), Br(1)-Ti(3) = 2.8322(8), Br(1)-Ti(2) = 2.8667(6), Ti(2)-N(6) = 2.168(2).

Selected average bond angles (in degrees): Ti(3)-Br(1)-Ti(2) = 64.908(17), O(1)-Ti(2)-O(2) = 164.18(10), Br(2)-Ti(3)-Br(1) = 84.32(3).

The structure was solved to give the unusual bromo- and oxo- capped, μ–oxo complex shown in Figure 3.11, with the molecular packing of the crystal structure illustrated in Figure 3.12. This molecule appears to be a stable product of oxidation of **9**. Complex **10** crystallises in the monoclinic space group $P2_1/m$, with 0.5 molecules per unit cell. The crystal structure reveals the presence of capping bromo and oxo ligands in addition to bridging oxygen atoms and NMe_2 moieties. A CSD database search indicates that the presence of a 3 co-ordinate Br with a Group 4 metal is unique. However, the central cage structure of three metal centres linked by equivalent bridging groups with a halogen and an oxygen cap is present in a number of Group 4 compounds. Some examples of titanium based cages are: $[Ti_3(\mu_3\text{-}O)(\mu_3\text{-}Cl)(\mu\text{-}Cl)_3(Me_2Si(N^tBu)_2)_3]$ (**11**), with both bridging chlorides and a chloro cap;[170] $[Ti_3(\mu_3\text{-}O)(\mu_3\text{-}Cl)(\mu\text{-}OCH_2CMe_3)_3(OCH_2CMe_3)_6]$ (**12**) with bridging OR ligands and a chloro cap[171] and $[Ti_3(\mu\text{-}O^iPr)_3(\mu_3\text{-}O)(\mu_3\text{-}F)(O^iPr)_6]$ (**13**) which has bridging OR ligands and a fluoro cap.[172]

	Ti–Ti (Å)	Ti–μE (Å)	Ti–μ_3X (Å)	Ti–μ_3O (Å)
10	3.058	2.168	2.855	1.979
11		2.474	2.750	1.998
12	3.041	2.031	2.782	1.934
13		n/a	2.144	2.054

Table 3.3: Comparison of selected bond lengths (Å) at the Ti metal centres of $[\{Ti(NMe_2)_3O\}_2Ti_3(NMe_2)_6OBr_2]$ (**10**) with those reported for complexes containing similar moieties.

The Ti–N bond lengths in the $Ti(NMe_2)_3$ moiety are almost identical with those in **9**. However, those of the bridging NMe_2 groups are 2.168 Å, reflecting the 4 co-ordinate nature of the nitrogen atom. Other NMe_2 bridged complexes exhibit this longer Ti–N bond, such as $[Ti(\mu\text{-}NMe_2)(NMe_2)(\mu\text{-}F)(F)]_6$ (2.1562 Å cf. non-bridging Ti–N of 1.8899 Å)[173] and $[\{Ti(NMe_2)(N_3)(\mu\text{-}NMe_2)\}_3(\mu_3\text{-}N_3)(\mu_3\text{-}NH)]$ (2.17 Å cf. 1.88 Å).[174] This has also been observed in other Group 4 complexes of this nature *e.g.* $[(NMe_2)_3Zr(\mu\text{-}Cl)_2(\mu\text{-}NMe_2)Zr(NMe_2)_2(THF)]$ where Zr–μ-NMe_2 = 2.408 Å and Zr–NMe_2 = 2.056 Å.[175]

The bridging Ti(1)–O(1)–Ti(2) bond angle is 172.03(13)°, comparable to the similar ones discussed in Section 3.2.3. The deviation of this angle from 180° suggests there is not a strong π-bonding interaction. With the NMe_2 groups engaging in a degree of

π-bonding at the Ti(1) centre and the additional co-ordination of Ti(2), strong π-bonding by the μ–O would not be expected.

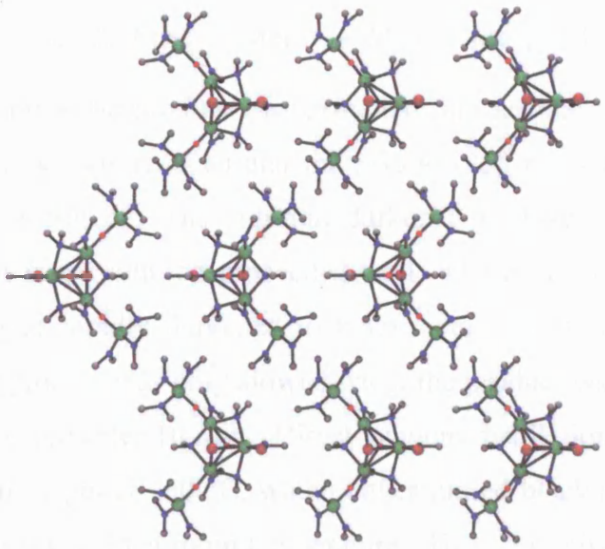

Figure 3.12: Molecular packing in the crystal structure of $[\{Ti(NMe_2)_3O\}_2Ti_3(NMe_2)_6OBr_2]$ (**10**).

The readily hydrolysed complex **10** proved to be insoluble in ethers, hydrocarbons and pyridine excluding the possibility of further analysis by solution NMR and mass spectrometry. The facile oxidation of this complex also precluded its characterisation by solid-state NMR spectroscopy and elemental analysis.

This initially serendipitous synthesis of **10** was repeated by deliberate introduction of atmospheric oxygen into a solution of $BrTi(NMe_2)_3$ (**9**). Thus, 10 ml of air contained in a small round-bottomed flask was bubbled through a hexane solution of **9** via a cannula. A white precipitate, presumed to be TiO_2, immediately formed in the clear yellow solution, but on standing at –30 °C for 24 h, small red block crystals were observed and isolated by manual separation. This direct synthetic route has proved to be repeatable, but yields remain too small to be quantified.

3.3.3 Attempted Synthesis and DFT studies of $MeTi(NMe_2)_3$ (14)

Synthesis of $MeTi(NMe_2)_3$ (**14**) was initially attempted following the reported literature route,[163] by reacting equimolar quantities of $BrTi(NMe_2)_3$ (**9**) with MeLi in diethyl ether at –20 °C. The dropwise addition of a dilute solution of MeLi to a stirred solution of **9** was conducted over 2 h, resulting in a yellow solution. After warming to room temperature, the reaction mixture was stirred for a further 1h and the solvent removed *in*

vacuo. The remaining mixture was the expected bright yellow, but sublimation onto a cold finger did not produce the reported low melting point yellow product. No material appeared on the cold finger on each attempted synthesis.

$$BrTi(NMe_2)_3 + MeLi \rightarrow MeTi(NMe_2)_3 + LiBr \qquad \textbf{[3.4]}$$

In subsequent reactions the product was extracted into hexane, giving a bright yellow solution. The volume was reduced and the solution left at –40 °C overnight, but no yellow precipitate resulted. The solution darkened to black over 48 h. Vacuum distillation of the hexane solution proceeded well, with a viscous yellow liquid being isolated. This liquid rapidly darkened to black over 2 min when warmed to room temperature. This process was only slowed when the product was kept at –50 °C, with decomposition observed after 10 min. Direct vacuum distillation of the initial reaction mixture gave a yellow gel at –50 °C, which either turned black as before, or remained an orange/yellow waxy solid at room temperature. The alternative methylating reagents MeMgI and Me_2Zn were employed, with similar results.

Investigation of the decomposition products by ^1H NMR showed no features at δ 0.47 and 3.31, (the literature values for Ti–*Me* and TiN*Me*$_2$).[163] In order to gain some understanding the decomposition pathway and thereby to avoid it, a reaction using CD_3MgI was conducted in a Young's NMR tube, and monitored by ^2H NMR spectroscopy. Decomposition of the yellow reaction mixture was followed over a 24 h period, with a peak observed at δ 7.81 in the free N–D region, indicating that the hydrogen originated from the methylating reagent. This suggested the decomposition was a result of an excess of methylating reagent; however repeating the reaction with a sub-stoichiometric amount of CD_3MgI did not lead to improved results. It is clear that additional investigation is required to understand the problems encountered in this synthesis.

The DFT calculations for **14** predicted the molecule to adopt a C_3 symmetry with planar NMe_2 groups angled around the metal centre, as shown in Figure 3.13. Table 3.4 gives a comparison between the calculated bond lengths and angles and those of some related compounds. This once again highlights the short Ti–L distance for Ti–NMe_2 when compared to bond lengths for both electron donating (L = Bz) and electron withdrawing (L = Cl) groups.

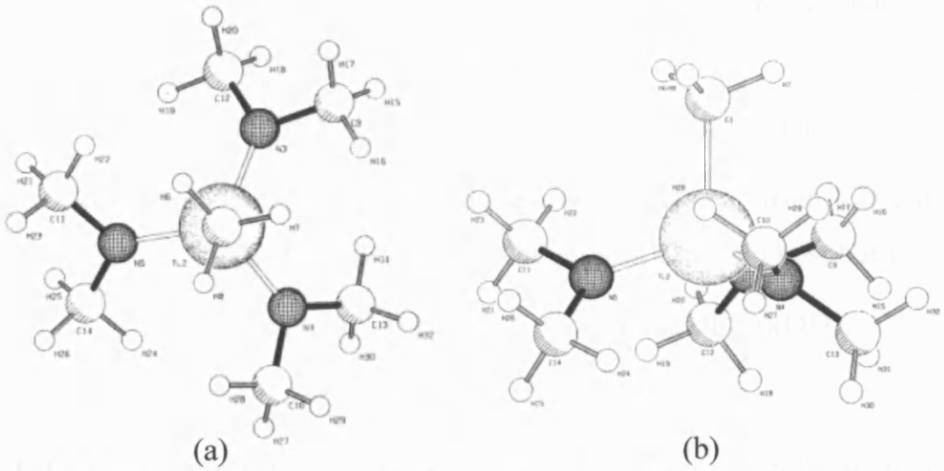

Figure 3.13: Calculated molecular structure of $MeTi(NMe_2)_3$ (**14**) (a) viewed down the rotational axis of symmetry, and (b) viewed from the side.

Molecule	Ti–C (Å) (Ti–X)	Ti–L (Å)	∠Ti–C–H (°)	∠L–Ti–C (°) (L–Ti–X)	∠L–Ti–L (°)
$MeTi(NMe_2)_3$ (**14**)	2.127	1.904	111.8	108.2	110.7
$MeTiCl_3$[176]	2.047	2.185	109.0	105.6	
$MeTi(N(SiMe_3)_2)_3$[177]	2.127	1.935	n/a	102.4	115.6
$ClTi(N(SiMe_3)_2)_3$[167]	(2.259)	1.940		(104.1)	114.3
$TiBz_4$ [178]	2.13	2.13			109.5
$BrTi(NMe_2)_3$	(2.472)	1.886		(113.5)	105.2

Table 3.4: Comparison of salient bond lengths and angles at the Ti centre of $MeTi(NMe_2)_3$ (**14**) with those of related compounds.

3.4 Synthesis and Spectroscopic Studies of $MeTi(O^iPr)_3$ (15)

Isotopic studies, particularly using deuterium, give a wealth of information regarding mechanisms, reactivity and rates by comparison with the protio isotopomer.[179] The zero-point energy (zpe) differences between C–H and C–D bonds can result in reduced quantum mechanical tunnelling in the deuteriated form of an active complex. H/D exchange processes illustrate differences between analogous systems,[180;181] and relative reaction rates give evidence for the extent of bond cleavage in the transition state of a reaction, as exemplified by σ-bond metathesis.[182] Isotopic perturbation can also be exploited to investigate agostic bonding through IR and NMR spectroscopic studies.[12]

3.4.1 Synthesis of MeTi(O^{i}Pr)$_3$ (15)

The isotopomers $CH_3Ti(O^iPr)_3$, $CH_2DTi(O^iPr)_3$ and $CD_3Ti(O^iPr)_3$ were each synthesised by metathesis following the literature procedure.[183]

$$ClTi(O^iPr)_3 + MeLi \rightarrow CH_3Ti(O^iPr)_3 + LiCl \quad \textbf{[3.5]}$$

The appropriate deuteriated Grignard reagents were prepared from CD_3I and CH_2DI synthesised from or CH_2DOH with iodine in the presence of red phosphorus.[184]

$$CD_3OD + 2\,P + 3\,I_2 \rightarrow 6\,CD_3I + 2\,DP(O)(OD)_2 \quad \textbf{[3.6]}$$

$$CD_3I + Mg \rightarrow CD_3MgI \quad \textbf{[3.7]}$$

The alkyl-titanium product was distilled *in vacuo* using a microdistillation unit, and collected in a narrow bore tube sealed with a Young's valve.

3.4.2 IR Spectroscopic Studies

The use of partially deuteriated species to explore C–H vibrational frequencies in IR spectroscopy has been applied to a range of compounds to investigate the geometry of the M–R and, in this case, the M–CH_3 moiety.[185-187] When the barrier to internal rotation is greater than 4 kJmol^{-1} non-equivalent C–H bonds can be independently observed in IR spectra.[185] The observation of two or three separate C–H stretching bands allows the identification of the different C–H bonds within a methyl group of a compound, something that is particularly useful for identifying agostic interactions.

Comparative studies with CD_3, CH_3 and CH_2D derivatives can yield information about the H–C–H angles and C–H bond lengths.[188] This partial deuteriation technique exploits the difference in the bond stretching frequencies between C–H and C–D and is based on the idea that the stretching frequency of a single, isolated CH bond, ν_{CH}^{is}, or CD bond, ν_{CD}^{is}, can be measured. Here the analysis of the IR spectra focuses on either the relatively empty C–D stretch region of 1800-2400 cm^{-1} or around 3000 cm^{-1} where the methyl C–H stretching vibrations occur. The difference in stretching frequency of the two bonds makes them effectively decoupled from one another enabling the measurement of ν_{CH}^{is} in the CHD_2 compound and ν_{CD}^{is} in the CH_2D one. McKean *et al.*[189] demonstrated that individual Me groups in Me_2X or Me_3X have negligible coupling between their C–H stretching modes. This is illustrated by the comparison of

the IR spectra of $CH_3(CD_3)_2X$ and $(CH_3)_3X$, where the differences in the C–H stretching region are imperceptible.

Empirical correlations link the ν^{is} frequency with the bond dissociation energy allowing assessment of the C–H and C–D bond strengths, equally a correlation between ν^{is}_{CH} and the bond length $\mathbf{r}_0$(CH) can be drawn using equation 3.8, given below.[188]

$$\mathbf{r}_0(\text{CH})\ (\text{Å}) = 1.3982 - 0.0001023\nu^{is}(\text{CH})\ (\text{cm}^{-1}) \qquad \textbf{[3.8]}$$

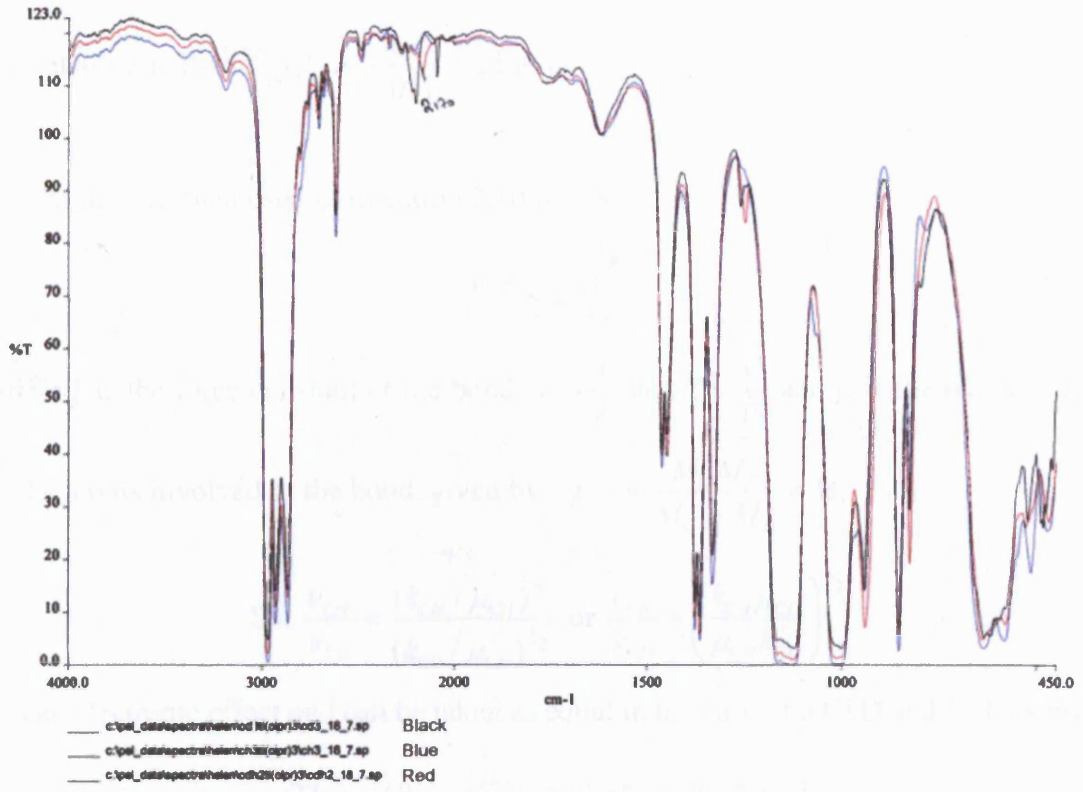

Figure 3.14: IR spectra of the CH_3, CH_2D and CD_3 isotopomers of $MeTi(O^iPr)_3$ (**15**) in the region 450-4000 cm^{-1}, measured in a diamond cell at room temperature.

The spectra of the CH_3, CH_2D and CD_3 isotopomers of **15** (Figure 3.14) were recorded at room temperature for the neat liquids in a diamond cell. The strong bands associated with the isopropoxyl group in the 2800-3000 cm^{-1} region prevented assignment of ν_{CH}. Analysis of the C–D stretching region was assisted by the approximate sum rule for CH or CD stretching frequencies; Equation 3.9.[190]

$$\sum \nu_i(CD_3) = \sum_i \nu^{is}_{CD} \qquad \textbf{[3.9]}$$

Three bands were observed in the IR spectrum of $CD_3Ti(O^iPr)_3$, at 2229, 2208 and 2098 cm^{-1}, with the pattern indicating there are 2 strong and 1 weak bonds in the methyl

group. Application of Equation 3.9 gives ν_{CD}^{is}= 2178 cm^{-1}, in accord with $\bar{\nu}_{CD}$ = 2170 cm^{-1} observed in the IR spectrum of $CH_2DTi(O^iPr)_3$. No additional bands associated with agostic C–H bonds were present in the 1800-1900 cm^{-1} region of the spectra of $CH_2DTi(O^iPr)_3$ or $CH_3Ti(O^iPr)_3$.

Calculation of ν_{CH}^{is} and r_0 from ν_{CD}^{is} of $MeTi(O^iPr)_3$ was conducted by the following route:

First the experimentally derived wavenumber, $\bar{\nu}$ (cm^{-1}), of the C–D stretch was corrected for anharmonicity:[188] $\nu_{CD}^{is} = \frac{\bar{\nu}_{CD}}{1.011} = 2146\ cm^{-1}$

This value was then used in Equation 3.10 below:

$$\bar{\nu} = \frac{1}{2\pi\bar{c}}\sqrt{\frac{k}{\mu}} \qquad \textbf{[3.10]}$$

where k is the force constant of the bond, $\bar{\nu} = \frac{1}{\lambda}$ and $\bar{c} = \frac{\nu}{\bar{\nu}}$ and μ is the reduced mass of the atoms involved in the bond, given by: $\mu_{CD} = \frac{M_C M_D}{M_C + M_D} \times M_n$

$$\text{So: } \frac{\nu_{CH}}{\nu_{CD}} = \frac{(k_{CH}/\mu_{CH})^{1/2}}{(k_{CD}/\mu_{CD})^{1/2}} \text{ or } \frac{\nu_{CH}}{\nu_{CD}} = \left(\frac{k_{CH}\mu_{CD}}{\mu_{CH}k_{CD}}\right)^{1/2}$$

k is an electronic effect and can be taken as equal in the case of a C–D and C–H bond.

$$\text{Thus } \frac{\nu_{CH}}{\nu_{CD}} = \sqrt{\frac{\mu_{CD}}{\mu_{CH}}} \text{ and } \nu_{CH}^{is} = 2925\ cm^{-1}$$

From Equation 3.8 r_0(CH) is therefore 1.099 Å, a comparable value to other methyl-metal derivatives (Table 3.5).

Molecule	ν_{CH}^{is} (cm^{-1})	r_0(CH) (Å)
$MeTi(O^iPr)_3$ (**15**)	2925	1.099
$MeTiCl_3$	2952	1.096
Me_2TiCl_2	2938	1.098
$CpTiMeCl_2$	2958 x 2 2918	1.096 1.100
Cp_2TiMe_2	2932 x 2 2915	1.098 1.100
$GeMe_4$	2954	1.096
$ZnMe_2$	2935	1.098

Table 3.5: Comparison of ν_{CH}^{is} and r_0(CH) values of $MeTi(O^iPr)_3$ (**15**) with corresponding parameters reported for other metal-methyl compounds.

During the course of this study, we also measured the IR spectra for the CH_3, CH_2D and CD_3 isotopomers of the complex $[(NC_6H_3{}^iPr_2\text{-}2,6)_2MoMe_2]$ (**16**) as part of a collaboration with Prof. Vernon Gibson, Imperial College London. This complex has been shown by neutron diffraction to possess two agostic methyl groups, in each of which two of the three C–H bonds display a close approach to the Mo centre. The IR spectra for **16** are shown in Fig. 3.15. The CH_2D- isotopomer shows a doublet ν_{CD}^{is} feature at 2190 and 2160 cm^{-1}; these values convert as described above to ν_{CH}^{is} ones of 2952 and 2912 cm^{-1}; corresponding to r_0(CH) bond lengths of 1.096 and 1.100 Å, respectively. Although the lack of resolution in the C–D stretching region for the CD_3 isotopomer precludes use of Equation 3.9 in this case, we conclude that the splitting observed in the mode for the CH_2D- isotopomer of **16** is constant with the two chemically distinct C–H bonds in the complex. This study serves once again to highlight the power of the method, which can detect very small differences (0.004 Å) between C–H bonds that are invisible to even neutron diffraction (esd values of 0.01 Å).

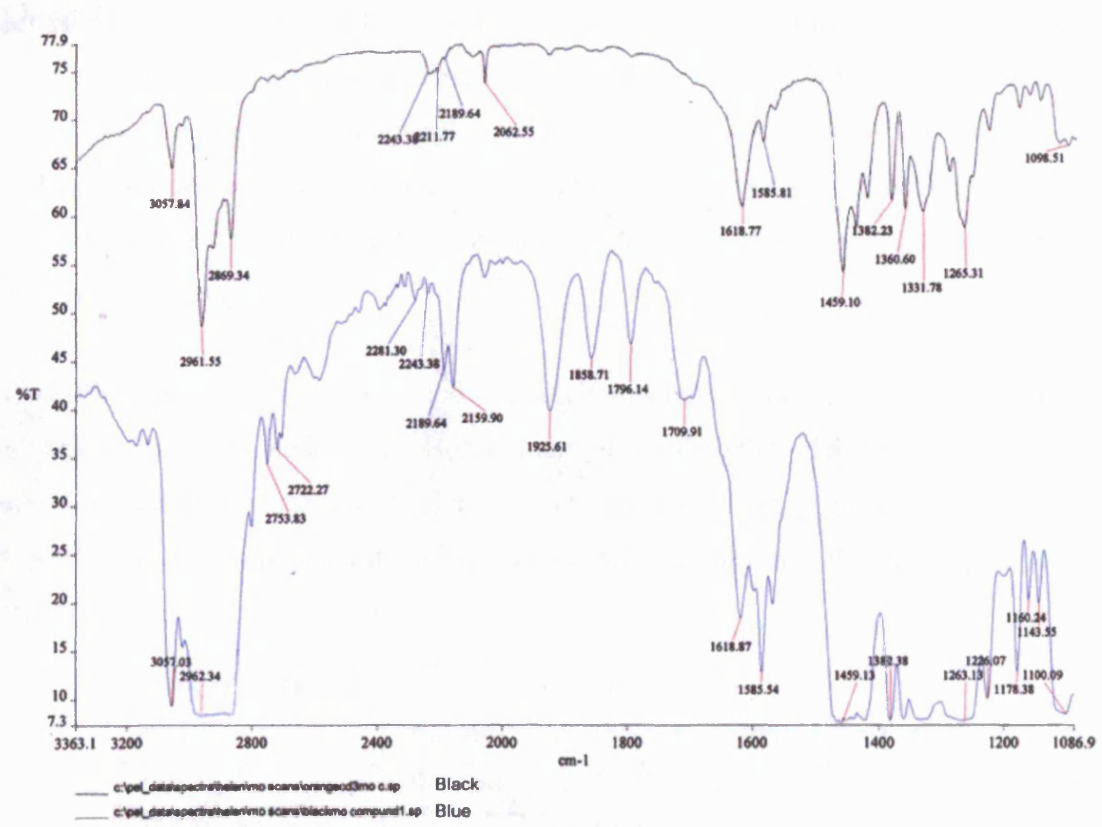

Figure 3.15: IR spectra of $[(NC_6H_3{}^iPr_2\text{-}2,6)_2MoMe_2]$ (**16**): (above) CD_3- isotopomer and (below) CH_2D-isotopomer in the region 1087-3363 cm^{-1}, measured in a diamond cell at room temperature.

3.4.3 NMR Spectroscopic Studies

Isotopic perturbation of resonance (IPR) studies have been conducted on a number of species demonstrating agostic bonding. First applied to a transition metal complex by Shapley in 1978,[13] the IPR approach assists identification of fluxional agostic bonding that is otherwise unobservable, even at low temperatures. A standard ^1H NMR experiment involves the study of an equal mixture of isotopomers in a single NMR sample over a range of temperatures; when considering a potential agostic methyl group, a mixture of the CH_3– and CH_2D– complexes are usually used. Where there is an agostic/terminal H exchange, there will be an average chemical shift δ_0 noted for the CH_3-, d_0 complex: $\delta_0 = \frac{2\delta_t + \delta_a}{3}$ with t and a indicating terminal and agostic respectively. The chemical shift, δ_1 for the d_1 complex will not be the same as δ_0, because the zpe differences between the C–H and C–D bonds ensures that H is favoured in the agostic position. The average chemical shift for the partially deuteriated complex is therefore not the result of an equal distribution and the weighting given to the agostic C–D is described by A, a Boltzman factor where A = $\exp \frac{\Delta E}{RT}$, and $\delta_1 = \frac{\delta_a + \delta_t + A\delta_t}{2 + A}$.

Measuring the chemical shifts over a range of temperatures allows confirmation of the proposed exchange through the dependence of A on *T*. Thus, if the ^1H spectrum shows a singlet and a doublet with a single chemical shift, corresponding to the methyl group of both isotopomers, over a range of temperatures, it indicates the methyl group in the static structures of both species is the same, with no effect from the unequal zero-point energies of ^1H and ^2H.

This IPR experiment was conducted over the temperature range 223-298 K on a sample containing the CH_3- and CH_2D- isotopomers of $MeTi(O^iPr)_3$ (**15**) in d_8-toluene At the upper temperature, a *pseudo*-triplet was observed at 0.745 ppm, corresponding to a singlet at that chemical shift and a doublet with a splitting of ~0.009 ppm centred around it.

Temperature (K)	$TiCH_3/TiCH_2D$			J
298.1	0.7496	0.7453	0.7410	0.0086
276.0	0.7798	0.7759	0.7721	0.0077
256.0		0.7975		
233.0		0.819		
223.0		0.827		

Table 3.6: Summary of IPR NMR data for the CH_3- and CH_2D- isotopomers of $MeTi(O^iPr)_3$ (**15**).

At 256 K a broad signal with a FWHH of 3.7 Hz or 0.009 ppm was observed. This is sufficiently broad to contain the two separate signals and is consistent with the coalesced doublet and singlet peaks. The symmetry of this signal and those observed at lower temperatures enabled it to be fitted with a Lorentzian curve, indicating there was no change in the relative chemical shifts of the methyl group in the isotopomers. It is possible that the change in chemical shift is very small, but in light of the results of the IR studies above it is concluded that the static states for the two complexes in solution do not involve C–H···M interactions to any significant degree. It is worth noting here that application of the IPR experiment to identify agostic interactions in d^0 systems has major drawbacks, and has failed to give a positive result for complexes like $[EtTiCl_3(dmpe)]$, where there is incontrovertible diffraction evidence of such an interaction.

3.5 Conclusions

This Chapter has explored the metal-ligand interactions in a series of d^0 Ti compounds through the application of a range of experimental and theoretical techniques. Detailed analysis of the molecular charge distribution for $[(Bz_3Ti)_2O]$ has confirmed the presence of ligand-induced charge concentrations at the titanium centre, showing those wrought by the more covalent Ti–C bonds to be larger than the corresponding features caused by the more ionic Ti–O moieties.

The known compound $BrTi(NMe_2)_3$ has been structurally characterised by X-ray diffraction. It adopts the hexagonal space group R3 leading to the formation of a polar crystal.

The novel cluster complex $[\{Ti(NMe_2)_2O\}_2Ti_3(NMe_2)_6OBr_2]$ was synthesised by the partial oxidation of $BrTi(NMe_2)_3$. It has also been characterised by X-ray diffraction, and shown to possess a unique capping bromo ligand.

Through a combination of NMR and IR spectroscopic techniques, $MeTi(O^iPr)_3$ has been shown to exhibit no α-agostic interactions.

Chapter 4

Variable Energy Photoelectron Spectroscopy and Absorption Spectroscopy

The studies described in Chapters 2 and 3 focused on the chemical environment around a transition metal centre and the impact of this environment on the nature of the bonding in, and the physical geometry of, a molecule in relation to its reactivity. The work presented in Chapters 5 and 6 will focus on the electronic structure of simple molecules of clearly defined physical geometry. The application of photoelectron and absorption spectroscopy, in conjunction with quantum chemical calculations, has permitted the exploration of the MOs of simple molecules to gain insight into the observed reactivity.

4.1 Photoelectron Spectroscopy (PES)

When an atom is exposed to light of sufficient energy, an electron may be expelled.

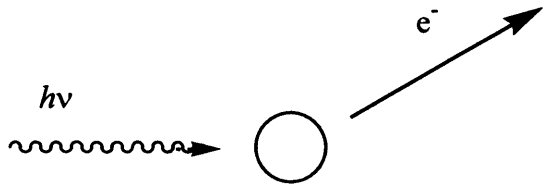

Figure 4.1: Schematic representation of the photoelectron effect.

From Planck's equation $E = h\nu$ and the conservation of energy, Einstein[191] inferred that the kinetic energy, KE, of an electron expelled as the result of the photoelectron effect may be expressed as:

$$KE = h\nu - BE \qquad [4.1]$$

where $h\nu$ is the energy of the incident photon beam and BE is the binding or ionisation energy of the electron, when there is no change in vibrational or rotational energy of the molecule on ionisation. The changes in molecular kinetic energy (such as vibrational and rotational energy) resulting from the ejection of an electron, affect the final kinetic energy of the electron. These changes can lead to the appearance of fine structure in photoelectron spectra and are mainly associated with vibrational transitions, as the spectral line width for rotational fine structure is typically only 10 meV,[192] too small to

be observed in PES spectra. Other changes in energy, *e.g.* molecular translation, are small enough to be ignored in terms of their impact on the observed binding energy.

4.1.1 The Basis of Photoelectron Spectroscopy

In the PES experiment, a gaseous sample is exposed to a monochromatic beam of photons generated from either a discharge lamp or a synchrotron. These cause excitation and ejection of electrons in the sample. The kinetic energies (KEs) of the ejected electrons are used to provide an insight into the chemical bonding within the molecule. PES records the relative number of electrons emitted at each *KE* in a given range. The spectrum consists of a series of bands and MO theory provides a good framework to interpret the energy data collected.[19] The bands observed in the PES spectrum of a closed-shell molecule can be regarded as mapping its MO structure where the bands are associated with a hole in its electronic structure. This simple model does not enable quantitative analysis, but rather observations of trends. For the closed shell molecules discussed in this thesis, we apply Koopmans' theorem,[193] described in Equation 4.2, in which the ionisation energy of an electron is taken as being the energy of the MO, *i*, it occupied.

$$IE \approx -\varepsilon_i \qquad \textbf{[4.2]}$$

This approximation uses the vertical rather than the adiabatic ionisation energy, so it holds true in some cases, particularly for non-bonding electrons, and less well in others. It is the difference between these two ionisations that, through the Franck-Condon principle,[194] gives rise to the extent of vibrational fine structure from the excited state of the ion.

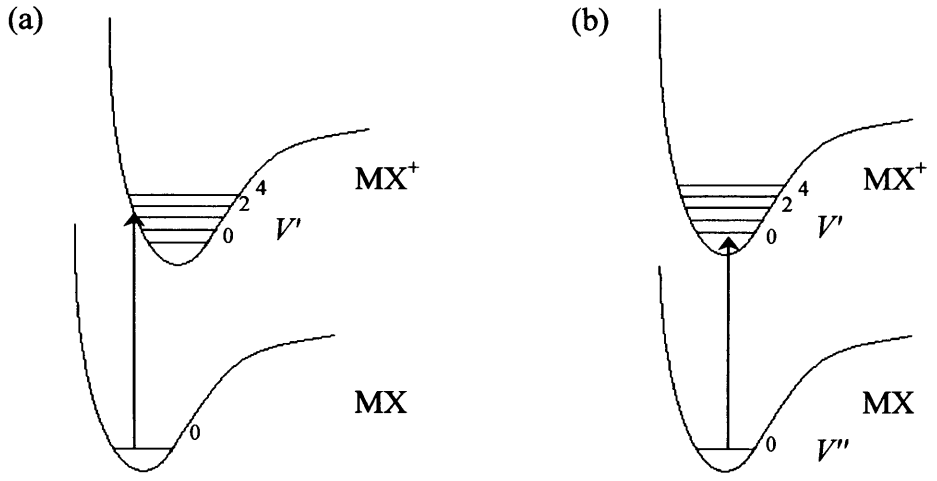

Figure 4.2: Potential energy curves for the photoionisation of a molecule (MX) resulting in (a) a vibrationally excited ion; and (b) a vibrationally unexcited ion.

Figure 4.2 considers a diatomic molecule, MX, in the vibrational ground state which is then ionised to MX^+. In part (a) the potential energy curve of the ion is offset along the internuclear (r) axis, indicating a change in bond strength so vertical ionisation results in a vibrationally excited ion. In part (b) there is little change in r from the ionisation, hence no vibrational excitation. In a PES spectrum (a) would be observed as a broad band, with vibrational fine structure, and (b) as a narrow band. From a structural point of view, the loss of an electron from a bonding orbital alters the associated bond strength: the atoms need to alter their positions to reflect the r_e associated with the new bond order, giving rise to vibrations; whereas the loss of a non-bonding electron does not perturb the bond order or strength so no atomic movement is necessary for the atoms to be in their equilibrium positions. The resolution required to see this fine structure is not always achievable, but the width of the spectral bands can be used to indicate the bonding or non-bonding nature of the associated MO.

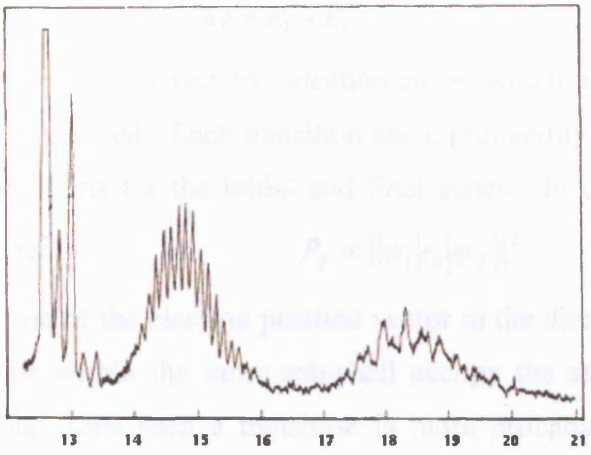

Figure 4.3: He(I) photoelectron spectrum of H_2O.[195]

For example in the He(I) spectrum for H_2O shown in Figure 4.3, the first band (of lowest ionisation energy) is narrow with little vibrational structure. In MO terms this band corresponds to the HOMO, the non-bonding π(y) electrons. The two other bands are much broader with clear vibrational structure and are associated with the bonding σ(x) and σ(z) orbitals.[195]

4.1.2 Experimental Photoelectron Spectroscopy

Turner[196] and Siegbahn[197] conducted the first experiments in the 1960s to investigate the electronic structure of molecules by exploiting the photoelectron effect. The technique has since been used to probe an extensive array of compounds enabling comparison of the ordering of valence orbitals of similar complexes. Experiments are

conducted by drawing a small stream of gas-phase molecules into a chamber under vacuum and bombarding them with monochromatic photons. The use of a He discharge lamp gives access to two different photon energies; He (I) $h\nu = 21.2$ eV (58.4 nm) and He (II) $h\nu = 40.8$ eV (30.4 nm). With the electrons being ejected in all directions, it is only those that pass through a slit in the ionisation chamber into the electrostatic analyser and on to an electron detector that are observed. The electron kinetic energy is measured by the extent of the deflection of its path in the analyser. Although PES can also be used to study surfaces, in this thesis it is considered only in terms of gas phase molecules.

4.2 VUV and X-ray Absorption Spectroscopy

In absorption spectroscopy, ground state electrons of energy E_i absorb photons and are excited to higher 'allowed' energy levels at energy E_f.

$$h\nu = E_f - E_i \qquad \textbf{[4.3]}$$

The possible transitions are governed by selection rules, which arise in part because angular momentum is conserved. Each transition has a probability dependent upon the overlap of the wavefunctions for the initial and final states. In quantum mechanical terms this is expressed as:

$$P_{if} \propto \left|\langle \psi_i | r_A | \psi_f \rangle\right|^2 \qquad \textbf{[4.4]}$$

where r_A is the projection of the electron position vector in the direction of polarisation of the photon. Orbitals within the same sub-shell occupy the same region of space giving a greater overlap, thus such a transition is more probable than one between orbitals of different quantum numbers.

Absorption spectroscopy is conducted in a similar manner to PES, but measurements are taken of the beam intensity before and after the sample, with the data recorded being the difference between the initial and final intensity. The spectra show absorption edges, which are sudden increases in absorption corresponding to the onset of the excitation of electrons from a given core level. The near edge refers to excitation to the lowest unoccupied MO orbitals and the far edge to excitation to the continuum above the ionisation limit. Edges may contain a number of bands corresponding to excitation of electrons from one state to a number of different states. When the photon energies are larger than the minimum ionisation energy, the absorption of photons is always very likely to result in photoionisation. The resonant features of PES are attributed to this

process, allowing comparison of the absorption co-efficient with the cross sections to facilitate interpretation.

4.3 Synchrotron Radiation

The use of discharge lamps to provide monochromatic light has enabled a wide range of molecules to be studied by PES. However, the technique has been limited by the wavelengths available to the study of valence electrons. The ability to investigate electrons with higher ionisation energies, and all electrons over a wider range of incident energies has only emerged with the increased availability of facilities able to produce light of an appropriately high energy.

When charged particles move at relativistic velocities on a curved trajectory they emit electromagnetic radiation. It is this synchrotron radiation that is used to conduct variable energy photoelectron and absorption spectroscopy. The theoretical basis for the emission of synchrotron radiation was initially developed when models were being explored to explain atomic structure and spectra.[198;199] After Bohr's model of the atom was accepted the phenomenon was not followed up until the 1940s when synchrotron radiation was observed as a frustrating by-product in particle accelerators, limiting the top speed of the particles.[200;201] It was initially investigated with the view of easing problems for experimental accelerator physics, but following the work of Tomboulian and Harmann[202] in the vacuum ultraviolet, its intensity and spectral width made it a desirable commodity. Initial facilities were optimised for the particle acceleration they were designed for rather than for synchrotron radiation, so completion of dedicated electron storage rings in the 1970s allowed the expansion of experimental time.[203] There are now many synchrotrons around the world including ELETTRA at Trieste, Italy where the variable energy photoelectron spectroscopy (VEPES) and absorption spectroscopy work in this thesis was conducted in collaboration with Prof. Jennifer Green, University of Oxford and Dr. Monica de Simone, University of Roma. Here, the Gas Phase Beamline is dedicated to studies in the gas-phase.

Figure 4.4: Aerial view of the ELETTRA Synchrotron at Trieste.

4.4 Applications of Synchrotron Radiation

Synchrotron radiation provides access to a very wide range of photon energies, enabling a more in depth investigation of molecular electronic structure than is possible with standard absorption spectroscopy and PES to be conducted.[204;205] One of the key benefits of using variable energy photoelectron spectroscopy exploits this wide photon energy range to allow both the valence and core electron states to be investigated, although for core states of transition metal complexes high energy photons are required. Use of lower-energy photons allows greater resolution to be obtained; this is attributed to the narrower intrinsic width of the source emission line.

Each valence spectral band can be investigated over a wide range of photon energies, with the change in band intensity over the incident energy range giving sufficient information to plot σ, the relative partial photoionisation cross-section (RPPICS) and the derived branching ratio. Used in conjunction with DFT calculations, it is a powerful tool in understanding the bonding and reactivity of a molecule. In particular, the very different behaviour of the partial cross-sections of *d* and *f* electrons compared to those of *s* and *p* electrons provides extensive information on metal-ligand covalency. The origin of the features observed in the cross-sections may also be probed by absorption spectroscopy, where observed excitations give information about resonance processes that may result in photoionisation.

The ability to probe the electron core through use of high-energy photons gives a clear indication of the electrons' involvement – or not – in bonding and helps to map the make-up of virtual orbitals through excitation from the core into unoccupied valence orbitals. For example, VEPES studies of OsO_4, backed up by calculations, showed evidence of interaction of the $5p$ core with the valence electrons.[206;207]

4.4.1 The Gas Phase Photoemission Beamline[208;209]

ELETTRA in Trieste, shown in Figure 4.4, is an electron storage ring with an operational energy of 2.4 – 2.0 GeV. The electrons are injected daily at 0.9 – 1.0 GeV and accelerated under ultrahigh vacuum by bending magnets at points around the ring to 2.4 GeV over 30-45 min. In the normal, multi-bunch, mode of operation the electrons circulate in bunches 5.4 mm long. The radiation is therefore not emitted continuously, but as pulses; however for our experiments the pulses are sufficiently close together that the beam can be considered constant. Thick, protective, concrete walls surround the storage ring and the initial part of the beamline allowing constant access to the user area. The beamline is situated at a tangent to the electron storage ring and all user operated valves are controlled through a computer system, bar that prior to the vacuum chamber, which is manually operated. It is this manual valve that is always closed first and opened last. On starting and stopping the beamline the valves are opened and closed in sequence, opening from the start of the beamline and closing from the end. The beamline layout is illustrated in Figure 4.5 below.

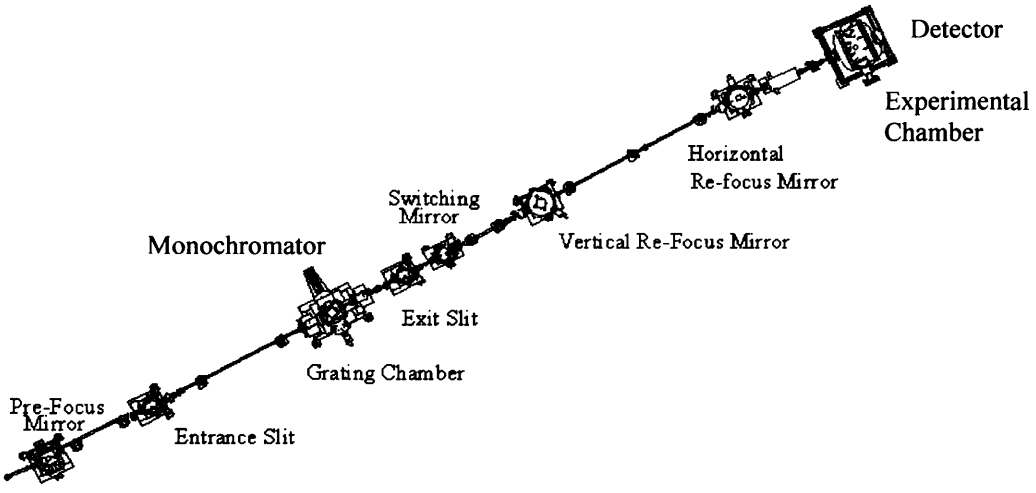

Figure 4.5: Schematic layout of the Gas Phase beamline, ELETTRA.[1]

[1] Modified from an original diagram by M. Alagia.

The white, unpolarised light from the synchrotron passes through the undulator where the GAP; i.e. the distance between the magnets of the undulator, is measured and set. It then travels through a stopper valve – the most important to remember to turn off – a double slit and then into a vacuum chamber at 10^{-9} mbar before reaching the initial switching mirror which directs it to the beamline. A prefocussing mirror, set at pitch 88 nm and roll 97 nm, precedes the in-slit to the monochromator, followed by a protective gate valve, the variable angle spherical grating monochromator and the out-slit. The slit widths are altered by manually operated Vernier gauges and the monochromator grating setting is selected in the same manner. The polarised light passes over a second switching mirror, sending it in our case to the main rather than the branch line, and is focussed by vertical and horizontal refocusing mirrors before entering the main vacuum chamber to which the diagnostic and experimental chambers are attached sequentially.

4.4.2 Using Synchrotron Radiation to Conduct PES

For our studies we used the experimental set-up shown in Figure 4.6. The experiment required the angle-resolved photoelectron spectrometer chamber, equipped with a 50 mm mean radius electron energy analyser mounted at the 'magic angle', where data are collected, so the intensities of the bands are independent of an angular parameter associated with beam polarisation,[204] and an ionisation cell.[210] The vacuum was generated by the combination of a turbo- and a cryo-pump, giving a backing pressure of ~ 6 x 10^{-7} mbar. The turbo-pump ran continuously, but the cryo-pump was isolated and turned off at the end of data collection.

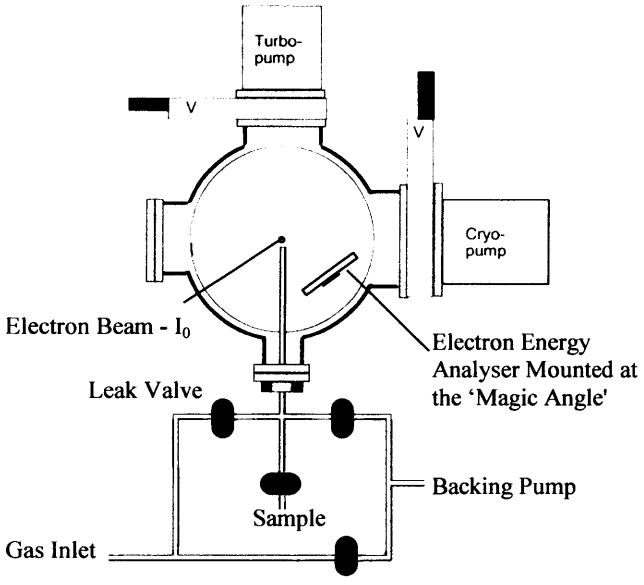

Figure 4.6: Experimental chamber for the acquisition of PES and absorption data.

The sample vapour was introduced via a needle valve and a narrow tube close to the ionisation region. The tube diameter was 6 mm for [$MeReO_3$] or 4 mm for [$M(BH_4)_4$] (M = Zr, Hf and U). The samples were attached to the experimental chamber via a network of pipes and valves. This network allowed the chamber to be isolated so that the sample could be evacuated via a separate backing pump or back filled through an additional gas inlet with either N_2 for storage or He to leak test. This gas inlet was also used when calibrating the detector with He and Ar. The band intensity for $MeReO_3$ was calibrated by measuring the intensity change of the helium spectrum over the same energy range. For the borohydride complexes studied in Chapter 6, the calibration gas, either argon or helium, was introduced simultaneously with the sample. The high ionisation energy of He means that only Ar can be used to calibrate spectra between 20 and 30 eV, but with a higher cross-section above 30 eV, He is the preferred calibrant for these energies. Both gases were used for $Zr(BH_4)_4$, but only Ar was employed for $Hf(BH_4)_4$ due to a coincidence of valence and He bands. For $U(BH_4)_4$, Ar was used for the 20-50 eV photon energy range and He for the photon energy range of 90-125 eV.

The signal intensity was optimised through the combination of the undulator GAP and the pass energy settings. A high pass energy gives high intensity bands, but the lower the pass energy used the higher the resolution obtained. The pass energy needed to be increased at higher photon energies to achieve a good signal-to-noise ratio. Valence state photoelectron spectra for $MeReO_3$ were recorded using a pass energy of 10 eV, corresponding to a resolution of 200 meV. A pass energy of 25 eV, corresponding to a resolution of 0.5 eV, was used for core and inner valence spectra. The work described in Chapter 6 used pass energies of 5 and 10 eV for the valence region and a pass energy of 10 eV for the core and inner valence spectra.

In the valence region, the range of photon energies was constrained at the low energy end by the orbital ionisation energies and at the high energy end by the decreasing band intensity. The initial scan range was determined via data from previous studies and modified after test runs. The experimental parameters were defined through the Labview programme written for the beamline. For each photon energy the undulator GAP setting was optimised to give maximum beam intensity by use of the GAP calculator.[211]

4.4.3 Using Synchrotron Radiation to Conduct Absorption Spectroscopy

Much of the experimental set-up for the X-ray and vacuum ultraviolet absorption spectroscopy mirrors that for the VEPES work. Samples were introduced to the experimental chamber in the same manner and the data processed using IGOR pro software. The photon flux of the incident monochromatic beam, I_0, was measured against that exiting the experimental chamber, I; the ratio indicating the level of absorption at that photon energy, as given in the Beer-Lambert law:

$$\log\frac{I}{I_0} = -\varepsilon[J]l \qquad \textbf{[4.5]}$$

where $[J]$ is the concentration of the sample, l the length of the sample through which the incident energy passes and ε the molar absorption co-efficient. l is constant for the experimental chamber and, by maintaining a consistent pressure in the chamber, $[J]$ too is constant.

VUV data collected in the photon energy range of 24-85 eV (52-15 nm) had a photon energy bandwidth of between 3 and 10 meV, with X-ray data collection having a photon energy resolution better than 100 meV. A constant pressure was maintained in the experimental chamber by establishing a steady flow rate of the sample, ensuring the results were comparable.

4.5 Analysis of the Spectra

4.5.1 VEPES

The spectra collected were normalised and referenced. For the photoelectron spectra, I_0 was measured during the course of a run by a calibrated photodiode positioned after the ionisation region in the path of the beam. Normalisation for beam flux within a run was conducted by dividing each data point by I_0 for every time point. The spectra recorded at each photon energy were combined to produce a time-weighted average spectrum and the background subtracted. The band energies were referenced to the internal calibrant gas N_2, He or Ar.

After manual placement of Gaussian peaks on the time-weighted spectra at the appropriate ionisation energies for the bands, Gaussian fitting was performed using the function available on the Igor Pro programme. An example from the data processing for Chapter 5 is given in Figure 4.7.

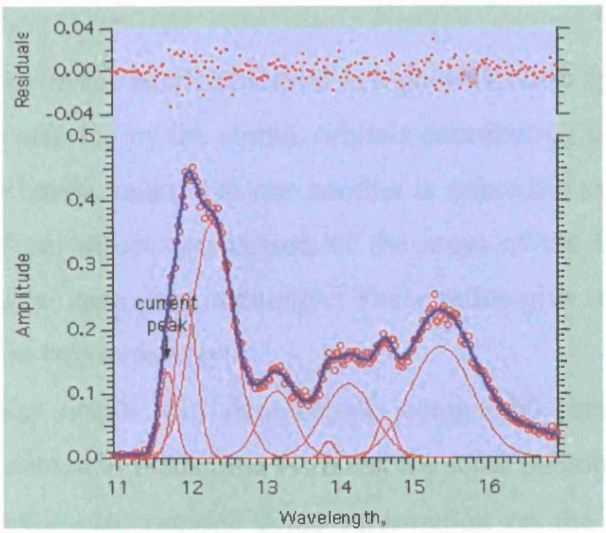

Figure 4.7: Time-weighted spectrum of the $MeReO_3$ valence region at photon energy of 89 eV, fitted with Gaussian functions.

The intensity data were used without further processing to extract the branching ratios. However to calculate the RPPICS, the relative band intensities in these spectra were normalised using the helium or argon data. The measured change in band intensity for the calibrant gas (I_{exp}) was plotted over the photon energy region and compared to the absolute cross-section, I_{abs}.[212] This showed there to be a fairly consistent ratio for each grating, except at the extremities of the grating ranges. The measured band intensities were multiplied by the I_{abs}/I_{exp} to correct for instrumental bias.

Cross sections

The intensity of the bands changes with incident photon energy and, when measured at the magic angle, is directly proportional to σ, the photoelectron/photoionisation cross section, and VEPES data sets can be used to establish the RPPICS for bands over a wide range of energies. σ is the probability of photoionisation to an ion state and its dependence upon photon energy is characteristic of the MO vacated. This interpretation is based on Gelius' model,[213] which assumes that σ for a particular MO is determined solely by those of the contributing atomic orbitals.

The very different partial cross-section behaviour of *d* and *f* electrons when compared with that of *s* and *p* electrons provides extensive information on metal-ligand covalency. Electrons with high angular momentum can be distinguished in their one-electron cross-sections by their maxima being some way from the ionisation threshold, and intensity increases from strong resonances.

Branching ratios

The change of intensity in the bands observed in a photoelectron spectrum over a range of photon energies is affected by the atomic orbitals contributing to the associated MO. The intensities of the bands, relative to one another is refered to as the branching ratio. These are obtained from direct comparison of the areas of the bands (calculated by Gaussian peak fitting) at each photon energy. These ratios give information about the make-up of the MOs in two main ways:

- Orbitals of similar origin will demonstrate comparable branching ratios, with features such as resonance or maxima visible at the same photon energy in both.
- The branching ratios also provide some information on the numbers of orbitals associated with a band; bands of e orbitals will have roughly twice the intensity of those of a orbitals and ⅔ that of triply degenerate t orbitals, provided they have similar atomic origins.

4.5.2 Interpretation of Absorption Spectra

Experimental data were normalised to the electron yield from a gold mesh positioned before the interaction region. This resulted in the complete removal of the wiggles due to the saw-tooth shape of I_0.

The bands observed in the spectra are assigned to transitions from the core to vacant orbitals where the energy spacing is in reasonable agreement with that predicted by calculations. The presence or absence of bands associated with a vacant MO gives an indication of the atomic orbitals contributing to it. For example, excitation from an *s* orbital on atom A is only allowed to MOs with A *p* character. The relative band intensities on an edge give an indication of the amount of *p* character in the final state MO.

Delayed Maxima

Some absorption edges do not display the expected sharp band, but have delayed onset or maxima, with a maximum above the threshold. This delay is due to a centrifugal barrier that tends to exclude electrons from the core region.[214;215] The centrifugal barrier is a phenomenon related to the angular momentum of the electronic state and is different for states with different angular momenta, but is related to the degree of overlap of the initial and final states. The $d \rightarrow f$ transition has a limited overlap of the

wavefunction as long as the *f*-like free electron has a low energy, so according to Equation 4.4 there will be a low probability of the transition occurring. When the final state is of a higher energy above the threshold, giving an increased overlap between the initial and final states, this probability increases. The photon energy required to give the maximum probability for excitation to the final state is well above the threshold, which gives rise to the delayed maximum in the absorption coefficient.

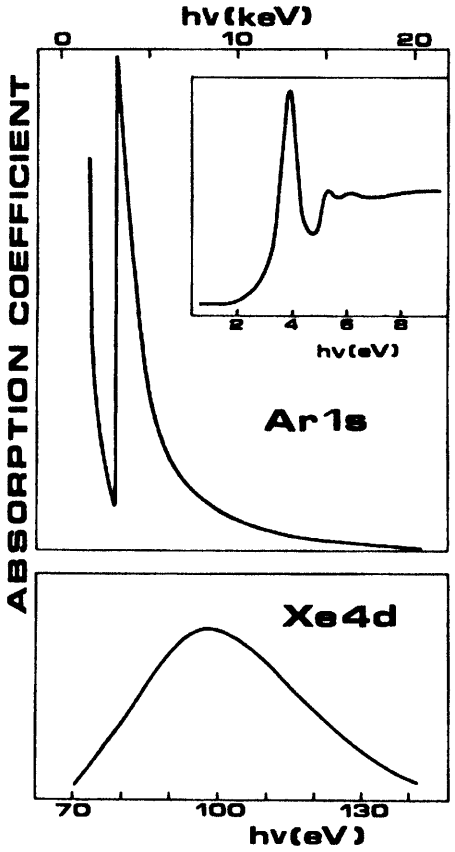

Figure 4.8: Example of a sharp absorption threshold and a delayed onset.[203]

Because direct photoionisation is controlled by the dipole selection rule a delayed maximum may also be observed in the RPPICS of bands associated with ionisation of orbitals with high angular momentum. The predominant ionisation channel for *d* electrons is through an *f* wave and for *f* electrons via a *g* wave. The centrifugal barrier ensures a low probability for these free electrons waves in the region of the ionising electron when they are of low energy.

4.5.3 VEPES Spectral Features

The presence or absence of features in a spectrum provides a valuable insight into the make-up MOs. Identification of the origin of observed resonance enhancements is important in understanding the nature of the orbital. In ideal circumstances they can be

interpreted in conjunction with the cross-sections and branching ratios to construct a quantitative model of key MOs.

Giant Resonance

Electrons with high angular momentum are not only distinguished by their one-electron cross-sections, which have maxima some way from the threshold, but also undergo strong resonances – a result of radiationless transitions known as Auger transitions. At certain photon energies core electrons can be excited to empty valence orbitals, starting a resonance process that results in the ejection of an electron from indirect ionisation. In the case of *d* electrons, these are a consequence of resonant absorption from the core $(n - 1)$ *p* shell to the valence $(n - 1)$ *d* shell followed by super Coster-Kronig decay, which results in the repopulation of the *p* hole and ejection of an electron with *d* character, illustrated below.

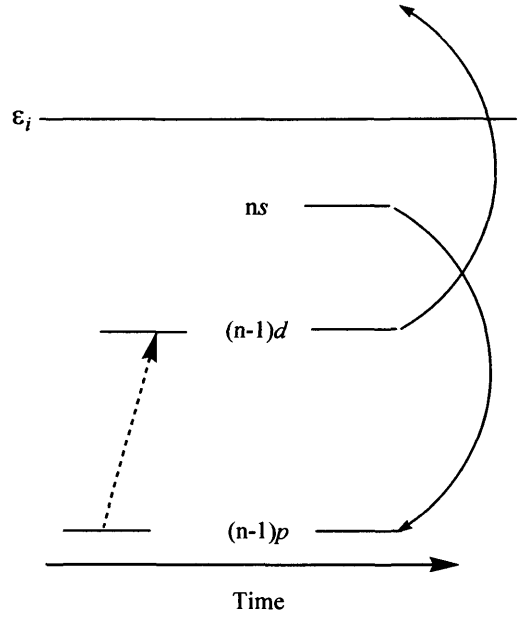

Figure 4.9: Schematic representation of the super Coster-Kronig decay mechanism. The absorption, a radiative transition, is represented by the dotted arrow and the Auger transitions by the solid arrows.

The final state has identical energy to that from direct photoionisation. Opening this second channel at photon energies close to the absorption energy gives additional features in the photoionisation cross-section, characterized by Fano profiles. These are the predicted lineshapes of the absorption coefficient from resonant phenomena.

$$\alpha = C\frac{(\varepsilon - q)^2}{\varepsilon^2 + 1} \qquad \textbf{[4.5]}$$

They are predicted for different states by varying the value of *q* in Equation 4.5, where C is a constant, *q* is Fano's index, an asymmetry parameter, and $\varepsilon = (h\nu - h\nu_0)/\Gamma$, where

$h\nu_0$ corresponds roughly to the centre of the resonance and Γ to its width. The excited state only exists long enough for super Coster-Kronig decay to occur when there is a centrifugal barrier arising from high angular momentum, hence observation of such giant resonances in a PES cross section leads to firm identification of *d* and *f* orbital contribution to bands. For this reason, the presence of these resonances also gives evidence of metal ligand *d* or *f* covalency when they arise in what is primarily a ligand PES band (where the ligand bonds only with *p* or *s* orbitals). The photon energy at which these features occur is predictable to within a few eV from the known ionisation energies of the sub-shell from which the electron is excited. It is also possible to detect the resonance processes that cause the additional channels by absorption spectroscopy.

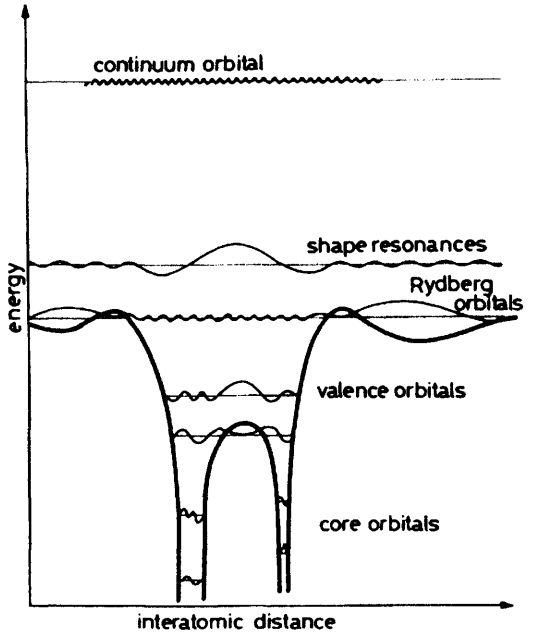

Figure 4.10: Schematic representation of the different types of MOs.[201]

Shape Resonance

As its name implies, a shape resonance is a feature of a spectrum that is associated with the geometry of the molecule in a particular physical phase (i.e. gas phase for this work) and is not dependent on the atomic nature of the MO. This has not always been a mainstream explanation of the features seen, but is widely acknowledged to be a real phenomenon. It has been defined as 'a resonance which is not turned into a bound state if the coupling between some degrees of freedom and the degrees of freedom associated to the fragmentation (reaction co-ordinates) were set to zero.'[216] It may be regarded as a result of the process whereby an electron absorbs energy *hv* and enters an unbound

state between the Rydberg orbitals at the periphery of the molecule and the unbound continuum; this state is shortlived and decays to produce an electron of energy *KE*.

Autoionisation

Autoionisation generally occurs when using low energy *hv*. It is another electronic effect that gives rise to an increase in intensity of a PES band not associated with the atomic orbital contribution. In this case again the incident energy absorbed by an electron is sufficient to ionise the molecule, but the electron is promoted into a Rydberg state in the ionisation continuum: a bound, quantised, electronic level, which may lie above an ionisation level for an alternative motion state. There is a Rydberg series associated with every vibrational and rotational groundstate, which converges towards an ionisation limit. The electronically excited, neutral molecule can autoionise by losing an electron and moving into a cationic state of the same energy and symmetry, as dictated by the rules of group theory. This cationic state may be of higher rotational energy, but it must be the same symmetry as the excited neutral state.

Relativistic Effects

When relativistic effects are considered within an atom, the position of electrons may be described by the Dirac equation rather than the traditional time-dependent Schrödinger equation, so time and space are considered equally.[217] The physical implications of this revolve around the inclusion of a term for relativistic mass corrections, the size of which depends upon atomic number and gives rise to the 'direct relativistic orbital contraction' when Z is large, typically in the 6^{th} and 7^{th} periods.[218] This contraction is a general stabilisation of *s* orbitals and a similar, but smaller stabilisation of *p* electrons, the magnitude of which depends upon the *j* value.[219] As a result of the increased shielding from these stabilised electrons and their high angular momentum (leading them to seldom be in the vicinity of the nucleus), *d* and *f* electrons experience an 'indirect relativistic orbital expansion', resulting in a reduced nuclear screening ability. One consequence of this is the effect this can have on the valence orbitals. If a filled, *d* or *f* shell experiencing relativistic expansion lies just inside the valence orbitals, the valence electrons experience an enhanced nuclear charge and the orbital becomes more contracted. This may result in contracted bond lengths. Relativistic effects are also observed in spin-orbit coupling.

Spin-Orbit Coupling

The inclusion of spin-orbit coupling in the interpretation of electronic spectra is especially important when considering molecules containing heavy atoms, e.g. Os or U. It arises from relativistic effects that predict electron spin and results in differing MO behaviour from that described by the linear combination of atomic orbitals (LCAO) approach to MO theory, where standard group theory is employed to predict the irreducible representations of MOs. It manifests in PES spectra as a differing number of bands from that predicted, at energies not in agreement with those calculated excluding the effect.

When an electron is part of an atom, the magnetic moment associated with its intrinsic spin angular momentum couples with the magnetic field generated by its orbital motion.[194] This 'spin-orbit' coupling occurs in all occupied orbitals that have integer angular momentum(l) to give a total angular momentum $j = l+½$ and $l-½$. The resulting states are illustrated by the $MeReO_3$ PES spectrum showing the Re 4*f* bands, discussed in Chapter 5. Rather than a single band, two bands are clearly observed associated with the $^2F_{5/2}$ and $^2F_{7/2}$ states arising from spin-orbit coupling.

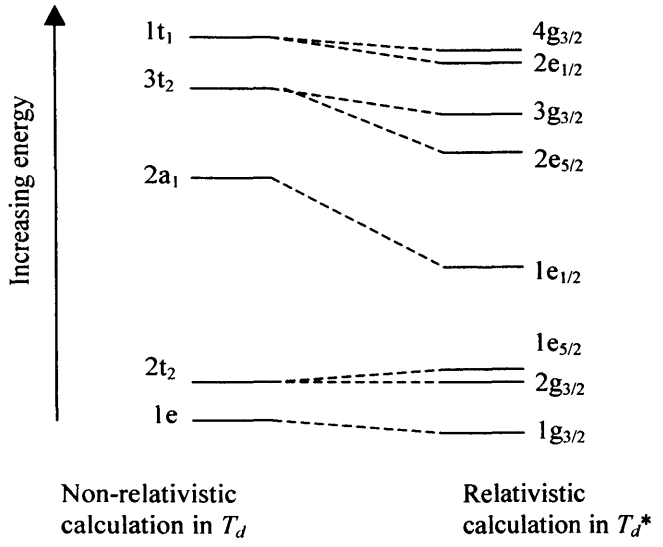

Figure 4.11: Qualitative MO energy level diagram of OsO_4 showing both the non-relativistic T_d and the relativistic, spin-orbit coupled T_d* levels.

Normal point groups do not describe states of a non-integral value of j, necessitating the extension of group theory to give additional groups called double groups. A molecule of spatial T_d symmetry, such as OsO_4, affected by spin-orbit coupling is more accurately described by the T_d*, tetrahedral double-point group. This involves a move from the

complex being described by 5 irreducible representations to only 3 different ones, as shown in Figure 4.11. The degeneracy of the t_1 and t_2 sets is lifted, giving rise to the possibility of orbital mixing not allowed under T_d symmetry. For example the t_1 set is now described by the representations $g_{3/2}$ and $e_{1/2}$. $g_{3/2}$ is also the symmetry of the e and some of the t_2 set, containing the 4*d* orbitals. Hence a calculated 100% O 2*p* orbital has symmetry allowed mixing available to it if spin-orbit coupling is present. The PES of OsO_4 shows 2 bands associated with the $3t_2$ orbitals where only 1 band would be expected in the absence of spin-orbit coupling, confirming its activity in the molecule.

It is the analysis of the features of the VEPES spectra that converts experimental data into a proposed model of the electronic structures of the molecules. The effects described above allow interpretation of these spectra and comparison with calculated results.

Chapter 5

Structure and Bonding Studies of $MeReO_3$

5.1 Introduction

$MeReO_3$ is a pseudotetrahedral, d^0 compound, first prepared in 1979 by Beattie and Jones.[220] It was not studied intensively until Herrmann et al. decided to investigate its reactivity in the late 1980s. The colourless, volatile, thermally stable, crystalline material is highly soluble in both polar and non-polar solvents and is readily synthesised from Re_2O_7 in high yields.[221;222] In combination, the vacant Re 5*d* orbitals and the co-ordinatively unsaturated metal centre endow the complex with a Lewis acidic nature, which heavily influences the reactivity of the molecule.

Given its wide-ranging applications in catalysis, the chemistry of $MeReO_3$ has been extensively studied and reviewed.[223-225] Its catalytic ability lies in two key areas:

- Olefin metathesis
- Olefin oxidation

5.1.1 Olefin Metathesis

Olefin metathesis relates to the exchange of the $=CR_2$ group of an alkene. Although the reaction was known and patented in the 1950s,[226] mechanisms were only proposed in 1970 by Chauvin[227] and Hughes.[228] Since then, there have been many studies to establish the route and identify reactive intermediates.[229] It is currently thought to proceed via the Chauvin mechanism, with the formation of a carbene, followed by a metallocyclobutane.

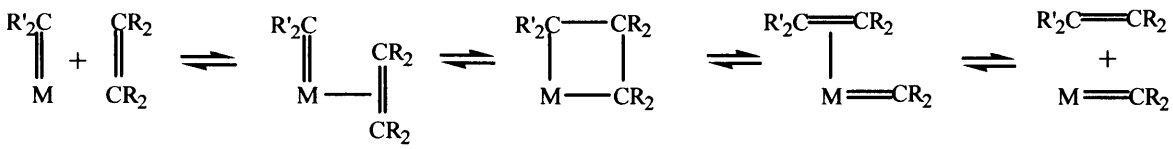

Figure 5.1: The Chauvin mechanism for olefin metathesis.

$MeReO_3$ is an efficient catalyst for this reaction when supported on alumina or silica.[225] Unlike in some d^0 catalytically active systems, *e.g.* the Ziegler-Natta type catalyst $MeTiCl_3$, where activation occurs with the facile breaking of the M–C bond, activation of $MeReO_3$ occurs through the breaking of at least one Re–O bond. For the

formation of a carbene compound it is essential that the metal-carbon bond of the parent molecule be stronger than that of at least one other ligand. Unfortunately, no definitive mechanistic studies are available for the transition from the intact $MeReO_3$ to the putative carbene intermediate. However, supported activated $MeReO_3$ has been shown to exhibit increased reactivity arising from a greater susceptibility to hydrolysis than the parent molecule. Although no carbene has ever been detected in catalytic studies, a correlation between activity and the presence of an alkyl fragment has been reported.[225;230;231] This supports the view that the reaction proceeds via the Chauvin mechanism, although Buffon et al. have proposed that the carbene species in the catalytic cycle does not originate from the methyl group.[232;233] Interestingly, Morris et al.[234;235] showed that when irradiated with light $\lambda \sim 254$ nm matrix-isolated $MeReO_3$ tautomerises to the simple carbene species $H_2C{=}Re(O)_2OH$, close to the putative intermediate in the Chauvin mechanism. Furthermore, simple model calculations using disilanol molecules explored the processes involved in condensing and supporting $MeReO_3$ on silicon. These calculations showed the $CH_2{=}Re$ tautomer to be energetically more accessible in the model supported case.

5.1.2 Olefin Oxidation

Addition of an oxygen atom across an alkene double bond or an alkyne triple bond produces epoxides, aldehydes or ketones. In the presence of concentrated hydrogen peroxide, $MeReO_3$ reacts to form a mono- or bis-peroxo complex, both of which are efficient catalysts in the oxidation of olefins and many other compounds.[236] Conditions can be tuned to tailor selectivity, primarily by affecting the Lewis acid metal centre through the addition of a variety of Lewis bases.

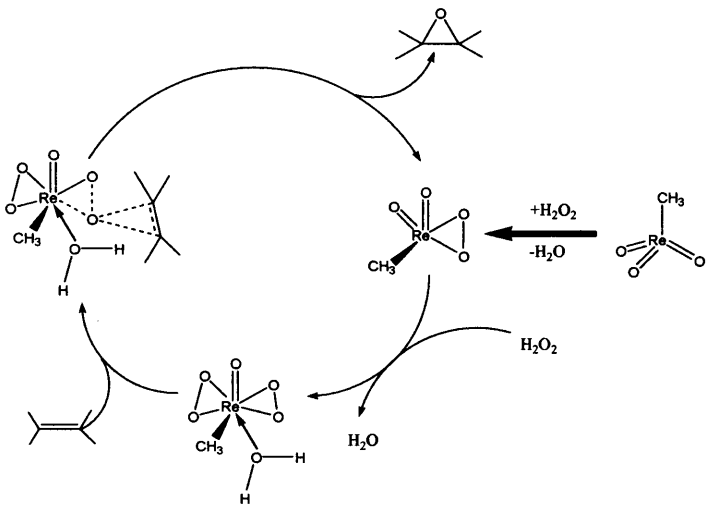

Scheme 5.1: Catalytic cycle for olefin oxidation by $MeReO_3$.

In this process it is the activity of the Re–O bonds that is significant, with the Re–C bond playing no mechanistic part. As with the activation of $MeReO_3$ for olefin metathesis, it demonstrates that the methyl group is not the most labile ligand.

5.1.3 Photochemistry

Homolytic cleavage of the Re–C bond occurs with light of λ = 200-400 nm, demonstrating the photosensitivity of alkyl–ReO_3 complexes in solution.[237] In view of this, the original reports of the photolability of $MeReO_3$ proposed an MO energy level scheme similar to that developed for the pseudoisoelectronic $MeTiCl_3$, with the HOMO being the pure M–C $5a_1$ orbital. This proposal tallied with the observed photodissociation, but not with the catalytic mechanisms described above, nor with subsequent electronic studies, described below in Section 5.1.4. The latter demonstrate that M–C character is present in both the HOMO and lower-lying orbitals of $MeReO_3$. On exposure to broadband 200-800 nm light $MeReO_3$ decays to a Re–CO containing product leading Morris et al.[234] to propose that the tautomerisation of $MeReO_3$ to $H_2C{=}Re(O)_2OH$ on exposure to light of λ = ca. 254 nm follows the path observed in the earlier work by Kunkely et al., giving $\bullet ReO_3$ and $\bullet CH_3$ moieties and weakened Re=O bonds. The two radical fragments are held in close proximity to one another in the matrix and rearrange to give the observed tautomer, whose presence demonstrates the potential for hydrogen migration within the molecule when the Re–O bond order is lowered, as it is when activated for catalysis.

5.1.4 Previous Structural and Electronic Studies

Both the ^1H- and ^{17}O-NMR spectra of $MeReO_3$ show a singlet, with the ^1H chemical shift dependent on the solvent used,[238] a reflection of the sterically unhindered, Lewis acidic metal centre and its affinity for solvent co-ordination. The highly symmetrical structure demonstrated in solution is also observed in the gas phase, with electron diffraction studies showing a staggered C_{3v} conformation. With a bond distance of 2.06-8 Å,[239;240] the Re–C bond lies at the short end of the range of Re–C distances,[239] as is expected for a high oxidation state complex. The Re=O distances were found to be unremarkable at 1.709(3) Å and compare favourably to the crystallographically determined Os=O distance of 1.711 Å in OsO_4.[230] Crystallographic data for $MeReO_3$ are poor, owing to decomposition of the sample on exposure to X-rays, an unsurprising

event in view of its photochemical lability. However, the data available[239] indicate these distances to be slightly shorter in the solid state. The data on the structure of $MeReO_3$ are complemented by information about the electronic structure through electron diffraction, He(I) and He(II) PES[239] and DFT[241] calculations. These studies produce orbital energies consistent with one another. Key points from these studies are:

- the contribution of the Re–C σ-interaction is distributed between multiple molecular orbitals.
- inclusion of the Re 6*p* orbitals in the calculations is necessary to achieve good correlation of ionisation energies with experimental findings.
- the two highest occupied orbitals are associated with the oxygen lone pairs, contrasting with the 2⅔ bond order proposed by Herrmann et al.,[242] in which the otherwise 14 electron complex is presented as one conforming to the 18 electron rule.

More recently, variable energy photoelectron spectroscopy (VEPES) studies of the tetrahedral molecules OsO_4[243] and $TiCl_4$[244] have produced unambiguous assignments of the PE bands; in the case of OsO_4, the assignment was new and gave evidence of interaction of the 5*p* core with the valence electrons. These two pseudo-isoelectronic molecules have very different orbital energy sequences, which can be related to the differing extent to which the contributing metal orbitals dominate. In the case of OsO_4, the Os 5*p*, 5*d* and 6*s* orbitals influence the nature of the molecular orbitals to a much greater extent than do the Ti 3*p*, 3*d* and 4*s* orbitals in $TiCl_4$. Related studies of $MeTiCl_3$ enabled identification of all the valence orbitals.

In light of the remarkably wide activity of $MeReO_3$ as an organometallic catalyst, the electronic nature of the Re–C and Re=O moieties are of particular interest. In addition, $MeReO_3$ provides a comparison with the T_d species OsO_4 as well as affording an isostructural, but chemically very different comparison with the C_{3v} molecule $MeTiCl_3$. This Chapter reports VEPES and VUV/X-ray absorption spectroscopic studies used to investigate the electronic structure of $MeReO_3$, and in particular probe the extent of orbital mixing in the valence region.

5.2 VEPES and Absorption Spectroscopy of $MeReO_3$

5.2.1 Synthesis of $MeReO_3$

Herrmann's original route[232] for the preparation of $MeReO_3$ from Re_2O_7 and $SnMe_4$ was able to generate a 50% yield at best, with $Me_3SnOReO_3$ formed as a by-product in a 1:1 ratio with the desired product. A significantly higher yield of $MeReO_3$ was obtained by following the general procedure described in a later paper,[222] and given below in Equation 5.1.

$$Re_2O_7 + 2ClSiMe_3 \rightleftharpoons 2\,ClReO_3 + O(SiMe_3)_2$$

$$ClReO_3 + SnMe_4 \longrightarrow MeReO_3 + ClSnMe_3 \qquad [5.1]$$

Me_3SiCl was added to a stirred suspension of Re_2O_7 in acetonitrile at room temperature. This established an equilibrium between the colourless Re_2O_7 and the pale green monometallic oxy-chloride $ClReO_3$. The methylating agent, $SnMe_4$, was added dropwise directly into the reaction mixture, irreversibly transforming the chloride into $MeReO_3$. On stirring overnight, the reaction proceeded to completion. The solvent and tin complexes were removed *in vacuo* at 0 °C, and the white residue was washed with cold hexane until the washings were no longer yellow. The material was purified by sublimation onto a cold finger at –30 °C, and its purity was confirmed by ^1H NMR and IR spectroscopy. Interestingly, the needle-like crystals initially formed were noted to rearrange overnight to form blocks. However, an X-ray study of these block crystals at 120 K did not produce data of sufficiently high quality to obtain a structure.

5.2.2 Data Collection for VEPES

The spectroscopically pure $MeReO_3$ was transferred to a small Young's tap ampoule equipped with a glass-to-metal seal. This was shielded for the light with Al foil and placed in a thermal bath at room temperature (ca. 22 °C). The $MeReO_3$ vapour was introduced into the experimental chamber described in Chapter 4, to give an overall pressure of ~ 4 x 10^{-6} mbar. The photoelectron spectra were normalised using the signal from a calibrated photodiode following the macro described in Equation 5.2 with the variables *hv* and bxxx (the run number).

Av_1=A1**hv*/I_0; V_volts_=*hv*-KE_eV_;

display A1 vs KE_eV_; appendtograph/r Av_1 vs KE_eV_;

Rename KE_eV_, KE_bxxx; Rename V_volts_, BE_bxxx; Rename I_0, I_0_bxxx;

Rename A1, A1_bxxx; Rename pW, pW_bxxx; Rename InslitUp, Inslitup_bxxx;

Rename Inslitdown, Inslitdown_bxxx; Rename Av_1, An_bxxx;
Removefromtable Av_0.d, Av_2.d, Av_3.d, Av_4.d;
Killwaves Av_0, Av_2, Av_3, Av_4; **[5.2]**

The valence bands were studied in the binding energy range 10.5 – 17 eV over a series of photon energies between 23 and 67 eV on grating 1 (400 l/mm); and on grating 3 (1200 l/mm) for energies between 67 and 110 eV. Data were collected at 67 eV with both gratings to check the calibration. Although the He calibration corrected well for the grating change, there is a small discontinuity in all the cross section curves at 67 eV, coincident with the grating change. This is not seen in the branching ratios. Typically three or four spectra were measured at each photon energy. With the photon energy bandwidth ΔE better than 30 meV for photon energies below 110.5 eV, the total energy bandwidth for the spectra arises mainly from the photoelectron analyser. The core and inner valence spectra were measured using a 150 mm VG photoelectron analyser at photon energies of 108, 210 and 330 eV.

5.2.3 Data collection for VUV and X-ray Absorption Spectroscopy

Absorption data were collected for the Re 4*d*, C 1*s* and O 1*s* edges and the Re 4*f*/5*d* edge region. The 400 l/mm grating was used to collect data on the Re 4*f*/5*d* edge region over the photon energy range of 30-80 eV, with the bandwidth varying from 3 to 10 meV. Acquisition in this photon energy range was possible through the parallel scan of the undulator gap and of the dispersed wavelength from the monochromator. X-ray absorption spectra at the Re 4*d* and C 1*s* edges were measured in the 205-305 eV region and O 1*s* edge in the 525-580 eV region with a grating with 1200 l/mm and a photon energy resolution better than 100 meV. Unfortunately, there was a strong decrease in I_0 in the region of the carbon 1*s* edge due to adsorbed carbon on the first optical elements of the beamline. As a consequence, the absorption spectrum in the region 290-300 eV is not reliable. Operating the undulator in the wiggler mode (gap = 30.1 mm) provides higher beam flux in the UV and soft-X-ray range by shifting the critical photon energy hv_c to higher photon energies.[201] This increased intensity allowed the acquisition of the oxygen 1*s* spectrum.

5.2.4 DFT Calculations

The calculations were used to optimise the geometry of the $MeReO_3$ molecule, with the constraint of C_{3v} symmetry in both eclipsed and staggered conformations. The energy

of the staggered form was found to be lower by 7 $kJmol^{-1}$. A frequency calculation confirmed this structure to be a minimum on the energy surface.

	Re-C	Re-O	C-H	O-Re-C	H-C-Re
Calc.	209.0	172.3	109.8	106.3	108.9
Exp.	206.0(9)	170.9(3)	110.5(1.2)	106.0	112(3)

Table 5.1: Calculated and experimental bond lengths (pm) and angles (deg.) for $MeReO_3$.

Table 5.1 shows the calculated bond lengths and angles to compare favourably with experimental values.[239] Ionisation energies for the valence, inner valence and selected core orbitals were calculated and were found to be in good agreement with those calculated by Rösch and co-workers.[241] Additional calculations including a spin-orbit coupling factor found that there were only significant differences for the 4*f* and 5*d* core orbitals.

5.3 Results and Discussion

The experimental results have been interpreted in conjunction with the calculations and are discussed in the context of the MO model presented in Figure 5.2 and the expected profiles of the AO cross sections[212] presented in Figure 5.5.

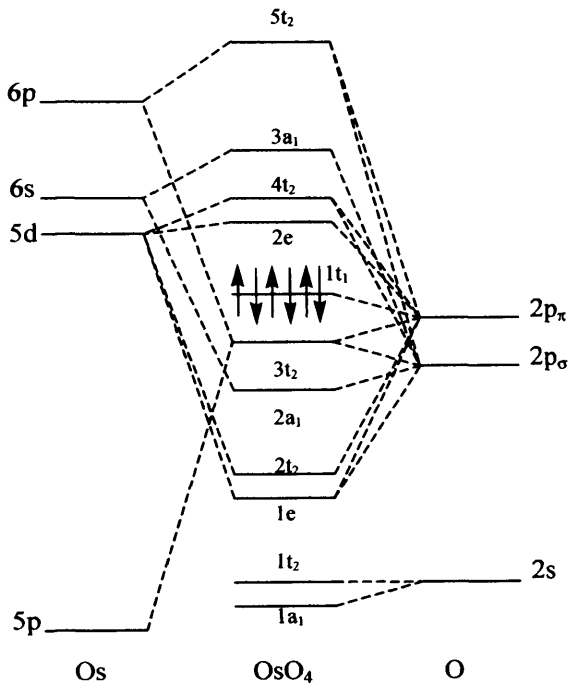

Figure 5.2: (a) Qualitative MO energy level diagram for OsO_4 with T_d symmetry.

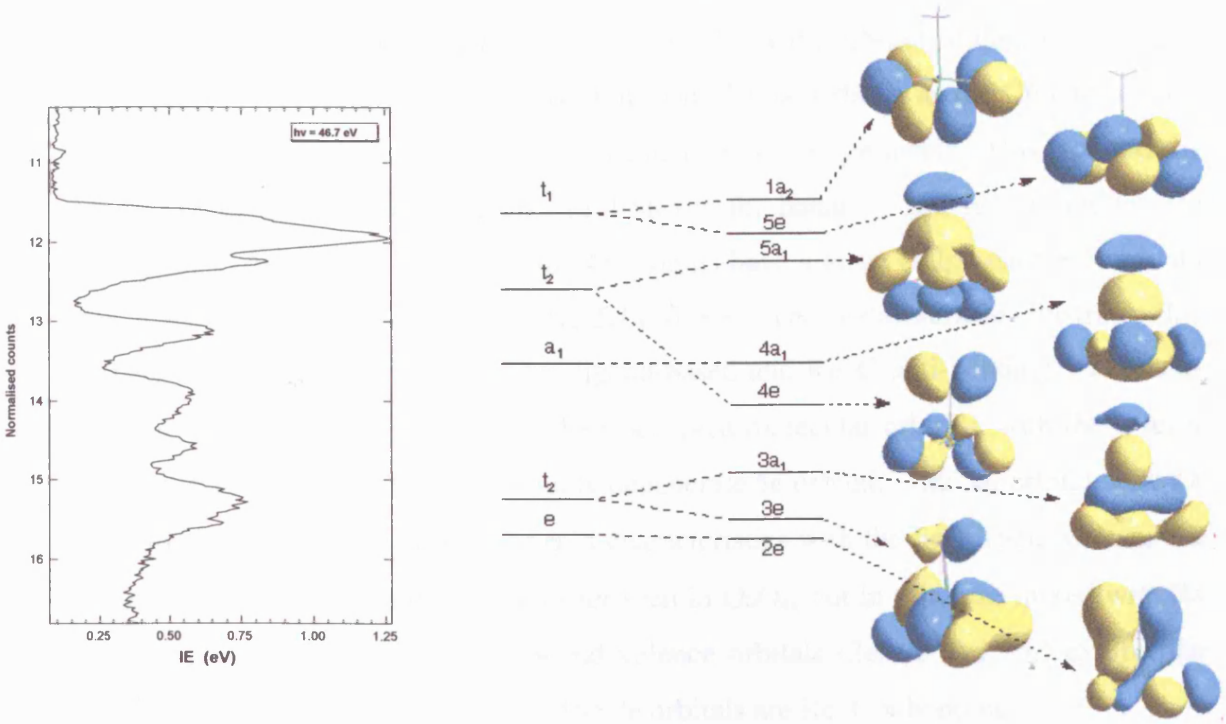

Figure 5.2: (b) PES spectrum of valence electron binding energies, related to the calculated MO diagram showing orbital splitting due to the distortion from T_d symmetry.

5.3.1 The Calculated Model

Calculations and electron diffraction studies show $MeReO_3$ to have a C_{3v} geometry and a staggered conformation in the gas phase. Its molecular structure may be viewed as a perturbation of a tetrahedral parent. When approached in this way, the MOs are easier to view as delocalised over the whole molecule, rather than being associated with a specific Re–L bond. This is particularly important in light of the spectrum of reaction types displayed by the molecule, described in Section 5.2. The MO diagram for the tetrahedral complex OsO_4 obtained by application of the LCAO approach is shown in Figure 5.2(a). The perturbation from the T_d symmetry of this parent molecule to the C_{3v} $MeReO_3$ and its relationship to the experimental PES spectrum is illustrated in Figure 5.2(b), together with the calculated isosurface for each energy level calculated by Prof. Jennifer Green for this study. The pseudoisoelectronic parent T_d molecule OsO_4,[243] has been chosen owing to its comparable size and bonding modes. For the mid-third-row transition metals, the nodal properties and energy ordering of the contributing metal AOs dominate those seen in the MOs, such that they fall in the order:

$$e(5d) \sim t_2(5d) < a_1(6s) < t_2(6p) < t_1 \text{ (non-bonding)}$$

Ligand replacement of O by CH_3 results in the T_d $t_2(6p)$ orbitals undergoing a major perturbation. The 4e levels are widely split from the $5a_1$ orbital, as the CH_3 4e orbitals are C–H bonding and considerably more stable than the O $2p\pi$ levels. This is shown by the difference in ionisation energies of 1.56 eV for bands C and E. In addition to significant C–H bonding character, the 4e orbitals have a large O $2p$ contribution, with only a small contribution from the Re $5d$ orbitals. The nodal surface illustrates this feature, with the orbital being mainly ligand-based and Re–C anti-bonding. The non-bonding O $p\pi$ orbitals remain the highest occupied molecular orbitals, with the t_1 level splitting to the $1a_2$ orbital and the doubly degenerate 5e orbital. The $5a_1$ orbital shows a small Re $6p$ contribution and mixed σ–π characteristics with the ligand set, whereas the $4a_1$ orbital retains the ligand $p\sigma$ character seen in OsO_4, but in this case mixed with Re $6p$ and $5d(z^2)$. The most tightly bound valence orbitals (2e, 3e and $3a_1$) exhibit the greatest degree of metal d character. The 2e orbitals are Re–C π bonding.

5.3.2 The Valence Bands

The valence photoelectron spectra of $MeReO_3$ measured at four different photon energies are shown in Figure 5.3(a). Despite the lower resolution arising from the line broadening, the seven valence bands can be clearly seen and are labelled A–G, with A arising from ionisation from the HOMO. The overall trend of decreasing band intensity with increasing photon energy is seen in the change of y-axis scale, whilst band D gives a good illustration of the change in relative intensity in comparison to bands A, B and C as shown in Figure 5.3(b). The ionisation energies of the principal features of the valence photoelectron spectra, shown in Table 5.2, are in agreement with the values from an earlier study.[239;241]

The bandwidth was generally too wide to allow observation of vibrational fine structure. However, band C does show two features on the high energy edge consistent with a vibrational progression of 1411 ± 80 cm^{-1}. Since band C is assigned as ionisation from an a_1 orbital, the vibration giving rise to any structure must also have a_1 symmetry. Group theory predicts 5 of the 18 vibrational fundamentals of $MeReO_3$ to be of a_1 symmetry. The closest totally symmetric mode in the vibrational spectrum of the molecule, at 1210.4 cm^{-1}, is assigned to the symmetric deformation, $\delta_s(CH_3)$, mode[234] and is presumed to be that observed here.

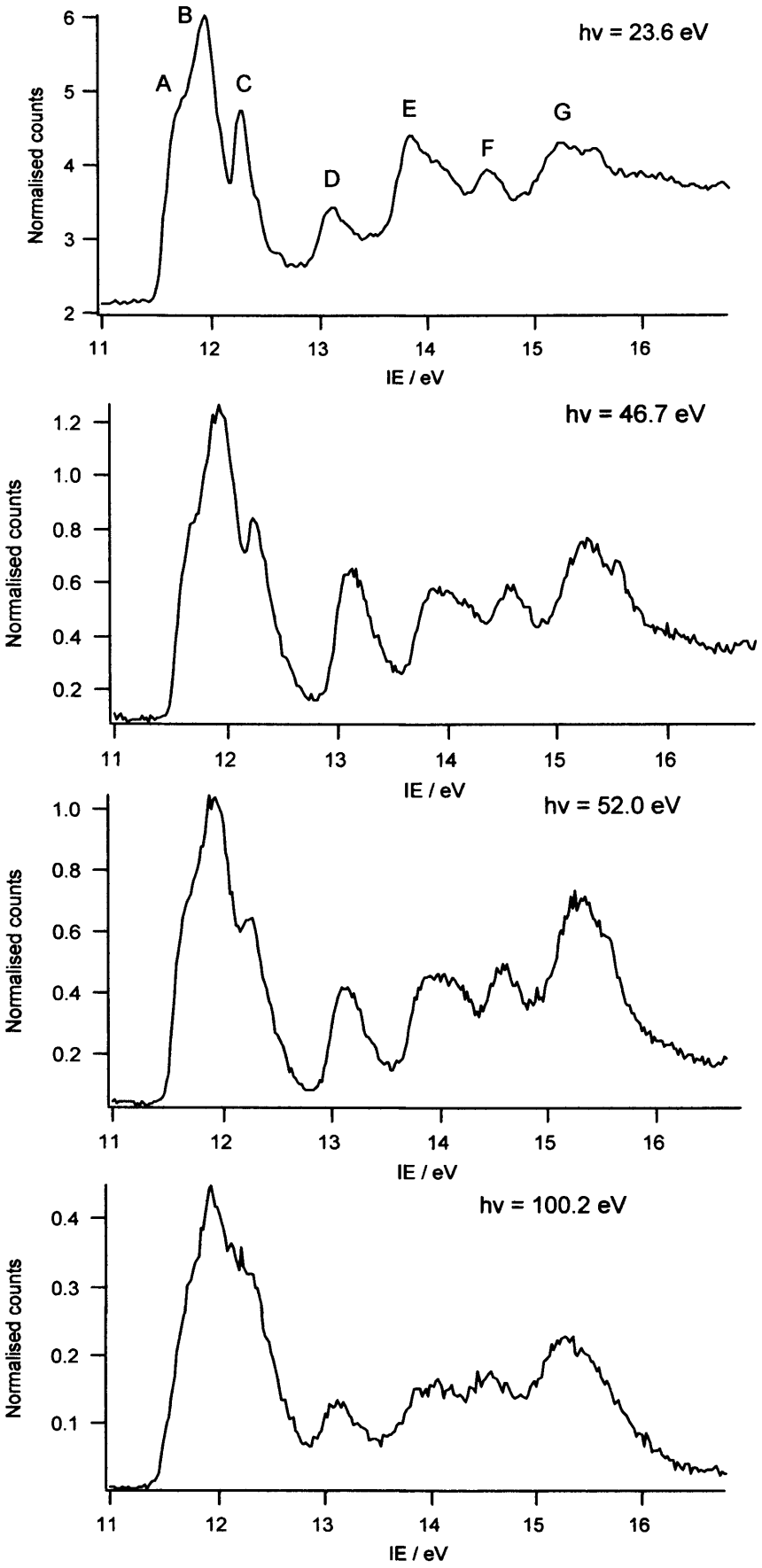

Figure 5.3: (a) Photoelectron spectra of $MeReO_3$ measured at photon energies of 23.6, 46.7, 52.0 and 100.2 eV.

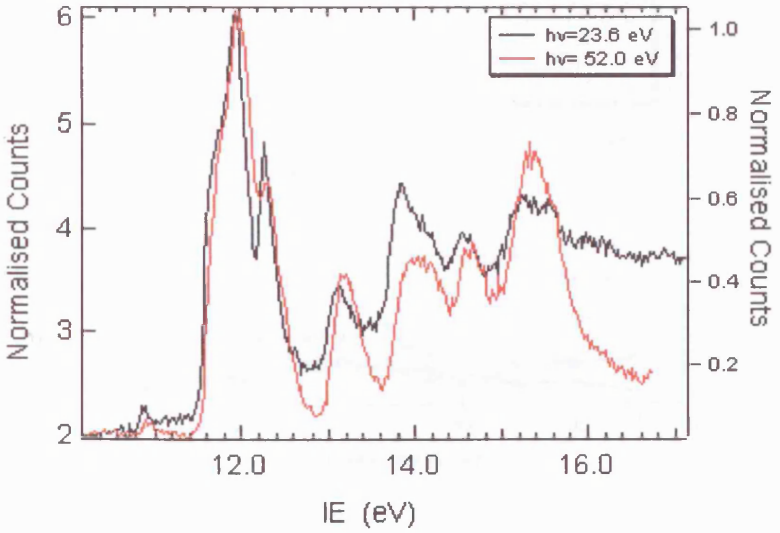

Figure 5.3: (b) Illustration of relative band intensity variation with *hv*.

	Band						
	A	B	C	D	E	F	G
IE	11.63	11.94	12.27 (12.44) (12.62)	13.08	13.83 14.08	14.54	15.26

Table 5.2: Vertical ionisation energies (eV) for $MeReO_3$.

Branching ratios were calculated for bands A–G and are shown in Figure 5.4. For comparison with the other valence bands, bands A, B and C were combined over the full range owing to the difficulty of deconvoluting them at high photon energies. The lower resolution with the higher grating led to an unsatisfactory assignment of area upon deconvolution, with too great a proportion being allocated to band C. Although this could conceivably reflect the changing cross sections, we consider it more likely to arise from experimental limitations. This assertion is supported by the relative partial photoionisation cross sections (RPPICS) and branching ratios of A, B and C which were obtained separately over the 23-67 eV region, where separate fits were satisfactorily achieved and an individual analysis possible.

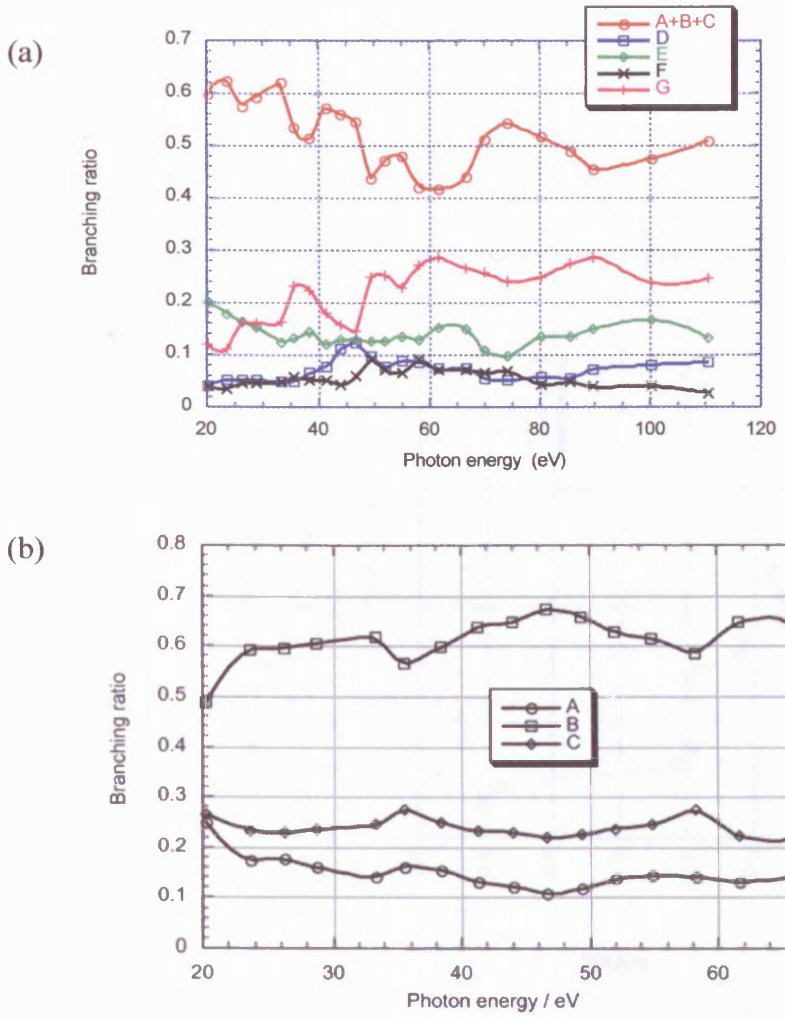

Figure 5.4: (a) Branching ratios for the valence bands of $MeReO_3$ and (b) Branching ratios as a fraction of the combined branching ratio for bands A, B and C in the photon region 23-67 eV.

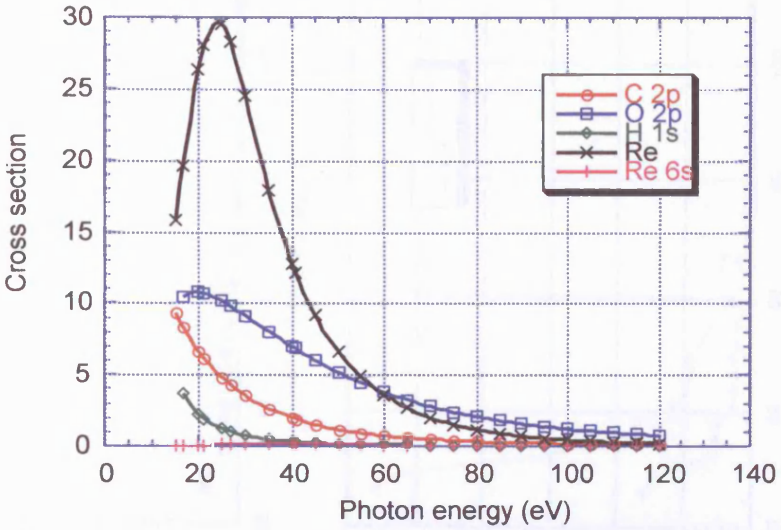

Figure 5.5: Calculated atomic cross sections of the O 2*p*, C 2*p*, H 1*s* and Re 5*d* and 6*s* atomic orbitals.

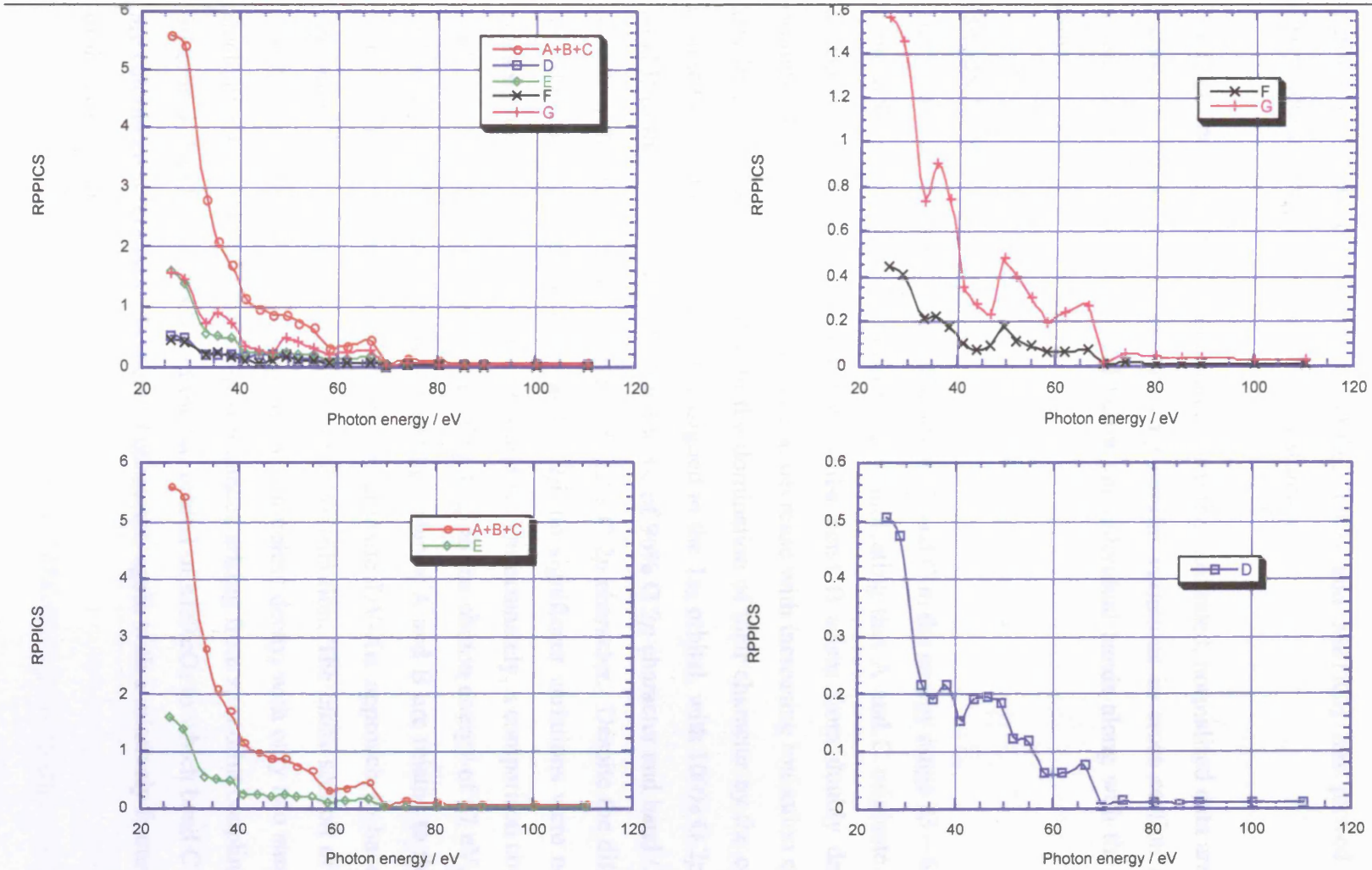

Figure 5.6: Relative partial photoionisation cross sections for the valence bands of $MeReO_3$ for (a) all bands, (b) A+B+C and E, (c) F and G and (d) D.

The AO cross sections are not quoted in exact relative magnitudes, but rather demonstrate well-established general features and relative trends. The Re 5*d* electrons are expected to show a giant resonance on excitation of the 5*p* sub-shell at approximately 45 and 56 eV. Such features have been observed in the branching ratios of the *d* bands of the $Re(CO)_5X$ (where X = Cl, Br).[245] Comparison with the cross sections of analogous bands of OsO_4, $TiCl_4$ and $MeTiCl_3$ has proved useful in assignment and identification of key features.

The experimental RPPICS calculated from the calibrated, normalised data are shown in Figure 5.6, with those bands showing similar variations in cross section also given separately. These are discussed below for individual bands along with the branching ratios.

Bands A, B and C

The branching ratios for valence bands A, B and C in the energy range 23 – 67 eV show them to have an intensity ratio of 1:2:1, indicating that A and C originate from non-degenerate orbitals of a symmetry, whilst band B arises from doubly degenerate e orbitals. Their RPPICS show a general decrease with increasing ionisation energy with few irregularities, consistent with the domination of their character by the contributing atomic O 2*p* orbitals. Band A is assigned to the $1a_2$ orbital, with 100% O 2*p* character; band B to the 5e orbitals, calculated to be of 96% O 2*p* character and band C to the $5a_1$ orbital, with only 60% O 2*p* and with 22% C 2*p* character. Despite the differences in the AO cross sections of O 2*p* and C 2*p*, no significant variations were noted in the cross section of band C to those of A and B. Unfortunately, a comparison could only be made with the data collected on grating 1 up to the photon energy of 67 eV, as a result of lower resolution on the higher grating. Bands A and B are related to the OsO_4 $1t_1$ HOMO, which is calculated via the relativistic DV-Xα approach to have 99.9% O character,[206] with only a tiny Os metal contribution. The cross section of band 1, to which it is assigned, shows a relatively featureless decay, with only two small intensity fluctuations associated with $p \rightarrow d$ resonances arising from spin orbit coupling. Both the $3t_2$ orbital (band 2) of OsO_4 and the $5a_1$ orbital of $MeReO_3$ to which band C is assigned are calculated to contain 7% metal *d* character, again with a relatively featureless decay of the cross sections.

Band E

Band E is assigned to the 4e orbitals, with contributions from the O 2*p* (42%), C 2*p* (17%), H 1*s* (19%) and Re 5*d* (16%) AOs. Despite the range of contributing AOs, the cross section is remarkably similar to that of bands A+B+C, with an overall decline with increasing photon energy and no resonant features. A possible reason for this is illustrated by the isosurface in Figure 5.2, which shows the 4e orbitals to be much less metal based than those associated with bands D, F and G. This diminished overlap leads to a lower probability of $5p \rightarrow 5d$ transitions occurring – the initial stage in the development of resonant features.

Band D

Band D has been assigned to the $4a_1$ orbital ionisation and its branching ratio is consistent with this. The calculations show the $4a_1$ orbital to have a small admixture of both Re 5*d* and Re 6*s* character in addition to high contributions by the C 2*p* and O 2*p* orbitals. Again, it is more ligand localised than the orbitals that give rise to bands F and G, but less so than band E. Its cross section (Figure 5.6(d)) has features in common with those of bands F and G, but there are also significant differences. These are emphasised by a comparison of the branching ratios of bands D and F in Figure 5.4. Both are associated with a non-degenerate orbital and thus have branching ratios of comparable magnitude, although at high photon energies band D gains in intensity relative to band F. This is most plausibly associated with the lower *d* orbital content of the $4a_1$ orbital, as the 5*d* cross section is calculated to decrease more rapidly than that of the O 2*p* orbital.

A small maximum is observed in the cross section of band D at 38 eV, slightly higher in energy than one seen in both bands F and G at 35 eV. This could be a shape resonance, with the excited state being an *f* wave trapped within the molecular potential. This would account for the differing maximum in band D from those in bands F and G, as the resonance originates from ground states of different symmetries.

Band D also displays a rise in cross section at 43 eV with a broad maximum between 40-50 eV, whereas F shows a later rise at 47 eV with a more clearly defined maximum. This suggests this latter feature is a $p \rightarrow d$ resonance common to both bands, but that there is an additional structure for band D. The related OsO_4 $2a_1$ orbital does not

contain any 5*d* character by symmetry although the cross section of the associated band 4 shows a pronounced maximum at 48 eV. Likewise, the totally symmetric $2a_1$ orbital of $TiCl_4$ shows a peak at 40 eV. Given the occurrence of similarly placed maxima in these pseudoisoelectronic molecules and the results of the absorption spectroscopy this structure has been attributed to a shape resonance from a totally symmetric ground state i.e. the $4a_1$ orbital, illustrated by the isosurface. The excited state in this case would be a *p* wave of a_2 or e symmetry in this C_{3v} molecule. The cross section of band D of $MeTiCl_3$, also assigned to a symmetric $4a_1$ orbital of low 3*d* character, has the slightest of increases at 41 eV. Despite this, no real comparison can be made due to significant overlap with the $MeTiCl_3$ band E, assigned to the 4e orbitals, which also exhibited this maximum.

Bands F and G

The branching ratios in Figure 5.4 show that bands F and G generally grow in relative intensity over the photon energy range 20-60 eV, a reflection of their combined Re 5*d* and O 2*p* character. Their relative cross sections, shown in Figure 5.6(c), show a sharp intensity increase with an onset at 47 eV and a maximum at 50 eV. This is followed by a second, less intense increase, with an onset at 58 eV, the maximum of which is difficult to define due to the unfortunate coincidence of the grating change with the resonance. Nevertheless, these features suggest a significant Re 5*d* contribution to the MOs from which the bands originate as their onsets match the expected giant resonances. The onset of the features at 47 and 58 eV are the result of $5p \rightarrow 5d$ excitation and super Coster-Kronig decay, giving an additional ionisation channel of electrons with 5*d* character. There is also a peak with a maximum at 35 eV, slightly lower than that observed for band D associated with excitation to a trapped *f* wave. Alternatively, it may be associated with the delayed maximum in the 5*d* cross section, which is calculated to occur at a photon energy of 25 eV.

Band	Assignment	Orbital energy	Orbital composition (%)				Calc. IE	Exp. IE
			Re	O 2p	C 2p	H 1s		
A	$1a_2$	-8.11		100			11.61	11.63
B	5e	-8.50		96			11.88	11.94
C	$5a_1$	-8.82	7 (z)	60	22		11.96	12.27
D	$4a_1$	-9.95	8 (s) 6 (z^2)	53	20		13.14	13.08
E	4e	-10.40	16 (xz,yz)	42	17	19	13.61	13.83
F	$3a_1$	-11.08	35 (z^2)	50	6		14.44	14.54
G	3e	-11.64	32 (xy, x^2-y^2) 6 (xz,yz)	51			14.93	15.26
	2e	-11.80	19 (xz,yz) 4 (xy, x^2-y^2)	19	26	23	15.43	

Table 5.3: Band assignment, valence orbital energies (eV) and composition, calculated and experimental IE (eV) values for $MeReO_3$.

The branching ratios in Figure 5.4(c) show the intensity ratio of band F to band G is approximately 1:4 over the whole photon energy range, suggesting similar AO character and a degeneracy consistent with the assignment of band F to ionisation of an a_1 orbital and band G to the ionisation of two e orbitals. The DFT calculations (Table 5.3) confirm that the 2e, 3e and $3a_1$ orbitals are those with the highest 5*d* character amongst the molecular orbitals ranging from 23-33%. These orbitals correlate with the 1e and $2t_2$ orbitals of OsO_4, which give rise to band 5 in its valence PES spectrum.[243] Giant resonances are also seen in the cross section of band 5 between 49 and 61 eV. As is expected for molecular orbitals of higher *d* content (43% for $2t_2$ and 49% for 1e) the resonances are stronger than those of $MeReO_3$. No similarities are apparent on comparison with the cross sections of bands of the $TiCl_4$ spectrum. This may be due to the reduced overlap of the *p* and *d* orbitals in the first transition row resulting from the lower diffuseness of the 3*d* orbitals.

5.3.3 Inner Valence and Core Electron Bands

Inner valence and core ionisations were calculated in two ways: neglecting and including the effects of spin-orbit coupling. The resulting calculated IEs are listed in Table 5.4, alongside the experimental and literature values.

Atom	Core orbital	Orbital energy	IE calc No SO	Core hole state	IE calc With SO	IE exp	IE lit.[246]
Re	5*s*	-87.67	92.62	$^2S_{1/2}$	92.78		86
	5*p* (x,y)	-50.15	54.74	$^2P_{1/2}$	60.77	64	56
	5*p* (z)	-49.76	54.37	$^2P_{3/2}$	56.75	53	45
	4*f*	-45.57 to -45.51	54.2	$^2F_{5/2}$	53.22	55.0	47
				$^2F_{7/2}$	51.79	52.5	45
O	2*s* ($1a_1$)	-24.50	28.13		28.24	29.8	28.48
	2*s* (1e)	-23.92	27.55		27.51		
C	2*s* ($2a_1$)[a]	-18.31	22.48		22.72	22.9	16.59
	1*s*			$^2S_{1/2}$	291.4	286.5	288

[a] The $2a_1$ orbital has 57% C 2*s* and 39% H 1*s* character.

Table 5.4: Core and inner valence orbital energies and calculated, experimental and literature ionisation energies (eV) for $MeReO_3$.

Figure 5.7(a) shows bands arising from the ionisation of inner valence and core electrons. These data were collected at a photon energy of 108 eV with an internal N_2 reference. The most prominent feature is the pair of Re 4*f* bands observed at 52.5 and 55.0 eV corresponding to the $^2F_{7/2}$ and $^2F_{5/2}$ core hole states. Figure 5.7(b) is an expansion of the 4*f* band region of 5.7(a), showing more clearly a broad structure underlying the $^2F_{7/2}$ band. The literature values for core ionisations suggest that the $^2F_{7/2}$ and $^2P_{3/2}$ hole states are coincident. Two additional features support this assignment:

1. The presence of an even broader structure centred at 64 eV which, at 11 eV higher than that assigned to the $^2P_{3/2}$ hole state, is suitably placed to be the $^2P_{1/2}$ state.
2. The change in relative intensity observed for the bands in data collected at 210 eV reflects the calculated cross sections, illustrated in Figure 5.8.

The atomic 5*p* cross section shows a reduction in intensity is expected at higher photon energies, whilst that of the 4*f* is predicted to increase. So it is expected that the bands attributed to the 5*p* orbitals would be much less visible in comparison to the 4*f* bands. Figure 5.7(b) shows this to be the case.

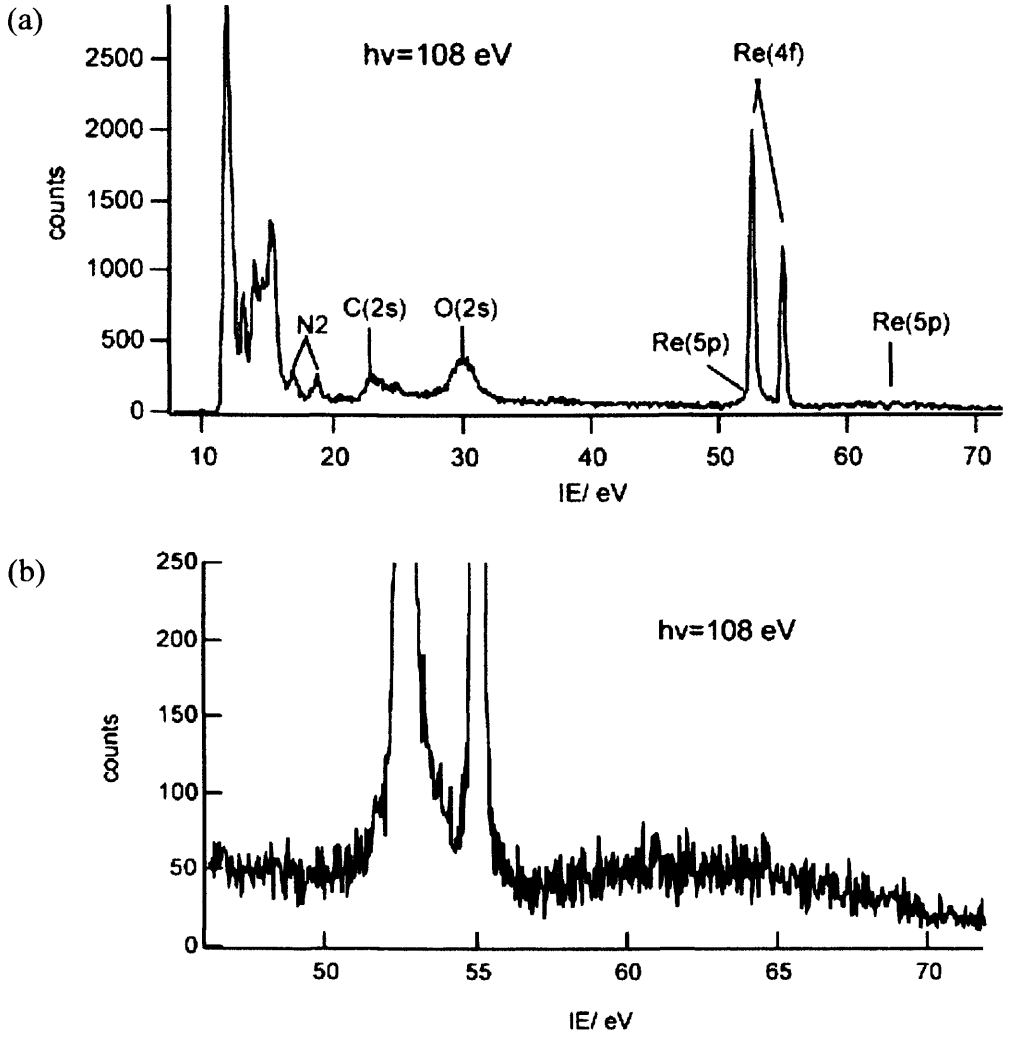

Figure 5.7: (a) f bands and valence bands and (b) Core and inner valence electron PES spectrum, at $h\nu$ = 108 eV for $MeReO_3$.

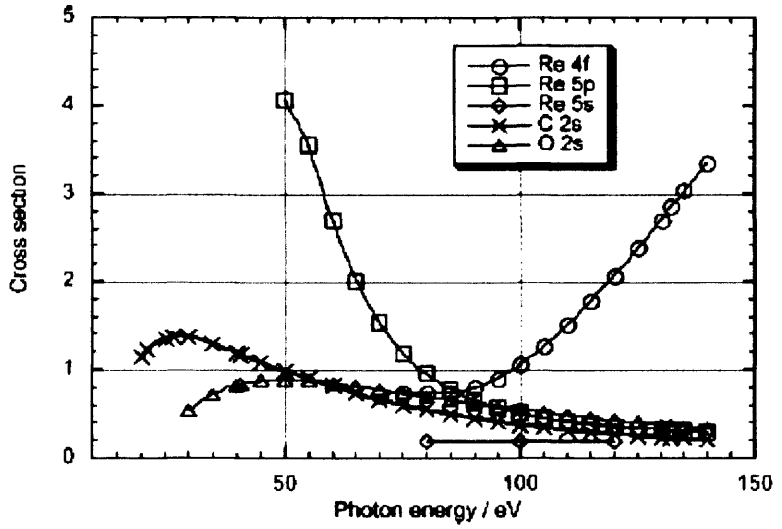

Figure 5.8: Calculated cross sections for Re 4*f*, Re 5*p*, Re 5*s*, C 2*s* and O 2*s* ionisations.

The 4*f* and $^2P_{3/2}$ ionisation energies are higher than both the literature metallic core values and those reported by Hu et al. for a series of $Re(CO)_5X$ complexes, where they ranged from 47.5-48.3; 49.9-50.7 and 48.4-50.0 eV.[245] This discrepancy is probably due to the presence of the electronegative O ligands.

The broad bands at 22.9 and 29.8 eV have been assigned to the C 2s and O 2s ionisations. Their breadth can be explained in part by the fact that both orbitals are involved in bonding. Calculations indicate that O 2*s* contributes to the $1a_1$ and 1e orbitals. With an energy difference of only 0.6 eV, both of these can be accommodated in the observed bandwidth. The $2a_1$ orbital is C–H bonding and is calculated to have 57% C 2*s* character and unresolved vibrational structure broadens the band. Figure 5.7(a) shows the additional presence of a shake-up satellite at 24.9 eV. This is the result of a two-electron process involving electronic excitation during the photoionisation process. A C 1*s* signal was observed using a photon energy of 330 eV. With no internal calibrant, the band is taken at its exact experimental value of 286.5 eV.

The experimental observations were not exactly mirrored by the calculations, either with or without the inclusion of the effect of spin-orbit coupling. For the C 2*s* electrons there was good agreement for the $2a_1$ band, but the calculated ionisation energy for the O 2*s* band was 1 eV too low. In neither case did the inclusion of spin-orbit coupling make a significant difference. The 5*p* ionisation is placed at the same energy as the 4*f* when spin-orbit coupling is omitted, but its inclusion gave a separation of only 4 eV (cf. the observed value of 11 eV and predicted higher ionisation energies). This was also found for the 4*f* electrons, where calculations give a value of 1.4 eV, but experimental observation showed the splitting to be 2.5 eV. Omission of spin-orbit coupling for the 4*f* photoionisations gave a value between the two observed bands, whereas when it was included, again the values were too low. Thus the calculations for the core electrons have been found to underestimate the ionisation energies and spin-orbit splittings.

5.3.4 Absorption Spectra

The absorption spectra of $MeReO_3$ acquired for the Re 4*d*, C 1*s* and O 1*s* core electrons are shown in Figure 5.9 and that for the Re 4*f* and 5*p* excitation region in Figure 5.10, with a summary of the excitation energies and assignments in Table 5.5.

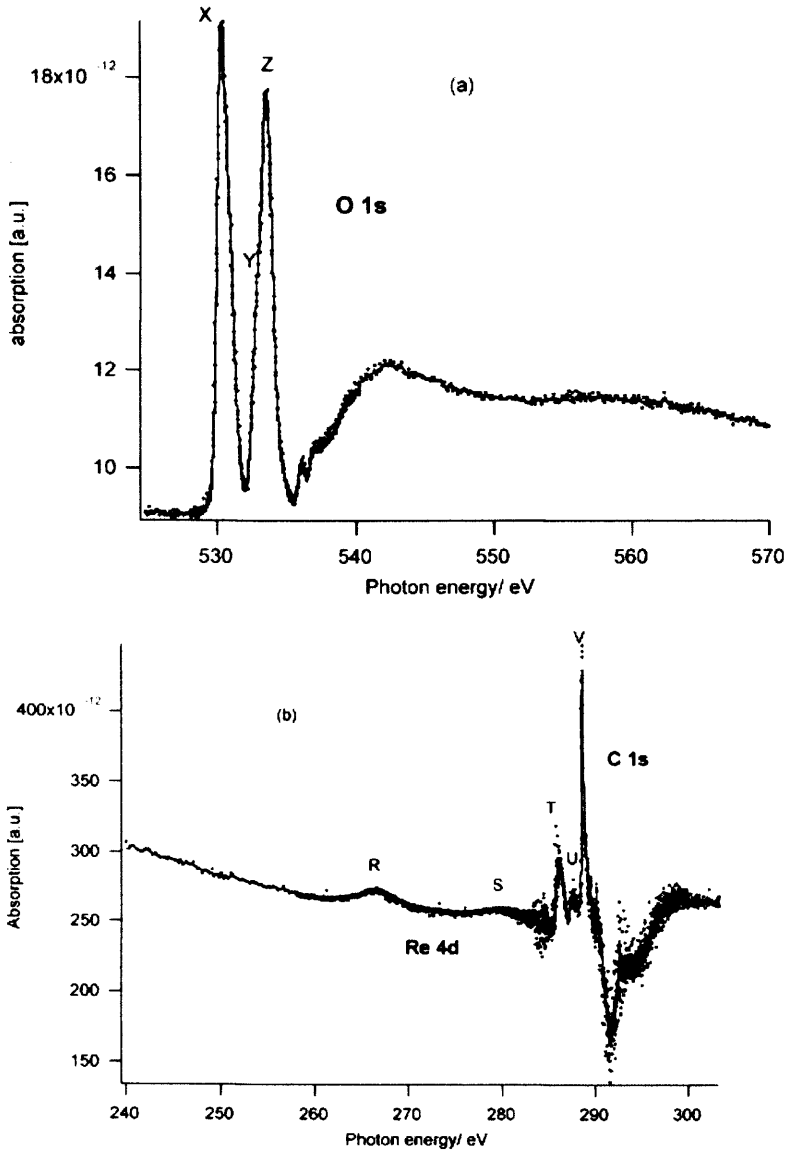

Figure 5.9: Absorption spectra of $MeReO_3$ in the regions (a) 525-570 eV and (b) 250-305 eV.

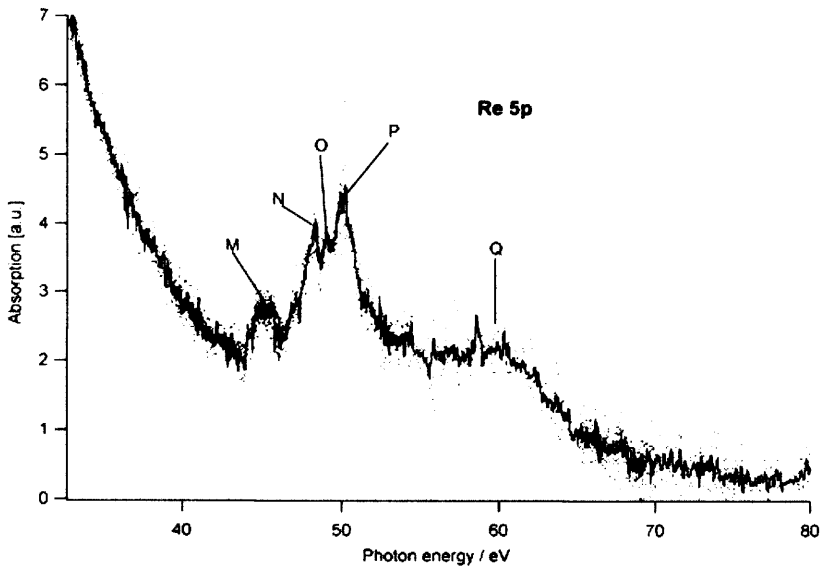

Figure 5.10: Absorption spectrum of $MeReO_3$ in the region 30-80 eV.

Band	Energy (eV)	Intensity	Assignment	Calcd. Energy	Calcd. Rel. Int.
M	44.9		$4a_1 \rightarrow$ Re n*p*		
N	48.2		Re 5*p* $\rightarrow$ 6e	46.1	3.1
O	49.0		Re 5*p* $\rightarrow 6a_1$	48.7	1.0
P	50.0		Re 5*p* $\rightarrow$ 7e	49.1	1.1
Q	59.7		Re 5*p* $^2P_{1/2}$		
R	266.6		Re 4*d* $^2D_{5/2}$		
S	279.6		Re 4*d* $^2D_{3/2}$		
T	286.1		C 1*s* $\rightarrow 6a_1$	285.8	
U	287.7				
V	288.8				
X	530.4	4.6	O 1*s* $\rightarrow$ 6e	530.4	4.1
Y	532.8	1	O 1*s* $\rightarrow 6a_1$	532.9	1.0
Z	533.6	3.1	O 1*s* $\rightarrow$ 7e	533.6	3.0

Table 5.5: $MeReO_3$ absorption bands, energies (eV), relative intensities and assignments, calculated energies (eV) and predicted band intensities.

The ligand atomic 2*p* orbital contribution to the lowest unoccupied molecular orbitals was explored through the excitation of the non-bonding 1*s* electrons. The previously calculated OsO_4 molecular orbital diagram predicts the LUMO to be a pair of doubly degenerate e orbitals, with the next empty valence level being a t_2 level.[206] As a C_{3v} molecule, $MeReO_3$ has reduced symmetry from this T_d model, the t_2 level will split into an a_1 and an e level, giving three closely spaced empty valence levels:

$$6e < 6a_1 < 7e$$

The covalent nature of the molecule means the *d* orbitals are strongly mixed with those of the ligands, and calculations predict all three levels to have Re 5*d* and O 2*p* content, but only the $6a_1$ level to have a contribution from the C 2*p*, as shown in Table 5.5.

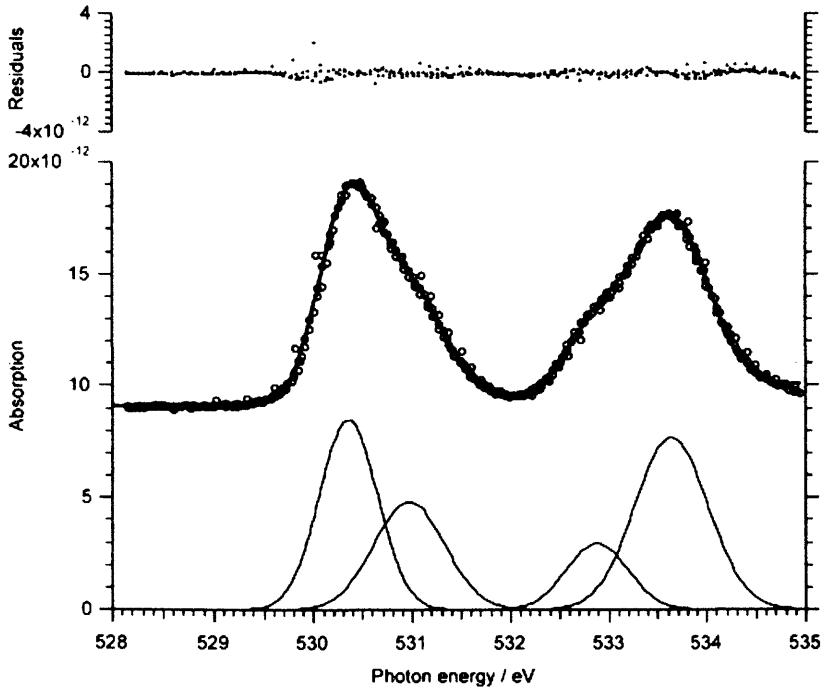

Figure 5.11: Fit of the O 1*s* absorption spectrum for $MeReO_3$ with Gaussian functions.

Ligand 1s edges

Atomic carbon 1*s* excitation occurs in the same energy region as that of the Re 4*d* electrons, so measurements were taken over the 240-300 eV photon energy range. However, the combination of carbon contamination of the first optical elements of the beamline and a strong photon flux drop leaves the C 1*s* edge not well defined. Despite the presence of three bands in the 285-290 eV region, only one, T, has been assigned to C 1*s* absorption with a maximum at 286.1 eV. The unassigned bands U and V are of too high an energy and inappropriately spaced to be related to the C 1*s* transition to the unoccupied valence levels.

The near edge of the oxygen 1*s* absorption edge spectrum, measured over the 525-580 eV photon energy range, showed two strong, sharp bands with maxima at 530.4 eV (X) and 533.6 eV (Z). Both bands are asymmetric, X having a sharp rise at the threshold and Z a leading shoulder. Deconvolution of this shoulder gives an additional band, Y, at 532.8 eV. There is reasonable agreement between the experimental (Y-X = 2.4 eV Z-Y = 0.8 eV) and calculated ($6a_1$-6e = 1.9 eV; 7e-$6a_1$ = 0.8 eV) band gaps, sufficient to assign the bands as O 1s transitions to the 6e, $6a_1$ and 7e energy levels (Table 5.5). The broad feature at 540-545 eV is the ionisation edge of the O 1*s* orbital, which has a literature value of 543.1 eV.[247]

Comparison of the relative band intensities supports the O 1*s* band assignments. The experimental band areas were fitted using Igor Pro software (Figure 5.11), giving an X:Y:Z ratio of 4.6:1.0:3.1. However, the relative areas of Y and Z are dependent on the deconvolution of the shoulder and, rather like bands A, B and C, are best treated together, giving an X:(Y+Z) of 1.1:1.0. This does not match the 2:3 ratio of the number of orbitals that one might expect on first glance at the molecular orbital diagram. Despite each band resulting from a $1s \rightarrow 2p$ transition, the probability of each transition does not reflect the number of orbitals in the valence energy level, or even the 2*p* contribution to the molecular orbital, but rather the degree of overlap of the ground and final states. Based on Equation 4.4, the relative intensities of the three transitions were estimated from the one-centre $\langle O(1s)|ez|O(2p)\rangle$ integrals, assuming that the two-centre contributions to the transition moment could be neglected. The coefficients of the O(1*s*) orbitals in the core states and the O(2*p*) orbitals in the three excited states were obtained from the ground state wave function. The calculations gave a ratio of 4.1:1.0:3.0 or 1.0:1.0, in close agreement with the experimental findings. Thus the calculations have been shown to provide a good model for the atomic orbital contributions to the lowest unoccupied orbitals of the molecule.

It is proposed that the asymmetry of band X is due to orbital splitting in the $(O1s)^{-1}(6e)^{1}$ excited state. This is probably due to either spin-orbit coupling or Jahn-Teller distortion arising from the presence of only one electron in the degenerate 6e molecular orbitals.

Re edges

The Re 4*d* edge has two broad bands at 266.6 eV (R) and 279.6 eV (S), assigned to Re 4*d* excitation from the splitting of the $^2D_{5/2}$ and $^2D_{3/2}$ core holes. The literature value of this splitting is 13.4 eV;[247] sufficiently close to our experimental value of 13 eV to confirm the band assignment, given their breadth. When the high oxidation state of the Re centre is taken into account, the fact that these excitations occur at photon energies above the ionisation energies for these core orbitals (260.5; 273.9) for neutral Re does not alter the assignment. The absorption spectrum collected between 35 and 80 eV was expected to include any Re 4*f* and 5*p* excitations. The probability of transitions from the 4*f* orbitals is low, and indeed no resultant bands were observed. $5p \rightarrow 5d$ excitations are the most probable as these orbitals have the greatest spatial similarity, so vacant valence levels containing 5*d* character should be identifiable from the bands present at

the 5*p* near edge. The calculations indicate that, as for the O 1*s* edge, three bands should be present. The bands N, O and P, observed at 48.2, 49.0 and 50.0 eV, have comparable separations (O–N = 1.8 eV; P–O = 1.0 eV) to those calculated for the 6e, $6a_1$ and 7e states, although they are slightly different from those of bands X, Y and Z. The signal-to-noise ratio for the spectra prevented a good fit of the band areas to compare their relative intensities to the 3.1:1.0:1.1 calculated. However these features were reproducible over a number of scans on different occasions and are assigned as 5*p*→6e, $6a_1$ and 7e transitions.

The broad and featureless band Q lies around 11 eV above the centroid of N, O and P; this separation is the size of the spin-orbit splitting of a Re 5*p* hole in the $^2P_{1/2}$ and $^2P_{3/2}$ states.[247] It has therefore been assigned as a 5*p* transition resulting in a $^2P_{1/2}$ hole state, shown in Figure 5.10. The shorter lifetime of the $^2P_{1/2}$ hole state than that of $^2P_{3/2}$ usually results in a broader fine structure, in accord with the Uncertainty Principle, but its absence may also be due to the lower inherent intensity of the excitation and the high signal-to-noise levels.

Assuming the previous bands have been correctly assigned, band M – lying below the Re 5*p* edge – cannot be associated with a primary Re 5*p* excitation. Not can it be attributed to a Re 4*f* transition, as its relative probability is too large (i.e. it is too intense). Comparison was made with the cross sections from the PES studies of the valence orbitals, as these suggested possible resonance structures in bands D, F and G occurring at 35, 38, 43, 47 and 58 eV, as discussed in Section 5.3. The initial stage in these resonances involves absorption by the ground state electrons, so the coincidence of the two features can be taken as confirmation of the assignment of both. Band D shows a resonance absent in other bands with an onset energy of 43 eV. At 44.9 eV, the maximum of band M is somewhat above this, but the comparable maximum of the band D resonance is obscured by the subsequent *p*→*d* resonance. It therefore seems likely that the two features are related and that band M results from the excitation from the *s*-like $4a_1$ orbital into an energy level of *p*-like character in the continuum. The comparison also supports the assignment of other resonances observed in the PES studies. Those at 47 and 58 eV coincide with the onset of bands N and Q, which have been convincingly assigned to 5*p*→5*d* transitions.

5.4 Electronic Structure and Chemical Reactivity

Although general comparisons may be drawn between $MeReO_3$ and OsO_4, the symmetry and ligand differences preclude direct correlation of individual molecular orbitals. In order to explore the links between its reactivity and bonding, comparisons have been made between $MeReO_3$ and $MeTiCl_3$, another d^0 complex exhibiting pronounced Lewis acidic character associated with a low lying vacant orbital of metal *d* character and with similar C_{3v} geometry.

5.4.1 Comparison with the C_{3v} Molecule $MeTiCl_3$

As for the calculations in this work, previous calculations for $MeTiCl_3$ were calculated using triple-ζ, Slater-type atomic orbital basis sets, but with differing exchange-correlation functionals.[248] In order to facilitate comparison with $MeReO_3$, comparable functional and basis sets were employed and the energy levels, composition and ionisation energies recalculated. In the most part, the results were similar to the previous work, but gave differing orbital energies, within the same orbital ordering. Figure 5.12(a) shows the calculated MO diagram for the two molecules, with cartoon representations of the orbitals generated by Prof. J.C. Green, and Figure 5.12(b) displays their valence ionisations from experimental PES studies. Three features are particularly noticeable:

- The predominantly non-bonding Cl or O based orbitals $1a_2$ and 5e are clearly of similar energy, with the metal centre exerting little influence on their ionisation energies.
- The orbitals with metal *d* content are stabilised in $MeReO_3$ in comparison to those in $MeTiCl_3$ and generally have higher coefficients for the Re 5d than the Ti 3*d* atomic orbitals.
- The Ti–Me and the C–H bonds are localised within the $MeTiCl_3$ molecule, whereas in $MeReO_3$ these basis orbitals mix with the O 2*p* orbitals resulting in Re–Me character being distributed throughout the valence orbital manifold.

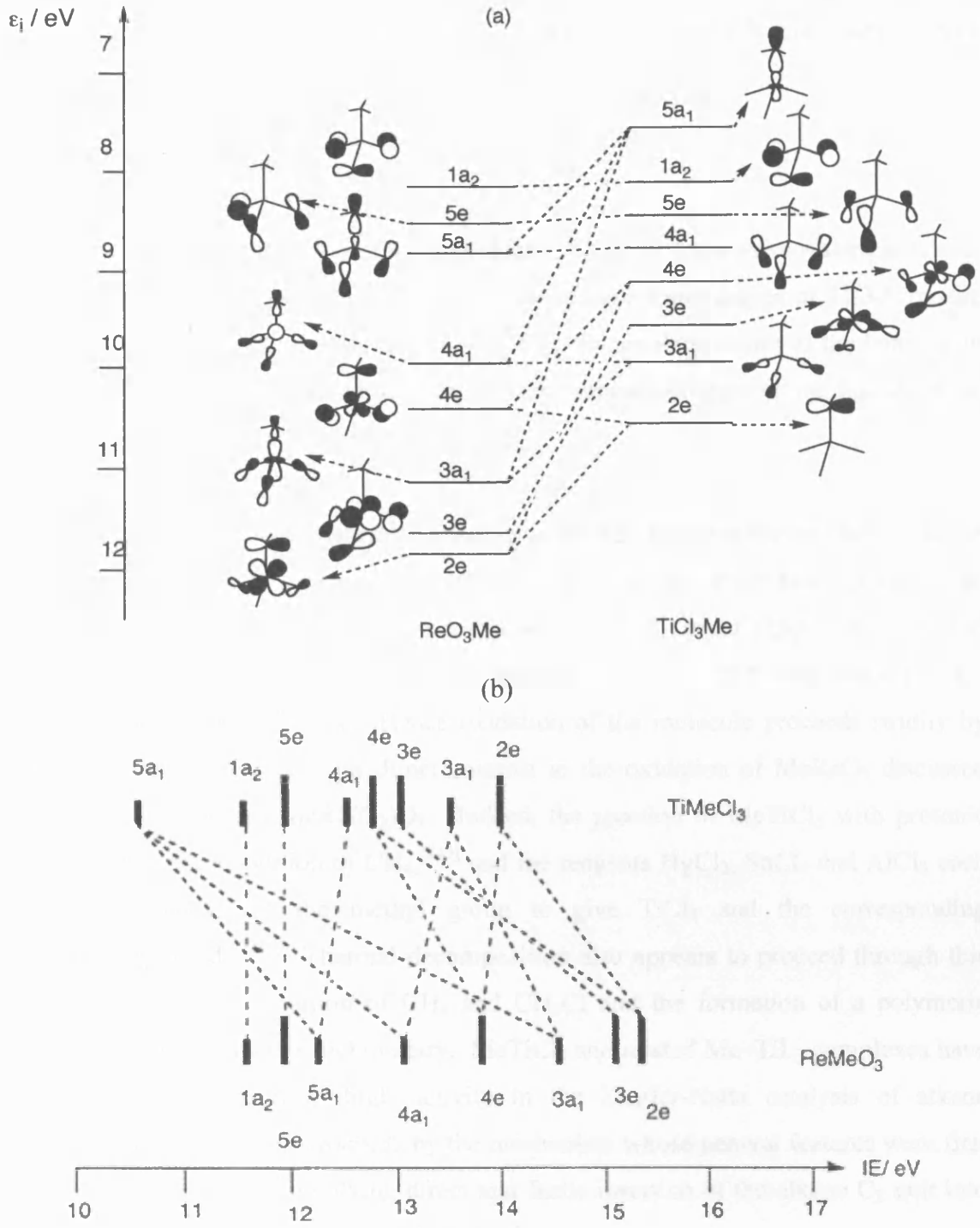

Figure 5.12: (a) Comparison of the MO energy level diagrams of $MeReO_3$ and $MeTiCl_3$ and (b) Comparison of PES spectra of the two molecules.

On the basis of their ratio of charge:electron density, the non-bonding, ligand-based electrons are expected to have similar ionisation energies; the greater electronegativity of the chlorine atoms being offset by the higher bond order of the Re–O bond. The two other features are a result of the differing factors that determine the overall ordering of the MOs, which is in part due to the more diffuse nature of the *5d* orbitals. Their overall

orbital ordering is dominated by bonding character in $MeTiCl_3$ and metal orbital character in $MeReO_3$:

$MeTiCl_3$ Ti–C(σ) > Cl(π nb) > Cl–Ti(π b) > C–H (b)

$MeReO_3$ O(nb) > Re(6*p*) > Re(6*s*) > Re(5*d*)

For $MeTiCl_3$ the localised bond character does not detract from the covalent nature of the bonding; indeed most of the molecular orbitals have some degree of Ti 3*d* content, where symmetry allows. In contrast to $MeTiCl_3$, the covalent nature of the bonding in $MeReO_3$ is evidenced by the delocalisation of the orbitals throughout the ligand set, as in OsO_4, through σ–π mixing.

This difference in the localisation of bonding is the key to the differing chemistries of the two compounds, the most striking of which is the nature of the M–C moiety. The $MeTiCl_3$ HOMO is a localised orbital composed of Ti($3d_{z^2}$) and C($2p_z$). This, allied to the high polarity of the Ti–C bond (the charge on Ti is +1.218 with respect to C) endows it with a high lability. Hence oxidation of the molecule proceeds readily by insertion to give $MeOTiCl_3$, in direct contrast to the oxidation of $MeReO_3$ discussed above, which produces $MeRe(O_2)O_2$. Indeed, the reaction of $MeTiCl_3$ with protonic species causes the evolution of CH_4,[249] and the reagents $HgCl_2$, $SnCl_4$ and $AlCl_3$ each react by exchange of the methyl group to give $TiCl_4$ and the corresponding metallorganic halide.[250] Thermal decomposition also appears to proceed through this Achilles' heel, with evolution of CH_4 and CH_3Cl and the formation of a polymeric material of indeterminate stoichiometry. $MeTiCl_3$ and related Me–TiL_3 complexes have long been known to have high activity in the Ziegler-Natta catalysis of alkene polymerisation,[251] which proceeds by the mechanism whose general features were first proposed by Cossee,[252] involving direct and facile insertion of the alkene C_2 unit into the labile Ti–C bond as described in Chapter 3.

In contrast, $MeReO_3$ is thermally robust with both the Re–C and Re=O moieties strongly bonded, exhibiting bond orders greater than 1 and 2 respectively.[239] This is borne out by the conclusions of this study, which shows the Re–C and Re–O bonding electrons lie at least 1.5 eV deeper in energy than their counterparts in $MeTiCl_3$. Rather than a M–C HOMO, $MeReO_3$ has a HOMO of primarily Re–O π-character, with the Re–C electrons being subject to a significant amount of delocalisation over the metal

and oxygen ligands in the HOMO – 3 and HOMO – 4 orbitals. The Re–C bond thus plays a less prominent rôle in the chemistry than its counterpart in $MeTiCl_3$. Rather it is the Re–O moieties that characterise the majority of the chemistry displayed, as discussed earlier. Hence, the strength, stability and covalent nature of the Re–C bond in $MeReO_3$ endow it with a chemistry markedly different from that displayed by its counterpart in $MeTiCl_3$.

5.5 Conclusions

In this Chapter the electronic structure of $MeReO_3$ has been explored by a combination of variable energy photoelectron and absorption spectroscopy, with the experimental results compared to calculations. It has been established that:

- The photoelectron cross sections of the valence region of $MeReO_3$ confirm a computational model of the molecule. The absorption spectra give supporting evidence, showing $5p \rightarrow 5d$ excitations where predicted for the resonant features observed in the photoelectron cross sections.

- The electronic structure is most readily described as a perturbed tetrahedral d^0 system with the most strongly bound molecular orbitals being those with most $5d$ character. The absorption spectra have provided evidence for the resonant processes observed in the photoionisation cross sections and indicate strong rhenium-$5d$ oxygen-$2p$ mixing in the lowest unoccupied orbitals.

- The photoelectron spectra of the core electrons show that the $4f$ orbitals retain their atomic nature and do not participate in the bonding of the molecule.

- In contrast to a previous study of $MeTiCl_3$, where the methyl ionisations were associated with two spectral bands, this work has shown that both the C–H and the Re–C bonds in $MeReO_3$ contribute to several molecular orbitals. The contrasting nature of the chemistry of the two systems may be accounted for by these differences in electronic structure.

Chapter 6

Structural and Bonding Studies of $Zr(BH_4)_4$, $Hf(BH_4)_4$ and $U(BH_4)_4$

The studies carried out in this chapter focussed on the electronic structure of a series of known, volatile pseudotetrahedral molecules $M(BH_4)_4$, with M = Zr, Hf and U. This series provides a unique view of M–H bonding through the sole presence of H as the co-ordinated species.

6.1 Introduction

The borohydride ion is a versatile ligand, which adopts a variety of co-ordination modes, and which acts as either an ionic or covalent ligand, as discussed in Chapter 1. The covalent bonding mode of the B–H unit may be regarded as donation of its σ-bonding electron pair to the metal centre to form a metal-ligand dative bond. The M–H–B angle of 80-84°[253;254] observed in neutron diffraction studies of $Hf(BH_4)_4$ and $U(BH_4)_4$ suggests that these are 3c-2e, σ-bond complexes, with the B–H→M bond best represented schematically as in Figure 6.1.

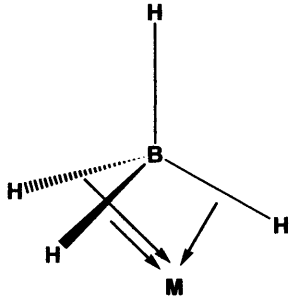

Figure 6.1: Schematic representation of σ–bond interaction for η^3-borohydride metal complexes.

The $M(\eta^3\text{-}BH_4)_4$ species considered in this study have unusual valence electron counts: 24 (M = Zr and Hf) or 26 (M = U) if each bridging B–H is counted as a two electron donor. This high valence electron count, along with the high co-ordination number around the metal centre, may be taken as evidence of ionic bonding. However, comparative X-ray PES studies[255] looking at the core binding energies of $U(BH_4)_4$ have shown the molecule to have some covalent nature. This is supported by previous calculations,[256] and those conducted for this study indicate that there is not only a high degree of electron localisation on the ligands – imparting ionic character to the

bonding – but that there is also a degree of AO mixing in the make-up of the MOs. For the Group 4 tetraborohydrides (M = Zr, Hf), the MO calculations have shown the 'excess' electrons (i.e. the 6 over the 18 electron rule count) to occupy a t_1 HOMO, a ligand-localised triply degenerate orbital set.[41] These orbitals are located on the ligands as a result of the lack of t_1 symmetry in the transition metal orbitals, enabling the additional electrons to be present without causing any destabilisation in the M–L interactions.

The capacity of *s, p* and *d* orbitals to form covalent bonds in inorganic molecules is well documented, but that of *f* orbitals is less so.[257-259] In lanthanide and actinide complexes the energies of the *f* orbitals place them in the valence region. However, as a consequence of their low principal quantum number they have a limited radial extension. As a result, the lanthanide 4*f* orbitals are core-like, whereas the actinide 5*f* orbitals, experiencing a greater relativistic expansion, do extend sufficiently to become involved in bonding, as found for uranocene, $[U(\eta^8\text{-}C_8H_8)_2]$.[260] With their high angular momentum, *f* orbitals have nodal properties that can lead to low overlap with ligand orbitals. In T_d symmetry however, the ligand symmetry-adapted linear combinations (SALCs) span the representations a_1, e, t_2 and t_1. With the *s* orbitals providing an a_1 symmetry match, the *p* orbitals a t_2 match and the *d* orbitals matches with t_2 and e, only an *f* orbital can provide a symmetry match for the t_1 combination. Probing the nature of the t_1 orbitals will therefore give insight into the involvement of the U 5*f* orbitals in the bonding of $U(BH_4)_4$.

The chemical properties of the three tetraborohydride molecules are similar, each being an air-sensitive volatile solid at room temperature, although the hydrolysis of $U(BH_4)_4$ proceeds at a slower rate.[33] A remarkable feature of the complexes is their volatility, exemplified by $Hf(BH_4)_4$, the most volatile compound of hafnium, with a significant vapour pressure at room temperature. The uranium compound, while significantly less volatile than either that of zirconium or hafnium, is the second most volatile compound of this element behind UF_6, whereas $Np(BH_4)_4$, which also has a monomeric crystal structure, has a vapour pressure comparable to $Zr(BH_4)_4$.[261] Another characteristic of covalent molecules, solubility in non-polar solvents, is demonstrated by $Zr(BH_4)_4$ and $Hf(BH_4)_4$, but to a far lesser extent by $U(BH_4)_4$.[34]

6.1.1 Previous Structural Studies

The structures of $Hf(BH_4)_4$ and $Zr(BH_4)_4$ have been extensively studied, and that of $U(BH_4)_4$ has also received considerable attention.[33] With no possibility of electronic stabilisation through additional π–bonding, they display high co-ordination numbers in both the solid and gas phases; indeed the co-ordination number around the central uranium atom increases from 12 to 14 in the solid state.[254]

Vibrational spectroscopic studies conducted on $Hf(BH_4)_4$ and $Zr(BH_4)_4$ in the 1970's concluded that their structures were nearly identical, with the BH_4^- unit bonding in an η^3-manner, demonstrated by a single terminal B–H stretching vibration in the 2450-2600 cm^{-1} region.[34] NMR spectroscopic studies conducted in the non-polar, co-ordinatively uncompetitive, solvent d_8-toluene reported in the same paper were unable to support this conclusion directly; at temperatures as low as –80 °C the BH_4^- unit remained fluxional. Few subsequent NMR studies have been conducted,[262] and more recent structural investigations have focused on diffraction and vibrational spectroscopic studies.

The crystal structures of $Hf(BH_4)_4$ and $Zr(BH_4)_4$ are isomorphous, with staggered BH_4 groups giving molecular T_d symmetry. $Hf(BH_4)_4$ was characterised by single-crystal neutron diffraction at 110 K, and was found to be monomeric and to have rigorous T_d symmetry (space group $P\bar{4}3m$) in the solid state.[253] $Zr(BH_4)_4$, characterised by X-ray diffraction at 110 K, was also found to be monomeric, but the locations of the bridging hydrides could not be established precisely.[263] Such strict T_d symmetry in the solid phase is not observed in $U(BH_4)_4$: neutron and X-ray diffraction studies of its dark green crystals have shown it to adopt a 14 co-ordinate, polymeric structure of interlocking helical chains, with four bridging η^2–η^2 BH_4 groups and two terminal η^3-BH_4 groups in a *cis* configuration.[254;264] A second polymorph, the emerald green form II, also displays a polymeric 14 co-ordinate structure. Identified by X-ray crystallography[265] it is a two-dimensional molecular network, also with four coplanar bridging η^2–η^2 BH_4 groups, but this time the two terminal η^3-BH_4 groups are *trans* to one another. This higher co-ordination number in $U(BH_4)_4$ is more a result of the larger size of the uranium (IV) metal centre (covalent radius 89 pm),[42] compared to those of Zr (IV) and Hf (IV) at 72 and 76 pm respectively,[42] than the presence of the two additional 5*f*

electrons in the valence shell. The structures adopted thus demonstrate complete co-ordinative saturation of the metal in each case.

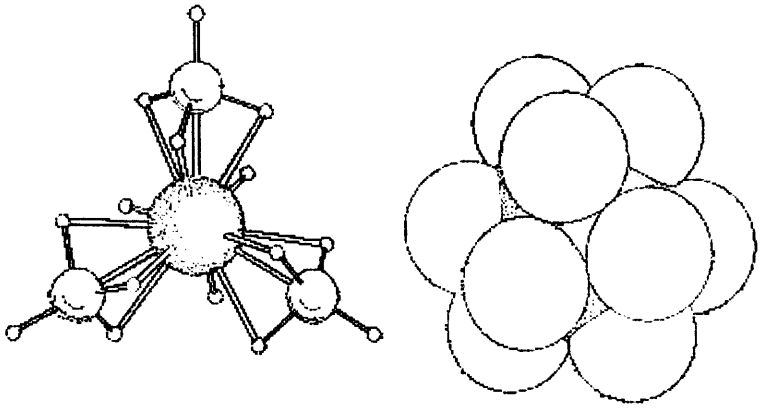

Figure 6.2: Gas phase structure of $Zr(BH_4)_4$, illustrating the twist of the BH_4 group.[266]

Vibrational spectroscopic studies have focussed mainly on $Zr(BH_4)_4$, with early results suggesting that the molecule adopts *T* symmetry in the gas phase,[267-269] as shown in Figure 6.2. Subsequent studies, including quantum mechanical calculations, have implied a structure with *T* symmetry, which is consistent with the IR and Raman spectra observed.[270] This structure involves a 'twist' of the BH_4 unit from the T_d staggered orientation, the angle of deformation being calculated as 15° for the Zr complex and as 14° for that of Hf. This 'twist' is a rotation of the η^3-BH_4 groups from the orientation in which the three bridging B-H bonds are staggered with respect to the opposing ZrB_3 fragment. Recent gas-phase electron diffraction studies[38;266] confirm this reduction in symmetry to T, and show all three compounds to have different gas-phase structures from those of their crystalline forms. This is most apparent with gaseous $U(BH_4)_4$, which is monomeric with four η^3-BH_4 groups and the associated reduced co-ordination number. Rather than the *T* symmetry observed for the transition metal compounds, $U(BH_4)_4$ has T_d symmetry, with the BH_4 groups adopting a staggered conformation. This difference in conformation to that observed in the *d*-block complexes is a result of the shortest distances between bridging H atoms (255 pm), being longer than the sum of their Van der Waals radii (240 pm)[266] and indicating that there is no steric repulsion between the bridging hydrogens around this larger metal centre.

6.1.2 Previous Electronic Studies

$Hf(BH_4)_4$ and $Zr(BH_4)_4$ are closed- shell molecules, unlike the U compound which has a partially filled 5*f* shell, giving rise to a triplet ground state. The electronic structures of each of the complexes have been studied previously,[256;271] as has that of $Th(BH_4)_4$.[272] The He(I) and He(II) PES spectra of $Zr(BH_4)_4$ and $Hf(BH_4)_4$ were identical in the two reports, but the orbital assignments were not. The earlier work by Downs et al.[271] interpreted the spectra in terms of localised terminal and bridging orbitals, leading to the $3t_2$ orbitals being assigned as the HOMO. A subsequent study[256] employed LCAO-HFS(Xα) calculations in addition to PES, resulting in a reassignment of the spectra. This suggested that the t_1 orbitals were associated with the lowest IE band for $Zr(BH_4)_4$ and $Hf(BH_4)_4$, an assignment confirmed by PES studies on $M(BH_3Me)_4$, (M = Zr, Hf, Th and U).[272] The quasi-relativistic Xα-SW calculations associated with the study indicate a change in the HOMO in $M(BH_4)_4$, from $1t_1$ for, M = Zr and Hf, to $3t_2$ for M = Th and U.[273] They found a weaker interaction of the $3t_2$ orbitals with the metal *d* orbitals and a small bonding interaction of the metal 5*f* orbitals with the $1t_1$ orbitals, which resulted in this reversal. An interesting possibility raised by both Downs et al. and Rösch and Hohl[273] is that of direct M–B bonding. They each note a discernible increase in the B 2*s* based $1a_1$ binding energy (0.4 eV) on going from $Zr(BH_4)_4$ to $Hf(BH_4)_4$, and attribute this to a direct M–B interaction. The 'direct relativistic orbital contraction' experienced by the Hf 6*s* orbital stabilises it with respect to the Zr 5*s* orbital, and consequently it mixes more strongly with the ligand a_1 orbitals, especially the $1a_1$ orbital.

In this Chapter, VEPES and VUV/X-ray absorption spectroscopy have been used to investigate the electronic structures of $Zr(BH_4)_4$, $Hf(BH_4)_4$ and $U(BH_4)_4$, allowing a comparative study of their bonding and, in particular, the extent of *f* orbital involvement in bonding in $U(BH_4)_4$ to be probed.

6.2 VEPES Studies of $Zr(BH_4)_4$, $Hf(BH_4)_4$ and $U(BH_4)_4$

6.2.1 Synthesis of $M(BH_4)_4$

Each of the tetrakis(borohydride) compounds studied in this Chapter was prepared by solid-state metathesis between the appropriate metal tetrachloride and fresh lithium borohydride at room temperature; Equation 6.1:

$$MCl_4 + 4\ LiBH_4 \rightarrow M(BH_4)_4 + 4\ LiCl \qquad \textbf{[6.1]}$$

The literature procedures for the preparations of $Hf(BH_4)_4$,[38] $Zr(BH_4)_4$ and $U(BH_4)_4$[266] are very similar. A general method, following the literature routes was employed for the synthesis of all three compounds; the only variation being the length of time each reaction mixture was stirred.

Working in a dry box, a 50% excess of fresh $LiBH_4$ was crushed to a fine powder with a pestle in a mortar and placed in a long-necked round bottom flask, sealed with a Teflon valve. Two or three small, glass-coated stirrer bars were added, along with either: ground, white $ZrCl_4/HfCl_4$, or bright green $^{238}UCl_4$. The reaction vessel was partially evacuated and the mixture of solids was stirred in the sealed glass flask for 4 – 21 d. In the case of both $Hf(BH_4)_4$ and $Zr(BH_4)_4$, white crystals of a volatile material formed at the neck of the vessel after 36 h. This product was collected after a further 3 d stirring to ensure the reaction had gone to completion. The $^{238}UCl_4$ required longer to react, and was stirred with the $LiBH_4$ for 3 weeks before any volatile product was collected. To isolate the product, the reaction vessel was cooled in liquid N_2 and all volatiles removed. On warming to room temperature, all remaining volatile material was transferred under reduced pressure into a trap cooled to –110 °C. The tetrakis(borohydride) product was purified by a trap-to-trap sublimation *in vacuo*, maintaining the initial trap at 0 °C and condensing the subsequent volatile material at –78 °C.

6.2.2 Data collection for VEPES and VUV Absorption Spectroscopy

The data for this study were collected in a similar manner to those for the study of $MeReO_3$ described in Chapter 5. The spectroscopically pure samples were each placed in a small ampoule sealed with a Young's valve with an arm ending in a glass-to-metal joint. The ampoule was wrapped in Al foil and connected via a Swagelok fitting to the manifold of pipes providing access to the experimental chamber. The samples were held at room temperature in a water bath. The $Zr(BH_4)_4$ and $Hf(BH_4)_4$ are highly

volatile, and the experimental chamber was maintained at an overall pressure of around ~1.1-1.9 x 10^{-6} mbar. $U(BH_4)_4$ is less volatile, and so was introduced with a carrier gas at a pressure of ~4.5 x 10^{-6} mbar. The signal for the photoelectron spectra was collected from a calibrated photodiode, normalised using the macro given in Equation 5.2.

VEPES data were collected in the 8 – 21 eV binding energy range for the valence bands of the three compounds over a series of photon energies between 20 – 60 eV using grating 1 (400 l/mm), and between 67 – 110 eV using grating 3 (1200 l/mm) for $U(BH_4)_4$ only. Unfortunately, the experimental limitations on data collection resulted in larger than desired intervals in *hv* of 4eV. Zr 4p bands were measured using a photon energy of 60 eV and B 1s ionisations were measured using grating 4 at a photon energy of 244.37 eV. An investigation over the photon range 46-60 eV was conducted into the band at 26.1 eV assigned in previous studies as the Hf 4*f* ionisation in $Hf(BH_4)_4$. Particular care was taken whilst working with the $U(BH_4)_4$, following the safety procedure given in Appendix 2. This complex had had a deleterious effect on the electron detector, which on exposure to the vapour lost sensitivity. On removal of the sample and following pumping, it recovered to a certain extent, but not completely, as reported by Downs et al.[271] Increasing the channeltron voltage helped the recovery of the signal, and the rate of signal decline was slowed by co-flowing Ar, making data collection possible, but never easy. The absorption spectrum for the region of the Zr *4p* edge was measured over the photon energy ranges 24 to 60 eV using grating 1, with a photon energy bandwidth varying from 3 to 10 meV in a similar manner to the Re 4*f*/5*d* edge described in Section 5.2.3.

6.2.3 Density Functional Theory Calculations

The gas-phase structures discussed in Section 6.1.1 show $U(BH_4)_4$ to have strict T_d symmetry, but $Zr(BH_4)_4$ and $Hf(BH_4)_4$ to have the reduced T symmetry. This makes very little difference to the results of the ionisation energy calculations, so for ease and relative speed T_d symmetry was assumed throughout. The geometries of the molecules were optimised and the calculated interatomic distances showed reasonable agreement with those previously reported from calculations, gas-phase electron diffraction and neutron diffraction, as described in Table 6.1.[38;253;266]

	Zr		Hf		U	
	Calc.	Exp.	Calc.	Exp.	Calc.	Exp.
B-H_t	119.7	118.8	119.6	121.0	119.7	117.8
	(119.4)		(118.8)	(115.0)	(119.5)	
B-H_b	125.3	127.8	125.2	127.6	126.1	131.6
	(125.3)		(124.3)	(123.5)	(126.0)	
M-H_b	210.9	214.4	210.7	221.5	223.2	231.5
	(214.8)		(212.5)	(213.0)	(227.7)	
M...B	227.4	232.4	227.1	231.4	243.3	251.2
	(232.2)		(229.2)	(228.1)	(248.8)	

Table 6.1: Calculated (DFT) and experimental (GED) bond lengths (pm) for $M(BH_4)_4$ (M = Zr, Hf and U), assuming T_d symmetry. Previously calculated values and those obtained in the solid state by neutron diffraction are given in parentheses.

6.3 Results and Discussion

The interpretation and assignment of the experimental results for the three molecules have been informed by the results of the calculations and the profiles of the atomic orbital cross sections shown in Figure 6.3. The proposed MO energy level diagram for $Zr(BH_4)_4$ and $Hf(BH_4)_4$ is shown in Figure 6.4(a) and that for $U(BH_4)_4$ in Figure 6.4(b). These are related to the valence electron PES spectra of $Zr(BH_4)_4$ and $U(BH_4)_4$ and the calculated iso-surfaces of the molecular orbitals in Figure 6.5. The symmetry assignments and ordering are discussed in the Sections below. Table 6.2 summarizes the experimental ionisation energies observed for the PES bands and Table 6.3 those expected for the core orbitals.

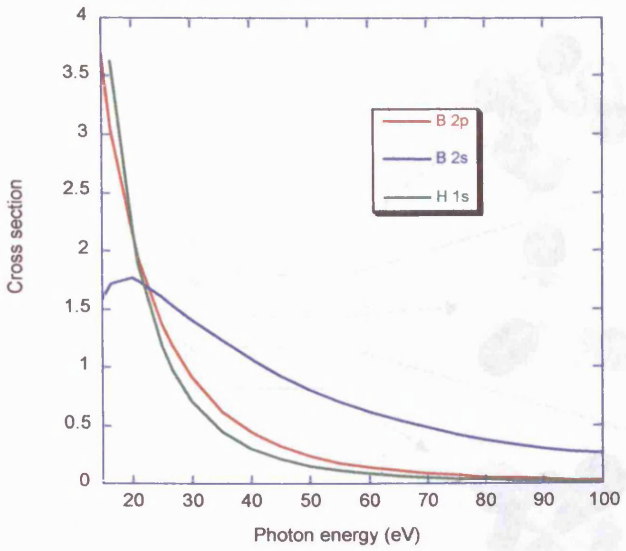

Figure 6.3: Calculated atomic cross sections for the B 2*p* and 2*s* and H 1*s* orbitals.[274]

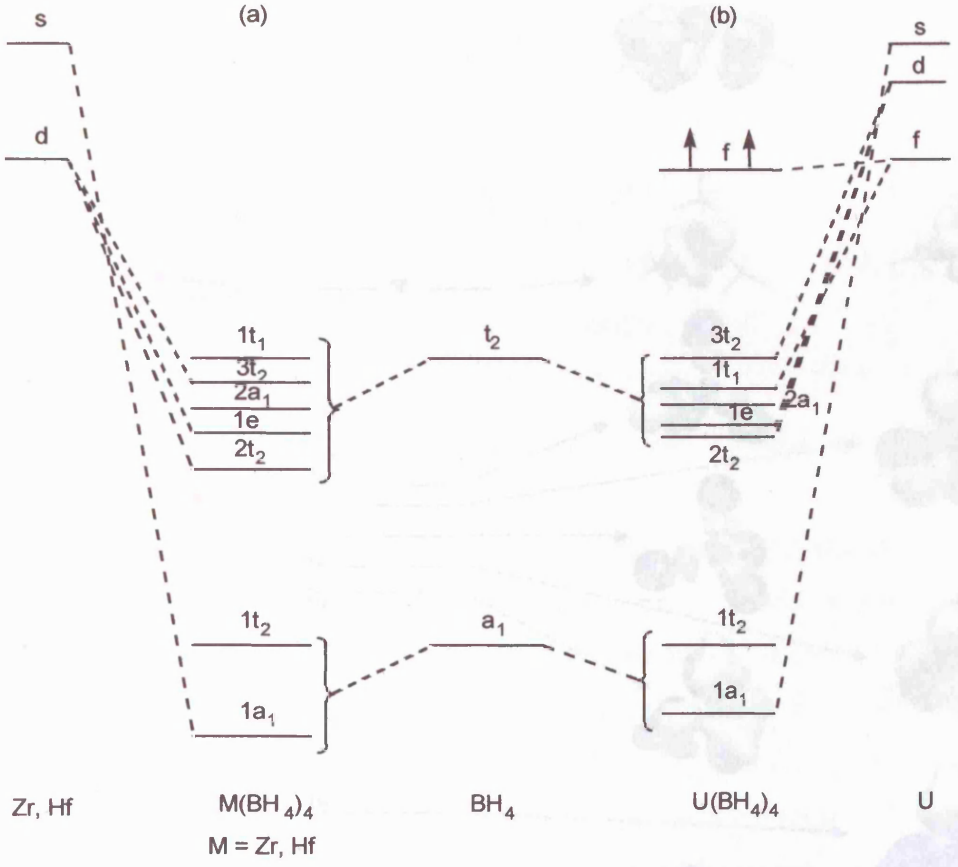

Figure 6.4: Qualitative MO energy level diagrams for (a) $Zr(BH_4)_4$ and $Hf(BH_4)_4$; and (b) $U(BH_4)_4$.

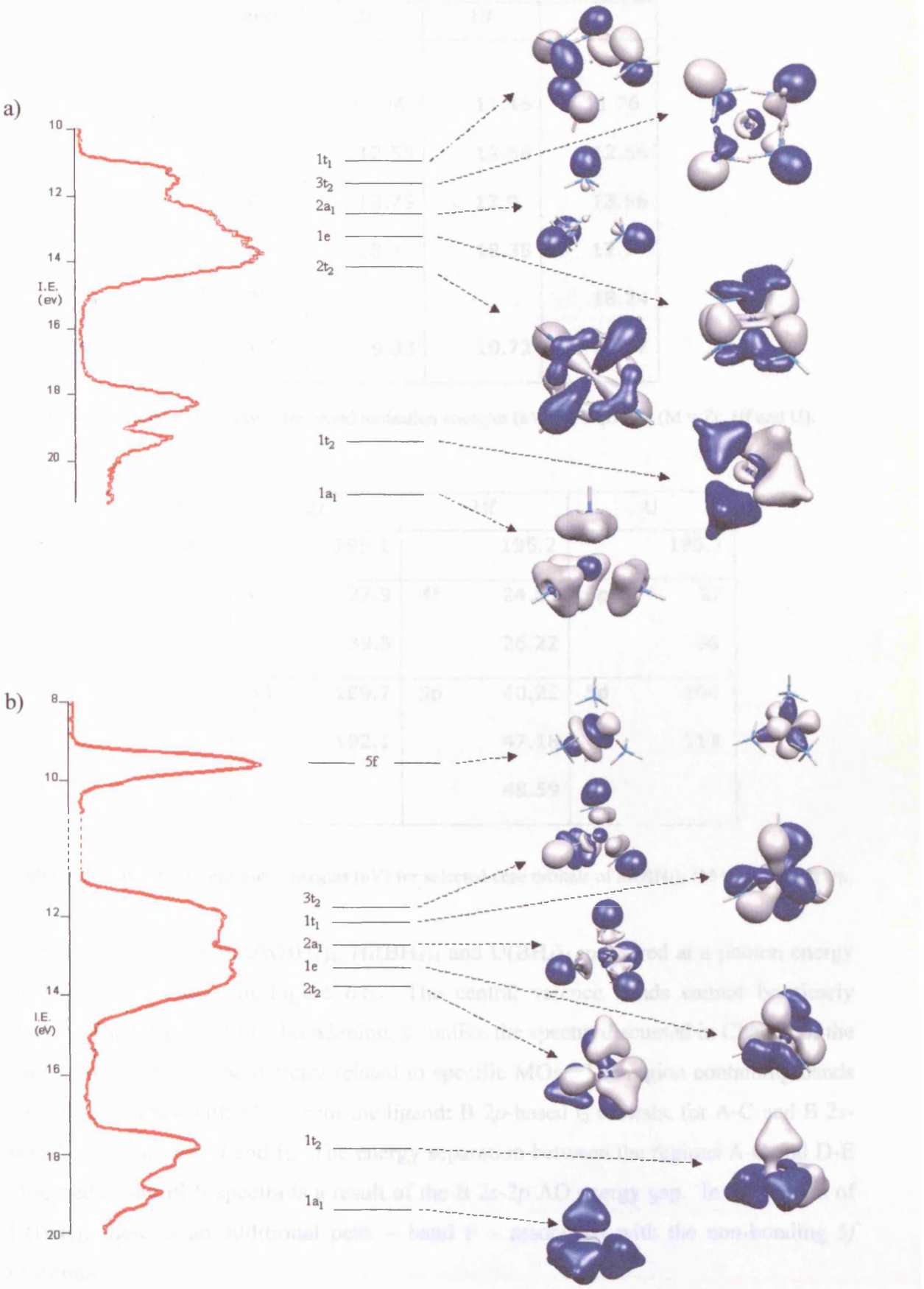

Figure 6.5: PES spectra of the valence electron binding energies, correlated with the calculated MO energy level diagram and associated iso-surfaces for (a) $Zr(BH_4)_4$ and (b) $U(BH_4)_4$.

Band	Zr	Hf	U
F			9.5
A	11.44	11.46	11.76
B	12.55	12.66	12.56
C	13.75	13.9	13.56
D	18.2	18.38	17.7
D'			18.24
E	19.33	19.72	18.97

Table 6.2: Experimentally determined ionisation energies (eV) for $M(BH_4)_4$ (M = Zr, Hf and U).

Core	Zr		Hf		U	
B 1s		195.1		195.2		195.1
M	4p	37.9	4f	24.55	6p	27
		39.5		26.22		36
	3d	189.7	5p	40.22	5d	104
		192.1		47.18		113
				48.59		

Table 6.3: Calculated ionisation energies (eV) for selected core orbitals of $M(BH_4)_4$ (M = Zr, Hf and U).

The valence spectra for $Zr(BH_4)_4$, $Hf(BH_4)_4$ and $U(BH_4)_4$ measured at a photon energy of 38 eV are shown in Figure 6.6. The central valence bands cannot be clearly distinguished owing to line broadening, so unlike the spectra discussed in Chapter 5, the bands cannot always be directly related to specific MOs. The region containing bands A-E is associated with MOs from the ligand: B 2*p*-based t_2 orbitals, for A-C and B 2*s*-based, a_1 orbital for D and E. The energy separation between the regions A-C and D-E observed in the PES spectra is a result of the B 2*s*-2*p* AO energy gap. In the spectra of $U(BH_4)_4$ there is an additional peak – band F – associated with the non-bonding 5*f* electrons.

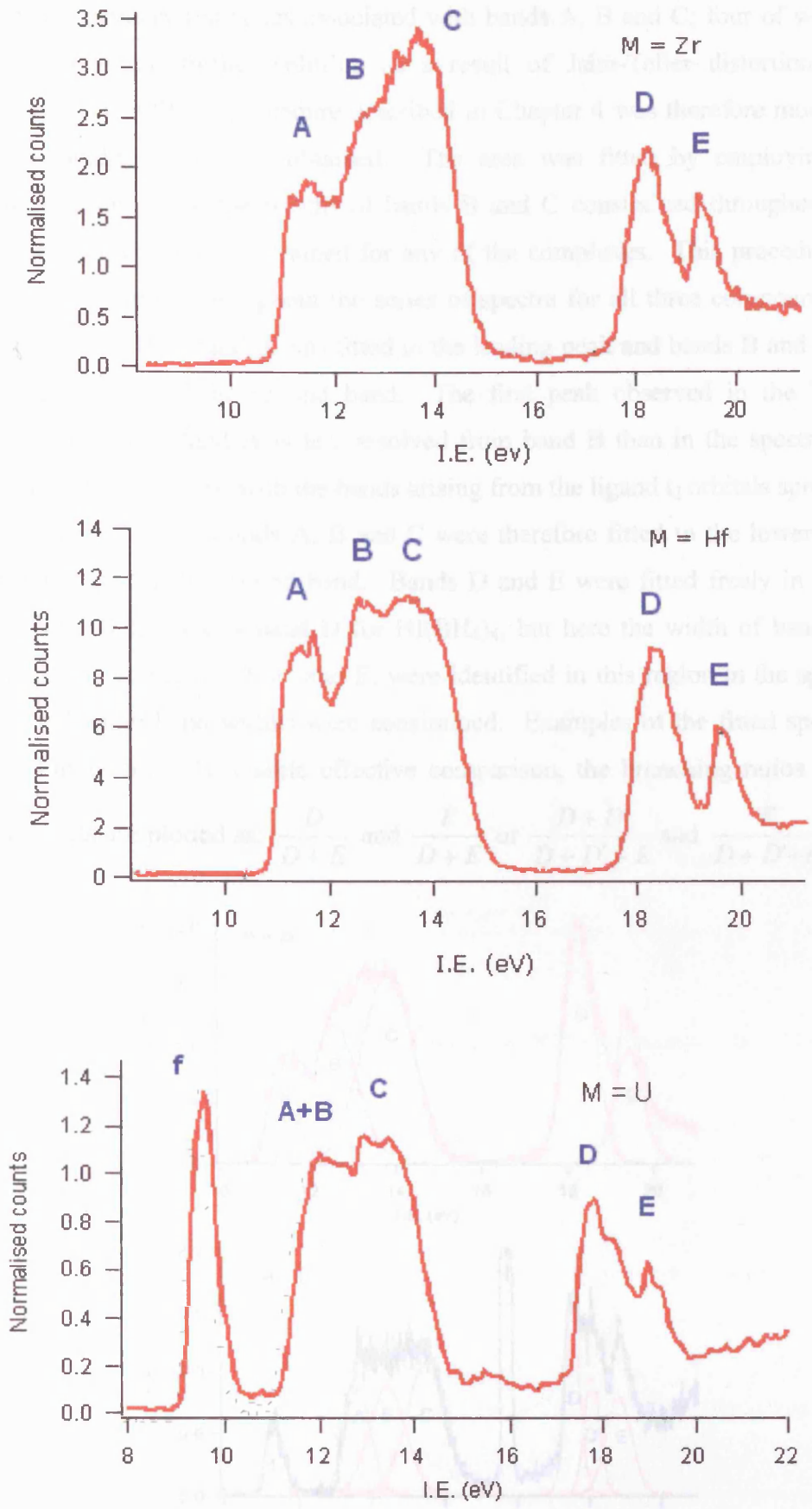

Figure 6.6: PES spectra for $M(BH_4)_4$ (M = Zr, Hf and U) measured at $h\nu$ = 38 eV.

There are five primary ion states associated with bands A, B and C; four of which are expected to undergo further splitting as a result of Jahn-Teller distortion of the molecular ion. The fitting procedure described in Chapter 4 was therefore modified to ensure comparable data were obtained. The area was fitted by employing three Gaussian functions, with the widths of bands B and C constrained throughout. The width of band A was not constrained for any of the complexes. This procedure gave constant peak positions throughout the series of spectra for all three compounds. For $Zr(BH_4)_4$ and $Hf(BH_4)_4$ band A was fitted to the leading peak and bands B and C to the low and high sides of the second band. The first peak observed in the $U(BH_4)_4$ spectrum is band F. Band A is less resolved from band B than in the spectra of the transition metal complexes, with the bands arising from the ligand t_2 orbitals spread over a smaller energy range. Bands A, B and C were therefore fitted to the lower, middle and upper regions of the second band. Bands D and E were fitted freely in the PES spectra of $Zr(BH_4)_4$, as was band D for $Hf(BH_4)_4$, but here the width of band E was constrained. Three bands; D, D' and E, were identified in this region in the spectra of $U(BH_4)_4$, and again band widths were constrained. Examples of the fitted spectra are shown in Figure 6.7. To enable effective comparison, the branching ratios of these two/three bands are plotted as: $\frac{D}{D+E}$ and $\frac{E}{D+E}$ or $\frac{D+D'}{D+D'+E}$ and $\frac{E}{D+D'+E}$.

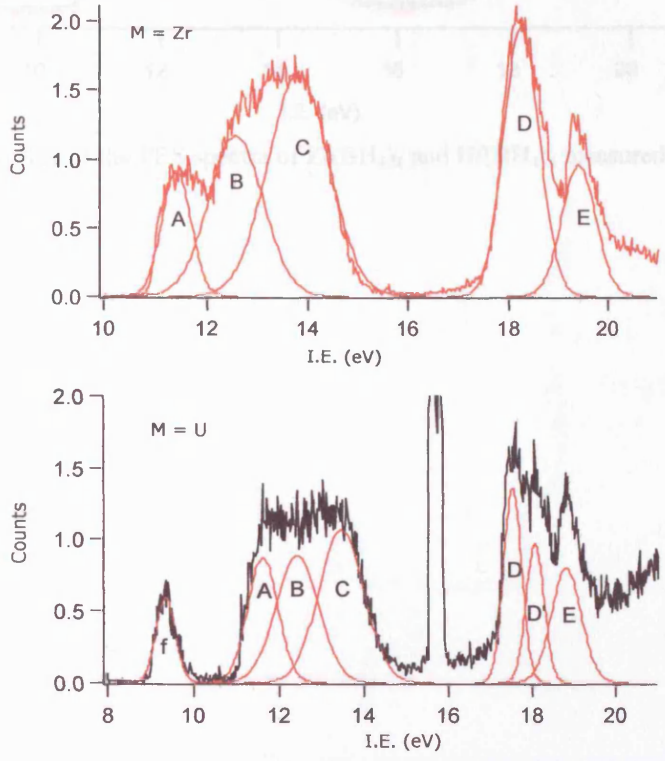

Figure 6.7: Time weighted PES spectra of $Zr(BH_4)_4$ and $U(BH_4)_4$ fitted with Gaussian functions.

6.3.1 The Valence Bands of $Zr(BH_4)_4$ and $Hf(BH_4)_4$

Overlaying the PES spectra of $Zr(BH_4)_4$ and $Hf(BH_4)_4$, as depicted in Figure 6.8, shows the main energetic difference to arise in band E, associated with the $1a_1$ orbital. This is the first indication that these complexes are not purely ionic. The $1a_1$ orbital has a higher ionisation energy in $Hf(BH_4)_4$ on account of its derivation from the BH_4 a_1 and the metal valence *s* orbitals; the Hf 6*s* orbital is more tightly bound than the Zr 5*s* orbital. There is a slightly lower calculated 6*s* contribution in this orbital, with the implied smaller overlap possibly reflecting its relative contraction. This is also seen in the 0.4 eV difference in calculated binding energy of the $1a_1$ orbitals for these two complexes reported in previous studies[256] and observed in this work. (Table 6.2)

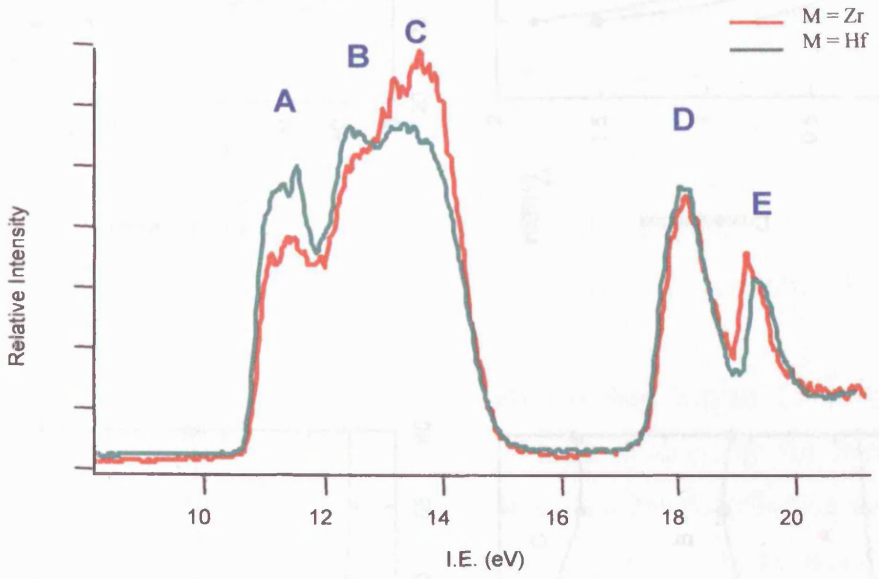

Figure 6.8: Overlay of the PES spectra of $Zr(BH_4)_4$ and $Hf(BH_4)_4$ measured at $h\nu$ = 38 eV.

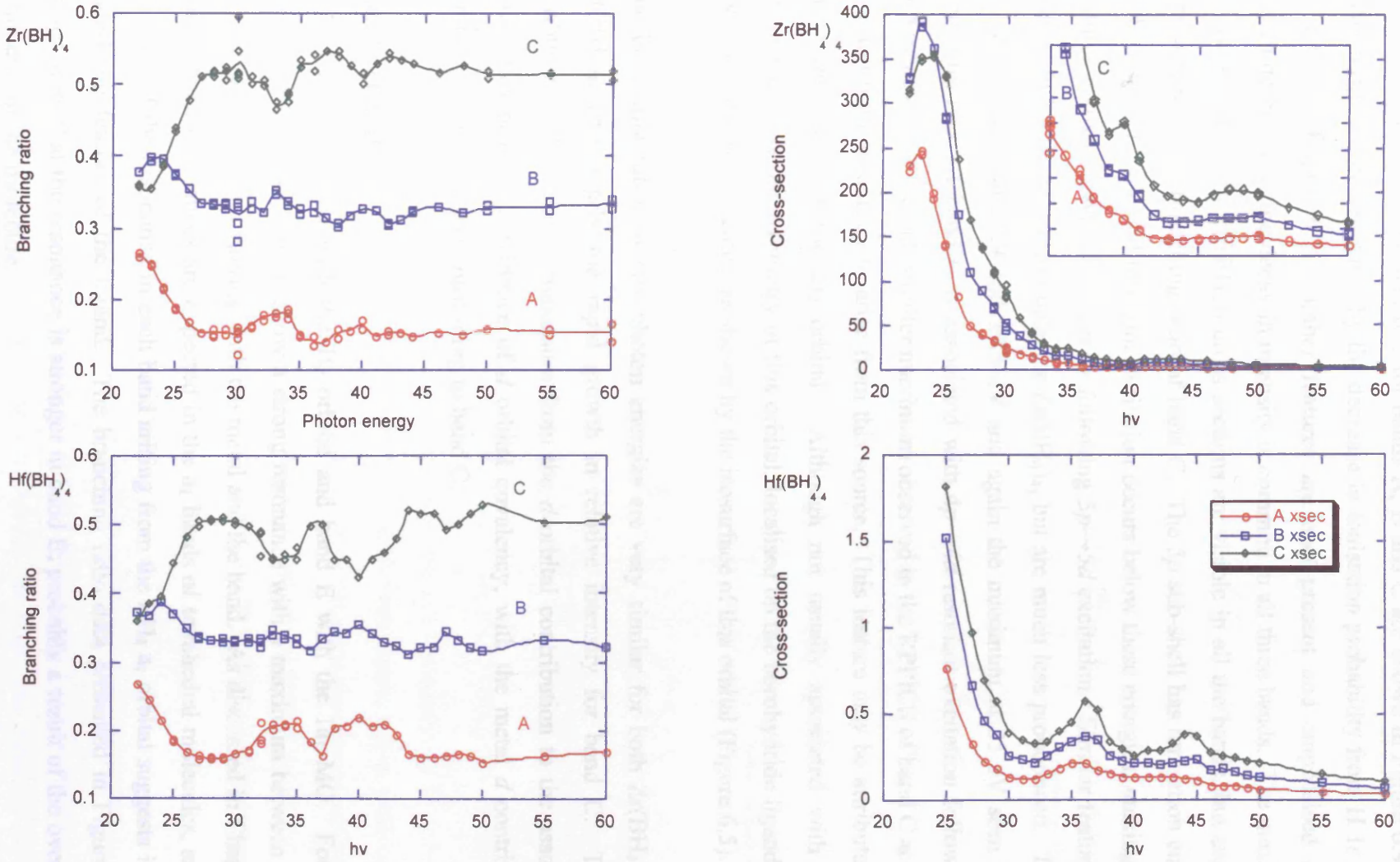

Figure 6.9: Branching ratios and cross sections for bands A, B and C of $Zr(BH_4)_4$ and $Hf(BH_4)_4$.

Bands A, B and C

The branching ratios and RPPICS for bands A, B and C are shown in Figure 6.9. The cross sections are dominated by the decrease in ionisation probability from H 1*s* and B 2*p* orbitals (Figure 6.3). Other features are also present and emphasised in the branching ratios, as the decay in intensity is common to all three bands. The maxima at 36 and 44 eV in the $Hf(BH_4)_4$ cross sections are visible in all the bands, but are most pronounced in the branching ratio of band C. The 5*p* sub-shell has ionisation energies of 40.3 and 47.2 eV and resonant excitation occurs below these energies, making these features consistent with SCK decay following $5p \rightarrow 5d$ excitation. Similar features are evident in the cross section data for $Zr(BH_4)_4$, but are much less pronounced. The 4*p* sub-shell ionises at 37.9 and 39.5 eV and again the maximum at 35 eV seen in the branching ratio of band C is associated with $4p \rightarrow 4d$ resonant excitation followed by SCK decay. The second, smaller maximum observed in the RPPICS of band C at 42 eV is at too high an energy to arise from this source. This feature may be attributed to a shape resonance of the $2t_2$ orbital. Although not usually associated with shape resonances, it is the symmetry of this orbital, localised on the borohydride ligands, that gives rise to this resonance, as shown by the isosurface of this orbital (Figure 6.5).

The branching ratios at low photon energies are very similar for both $Zr(BH_4)_4$ and $Hf(BH_4)_4$, particularly the rapid growth in relative intensity for band C. This is attributed to the delayed maximum from the *d* orbital contribution to the associated MOs, thus providing evidence of *d* orbital covalency, with the metal *d* contribution centring on the orbitals contributing to band C.

Bands D and E

Band D is associated with the $1t_2$ orbital and band E with the $1a_1$ MO. For both compounds, bands D and E show a strong resonance with a maximum between 30-35 eV, the exact position varying with the metal and the band. As discussed in Chapter 4, strong shape resonances are expected in the a_1 bands of tetrahedral molecules, and the presence of the resonance in each band arising from the BH_4 a_1 orbital suggests it is an underlying feature of the ligand. The branching ratio data presented in Figure 6.10 demonstrate that the resonance is stronger in band E; probably a result of the overall T_d symmetry of the molecule.

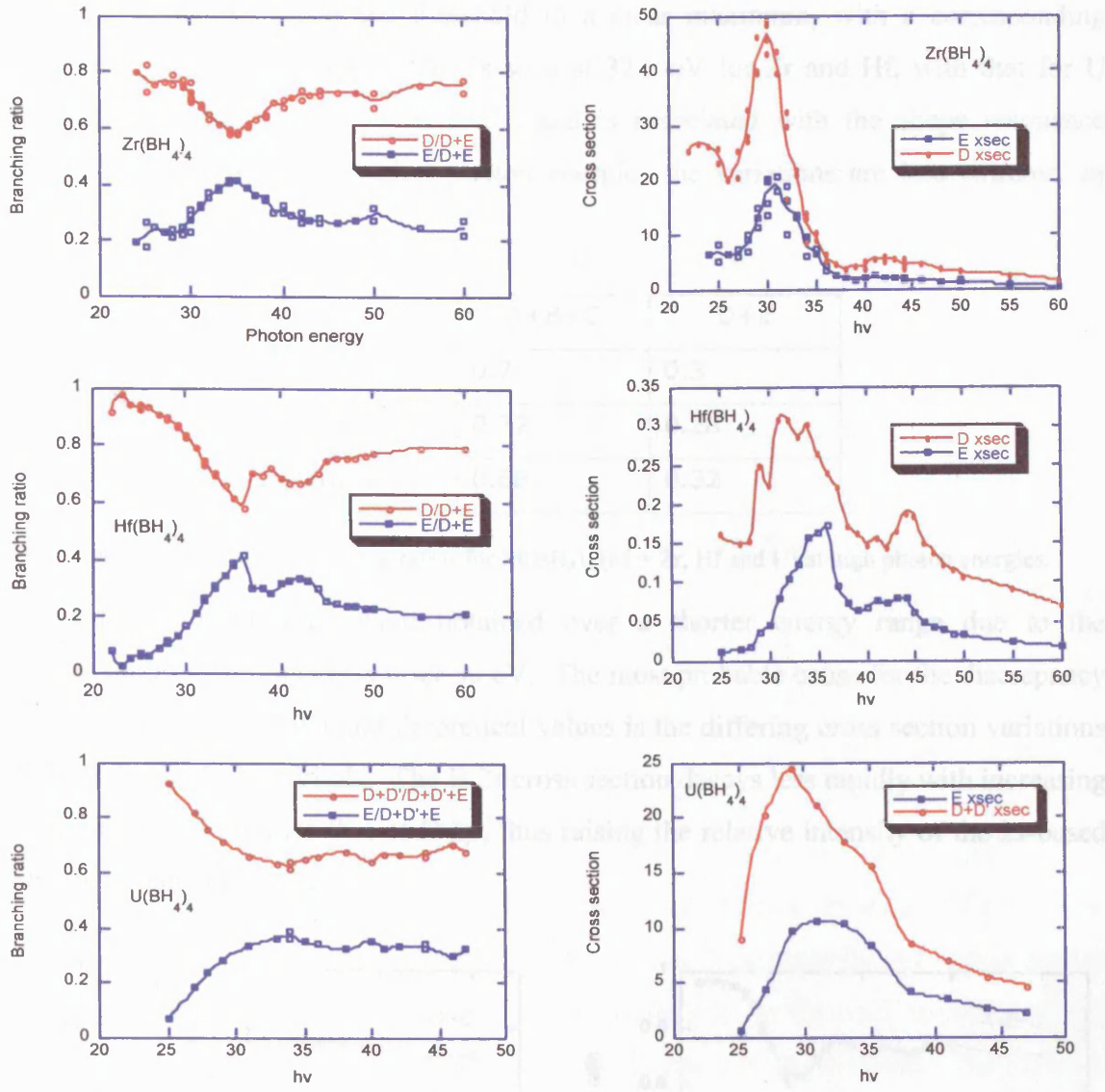

Figure 6.10: Branching ratios and cross sections of bands D, D' and E for $M(BH_4)_4$ (M = Zr, Hf and U).

The cross section of band D for $Hf(BH_4)_4$ shows additional resonances at 36 and 44 eV. That at 36 eV overlays the upper region of the shape resonance, but is visible in the branching ratio. These features are assigned to $5p \rightarrow 5d$ giant resonances, indicating a $5d$ contribution to the $1t_2$ MO. These resonances are not detected in the spectra of $Zr(BH_4)_4$, but may be masked by the shape resonance. The peak at 29 eV is unassigned.

Comparison of the Branching Ratios

The relative areas of bands A+B+C and D+E for all three complexes are shown in Figure 6.11. The statistical ratio of the number of orbitals from the proposed MO diagram contributing to the two regions is 0.75:0.25 (i.e. 3:1). The observed branching ratios are not consistent with this ratio. The D+E branching ratio increases rapidly from

a very low intensity near the threshold to a clear maximum, with a corresponding minimum in that of A+B+C. This is seen at 32.5 eV for Zr and Hf, with that for U somewhat broader centred at 31.2 eV, and is associated with the shape resonance discussed previously. At higher photon energies the variations are less extreme, as shown in Table 6.4.

	A+B+C	D+E
$Zr(BH_4)_4$	0.7	0.3
$Hf(BH_4)_4$	0.72	0.28
$U(BH_4)_4$	0.68	0.32

Table 6.4: Observed branching ratios for $M(BH_4)_4$ (M = Zr, Hf and U) at high photon energies.

The values for $U(BH_4)_4$ were obtained over a shorter energy range due to the curtailment of data collection after 50 eV. The most probable cause for the discrepancy between the experimental and theoretical values is the differing cross section variations of the B 2*s* and B 2*p* orbitals. The B 2*s* cross section decays less rapidly with increasing photon energy than does that of B 2*p*, thus raising the relative intensity of the 2*s*-based orbitals of bands D and E.

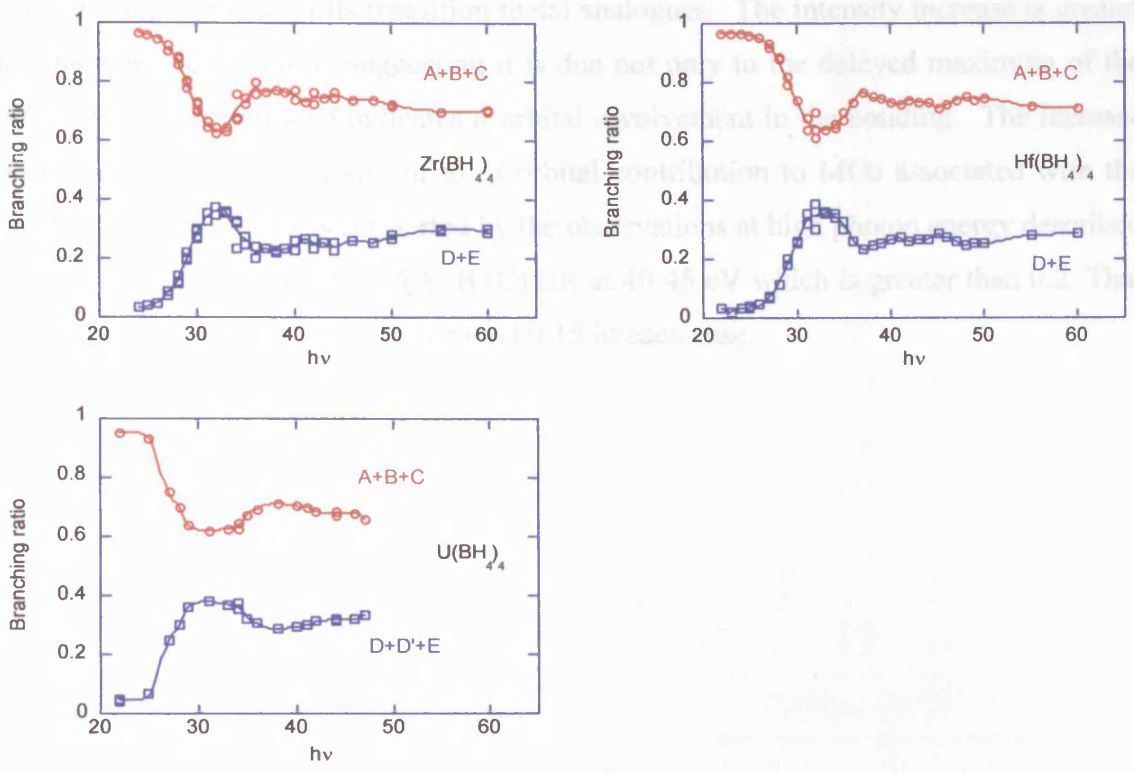

Figure 6.11: Branching ratios of A+B+C *vs.* D+E for $M(BH_4)_4$ (M = Zr, Hf and U).

6.3.2 The Valence Bands of $U(BH_4)_4$

Bands F, A, B and C

The branching ratios and RPPICS of the bands are given in Figure 6.12. The feature of most obvious note is the rise in intensity of band F with increasing photon energy. This is observed in both the cross section and branching ratio reflecting the delayed maximum associated with *f* orbitals. Band F is therefore assigned to the non-bonding U 5*f* orbitals.

Band A also exhibits a perceptible increase in intensity between 30-35 eV, consistent with U 5*f* orbital contribution to the MOs associated with this band. However, the U 6*p* sub-shell ionisation energies are 27 and 36 eV, so giant resonance features just below these energies were anticipated in bands associated with MOs having U 6*d* orbital content. The second of these features is coincident with the rise in *f* orbital cross section, complicating the interpretation of this low energy region. The cross sections of both bands B and C show a sharp intensity increase at 35 eV. Figure 6.13 shows the change in relative intensities of bands A, B and C over the region of U 6*p*→6*d* resonant excitation. The maxima observed in bands B and C are assigned to giant resonances, a conclusion supported by comparison of the intensity of band C in the 20-27 eV region for $U(BH_4)_4$, to those of its transition metal analogues. The intensity increase is greater for the actinide complex, suggesting it is due not only to the delayed maximum of the 6*d* cross section, but also indicates *d* orbital involvement in the bonding. The increase observed in band A is assigned to 5*f* orbital contribution to MOs associated with the band. This assignment is supported by the observations at high photon energy described below, and the value of the A/(A+B+C) BR at 40-45 eV which is greater than 0.2. That found for both M = Zr and Hf is around 0.15 in each case.

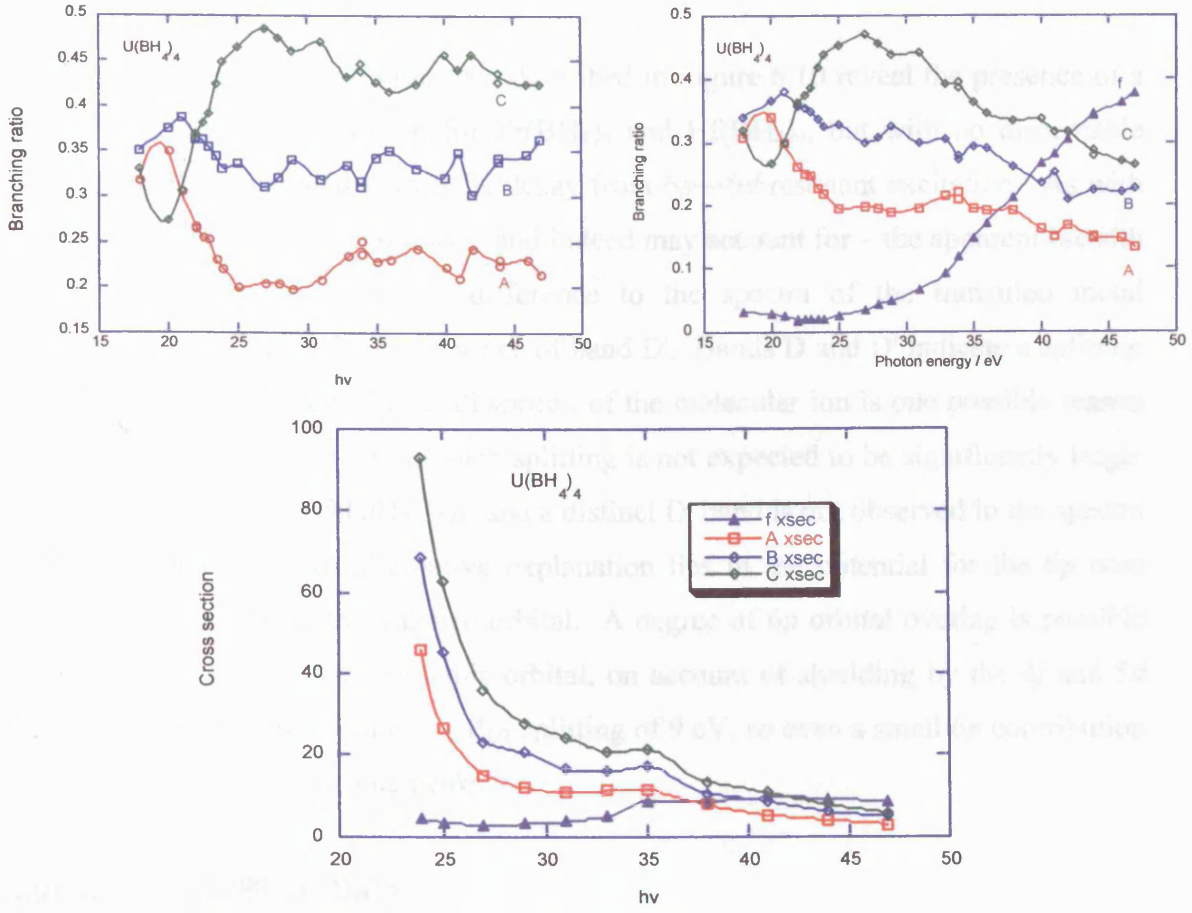

Figure 6.12: Branching ratios and cross sections for bands F, A, B and C for $U(BH_4)_4$.

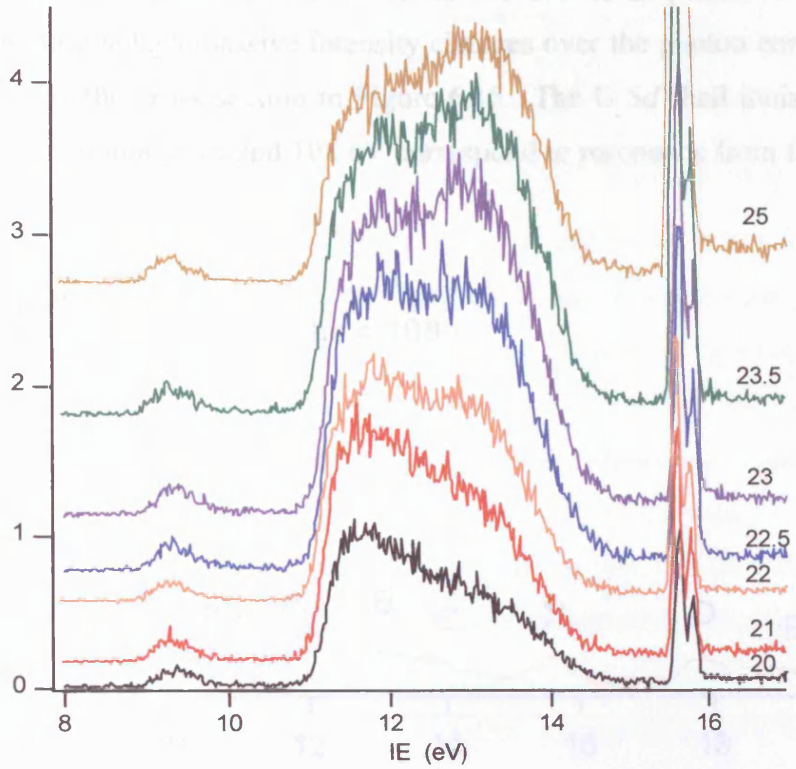

Figure 6.13: PES spectra of $U(BH_4)_4$ showing changes in bands A,B and C over the 20-25 eV photon energy range.

Bands D and E

The RPPICS and branching ratio data described in Figure 6.10 reveal the presence of a strong shape resonance as seen for $Zr(BH_4)_4$ and $Hf(BH_4)_4$, but with no discernable giant resonance associated with SCK decay from $6p \rightarrow 6d$ resonant excitation. As with $Zr(BH_4)_4$, this may be disguised by – and indeed may account for – the apparent breadth of the shape resonance. A key difference to the spectra of the transition metal complexes in this region is the presence of band D'. Bands D and D' indicate a splitting of the $1t_2$ orbital set. Jahn-Teller distortion of the molecular ion is one possible reason for this observation. The size of such splitting is not expected to be significantly larger than that of $Zr(BH_4)_4$ and $Hf(BH_4)_4$, and a distinct D' band is not observed in the spectra of these complexes. An alternative explanation lies in the potential for the 6*p* core orbitals to contribute to the valence orbital. A degree of 6*p* orbital overlap is possible because of the diffuse nature of this orbital, on account of shielding by the 4*f* and 5*d* electrons. The 6*p* core has a $P_{3/2} - P_{1/2}$ splitting of 9 eV, so even a small 6*p* contribution could give rise to two separate peaks.

High Energy $U(BH_4)_4$ Data

The principal features of the PES spectra of $U(BH_4)_4$ recorded at higher photon energies are the band intensities and the observation of two additional peaks, shown in Figure 6.14. The F band displays massive intensity changes over the photon energy range 90-120 eV, shown by the cross section in Figure 6.15. The U 5*d* shell ionises at 104 and 113 eV, and the maxima at 98 and 108 eV correspond to resonance from the J = 5/2 and 3/2 core holes.

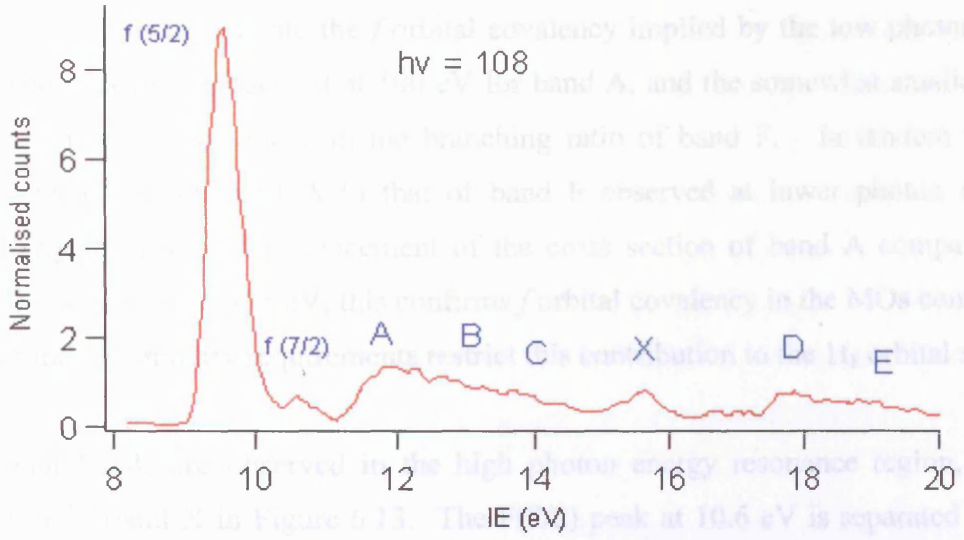

Figure 6.14: PES spectrum for $U(BH_4)_4$ at $h\nu$ = 108 eV.

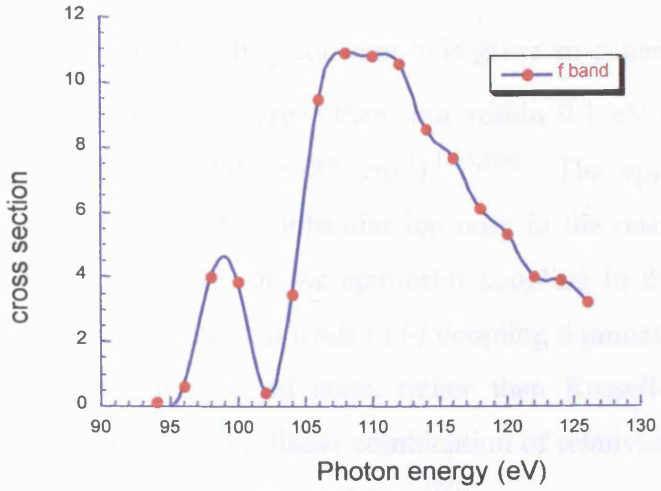

Figure 6.15: Cross section of band F for $U(BH_4)_4$ over the 90-130 eV range.

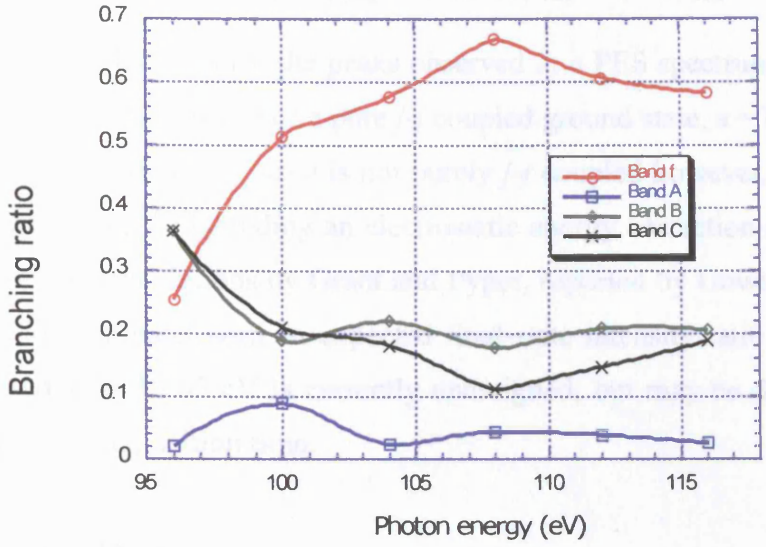

Figure 6.16: Branching ratios of bands F, A, B and C for $U(BH_4)_4$ over the 96-116 eV range.

The intensities of bands A-E are extremely low, but branching ratios for A, B and C were extracted to investigate the *f* orbital covalency implied by the low photon energy data. The maximum observed at 100 eV for band A, and the somewhat smaller one at 108 eV, correspond to those in the branching ratio of band F. In tandem with the similar behaviour of band A to that of band F observed at lower photon energies, particularly the resonant enhancement of the cross section of band A compared with bands B and C from 30-35 eV, this confirms *f* orbital covalency in the MOs contributing to this band. Symmetry requirements restrict this contribution to the $1t_1$ orbital set.

Additional bands are observed in the high photon energy resonance region, and are labeled F(7/2) and X in Figure 6.13. The F(7/2) peak at 10.6 eV is separated by 1 eV from band F, and is assigned to the $^2F_{7/2}$ ion state. With the spin orbit coupling given by

$\frac{7}{2}\zeta_{5f}$ where ζ_{5f} is the spin-orbit coupling constant, this gives an experimental value of 0.286 eV for ζ_{5f} in U(IV); somewhat larger than, but within 0.1 eV of, the literature values of 0.2365 and 0.221 eV(1908, 1783 cm^{-1}).[275;276] The appearance of this additional band associated with the $5f^1$ molecular ion only in the resonance-enhanced high photon energy region is a result of the spin-orbit coupling in the triplet ground state. The high nuclear charge of uranium leads to *j-j* coupling dominating the nature of the perturbation observed in the ground state, rather than Russell-Saunders (L-S) coupling. When described in terms of a linear combination of relativistic configuration states, the initial state $|I\rangle$ is given in Equation 6.2 as:[271]

$$|I\rangle_{J=4} = a\left|f^2_{5/2}\right\rangle_{J=4} + b\left|f_{5/2}f_{7/2}\right\rangle_{J=4} + c\left|f^2_{7/2}\right\rangle_{J=4} \qquad \textbf{[6.2]}$$

The final-state intensity ratio for the peaks observed in a PES spectrum for $^2F_{5/2}$:$^2F_{7/2}$ is given by: $(2a^2 + b^2):(2c^2 + b^2)$. For a pure *j-j* coupled ground state, a = 1, b = 0 and c = 0, giving a 1:0 ratio. The ground state is not purely *j-j* coupled however, but experiences intermediate coupling,[217] including an electrostatic energy correction arising from L-S coupling. Previous calculations by Grant and Pyper, reported by Downs et al.[271] show the $^2F_{5/2}$ state to dominate, with an expected final-state intensity ratio for $^2F_{5/2}$:$^2F_{7/2}$ of *ca.* 40:1. Band X at 15.65 eV is currently unassigned, but may be due to N_2, visible because of the long acquisition time.

6.3.3 The Core Bands

The B 1*s* ionisation energy was invariant throughout the series of complexes, at 195 eV. This indicates it is a purely core orbital. Core ionisations were also measured for the Zr 4*p* and 3*d*, Hf 4*f* and 5*p* and the U 6*p* and 5*d* orbitals, with the results shown in Table 6.3. Selected spectra are shown in Figures 6.17 and 6.18. The 4*p* ionisations of the Zr core were observed at 37.9 and 39.5 eV, a few eV higher than the maxima observed in the cross section plots attributed to $p \rightarrow d$ resonance. This is consistent with the assignments, as the energies required for $p \rightarrow d$ excitation are less than those required for *p* ionisation. This is also noted in the $Hf(BH_4)_4$ and $U(BH_4)_4$ spectra.

Figure 6.18 shows the 4*f* and 5*p* bands of Hf and their change in intensity over the photon energy range of 46-60 eV. A fixed kinetic energy band (KE = 11.2 eV) was also observed in the spectra.

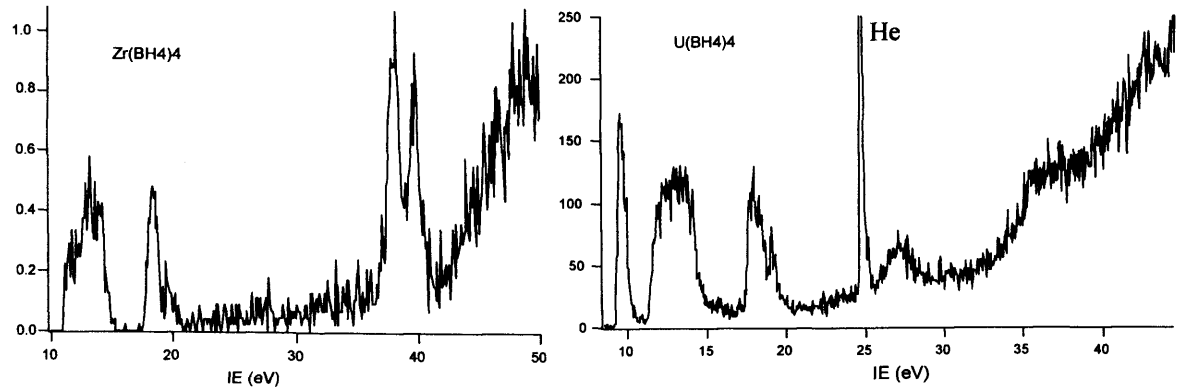

Figure 6.17: Core *p* ionisations of $Zr(BH_4)_4$ and $U(BH_4)_4$.

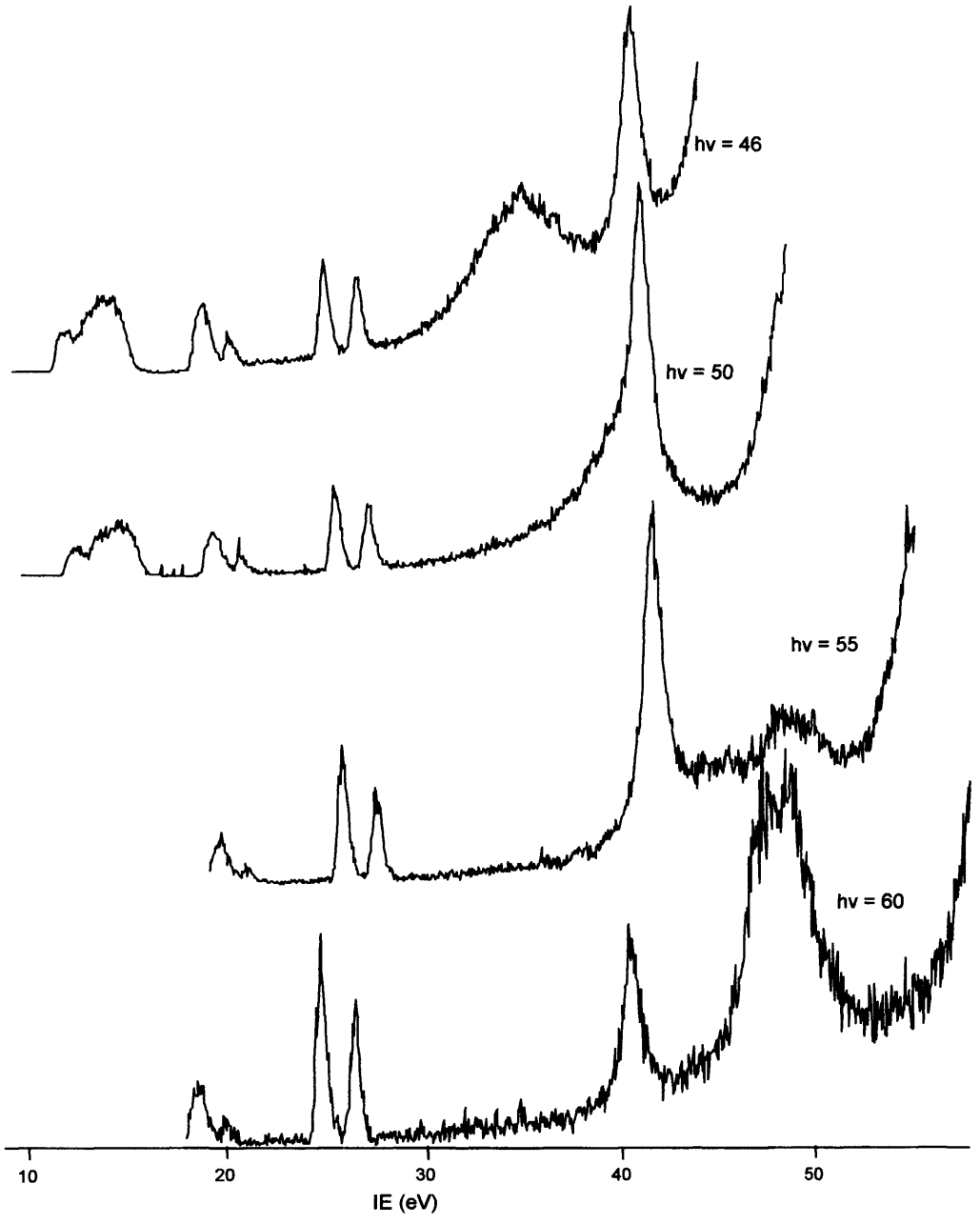

6.18: Core spectra of $Hf(BH_4)_4$ at 46, 50, 55 and 60 eV; showing the 4*f* and 5*p* bands together with an Auger peak.

6.3.4 Absorption Spectra of $Zr(BH_4)_4$

Figure 6.19 shows an absorption spectrum recorded for the Zr 4*p* edge of $Zr(BH_4)_4$ in the 24 to 60 eV region. It can be seen that in addition to the leading edge at 35.5 eV, there are features preceding it at 32.5 eV and 33.8 eV. Additional structure to the leading edge is seen at 36.7 eV, followed by a broad hump after the near edge at around 38.4 eV. The Zr 4*p* edge is expected to have two bands, corresponding to the $^2P_{3/2}$ and $^2P_{1/2}$ core holes, with a literature value for this splitting of 1.4 eV. Given the high oxidation state of the zirconium metal centre, these absorptions were expected at higher energies than the atomic values of 27.1 eV and 28.5 eV.[247] The experimental observations presented in Table 6.2 indicate peaks are expected at 37.9 and 39.5 eV, with a 1.6 eV split.

At 35.5 eV, the leading edge of the spectrum occurs at significantly lower energy than the calculated $^2P_{3/2}$ core hole, as does the additional structure at 36.7 eV. They are close to the cross-section maximum observed in band C (Figure 6.8), assigned to a $p \rightarrow d$ resonance followed by SCK decay. Calculations predict a 4*d* contribution to the 1e and all the t_2 MOs. These features are therefore attributed to excitation to the unoccupied *d* levels of e and t_2 symmetry. The pre-edge features at 32.5 eV and 33.8 eV are also not assigned to primary Zr 4*p* excitations. The absorptions coincide with shape resonance features observed in bands D and E, and are thought to be associated with them. Similarly, the broad, intense absorption around 41.3 eV coincides with a maximum in the cross-section of band C attributed to a shape resonance. This prevents definitive assignment of the feature at 38.4 eV, which may be due to the $^2P_{3/2}$ ionisation.

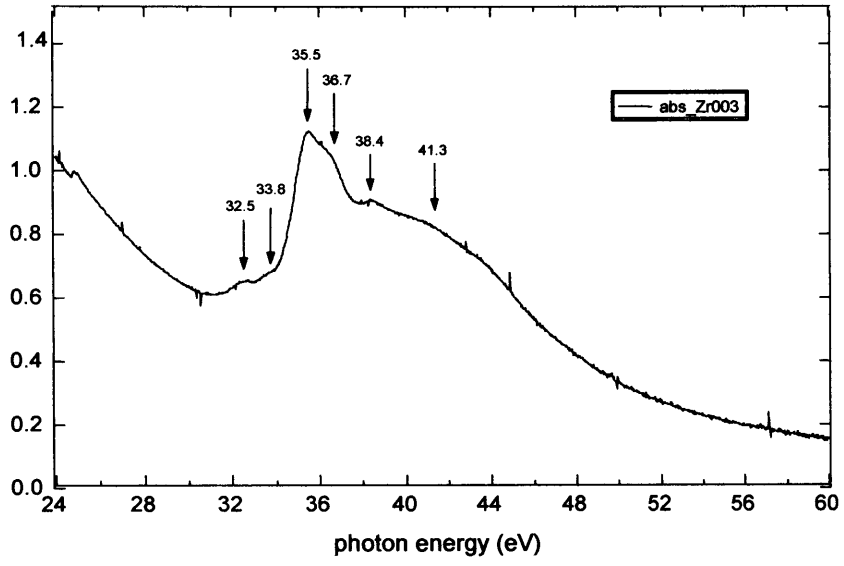

Figure 6.19: Absorption spectrum of the Zr 4*p* edge in $Zr(BH_4)_4$.

6.3.5 The Calculated Model

The DFT calculations conducted by Prof. Jennifer Green provided a good basis for comparison with, and confirmation of, the interpretation of the spectra recorded in this study.

The Kohn Sham orbital energies, e_i (eV) and calculated ionisation energies (eV) for the valence and selected core orbitals were calculated for ion states formed by creating a hole in the occupied valence orbitals, and are given in Table 6.5. The e_i values were used to generate the iso-surfaces shown earlier in Figure 6.4 and are included to enable comparison of the $1t_1$ and $3t_2$ values for $U(BH_4)_4$. The IEs differ from those previously reported for $Zr(BH_4)_4$ by Hitchcock et al. using LCAO-HFS calculations,[256] but apart from the $1t_1$ orbital the difference is no more than 0.7 eV.

	Zr		Hf		U	
	e_i	IE	e_i	IE	e_i	IE
F					-5.21 -5.51	8.44 8.74
$1t_1$	-8.44	10.97	-8.33	10.91	-9.09	11.53
$3t_2$	-8.86	11.29	-8.87	11.34	-8.55	10.87
$2a_1$	-9.3	11.73	-9.45	11.91	-9.25	11.59
2e	-9.84	12.35	-9.76	12.32	-9.71	12.14
$2t_2$	-10.39	12.88	-10.36	12.91	-9.89	12.27
$1t_2$	-13.95	16.57	-13.98	16.65	-13.61	16.12
$1a_1$	-15.1	17.6	-15.41	18.06	-14.75	17.26

Table 6.5: Kohn Sham orbital energies and calculated ionisation energies for $M(BH_4)_4$ (M = Zr, Hf and U).

Given the composite nature of the ligand-related t_2 bands A, B and C; an exact comparison of calculated and experimental ionisation energies is not possible for all the ion states. However, various points emerged on comparing the ionisation energy values in Table 6.5 with the band positions in Table 6.2. The agreement in absolute values is superior for M = Zr and Hf than M = U. The difference increases with increasing IE, and for the $^2a_1$ IE and band E it is 1.63 eV for $Zr(BH_4)_4$ and 1.66 eV for $Hf(BH_4)_4$. For M = U the difference for the $^2t_2$ ionisation and band A is 1 eV and for the $^2a_1$ IE and band E 1.71 eV. Given the general underestimate of IE however, many features of the spectra are well reproduced by the calculations. The spacings of bands A, B and C for all three compounds correspond well with the grouping of ion states associated with the

BH_4 t_2 ionisations, with the separations for M = U significantly less than for M = Zr and Hf. For bands D and E, the assignments are clear-cut and the calculations reflect the lower IE for M = U and the increase in the D-E separation for Hf (1.34 eV experimental, 1.41 eV calculated) compared to Zr (1.13 eV experimental, 1.03 eV calculated) and U (1.09 eV experimental, 1.14 calculated).

One feature of particular note is the reversal in order of the $1t_1$ and $3t_2$ ionisations in the Kohn Sham orbital energies and the calculated ionisation energies. This is an illustration of the approximate nature of Koopmans' Theorem. Therefore the ordering shown in the Kohn Sham orbital energies is adopted, which is in agreement with that given by Rösch and Hohl.[273] The experimental evidence that band A is related at least in part to the $1t_1$ orbitals can support either orbital ordering.

The calculations also support the proposed M–B bonding interaction described above (see Table 6.6), with the Muliken population analysis giving an atom-atom population matrix with non-zero values for the M–B moiety. The lower values for B–H_b vs. B–H_t reflect the lower B–H bond order for the bridging hydrides:

	Zr	U
M–B	0.1395	0.0548
M–H_b		0.0440
M–H_t	-0.0309	-0.0203
B–B	0.0104	0.0012
B–H_b	0.2771	0.1322
B–H_t	0.3252	0.1806

Table 6.6: Selected atom-atom population matrix values for $M(BH_4)_4$ (M = Zr and U).

The calculated atomic orbital contributions to the MOs are given in Table 6.7. The metal *d* orbital content suggested by experimental observation of resonance features is confirmed by the calculations. The placement of the $2t_2$ and 1e orbitals is corroborated by the calculations, indicating they have the highest metal *d* orbital content and the strongest associated resonances being observed in band C.

		H 1*s*	B 2*s*	B 2*p*	M (*n*-1)*d*	M *ns*	M *np*	M(*n*-2)*f*	M (*n*-1)*p*
Zr	$1a_1$	72	21			19			
	$1t_2$	54	28		7		6		
	$2t_2$	53		24	18				
	1e	45		28	23				
	$2a_1$	59	7	25		3			
	$3t_2$	55		31	2				
	$1t_1$	56		32					
Hf	$1a_1$	73	22			16			
	$1t_2$	53	27		7		7		
	$2t_2$	49		25	19				
	1e	44		28	23				
	$2a_1$	56	7	27		2			
	$3t_2$	56		28	2				
	$1t_1$	56		32					
U	$1a_1$	78	24						
	$1t_2$	55	26		8		3		3
	$2t_2$	61		23	14				
	1e	54		24	18				
	$2a_1$	57	5	32					
	$3t_2$	58		31					
	$1t_1$	50		26				13	
	f							96	

Table 6.7: Percentage AO contributions to the occupied valence MO of $M(BH_4)_4$ (M=Zr, Hf and U), as determined by Muliken population analysis.

The orbital mixing in $U(BH_4)_4$ is interesting, as the calculations also indicate the *5f*, *7p* and *6p* orbital mixing suggested by the experimental data. The $1t_2$ orbitals are nodally better suited to mixing with metal *p* orbitals than are other t_2 orbitals. Mixing occurs to a small extent with both the valence *7p* and the semi-core *6p* orbitals, the latter which causes the D, D' split due to spin-orbit coupling.[206;243] The *5f* contribution to the $1t_1$ orbital is in agreement with both the cross section data observed for band A and its lower energy compared to that in the Zr and Hf complexes, which leads to the merging of band A with band B. Equally, the gap observed between band A and band B in the PES spectra of $Zr(BH_4)_4$ and $Hf(BH_4)_4$ illustrates the strictly non-bonding nature of the borohydride $1t_1$ orbitals.

The metal *s* orbital is calculated to make a significant contribution to the $1a_1$ MOs of $Zr(BH_4)_4$ and $Hf(BH_4)_4$: in Figure 6.4 the surface around the Zr atom is an inner lobe of the 5*s* orbital. The contribution of the Hf 6*s* orbital is slightly less than that of Zr 5*s*; hence the observed stabilisation of orbitals associated with band E in $Hf(BH_4)_4$ compared to those in $Zr(BH_4)_4$ originates from the relativistic stabilisation of the 6*s* orbital. The diffuse nature of the U 7*s* orbital results in only a very small overlap with the ligand orbitals, leading to a negligible contribution to the $1a_1$ orbital.

Spin-orbit calculations were performed on $U(BH_4)_4$ and the resulting orbital energies given in Table 6.8. Little variation is found in the energies calculated, although it is interesting to note that the two *f* electrons are paired in an $e_{1/2}$ orbital with spin-orbit coupling. The 1t orbital is split by 0.52 eV into a $u_{3/2}$ and an $e_{5/2}$ orbital, in good agreement with the experimentally observed separation between the D and D' bands of 0.54 eV.

Without spin-orbit coupling		With spin-orbit coupling	
Orbital symmetry	Energy	Energy	Orbital symmetry
f	-5.21, -5.51	-5.16	$e_{1/2}$
$3t_2$	-8.55	-8.44	$u_{3/2}$
		-8.89	$e_{5/2}$
$1t_1$	-9.09	-9.10	$u_{3/2}$
		-9.11	$e_{1/2}$
$2a_1$	-9.25	-9.31	$e_{1/2}$
1e	-9.71	-9.76	$u_{3/2}$
$2t_2$	-9.89	-9.90	$u_{3/2}$
		-10.02	$e_{5/2}$
$1t_2$	-13.61	-13.47	$u_{3/2}$
		-13.99	$e_{5/2}$
$1a_1$	-14.75	-14.79	$e_{1/2}$

Table 6.8: Comparison of orbital energies (eV) of $U(BH_4)_4$ with and without spin-orbit coupling.

6.4 Conclusions

This chapter has explored the electronic structures of the tetrakis(tetrahydroborates) of zirconium, hafnium and uranium through the application of variable energy photoelectron and absorption spectroscopy, with the experimental results compared to calculated values. It has been established that:

- The PES spectra of $Hf(BH_4)_4$ and $Zr(BH_4)_4$ are very similar, with bands A-D occurring at similar energies and spacings. The only significant difference is observed in band E, with that of $Hf(BH_4)_4$ having a higher ionisation energy than that of $Zr(BH_4)_4$, reflecting the more tightly bound nature of the 6*s* orbital.

- The cross sections of bands A, B and in particular C for both *d* block compounds show evidence of *d* orbital covalency, with maxima consistent with SCK decay resulting from $p \rightarrow d$ resonant excitation. The absorption spectra of the Zr 4*p* edge provide evidence for this resonant process. Resonant features at 36 and 44 eV in the cross section in band D for $Hf(BH_4)_4$ indicate a 5*d* contribution to the $1t_2$ molecular orbital. The photoelectron cross section of band C of $U(BH_4)_4$ also shows a feature consistent with $6p \rightarrow 6d$ resonance.

- The PES spectrum of $U(BH_4)_4$ is significantly different. In addition to the presence of band F, arising from the 5*f* electrons, there is the splitting of band D and D' and a greater proximity of band A to bands B and C. The observation of bands D and D' shows a small degree of mixing of the $1t_2$ molecular orbital with the core 6*p* orbitals, the splitting being a result of the core consisting of $P_{3/2}$ and $P_{5/2}$ states from spin-orbit coupling. The relative increase in ionisation energy of band A, associated with the $1t_1$ orbital, combined with the maxima in the branching ratio of this band corresponding to those observed for band F, are strong indications of 5*f* orbital covalency.

- Of particular note in the high energy PES spectrum of $U(BH_4)_4$, is the presence of a small feature associated with the normally unobserved $F_{7/2}$ state of the 5*f* electrons.

- The calculated model for $U(BH_4)_4$ indicates involvement of the 5*f*, 5*d* and 6*p* orbitals in the metal-ligand bonding of the molecule, in agreement with experimental

observations. The calculated 13% 5*f* contribution to the symmetrically compatible $1t_1$ orbital results in the reversal in order of the $1t_1$ and $3t_2$ orbitals as calculated for $Zr(BH_4)_4$ and $Hf(BH_4)_4$. The calculated degree of 5*f* contribution may be excessive, indicated by the differing ordering in the calculated IE and Kohn Sham orbital energies and the experimental evidence linking band A to the $1t_1$ orbitals alone. Hence, no firm conclusion can be drawn as to whether the HOMO is indeed the $1t_1$ or the $3t_2$ orbitals.

- The calculated model for the zirconium and hafnium compounds indicates *d* character in the $1t_2$ orbital, as observed for $Hf(BH_4)_4$. The model shows *d* content for the $3t_2$, 1e and $2t_2$ orbitals, in good agreement with the experimental data, and particularly with the ordering of the orbitals of greatest *d* character in the region of band C.

- The calculations and experimental data each indicate that the molecules are not completely ionic, with the *d* – and *f* for $U(BH_4)_4$ – contributions clearly observed in the experimental cross sections of bands C and A, respectively. The positive values of the calculated atom-atom populations of M–H_b, and interestingly M–B, are strong indicators of some degree of covalency in the complexes.

- The molecules of reduced *T* symmetry $Hf(BH_4)_4$ and $Zr(BH_4)_4$ share the same non-bonding, ligand localised HOMO as OsO_4; $1t_1$, but the lower-lying valence orbitals of 1e and $2t_2$ are reversed. Despite having the same molecular symmetry as OsO_4, $U(BH_4)_4$ does not share the same valence molecular orbital ordering.

Summary

Overview and Future Research

The reactivity of a transition metal centre is the result of a combination of a number of factors, including the intrinsic properties of the metal and the type, number and bonding modes of the ligands. In addition to their academic interest, an understanding of the structure–bonding–reactivity relationship in transition metal complexes is central to their use in catalytic processes like olefin polymerisation.

We sought to gain an increased insight into the interrelationship between the bonding, reactivity and structure of some small inorganic molecules through the application of a range of techniques. In this study, we employed a range of high oxidation state, early and mid-transition metal complexes, and one f^2 actinide complex. A common feature of all these systems is their d^0 electron configuration, which removes a degree of complexity from the bonding, by eliminating the potential for M→L electron donation and any steric effects resulting from non-bonding *d* electrons. We explored both the change in bonding and reactivity caused by variation of the chemical environment around the metal centre and that demonstrated by different metal centres within a fixed ligand environment. Chapters 2 and 3 concentrate on the former aspect, whereas Chapter 6 focuses on the latter one. In addition, the study of $MeReO_3$ in Chapter 5 enables comparison with a series of pseudoisoelectronic complexes of related structure and different chemistry.

In Chapter 2, a series of novel, highly reactive, Group 5 cationic complexes $[Tp^{Me2}NbMe(L)(MeCCMe)]^+[BAr^f_4]^-$ (L = Et_2O, PMe_2Ph and PEt_3) was synthesised and their structures determined using NMR spectroscopy and X-ray crystallography. These studies also encompassed the use of the neutral ether donors L = O^iPr_2 and THF, but full characterisation of the complexes formed with these ligands was not achieved. Exploration of the structure of $[Tp^{Me2}NbMe(L)(MeCCMe)][BAr^f_4]$ both in solution and the solid state demonstrated shortened M–L bonds, an expression of the Lewis acidity of the cationic metal centre. Preliminary studies of the reactivity of the complexes towards ligand exchange and their catalytic ability in the presence of ethene were conducted. It was demonstrated that the cationic complex is more stable, and the ligand less labile,

when L is a strong electron donor (*e.g.* PMe_2Ph) than when L is a weaker electron donor (*e.g.* Et_2O). However, in contrast to the case where L = Et_2O, when $^iPr_2O$ was employed as a ligand, its increased steric bulk prevented the formation of a stable adduct and the resulting cationic complex was highly reactive, decomposing readily at –60 °C. In addition, the novel complex $[Tp^{Me2}TaMe(Et_2O)(MeCCPh)][BAr^f_4]$ was synthesised and characterised by NMR spectroscopy. Future work to extend this series of complexes, ideally to Ta to allow comparison between the second- and third-row Group 5 elements, would enable a more comprehensive exploration of the chemical reactivity and catalytic activity of the systems. This reactivity could also be explored with studies to elucidate the structure of the complex formed when L = THF. The effects of employing a different methyl abstraction procedure, using reagents such as Ph_3CCl_4 or $B(C_6F_5)_3$ should also be investigated.

The study of some reactive Group 4 complexes was outlined in Chapter 3. During the course of this research, a large amount of effort was expended pursuing $MeTiR_3$ (R = NMe_2, O^iPr), whose isolation would have allowed an investigation of the influence of ligand basicity on the nature of the Ti–C bond. The limited results we obtained demonstrate the highly reactive nature of d^0 titanium complexes, and the difficulties inherent in their study. In spite of this reactivity thwarting the overall aim of the work, some interesting results were obtained. IR and low-temperature NMR spectroscopic studies were conducted on $MeTi(O^iPr)_3$ (Me = CH_3, CH_2D and CD_3), demonstrating an absence of agostic interactions in the Ti–Me moiety. Isolation of intermediate materials employed in the synthesis of $MeTi(NMe_2)_3$ resulted in the characterisation of the novel cluster complex $[\{Ti(NMe_2)_3O\}_2Ti_3(NMe_2)_6OBr_2]$. The partially oxidised complex was characterised by X-ray diffraction, and hence shown to exhibit unusual capping, by both bromo and oxo ligands. X-ray diffraction studies also showed $BrTi(NMe_2)_3$ to form a polar solid. Future work in this area could focus on Zr or Hf analogues, or employ $MeTi(NEt_2)_3$, which represents a more tractable and acceptable substitute for $MeTi(NMe_2)_3$, to be studied in conjunction with freshly prepared $MeTi(O^iPr)_3$.

In Chapters 5 and 6, the electronic structures of some high oxidation state transition and lanthanide metal complexes were studied using photoelectron and absorption (UV and X-ray) spectroscopy. The results were compared with calculated models and a full

assignment of the valence spectra was made. The inner valence and core spectra were also assigned, but a number of peaks could not be identified.

The study of the versatile catalyst $MeReO_3$ shed light on the complicated reactivity displayed by this molecule by demonstrating the mixing of metal atomic orbitals in with the primarily ligand orbitals to form the valence orbitals. The significantly greater strength of the M–C bond in $MeReO_3$ relative to that observed in the isostructural complex $MeTiCl_3$ is clearly explained by the admixture of the C 2*p* orbitals deep into the valence orbitals. This extent of orbital mixing has a clear influence on the overall reactivity of the molecule, as the degree of covalency alters the way that bonds can be viewed. $MeTiCl_3$ has a polar. localised M–C bond which is the HOMO of the molecule, as demonstrated by the highly reactive nature of this moiety in $MeTiCl_3$.

Finally, the series of pseudotetrahedral $M(BH_4)_4$ (M = Zr, Hf and U) complexes was studied in Chapter 6. These systems are significantly more ionic than $MeReO_3$, as a result of the nature of the borohydride ligand and the smaller degree of mixing of metal orbitals into the M–L bonding. The spectra obtained demonstrate that a degree of covalency is present in all three molecules, through the involvement of the *d* orbitals in the bonding, with additional interactions occurring in $U(BH_4)_4$ through the U 5*f* and 6*p* orbitals. This additional metal orbital involvement in bonding is one possible reason for the lower reactivity of $U(BH_4)_4$ compared to that observed for $Zr(BH_4)_4$ and $Hf(BH_4)_4$. Further research in this area should investigate $Th(BH_4)_4$ in more detail if it proves to be more compatible with the apparatus than did $U(BH_4)_4$. No lanthanide analogues are known, so no comparative studies could be conducted.

Chapter 7

Experimental Details

7.1 General Laboratory Techniques

7.1.1 Inert Atmosphere Procedures

The high reactivity of the compounds studied in this project required most operations to be carried out under strictly inert atmosphere conditions, either on a vacuum line or in a dry box[277] (MBraun; Labmaster 130). Reactions were performed in a fume hood where appropriate. Safety equipment – spectacles, gloves and a laboratory coat – were worn for all procedures.

Schlenk lines consisted of combined vacuum and inert gas manifolds made of Pyrex and connected by numbered double-oblique stopcocks. A residual pressure of $5x10^{-2}$ Torr, measured by a Pirani gauge, was usually achieved; the vacuum pump being protected by a liquid N_2 trap to condense any vapours. The trap was isolated from the manifold, pump and atmosphere by greaseless Teflon stopcocks (J. Young). The inert atmosphere used in these projects was generally Ar, or where stated, N_2. Oxygen and moisture were removed from the gas by passing it first through a column of supported manganese oxide, then through one containing pre-baked 4 Å molecular sieves. A slight overpressure of gas was maintained by a Hg bubbler. Non-glass connections were made using high-vacuum tubing.

For some manipulations the dry box was employed. Its dry N_2 atmosphere with oxygen levels below 10 ppm was maintained by circulation through a catalyst bed. Evacuable vessels were introduced into the dry box via a port, which was evacuated then flushed with nitrogen and pumped again a total of three times. Non-evacuable items were flushed in through the port. High water-content items such as tissues were pumped in overnight.

Clean, dry glassware was attached to the vacuum line, evacuated and pump-purged three times. The Pyrex Schlenk tubes used in most procedures were sealed by a cap with a ground glass joint and either a ground glass or Teflon valve. NMR tubes (5 mm o.d) were closed by a Teflon valve or ring. Liquids and solutions were transferred between vessels using the pressure-driven cannula technique.

7.1.2 Solvents

Solvents (supplied by BDH) were dried under an atmosphere of N_2 using standard methods of distillation from either sodium with a benzophenone indicator (THF, Et_2O, Bu_2O, toluene) or calcium hydride ($^iPr_2O$, CH_2Cl_2, 1,2-dimethoxyethane). Pentane was dried, and the freshly distilled solvents were stored, over activated 4 Å molecular sieves (pre-baked to 200°C *in vacuo*) in ampoules sealed with a Teflon valve (J.Young) and degassed by bubbling argon through the liquid for 5-10 min. Triglyme was dried over sodium and freshly vacuum distilled before use.

Deuteriated solvents (supplied by Cambridge Isotope Laboratories Inc.) were degassed and dried over sodium (d_8-toluene, d_8-THF) or over activated 4 Å molecular sieves ($CDCl_3$, CD_2Cl_2, d_5-pyridine) and stored in ampoules.

7.1.3 Starting Materials

All Grignard reagents (CH_3MgI, CD_3MgI, CDH_2MgI and BzMgCl) were freshly prepared. Commercial materials (Aldich, BDH or Sigma) were not purified before use unless specified. $^{238}UCl_4$ (ex. British Nuclear Fuels Plc) was obtained from Prof. Geoff Cloke, University of Sussex.

7.2 Methods of Characterisation and Investigation

7.2.1 NMR Spectroscopy

Routine ^1H, $^{13}C\{^1H\}$ and $^{31}P\{^1H\}$ solution NMR spectra were recorded using a Bruker AM360 spectrometer operating at 360 MHz, 91 MHz and 145 MHz respectively. Additional NMR spectra were measured on a Bruker AV400 spectrometer operating at 400 MHz (^1H) and 101 MHz (^{13}C) or a Bruker DRX500 machine operating at 500 MHz (^1H), 76.8 MHz (^2H), 125.8 MHz (^{13}C) or 208.4 MHz (^{31}P). Many of the NMR spectra described in Chapter 2 were obtained using a Bruker DPX300 operating at 300 MHz (^1H), 75 MHz (^{13}C), and 121.5 MHz (^{31}P). Chemical shifts are referenced to the solvent and reported in parts per million (ppm). Coupling constants (J) are reported in Hz and only pertinent $^1J_{CH}$ values are quoted in the ^{13}C spectra. Standard Bruker software was used for data collection and 2D representations, and Maestrec23 for 1D graphical representations.

7.2.2 Vibrational Spectroscopy

Routine FT-IR spectra of both solid and liquid samples were recorded using a Perkin Elmer Spectrum One spectrometer with a beam-condensing accessory (BCA). Samples were loaded into a diamond compression cell under inert atmosphere in the dry box. The sample spectra consist of four scans with a background correction. Data was collected and graphical representations created using the OMNIC ESP programme.

7.2.3 Elemental Analysis

Elemental analyses were performed in the Analytical Service of the Laboratoire de Chemie de Coordination, Toulouse.

7.2.4 X-Ray Diffraction

X-ray crystallography was performed on a Nonius^{Kappa} CCD diffractometer (graphite monochromatic Mo-K_α radiation, $\lambda = 0.71073$ Å) equipped with an Oxford Cryostream liquid N_2 low-temperature attachment. In the dry box, air-sensitive crystals were transferred into a Petri dish containing a small amount of perfluropolyalkylether and rotated to ensure complete coverage. A crystal was then mounted on a thin glass fibre with a crystal-to-detector distance of 30 mm. The crystal was cooled and the Nonius Collect programme[278] used to determine approximate cell dimensions from five index frames of 2 ° in ϕ. A data collection strategy was calculated by the software to 99.5% completeness for $\theta = 27.5$ °, using a combination of 0.5-2 ° ϕ and ω scans with an exposure time of 10-60 sdeg^{-1}, depending on the crystal quality.

The crystal data were indexed using the DENZO-SMN package[279] and positional data refined, along with the diffractometer constants, to give the final unit cell parameters. Integration and scaling gave corrected data sets. Structures were solved using SHELXS-97[280] and developed via alternating least-squares cycles and difference Fourier synthesis by SHELXL-97 with the aid of Xseed.[281] All non-hydrogen atoms were refined anisotropically. POV-ray[282] was used for graphical representations. Assistance in using the computer programmes was provided by various members of the Steed group.

Additional X-ray crystallography (for **2**) was conducted by the crystallographers at the Laboratiore de Chemie de Coordination, Toulouse. Data collection was carried out on

an Xcalibur Oxford Diffraction diffractometer with a graphite-monochromated Mo-Kα radiation (λ = 0.71073 Å) and using an Oxford Cryosystems Cryostream Cooler Device. Final unit cell parameters were obtained by means of least-squares refinement on a set of 5000 well measured reflections. The crystal structure was solved by direct methods using SIR92[283] and refined as above using SHELXL97.

7.2.5 Photoelectron and Absorption Spectroscopy

Variable energy photoelectron spectroscopy was conducted using the undulator based gas-phase beamline at the ELETTRA synchrotron light laboratory Trieste, Italy,[69] using the angle resolved photoelectron spectrometer chamber and an ionisation cell.[284] The electrons are injected daily over 30 min, at 0.9 – 1.0 GeV and accelerated around a ring of circumference 259.2 m at a frequency of 1.157 Hz under a bending magnetic field of 1.2-1.45 T and vacuum of 1 x 10^{-7} Torr to an operating energy of 2.0 – 2.4 GeV. The white energy electrons enter the beamline at a tangent to the ring and the desired incident energy is isolated through the variable angle spherical grating monochromator, which has four gratings to cover the energy range 15-1000 eV, with a mean energy resolution $\Delta E/E \geq 10.000$. The beamline valves are operated via a computer and the monochromator gratings adjusted manually with the settings read by Vernier gauges. Data collection was achieved using the local Labmaster programme, with data points at steps of 0.1, 0.2 or 0.5 eV; and processed using Igor Pro 4.0.

7.2.6 Charge Density Studies

X-ray diffraction data collection

High resolution X-ray diffraction data for $[(Bz_3Ti)_2O]$ **8** were collected from a crystal glued inside a 0.01 mm thin-walled capillary and mounted on a Nonius^{Kappa} CCD detector system, cooled with an Oxford Cryostream System to 120 K in 2.5 hr, with a mean temperature gradient of –1 $Kmin^{-1}$. Preliminary examination and final data collection were carried out with graphite-monochromated MoK_α radiation (λ = 0.71073 Å) generated from a Nonius FR591 rotating anode running at either 50 kV and 60 mA (low and medium resolution) or 50 kV and 80 mA (high resolution). Intensity data were collected using 1° φ and ω scans with a detector-to-sample distance of 40 mm. For the low and medium order data 11 scan sets (1417 frames in total) were collected at a scan angle θ of –16.8, -7.8, 0.0, 7.8, 16.8 and 17.0 ° and a scan time between 20 and

80 s/frame. For the high order data 7 scan sets (604 frames in total; scan angle θ of –35.0, –30.3 and 30.3 °) with a scan time of 240 s/frame were chosen.[278]

X-ray data reduction

The unit cell was determined from 35571 reflection positions. An initial orientation matrix was determined from 10 frames of the first scan set and refined during the integration of the individual scan sets. The intensities were first corrected for beam inhomogenity and crystal decay by the program 'Scalepack' using a tight scale restraint (0.02).[279] An absorption correction was the applied [T_{min} = 0.768(3), T_{max} = 0.830(2)] and symmetry equivalent and multiply measured reflections were averaged with the program 'Sortav'.[285]

Multipolar refinements and determination of the deformation density

First, an independent atom model (AIM) refinement was conducted, in which all atoms were treated as spherical. Anisotropic thermal parameters were introduced to describe the thermal motion of all non-hydrogen atoms. All hydrogen atoms were found in the difference map and refined isotropically using SHELXL-97. The refinement finally converged at R_1 = 0.0280, wR_2 = 0.0837 and GOF = 1.03 for 4645 reflections ($\sin\Theta/\lambda <$ 1.00 Å^{-1}) and 90 parameters.

A multipole model was the adopted to describe the deformation of $\rho(\mathbf{r})$ from a spherical distribution. According to a method proposed by Stewart,[286] the electron density $\rho(\mathbf{r})$ in a crystal is described by a sum of aspherical pseudoatoms at the nuclear positions $\{\mathbf{R}_j\}$:

$$\rho(\mathbf{r}) = \sum_j \rho_j(\mathbf{r} - \mathbf{R}_j)$$

Based on the Hansen-Coppens formalism,[287] the pseudoatom density $\rho_j(\mathbf{r} - \mathbf{R}_j)$ is expressed in terms of multipoles ($\mathbf{r}_j = \mathbf{r} - \mathbf{R}_j$):[288]

$$\rho_j(\mathbf{r}_j) = P_c\rho_c(r_j) + \kappa'^3 P_v\rho_v(\kappa' r_j) + \sum_{l=0}^{l_{max}} \sum_{m=-l_{max}}^{+l_{max}} \kappa''^3 P_{lm} R_l(\kappa'' r_j) Y_{lm}(\theta_j, \varphi_j)$$

In the refinement of our best model the multipole expansion was truncated at the hexadecapole level (l_{max} = 4) for the heavy atoms, but C1 and hydrogens were treated with monopoles (l = 0) and with bond-directed dipoles (l = 1). Core and spherical valence densities were constructed using Clementi and Roetti Hartree-Fock (HF)[289]

atomic wave functions expanded over Slater-Type basis functions. The radial functions for the valence deformation densities were of single Slater-type orbitals.[290] Anisotropic atomic displacement parameters were introduced to describe the thermal motion of all non-hydrogen atoms. Isotropic temperature parameters for the hydrogen atoms were derived from the parent carbon atom ($U_H = 1.5U_{Csp^3}$, $U_H = 1.2U_{Csp^2}$). The hydrogen atom positions were then fixed at (C–H) = 1.10 Å.

To reduce the number of multipole populations to be refined, local C_3 and S_6 pseudo symmetries were imposed on Ti and O atoms, respectively, and a local pseudo mirror plane was imposed on the carbon atoms in a phenyl ring. A radial scaling (κ') for the spherical density was refined for each heavy atom type whilst for H atoms κ' was kept fixed (1.20). In addition, κ'' was kept equal to κ' for Ti and different κ' factors were used for chemically non-equivalent C atoms (2 in total). The molecule was kept neutral during all refinements.

With the experimental model this procedure refined to $\kappa' = \kappa'' = 1.193(31)$ for Ti, $\kappa' = 0.953(5)$ for O, $\kappa' = 0.892(5)$ for Cl and $\kappa' = 0.951(13)$, $\kappa'' = 0.934(13)$ for carbon atoms in a phenyl ring. The final agreement factors were $R_1 = 0.0152$, $wR_2 = 0.0425$ and $GOF = 0.8533$ for 4118 reflections ($F_o > 3\sigma(F_o)$; $\sin\Theta/\lambda < 1.00$ Å^{-1}) and 213 parameters ($N_{ref}/N_{var} = 19.9$). The residual electron density map was practically featureless with the maximum and minimum values of 0.201 and –0.311 eÅ^{-3} ($\sin\Theta/\lambda < 0.8$ Å^{-1}), respectively.

Hirshfeld's rigid bond test[291] was applied to the atomic displacement parameters obtained from the refinements. The difference between mean-square amplitudes for all C–C bonds is within the limit of 1.0 x 10^{-3} Å^2, as proposed by Hirshfeld. However the difference for the Ti–C bonds due to the different masses of the bonded atoms is somehow larger, but never exceeds a value of 3.0 x 10^{-3} Å^2.[292;293]

7.3 Computational Details

7.3.1 Chapter 3

All refinements of the [$(Bz_3Ti)_2O$] data were carried out with the full-matrix least-squares program 'XDLSM' of the 'XD' suite of programs;[288] the quantity minimized was $\varepsilon = \sum w_1(|F_o| - k|F_c|)^2$, where k is a scale factor, based on 4118 reflections with

$F_o > 3\sigma(F_o)$. Weights were taken as $w_1 = 1/\sigma^2(F_o)$ and $w_2 = 1/\sigma^2(F_o^2)$. Convergence was assumed when a maximal shift/esd < 0.06 was achieved. For the topological analysis, critical points of the electron density were searched via a Newton Raphson algorithm implemented in 'XD'. Properties of $\rho(\mathbf{r})$ and $\nabla^2\rho(\mathbf{r})$ were calculated after transformation of the local axis system into a global system.

DFT calculations using the Becke3LYP density functional[294;295] were carried out with the 'Gaussian98' program suite (release A.3).[296] The 6-311G(d.p.) basis set combination as specified in 'Gaussian98' was used, with one additional *f*-polarisation function employed for Ti, given in Appendix 3.2. The topological analysis of theoretical electron density was carried out with the 'AIMPAC' software package[297] and experimental electron density analysis was conducted with the XD program system.[288]

7.3.2 Chapters 5 and 6

DFT calculations were performed by Prof. Jennifer Green, Department of Chemistry, University of Oxford. All data quoted were calculated using the Amsterdam Density Functional (ADF) code (version ADF2000.02).[298] Scalar relativistic corrections were included via the ZORA method.[299;300] The generalised gradient approximation was employed, using the local density approximation of Vosko, Wilk and Nusair,[301] together with nonlocal exchange correction by Becke[302] and nonlocal correlation corrections by Perdew.[303] For the calculations dexcribed in Chapter 5, Type IV basis sets were used with triple ζ accuracy sets of Slater type orbitals, with a single polarisation function added to the main group atoms and the cores of the atoms were frozen up to 1*s* for C and O, and 4*d* for Re. TZ2P basis sets were used for the calculations described in Chapter 6, again with triple ζ accuracy sets of Slater type orbitals, but this time with two polarisation functions added to the main group atoms and without freezing the cores of the atoms. Ionisation energies were obtained by direct calculations on the molecular ions in their ground and approximate excited states, and subtraction of the energy of the neutral molecule. Spin-orbit calculations, as available in the ADF programme suite, were also carried out for $MeReO_3$ and $U(BH_4)_4$ both for the ground state molecule and the molecular ion states.

7.4 Synthesis and Characterisation

7.4.1 Chapter 2

$[Tp^{Me2}NbMe(OEt_2)(MeC{\equiv}CMe)][BAr^f{}_4]$ (2)

$[H(OEt_2)_2][BAr^f{}_4]$ (55.5 mg, 0.055 mmol) and $[Tp^{Me2}NbMe_2(MeC{\equiv}CMe)]$ (26 mg, 0.055 mmol) were placed in an NMR tube and cooled (–60 °C, ethanol/liquid N_2 bath). Cooled d_2-DCM (0.5 ml, –60 °C) was added via syringe and the solution gently shaken to ensure all solids dissolved. The solution rapidly changed colour from yellow to orange and the evolution of gas over 2-3 min. was noted.

Analysis. $C_{56}H_{53}N_6B_2F_{24}ONb$

Calc: C 48.16, H 3.83, N 6.01. Found: C 36.58, H 1.98, N 3.35.

^{1}H NMR (300 MHz, d_2-DCM, 213 K) δ 7.79 (br, 8 H, *orthoH* $Ph(CF_3)_2$), 7.59 (br, 4 H, *paraH* $Ph(CF_3)_2$), 6.02, 5.96, 5.79 (s, 1 H each, $Tp^{Me2}CH$), 4.69 (br, 1 H, $Tp^{Me2}BH$) 4.27, 4.13, 3.5, 3.4 (m, 1 H each, $O(CH_2Me)_2$) 3.25, 2.40 (s, 3 H each, *Me*C≡C*Me*), 2.44, 2.39, 2.32, 2.21, 1.97, 1.60 (s, 3 H each, $Tp^{Me2}Me$), 1.80 (s, 3 H, Nb*Me*), 1.35, 0.92 (m, 3 H each, $O(CH_2Me)_2$)

NMR ^{13}C (75 MHz, d_2-DCM, 213 K) δ 254.8, 245.8 (s, MeC≡CMe), 161.6 (q, *ipsoC* $Ph(CF_3)_2$ J_{BH} = 50 Hz), 151.5, 151.1, 149.4, 146.91, 146.87, 145.4 (s, $Tp^{Me2}CMe$), 134.5 (br, *orthoC* $Ph(CF_3)_2$ $^1J_{CH}$ = 159 Hz), 128.6 (q, *metaC* $Ph(CF_3)_2$ J_{CF} = 30 Hz), 124.3 (q, CF_3 J_{CF} = 272 Hz), 117.4 (br, *paraC* $Ph(CF_3)_2$ $^1J_{CH}$ = 164 Hz), 108.3, 108.1, 107.3 (s, $Tp^{Me2}CH$), 74.9 (s, $NbCH_3$ $^1J_{CH}$ = 121 Hz), 75.0, 74.4 (s, $O(CH_2Me)_2$), 23.2, 22.0 (s, *Me*C≡C*Me*), 15.7, 14.2, 13.89, 13.12, 12.60, 12.44 (s, $Tp^{Me2}CMe$), 13.89, 12.19 ($O(CH_2Me)_2$).

Crystal Data

$C_{56}H_{55}B_2F_{24}N_6NbO$; M = 1398.59, orange block, 0.4 x 0.16 x 0.08 mm^3, Triclinic, space group $P\bar{1}$, a = 12.7185(6) Å, b = 12.0870(7) Å, c = 18.5693(10) Å, α = 91.249(4) °, β = 94.824(4) °, γ = 99.599(4) °, V = 3034.7(3) Å^3, Z = 2, D_c = 1.531 mg/m^3, F_{000} = 1416, T = 180(2) K, $2\theta_{max}$ = 57.55 °, 17779 reflections collected, 8700 unique (R_{int} = 0.0437) Final *GooF* = 1.057, *R1* = 0.0793, *ωR2* = 0.2155, *R* indices based on 6918 reflections with I>2sigma(I) (refinement on F^2), 820 parameters, 48 restraints. Lp and absorption corrections applied, μ = 0.317 mm^{-1}

[Tp^{Me2}NbMe(THF)(MeC≡CMe)][BAr^f_4] (4)

[$H(OEt_2)_2$][BAr^f_4] (40 mg, 0.040 mmol) and $Tp^{Me2}NbMe_2$(MeC≡CMe) (19 mg, 0.040 mmol) were placed in an NMR tube and cooled (–60 °C, ethanol/liquid N_2 bath). Cooled d_2-DCM (0.5 ml, –60 °C) was added via syringe and the solution gently shaken to ensure all solids dissolved. The solution rapidly changed colour from yellow to orange and the evolution of gas over 10 min was noted.

^{1}H NMR (500 MHz, d_8-THF, 253 K) δ 7.84 (br, 8 H, *orthoH* $Ph(CF_3)_2$), 7.64 (br, 4 H, *paraH* $Ph(CF_3)_2$), 6.11, 6.00, 5.97 (s, 1 H each, $Tp^{Me2}CH$), 4.80 (br, 1 H, $Tp^{Me2}BH$) 2.98, 2.14 (s, 3 H each, *Me*C≡C*Me*), 2.48, 2.45, 2.44, 2.33, 1.97, 1.84 (s, 3 H each, Tp^{Me2}*Me*).

NMR ^{13}C (125.8 MHz, d_8-THF, 253 K) δ 216.4, 296.1 (s, MeC≡CMe), 162.7 (q, *ipsoC* $Ph(CF_3)_2$ J_{BH} = 49 Hz), 152.7, 151.84 151.77, 146.8, 146.7, 146.6 (s, Tp^{Me2}CMe), 135.4 (br, *orthoC* $Ph(CF_3)_2$), 129.9 (q, *metaC* $Ph(CF_3)_2$ J_{CF} = 34Hz), 125.4 (q, CF_3 J_{CF} = 272 Hz), 118.2 (br, *paraC* $Ph(CF_3)_2$), 108.6, 108.5, 107.9 (s, Tp^{Me2}CH), 21.9, 18.9 (s, *Me*C≡C*Me*), 15.0, 13.9, 13.7, 12.9, 12.5, 12.3 (s, Tp^{Me2}C*Me*).

[Tp^{Me2}NbMe(O^iPr_2)(MeC≡CMe)][BAr^f_4] (5)

Cooled d_2-DCM (0.3 ml, –20 °C, ethanol/liquid nitrogen bath) was added via syringe to a cooled NMR tube containing [$H(O^iPr_2)_2$][BAr^f_4] (52.2 mg, 0.049 mmol, –20 °C). A further 0.2 ml was added to a separate NMR tube containing [$Tp^{Me2}NbMe_2$(MeC≡CMe)] (23.1 mg, 0.049 mmol, –20 °C). Once all solid material was dissolved the solutions were cooled further to –90 °C and the yellow [$Tp^{Me2}NbMe_2$(MeC≡CMe)] added to the solid solution of [$H(O^iPr_2)_2$][BAr^f_4]. Upon warming to –80 °C, gas evolution and a colour change from yellow to orange were noted.

NMR ^{1}H (300 MHz, d_2-DCM, 193 K) δ 7.77 (br, 8 H, *orthoH* $Ph(CF_3)_2$), 7.56 (br, 4 H, *paraH* $Ph(CF_3)_2$), 5.85, 5.80, 5.57 (s, 1 H each, $Tp^{Me2}CH$), 4.65 (br, 1 H, $Tp^{Me2}BH$), 3.27, 2.42 (s, 3 H each, *Me*C≡C*Me*), 2.41, 2.36, 2.31, 2.24, 2.07, 1.62, 0.90 (s, 3 H each, Tp^{Me2}*Me* and Nb*Me*)

NMR ^{13}C (75 MHz, d_2-DCM, 193 K) δ 255.8, 244.4 (s, MeC≡CMe), 161.4 (q, *ipsoC* $Ph(CF_3)_2$ J_{BH} = 50 Hz), 151.0, 149.7, 149.5, 145.89, 145.0, 144.9 (s, Tp^{Me2}CMe), 134.2 (br, *orthoC* $Ph(CF_3)_2$), 128.2 (q, *metaC* $Ph(CF_3)_2$ J_{CF} = 30Hz), 124.0 (q, CF_3 J_{CF} = 272

Hz), 117.1 (br, *paraC* $Ph(CF_3)_2$), 108.1, 107.4, 106.9 (s, $Tp^{Me2}CH$), 70.5 (s, $NbCH_3$ $^1J_{CH}$ = 121 Hz), 22.7, 22.6 (s, *Me*C≡C*Me*), 14.3, 14.3, 12.9, 12.45, 12.42, 10.7 (s, $Tp^{Me2}CMe$).

$[Tp^{Me2}NbMe(PPhMe_2)(MeC{\equiv}CMe)][BAr^f_4]$ (6a)

Cooled d_2-DCM (0.3 ml, –20 °C, ethanol/liquid N_2 bath) was added via syringe to a pre-cooled NMR tube containing $[H(OEt_2)_2][BAr^f_4]$ (50.8 mg, 0.050 mmol, –20 °C); this was then cooled to –60 °C. To a separate NMR tube containing $Tp^{Me2}NbMe_2(MeC{\equiv}CMe)$ (23.5 mg, 0.050 mmol, –20 °C) cooled d_2-DCM (0.2 ml, –20 °C) was added, followed by an excess of cooled $PPhMe_2$ (25 µl, 0.176 mmol, –20 °C). This yellow solution was added via a cannula to that of $[H(OEt_2)_2][BAr^f_4]$ and allowed to warm to –20 °C. This temperature was maintained for 20 min and a gradual colour change from yellow to orange with the evolution of gas was noted. On completion of the reaction, the solution was cooled to –60 °C.

^{1}H NMR (300 MHz, d_2-DCM, 213 K) δ 7.82 (br, 8 H, *orthoH* $Ph(CF_3)_2$), 7.60 (br, 4 H, *paraH* $Ph(CF_3)_2$), 7.18, 6.70 (m, P*Ph*Me_2) 5.96, 5.88, 5.67 (s, 1 H each, $Tp^{Me2}CH$), 3.52, 2.57 (s, 3 H each, *Me*C≡C*Me*), 2.47, 2.43, 2.37, 1.88, 1.70, 1.63 (s, 3 H each, $Tp^{Me2}Me$), 1.68 (s, 3 H, Nb*Me*), 1.93, 1.25 (d, 3 H each, PPhMe_2)

NMR ^{13}C (75 MHz, d_2-DCM, 213 K) δ 257.8, 252.2 (s, MeC≡CMe), 161.6 (q, *ipsoC* $Ph(CF_3)_2$ J_{BH} = 50 Hz), 152.2, 152.1, 150.2, 147.6, 146.4, 145.6 (s, $Tp^{Me2}CMe$), 134.4 (br, *orthoC* $Ph(CF_3)_2$), 131.0, 129.7, 128.8 (br, P*Ph*Me_2), 128.2 (q, *metaC* $Ph(CF_3)_2$), 124.2 (q, CF_3 J_{CF} = 272 Hz), 117.3 (br, *paraC* $Ph(CF_3)_2$), 108.6, 108.3, 107.1 (s, $Tp^{Me2}CH$), 95.1 (s, $NbCH_3$ $^1J_{CH}$ = 122 Hz), 24.0, 23.95 (s, *Me*C≡C*Me*), 15.7, 15.4, 14.8, 13.0, 12.7 (s, $Tp^{Me2}CMe$), 13.9 (br, PPhMe_2).

NMR ^{31}P (121.5 MHz, d_2-DCM, 213K) δ -1.75 (*P*$PhMe_2$) (main rotamer)

$[Tp^{Me2}NbMe(PEt_3)(MeC{\equiv}CMe)][BAr^f_4]$ (6b)

Cooled, degassed PEt_3 (20 µl, 0.135 mmol, –60 °C) was added via syringe to a d_2-DCM solution of $[Tp^{Me2}NbMe(OEt_2)(MeC{\equiv}CMe)][BAr^f_4]$ (0.5 ml, 0.05 mmol, –60 °C) prepared as described above. This mixture was left for 18 h at –35 °C, to ensure complete exchange between the diethyl ether and phosphine.

^{1}H NMR (500 MHz, d_2-DCM, 233 K) δ 7.75 (br, 8 H, *orthoH* $Ph(CF_3)_2$), 7.58 (br, 4 H, *paraH* $Ph(CF_3)_2$), 6.10, 5.91, 5.82 (s, 1 H each, $Tp^{Me2}CH$), 3.40, 2.55 (s, 3 H each, *Me*C≡C*Me*), 2.50, 2.39, 2.34, 2.23, 1.90, 1.62 (s, 3 H each, $Tp^{Me2}Me$), 1.70 (br, 3 H, Nb*Me*), 1.78, 1.52 (m, $P(CH_2Me)_3$) 0.62 (m, $P(CH_2Me)_3$)

NMR ^{13}C (125.8 MHz, d_2-DCM, 233 K) δ 161.6 (q, *ipsoC* $Ph(CF_3)_2$ J_{BH} = 50 Hz), 151.5, 151.1, 149.4, 146.91, 146.87, 145.4 (s, $Tp^{Me2}CMe$), 134.5 (br, *orthoC* $Ph(CF_3)_2$), 128.6 (q, *metaC* $Ph(CF_3)_2$ J_{CF} = 34 Hz), 124.3 (q, CF_3 J_{CF} = 272 Hz), 117.4 (br, *paraC* $Ph(CF_3)_2$), 109.3, 108.3, 107.1 (s, $Tp^{Me2}CH$), 94.7 (s, $NbCH_3$), 24.42, 24.37 (s, *Me*C≡C*Me*), 15.8, 15.6 (d, $P(CH_2Me)_3$), 16.5, 15.2, 14.7, 13.1, 12.9, 12.7 (s, $Tp^{Me2}CMe$), 6.7 (br, $P(CH_2Me)_3$).

NMR ^{31}P (208.4 MHz, d_2-DCM, 233K) δ 15.31 (s, $P(CH_2CH_3)_3$)

$[Tp^{Me2}TaMe(OEt_2)(MeC{\equiv}CMe)][BAr^f{}_4]$ (7)

Following a similar procedure to that for complex **2**, $Tp^{Me2}TaMe_2(PhC{\equiv}CMe)$ (29.7 mg, 0.048 mmol) and $[H(Et_2O)_2][BAr^f{}_4]$ (48.6 mg, 0.048 mmol) were placed in an NMR tube and cooled (–60 °C, ethanol/liquid N_2 bath). d_2-DCM (0.5 ml, –60 °C) was added, via syringe, with the evolution of gas and a colour change to orange noted within 2 min. The solution was decanted via a cannula to remove undissolved solids.

^{1}H NMR (300 MHz, d_2-DCM, 213 K) δ 7.77 (br, 8 H, *orthoH* $Ph(CF_3)_2$), 7.57 (br, 4 H, *paraH* $Ph(CF_3)_2$), 7.29 (br, 5 H, MeC≡C*Ph*), 6.08, 5.89, 5.73 (s, 1 H each, $Tp^{Me2}CH$), 4.75 (br, 1 H, $Tp^{Me2}BH$) 4.64, 4.34 (m, 1 H each, $O(CH_2Me)_2$) 3.75 (s, 3 H, *Me*C≡CPh), 2.45, 2.43, 2.36, 2.31, 1.60, 1.33 (s, 3 H each, $Tp^{Me2}Me$), 1.29 (s, 3 H, Ta*Me*), 1.60, 0.93 (m, 3 H each, $O(CH_2Me)_2$)

NMR ^{13}C (75 MHz, d_2-DCM, 213 K) δ 263.5, 240.3 (s, MeC≡CPh), 161.6 (q, *ipsoC* $Ph(CF_3)_2$ J_{BH} = 50 Hz), 152.8, 151.8, 151.2, 147.3, 146.7, 146.0 (s, $Tp^{Me2}CMe$), 140.2, 130.1, 128.9 (br, MeC≡C*Ph*), 134.5 (br, *orthoC* $Ph(CF_3)_2$), 128.4 (q, *metaC* $Ph(CF_3)_2$), 124.3 (q, CF_3 J_{CF} = 273 Hz), 117.4 (br, *paraC* $Ph(CF_3)_2$), 108.9, 108.5, 107.4 (s, $Tp^{Me2}CH$), 77.0, 76.0 (s, $O(CH_2Me)_2$), 66.4 (s, $TaCH_3$), 25.8 (s, *Me*C≡CPh), 15.9, 14.6, 14.4, 13.2, 12.5, 12.5 (s, $Tp^{Me2}CMe$), 14.3, 12.5 (s, $O(CH_2Me)_2$).

Starting Materials

$[Tp^{Me2}NbMe_2(MeC{\equiv}CMe)]$ (**1**)

Following a similar procedure to that of E. Teuma,[110] $Tp^{Me2}NbCl_2(MeC{\equiv}CMe)$ (1.83g, 3.55mmol) was placed in a Schlenk tube and gently degassed. 40 ml Toluene was added, the solution stirred vigorously and cooled (–20 °C, ethanol/liquid nitrogen bath). A 10% excess of MeLi (4.9 ml of 1.6 M solution in OEt_2, 7.81 mmol) was added dropwise via syringe and the reaction mixture stirred for 30 min cold and a further 30 min at room temperature. The reaction was monitored by NMR spectroscopy to ensure completion. The colour gradually changed from purple to a yellow/brown and a white precipitate was observed and removed by filtration over a fritt and celite with a glass-wool plug. The residue was washed with 5 ml toluene and 10 ml hexane. The filtrate was pumped to dryness and extracted into toluene/pentane (1:3, 40 ml total), filtered as before, washed and extracted into 5 ml toluene. The volume was reduced to 3 ml, 10 ml pentane added and left to crystallise. Yellow crystals were isolated by decanting off the mother liquor and washing with cold pentane (2 ml). Yield: 1.46 g; 86%

$[Tp^{Me2}NbCl_2(MeC{\equiv}CMe)]$

Following a similar method to that described by Etienne et al.[112] but-2-yne (1.5 ml, 19.16 mmol) in 10 ml DCM was added to a stirred solution of $NbCl_3$.dme (5.55 g, 19.16 mmol) in 50 ml DCM and allowed to stir for 18 h. The reaction mixture was evaporated to dryness and degassed KTp^{Me2} (6.44 g, 19.16 mmol) added. The reactants were dissolved in 80 ml THF and stirred at room temperature for 6 h. The resulting plum coloured solution was evaporated to dryness and the purple/brown solid extracted into a toluene/pentane (200/30 ml) mixture. This was filtered over celite on a frit and the residue washed with toluene/pentane (5 x 20 ml), until the washings were clear. The filtrate was pumped to dryness, the purple solid washed with cold ethanol (5 x 6 ml) and dried *in vacuo*.

$NbCl_3$.dme was prepared from $NbCl_5$ by the literature method.[111]

$[H(OEt_2)_2][BAr^f{}_4]$ (**3**)

Following a similar procedure to that of Brookhart et al.[106] $NaBAr^f{}_4$ (1.1 g, 1.24 mmol) was dissolved in 40 ml dry diethyl ether and left over pre-baked 4 Å molecular sieves for 12 h. This solution was slowly added via cannula to a cooled Schlenk tube

containing dry HCl (100 ml, 2.74 mmol, 0 °C, ice/NaCl bath) and stirred for 30 min. The white precipitate was allowed to settle out and the liquor filtered off at low temperature (0 °C). The residue was washed with cold diethyl ether (5 x 10 ml, –10 °C) and the washings and liquour combined. The volume was reduced to 5 ml and stored at –35 °C for the product to crystallise. The crystals were isolated by cooling the solution to –80 °C and decanting off the remaining solution (retained to gain a second crop) and pumped to dryness. Yield: 690 mg; 55%

$[H(O^iPr_2)_2][BAr^f_4]$

Following the procedure of White et al.[109] $[H(OEt_2)_2][BAr^f_4]$ (850 mg, 0.84 mmol) was dissolved in 20 ml freshly distilled O^iPr_2 and stirred for 1 h. The volume was reduced and the solution stored at –35 °C overnight. Colourless crystals of $[H(O^iPr_2)_2][BAr^f_4]$ were isolated by cooling the solution to –80 °C, decanting off the liquor and pumping to dryness. A second crop was obtained by reducing the volume of the liquor and repeating the process. Yield: 718 mg; 80%

Catalytic trials for the polymerisation of ethene

A stirred, cooled (–30 °C) DCM solution of **2** (3 ml, 0.01 mmol) was placed in a catalysis flask connected to both vacuum and ethene. The N_2 atmosphere was replaced with a 2 bar pressure of C_2H_4, the time noted and the solution stirred vigorously at a constant temperature for 30 min. The temperature was raised to 0°C and the solution stirred for 1 h, and a further 30 min at 25 °C. The small amount of white precipitate obtained was too little to isolate and analyse.

7.4.2 Chapter 3

$[(Bz_3Ti)_2O]$ (8)

Following the literature route for the preparation of $Ti(Bz)_4$[304] a freshly prepared solution of BzMgCl (80 ml, 151 mmol) was added dropwise to a stirred suspension of $TiCl_4$ (3.8 ml, 35 mmol) in 50 ml Et_2O. The solution was stirred for a further 16 h, left to settle and the deep red supernatant liquid decanted off. The residue was washed with 3 x 10 ml Et_2O and the combined solution reduced to dryness. The solid was extracted into pentane, the volume reduced and left to recrystallise at –40 °C over 6 weeks. The identity of the product was confirmed by high resolution X-ray diffraction at 120 K.

$BrTi(NMe_2)_3$ (9)

Following a similar method to that described in the literature,[163] $Ti(NMe_2)_4$ (5 g, 22.3 mmol) was dissolved in hexane and cooled to –30 °C (acetone/solid CO_2) and added dropwise to a stirred solution/suspension of $TiBr_4$ (2.73 g, 7.43 mmol, -30 °C). White fumes were observed as the orange solution turned brown. After allowing the solution to warm to room temperature, it was refluxed for 1 h and small yellow crystals in a clear orange solution were observed. Further yellow crystals appeared on storing the solution at –10 °C for 72 h.

^1H NMR: (360 MHz, d_8-toluene, 293 K) δ 3.12

Crystal Data

$C_6 H_{18} N_3 Ti Br$; M = 260.01, yellow block, 0.1 x 0.1 x 0.1 mm^3, Trigonal, space group R3, a = 11.4614(16) Å, b = 11.4614(16) Å, c = 7.3885(15) Å, α = 90 °, β = 122.9313(45) °, γ = 90 °, V = 840.5 $Å^3$, Z = 3, D_c = 1.541 g/cm^3, F_{000} = 396, T = 120(2) K, $2\theta_{max}$ = 54.72°, 1295 reflections collected, 618 unique (R_{int} = 0.0831) Final $G_{00}F$ = 0.917, $R1$ = 0.0299, $\omega R2$ = 0.0671, R indices based on 610 reflections with I>2sigma(I) (refinement on F^2), 65 parameters, 1 restraint. Lp and absorption corrections applied, μ = 4.28 mm^{-1}.

$[\{Ti(NMe_2)_3O\}_2Ti_3(NMe_2)_6OBr_2]$ (10)

The air (10 ml) contained in a round bottomed flask was displaced by Ar via a cannula and bubbled through a solution of $BrTi(NMe_2)_3$ (0.4 g, 1.54 mmol) dissolved in 20 ml hexane. A white precipitate formed immediately. The mixture was placed at –40 °C for 24 h, resulting in the precipitation of small red triangular block crystals of **3** in addition to the white precipitate.

Crystal Data

$C_{24} H_{72} Br_2 N_{12} O_3 Ti_5$, M = 976.26, red block, 0.40 × 0.30 × 0.10 mm^3, Monoclinic, space group $P2_1/m$ (No. 11), a = 8.5908(2) Å, b = 23.6320(10) Å, c = 11.2843(4) Å, α = 90 °, β = 103.465(2) °, γ = 90 °, V = 2227.94(13) $Å^3$, Z = 2, D_c = 1.455 g/cm^3, F_{000} = 1008, T = 130(2) K, $2\theta_{max}$ = 55.0 °, 14421 reflections collected, 5202 unique (R_{int} = 0.0603). Final $GooF$ = 1.090, $R1$ = 0.0434, $wR2$ = 0.0835, R indices based on 4345 reflections with I >2sigma(I) (refinement on F^2), 234 parameters, 0 restraints. Lp and absorption corrections applied, μ = 2.689 mm^{-1}.

$CH_3Ti(O^iPr)_3$ (14)

In a similar manner to that described in the literature,[305] MeLi (4.8 ml, 7.67 mmol) was added dropwise to a stirred, cooled (–30 °C, acetone/$CO_{2(s)}$) solution of $ClTi(O^iPr)_3$ (2 g, 7.67 mmol) in 40 ml diethylether and allowed to warm to room temperature over a period of 90 min. The volume was reduced and the remaining liquid transferred to a mini distillation apparatus. The pressure was reduced very slowly to avoid bumping, and the green liquid distilled at 40-60 °C was collected into a small ampoule sealed with a Teflon valve.

$CH_2DTi(O^iPr)_3$

This was prepared in a similar manner to that described for $MeTi(O^iPr)_3$ above; except that a fresh diethylether solution of the Grignard reagent CH_2DMgI, prepared from CH_2DI, by standard methods, was used as the methylating reagent. The fraction distilled at 35-45 °C was collected.

$CD_3Ti(O^iPr)_3$

This was also prepared in a similar manner to that described for $MeTi(O^iPr)_3$ above, except that a fresh diethylether solution of the Grignard reagent CD_3MgI, prepared from CD_3I, by standard methods, was used as the methylating reagent. The fraction distilled at 35-45 °C was collected.

Starting Materials

CD_3I

Red phosphorus (2.87 g, 92.6 mmol) was placed in an ampoule closed with a Rotaflow valve, degassed and CD_3OH (10 g, 0.278 mol) added. The mixture was cooled (–40 °C, acetone/$CO_{2(s)}$) and swirled as aliquots of iodine (35.24 g, 0.1389 mol) <1 g were added. Swirling continued until the reaction started. The mixture was warmed to room temperature and stirred for 12 h, then heated to 50°C and stirred for a further 4 h. All volatiles were removed *in vacuo* into a glass bulb. CD_3I was condensed at 77 K into an ampoule containing activated 3 Å sieves. Three drops of Hg were added to remove any excess I_2.

7.4.3 Chapter 5

$MeReO_3$

$MeReO_3$ was prepared in a modified version of the literature method of Herrmann et al.[163] A solution of Me_3SiCl (2.21 ml, 17.3 mmol) in 20 ml Acetonitrile was added dropwise to a stirred suspension of Re_2O_7 (4 g, 8.26 mmol) in 50 ml CH_3CN. Me_4Sn (2.36 ml, 17.3 mmol) was added dropwise to this green solution, and the solution was stirred for 12 h. It was then cooled to 0 °C and the solvent and tin complexes removed under reduced pressure. The resulting white crystals were washed with cold hexane (3 x 5 ml) and sublimed under reduced pressure.

^1H NMR (360 MHz, d_6-benzene, 293 K) δ 7.79

7.4.4 Chapter 6

$Zr(BH_4)_4$

$Zr(BH_4)_4$ was prepared by a method slightly modified from that in the literature.[266] In the dry box, a 50% excess of finely ground $LiBH_4$ (3.0 g, 0.138 mol) was combined with $ZrCl_4$ (5.35 g, 23 mmol) and some anti-bumping granules, in a long necked round bottomed flask sealed with a Young's valve. The powders were stirred slowly under reduced pressure for 4.5 d using a glass covered magnetic stirring flea. The mixture was then cooled to 77 K and all volatiles removed. The white solid was allowed to warm to room temperature, and the volatiles were removed under reduced pressure and isolated in a cooled trap (163 K, ethanol/liquid N_2). The resulting crude white material was purified by warming to 273 K and isolating all volatile materials in a cooled trap (195 K, acetone/$CO_{2(s)}$).

$Hf(BH_4)_4$

White crystalline $Hf(BH_4)_4$ was synthesised in the same manner as $Zr(BH_4)_4$; from $LiBH_4$ (2 g, 92 mmol) and $HfCl_4$ (4.90 g, 15 mmol).

$U(BH_4)_4$

$U(BH_4)_4$ was prepared following a similar procedure to that for $Zr(BH_4)_4$, and in the literature.[266] Depleted $^{238}UCl_4$ (2.54 g, 6.7 mmol) was reacted with a four-fold excess of $LiBH_4$ (2.33 g, 107 mmol) and the mobile reaction mixture stirred for 3 weeks. All volatile gases were removed from the reaction mixture after cooling to 77 K. The $U(BH_4)_4$ was isolated from the remaining mixture by vacuum fractionation, giving a dark crystalline product with a fluid-like appearance.

Appendix 1

References

[1.] A. E. Shilov, G. B. Shul'pin, *Chem.Rev.* **1997,** *97*, 2879.

[2.] B. C. G. Söderberg, *Coord.Chem.Rev.* **2003,** *247*, 79.

[3.] M. Peruzzini, R. Poli, *Recent Advances in Hydride Chemistry*, 1st ed. Elsevier Science, Amsterdam **2001**.

[4.] Ch. Elschenbroich, A. Salzer, *Organometallics: A Concise Introduction*, 1st ed. VCH, Weinheim/New York **1989**.

[5.] R. H. Crabtree, *The Organometallic Chemistry of the Transition Metals*, 1st ed. Singapore **1988**.

[6.] R. D. Peacock, in *Comprehensive Inorganic Chemistry Vol. 3 ,Vol. 3*, (, Pergamon Press, Oxford **1973**, p. 912.

[7.] F. A. Cotton, G. Wilkinson, C. Murillo, M. Bochmann, *Advanced Inorganic Chemistry*, 6th ed. Wiley-Interscience, New York **1999**.

[8.] J. F. Young, J. A. Osborne, F. H. Jardine, G. Wilkinson, *J.Chem.Soc., Chem.Commun.* **1965,** 131.

[9.] (a) www.nationbynation.com/canada,
(b) www.emsl.pnl.gov/new/ems/2002/symposia.html, *J.Aerosol Sci.* **2005**.

[10.] J. J. Schneider, *Angew.Chem., Int.Ed.Engl.* **1996,** *35*, 1068.

[11.] M. Brookhart, M. L. H. Green, *J.Organomet.Chem.* **1983,** *250*, 395.

[12.] W. Scherer, G. S. McGrady, *Angew.Chem., Int.Ed.Engl.* **2004,** *43*, 1782.

[13.] R. B. Calvert, J. R. Shapley, *J.Am.Chem.Soc.* **1978,** *100*, 7726.

[14.] J. Jaffart, M. Etienne, F. Maseras, J. E. McGrady, O. Eisenstein, *J.Am.Chem.Soc.* **2001,** *123*, 6000.

[15.] G. S. McGrady, A. J. Downs, A. Haaland, W. Scherer, D. C. McKean, *Chem.Commun.* **1997,** 1547.

[16.] X. N. Chen, S. y. Lim, C. E. Plecnik, S. Liu, B. Du, E. A. Meyers, S. G. Shore, *Inorg.Chem.* **2004,** *43*, 692.

[17.] A. Haaland, W. Scherer, K. Ruud, G. S. McGrady, A. J. Downs, O. Swang, *J.Am.Chem.Soc.* **1998,** *120*, 3762.

[18.] W. A. Herrmann, *Angew.Chem., Int.Ed.Engl.* **2002,** *41*, 1290.

[19.] D. F. Shriver, P. W. Atkins, C. H. Langford, *Inorganic Chemistry*, 1st ed. Oxford University Press, Oxford **1990**.

[20.] J. A. Martinho Simões, J. L. Beauchamp, *Chem.Rev.* **1990,** *90*, 629.

[21.] B. A. Arndtsen, R. G. Bergman, T. A. Mobley, T. H. Peterson, *Acc.Chem.Res.* **1995,** *28*, 154.

[22.] G. Wilkinson, J. M. Birmingham, *J.Am.Chem.Soc.* **1955,** *77*, 3421.

[23.] D. Gregson, S. A. Mason, J. A. K. Howard, J. L. Spencer, D. G. Turner, *Inorg.Chem.* **1984,** *23*, 4103.

[24.] D. W. Hart, R. Bau, T. F. Koetzle, *Organometallics* **1985,** *4*, 1590.

[25.] G. J. Kubas, R. R. Ryan, B. I. Swanson, P. J. Vergamini, H. J. Wasserman, *J.Am.Chem.Soc.* **1984,** *106*, 451.

[26.] R. H. Crabtree, P. E. M. Siegbahn, O. Eisenstein, A. L. Rheingold, *Acc.Chem.Res.* **1996,** *29*, 348.

[27.] B. E. Green, C. H. L. Kennard, G. Smith, B. D. James, *Cryst.Struct.Commun.* **1981,** *10*, 1245.

[28.] D. W. Hart, R. G. Teller, C.-Y. Wei, R. Bau, G. Longoni, S. Campanella, P. Chini, T. F. Koetzle, *J.Am.Chem.Soc.* **1981,** *103*, 1458.

[29.] G. J. Kubas, *Acc.Chem.Res.* **1988,** *21*, 120.

[30.] F. A. Cotton, R. L. Luck, *Inorg.Chem.* **1989,** *28*, 6.

[31.] F. Maseras, A. Lledós, E. Clot, O. Eisenstein, *Chem.Rev.* **2000,** *100*, 601.

[32.] D. M. Heinekey, W. J. Oldham, *Chem.Rev.* **1993,** *93*, 913.

[33.] T. J. Marks, J. R. Kolb, *Chem.Rev.* **1977,** *77*, 263.

[34.] T. J. Marks, L. A. Shimp, *J.Am.Chem.Soc.* **1972,** *94*, 1542.

[35.] F. Takusagawa, A. Fumagalli, T. F. Koetzle, S. G. Shore, T. Schmitkons, K. W. Morse, C.-Y. Wei, R. Bau, *J.Am.Chem.Soc.* **1981,** *103*, 5165.

[36.] P. W. Frost, J. A. K. Howard, J. L. Spencer, *J.Chem.Soc., Chem.Commun.* **1984,** 1362.

[37.] M. A. Esteruelas, Y. Jean, A. Lledos, L. A. Oro, N. Ruiz, F. Volatron, *Inorg.Chem.* **1994,** *33*, 3609.

[38.] K. B. Borisenko, A. J. Downs, H. E. Robertson, D. W. H. Rankin, C. Y. Tang, *J.Chem.Soc., Dalton Trans.* **2004,** 967.

[39.] N. N. Greenwood, A. Earnshaw, *Chemistry of the Elements*, 1st ed. Pergamon Press, Oxford **1990,** p. 189.

[40.] D. L. Reger, S. S. Mason, A. L. Rheingold, *J.Am.Chem.Soc.* **1993,** *115*, 10406.

[41.] Z. Xu, Z. Lin, *Coord.Chem.Rev.* **1996,** *156*, 139.

[42.] Fluck and Heumann. Periodic Table of the Elements. 1997. Weinheim, VCH.

[43.] C. Pulham, A. Haaland, A. Hammel, K. Rypdal, H. P. Verne, H. V. Volden, *Angew.Chem., Int.Ed.Engl.* **1992,** *31*, 1464.

[44.] A. L. Beauchamp, M. J. Bennett, F. A. Cotton, *J.Am.Chem.Soc.* **1968,** *90*, 6675.

[45.] R. J. Gillespie, *Chem.Soc.Rev.* **1992,** *21*, 59.

[46.] M. Kaupp, *Angewandte Chemie-International Edition* **2001,** *40*, 3535.

[47.] S. K. Kang, H. Tang, T. A. Albright, *J.Am.Chem.Soc.* **1993,** *115*, 1971.

[48.] P. M. Morse, G. S. Girolami, *J.Am.Chem.Soc.* **1989,** *111*, 4114.

[49.] S. Kleinhenz, V. Pfennig, K. Seppelt, *Chem.Eur.J.* **1998,** *4*, 1687.

[50.] S. K. Kang, T. A. Albright, O. Eisenstein, *Inorg.Chem.* **1989,** *28*, 1611.

[51.] A. Haaland, A. Hammel, K. Rypdal, H. V. Volden, *J.Am.Chem.Soc.* **1990,** *112*, 4547.

[52.] B. Roessler, K. Seppelt, *Angew.Chem., Int.Ed.Engl.* **2000,** *39*, 1259.

[53.] V. Pfennig, K. Seppelt, *Science* **1995,** *271*, 626.

For example: [54.] T. Cleveland, C. R. Landis, *J.Am.Chem.Soc.* **1996,** *118*, 6020.

[55.] M. J. Bearpark, G. S. McGrady, P. D. Prince, J. W. Steed, *J.Am.Chem.Soc.* **2001,** *123*, 7736.

[56.] C. R. Landis, T. Cleveland, T. K. Firman, *J.Am.Chem.Soc.* **1995,** *117*, 1859.

[57.] C. R. Landis, T. K. Firman, D. M. Root, T. Cleveland, *J.Am.Chem.Soc.* **1998,** *120*, 1842.

[58.] G. S. McGrady, A. J. Downs, *Coord.Chem.Rev.* **2000,** *197*, 95.

[59.] R. J. Gillespie, I. Bytheway, T.-H. Tang, R. F. W. Bader, *Inorg.Chem.* **1996,** *35*, 3954.

[60.] I. Bytheway, R. J. Gillespie, T.-H. Tang, R. F. W. Bader, *Inorg.Chem.* **1995,** *34*, 2407.

[61.] R. J. French, L. Hedberg, K. Hedberg, G. L. Gard, B. M. Johnson, *Inorg.Chem.* **1983,** *22*, 892.

[62.] W. Scherer, P. Sirsch, D. Shorokhov, M. Tafipolsky, G. S. McGrady, E. Gullo, *Chem.Eur.J.* **2003,** *9*, 6057.

[63.] E.Y.-X.Chen, T.J.Marks, *Chem.Rev.* **2000,** *100*, 1391.

[64.] M.Bochmann, *J.Chem.Soc., Dalton Trans.* **1996,** 255.

[65.] R.F.Jordan, *Adv.Organomet.Chem.* **1991,** *32*, 325.

[66.] Chem.Rev. **2000,** *100*, 1167.

[67.] Z. Guo, D. C. Swenson, R. F. Jordan, *Organometallics* **1994,** *13*, 1424.

[68.] R. F. Jordan, C. S. Bajgur, R. Willett, B. Scott, *J.Am.Chem.Soc.* **1986,** *108*, 7410.

[69.] G. G. Hlatky, H. W. Turner, R. R. Eckman, *J.Am.Chem.Soc.* **1989,** *111*, 2728.

[70.] G. G. Hlatky, R. R. Eckman, H. W. Turner, *Organometallics* **1992,** *11*, 1413.

[71.] W. Kaminsky, M. Arndt, *Applied Homogeneous Catalysis with Organometallic Compounds*, 1st ed. (Eds.: B.Cornils, W.A.Herrmann) VCH, Weinheim, Germany **1996,** p. 220.

[72.] V. C. Gibson, S. K. Spitzmesser, *Chem.Rev.* **2003,** *103*, 283.

[73.] G. J. P. Britovsek, V. C. Gibson, D. F. Wass, *Angew.Chem., Int.Ed.Engl.* **1999,** *38*, 428.

[74.] K. Mashima, S. Fujikawa, Y. Tanaka, H. Urata, T. Oshiki, E. Tanaka, A. Nakamura, *Organometallics* **1995,** *14*, 2633.

[75.] C. Andes, S. B. Harkins, S. Murtuza, K. Oyler, A. Sen, *J.Am.Chem.Soc.* **2001,** *123*, 7423.

[76.] P. J. W. Deckers, B. Hessen, J. H. Teuben, *Organometallics* **2002,** *21*, 5122.

[77.] S. Feng, G. R. Roof, E. Y.-X. Chen, *Organometallics* **2002,** *21*, 832.

[78.] J. M. Decker, S. J. Geib, T. Y. Meyer, *Organometallics* **1999,** *18*, 4417.

[79.] M. P. Coles, C. I. Dalby, V. C. Gibson, I. R. Little, E. L. Marshall, H. Ribeiro da Costa, S. Masroianni, *J.Organomet.Chem.* **2004,** *591*, 78.

[80.] D. M. Antonelli, A. Leins, J. M. Stryker, *Organometallics* **1997,** *16*, 2500.

[81.] G. C. Bazan, S. J. Donnelly, G. Rodriguez, *J.Am.Chem.Soc.* **1995,** *117*, 2671.

[82.] G. Rodriguez, G. C. Bazan, *J.Am.Chem.Soc.* **1995,** *117*, 10155.

[83.] A. Spannenberg, H. Fuhrmann, P. Arndt, W. Baumann, R. Kempe, *Angew.Chem., Int.Ed.Engl.* **1998,** *37*, 3363.

[84.] J. Jaffart, C. Nayral, R. Choukroun, R. Mathieu, M. Etienne, *Eur.J.Inorg.Chem.* **1998,** 425.

[85.] K. Mashima, S. Fujikawa, H. Urata, E. Tanaka, A. Nakamura, *J.Chem.Soc., Chem.Commun.* **1994,** *14*, 1623.

[86.] K. Mashima, S. Fujikawa, A. Nakamura, *J.Am.Chem.Soc.* **1993,** *115*, 10990.

[87.] E.Y.-X.Chen, K.A.Abboud, *Organometallics* **2000,** *19*, 5541.

[88.] S. Trofimenko, *Chem.Rev.* **1993,** *93*, 943.

[89.] A. L. Rheingold, R. L. Ostrander, B. S. Haggerty, S. Trofimenko, *Inorg.Chem.* **1994,** *33*, 3666.

[90.] R. Toreki, The Oragnometallic Hyper Text Book. http://www.ilpi.com/organomet/ . **2005.**

[91.] U. Siemeling, V. C. Gibson, *J.Organomet.Chem.* **1992,** *426*, C25.

[92.] D. N. Williams, J. P. Mitchell, A. D. Poole, U. Siemeling, W. Clegg, D. C. R. Hockless, P. A. O'Neil, V. C. Gibson, *J.Chem.Soc., Chem.Commun.* **1992,** 739.

[93.] A. D. Poole, V. C. Gibson, W. Clegg, *J.Chem.Soc., Chem.Commun.* **1992,** 237.

[94.] D. M. Antonelli, A. Leins, J. M. Stryker, *Organometallics* **1997,** *16*, 2500.

[95.] D. S. Williams, R. S. Schrock, *Organometallics* **1993,** *12*, 1148.

[96.] M. Etienne, P. S. White, J. L. Templeton, *Organometallics* **1991,** *10*, 3801.

[97.] K. S. Cook, W. E. Piers, S. J. Rettig, R. McDonald, *Organometallics* **2000,** *19*, 2243.

[98.] R. H. Grubbs, G. W. Coates, *Acc.Chem.Res.* **1996,** *29*, 85.

[99.] M. Etienne, *Organometallics* **1994,** *13*, 410.

[100.] M. Etienne, R. Mathieu, B. Donnadieu, *J.Am.Chem.Soc.* **1997,** *119*, 3218.

[101.] A. D. Horton, *Organometallics* **1996,** *15*, 2675.

[102.] X. Yang, T. J. Marks, *J.Am.Chem.Soc.* **1993,** *115*, 3392.

[103.] J. Jaffart, R. Mathieu, M. Etienne, J. E. McGrady, O. Eisenstein, F. Maseras, *Chem.Commun.* **1998,** 2011.

[104.] Â. Domingos, M. R. J. Elsegood, A. C. Hillier, G. Lin, S. Ying Liu, I. Lopes, N. Marques, G. H. Maunder, R. McDonald, A. Sella, J. W. Steed, J. Takats, *Inorg.Chem.* **2002,** *41*, 6761.

[105.] K. Mashima, S. Fujikawa, Y. Tanaka, H. Urata, T. Oshiki, A. J. Sillanpää, E. Tanaka, A. Nakamura, *Organometallics* **1995,** *14* 2633.

[106.] M. Brookhart, B. Grant, A. F. Volpe Jr, *Organometallics* **1992,** *11*, 3920.

[107.] M. D. Leatherman, S. A. Svejda, L. K. Johnson, M. Brookhart, *J.Am.Chem.Soc.* **2003,** *125*, 3068.

[108.] F. M. Alias, M. L. Poveda, M. Sellin, E. Carmona, *J.Am.Chem.Soc.* **1998,** *120*, 5816.

[109.] P. A. White, J. Calabrese, K. H. Theopold, *Organometallics* **1996,** *15*, 5473.

[110.] E. Teuma, Final stage project thesis, Université Paul Sabatier, **1999.**

[111.] S. F. Pedersen, J. B. Hartung Jr., E. J. Roskamp, P. S. Dragovich, in *Inorganic Synthesis - Transition Metal Coordination Compounds* **2003,** pp. 119-123.

[112.] M. Etienne, F. Biasotto, R. Mathieu, J. L. Templeton, *Organometallics* **1996,** *15*, 1106.

[113.] M. Brookhart, M. L. H. Green, L. L. Wong, *Prog.Inorg.Chem.* **1988,** *36*, 1.

[114.] J. L. Templeton, *Adv.Organomet.Chem.* **1989,** *29*, 1.

[115.] M. Etienne, C. Carfagna, P. Lorente, R. Mathieu, D. de Montauzon, *Organometallics* **1999,** *18*, 3075.

[116.] J. Jaffart, M. Etienne, M. Reinhold, J. E. McGrady, F. Maseras, *Chem.Commun.* **2003,** 876.

[117.] J. Jaffart, M. L. Cole, M. Etienne, M. Reinhold, J. E. McGrady, F. Maseras, *Dalton Trans.* **2003,** 4057.

[118.] J. L. Templeton, *Adv.Organomet.Chem.* **1989,** *29*, 1.

[119.] P. Lorente, C. Carfagna, M. Etienne, B. Donnadieu, *Organometallics* **1996,** *15*, 1090.

[120.] R. F. Jordan, R. E. LaPointe, C. S. Bajgur, S. F. Echols, R. Willett, *J.Am.Chem.Soc.* **1987,** *109*, 4111.

[121.] R. F. Jordan, *Adv.Organomet.Chem.* **1991,** *32*, 325.

[122.] S. LaPlaca, J. A. Ibers, *Inorg.Chem.* **1965,** *4*, 778.

[123.] N. A. Bailey, J. M. Jenkins, R. Mason, B. L. Shaw, *Chem.Commun.(London)* **1965,** 237.

[124.] S. Trofimenko, *J.Am.Chem.Soc.* **1968,** *90*, 4754.

[125.] S. Trofimenko, *Inorg.Chem.* **1970,** *9*, 2493.

[126.] F. A. Cotton, T. LaCour, A. G. Stanislowski, *J.Am.Chem.Soc.* **1974,** *96*, 754.

[127.] M. Brookhart, M. L. H. Green, *J.Organomet.Chem.* **1983,** *250*, 395.

[128.] R. H. Grubbs, G. W. Coates, *Acc.Chem.Res.* **1996,** *29*, 85.

[129.] M. Bochmann, *J.Chem.Soc., Dalton Trans.* **1996,** 255.

[130.] E. J. Arlman, P. Cossee, *J.Catal.* **1964,** *3*, 99.

[131.] G. F. Schmidt, M. Brookhart, *J.Am.Chem.Soc.* **1985,** *107*, 1443.

[132.] L. Clawson, J. Soto, S. L. Buchwald, M. L. Steigerwald, R. H. Grubbs, *J.Am.Chem.Soc.* **1985,** *107*, 3377.

[133.] W. A. Piers, J. E. Bercaw, *J.Am.Chem.Soc.* **1990,** *112*, 9406.

[134.] I. J. Ackeman, M. L. H. Green, J. C. Green, J. E. Bercaw, *Organometallics* **2003,** *22*, 188.

[135.] H. Krauledat, H. H. Brintzinger, *Angew.Chem., Int.Ed.Engl.* **1990,** *29*, 1412.

[136.] A. Berry, Z. Dawoodi, A. E. Derome, J. M. Dickinson, A. J. Downs, J. C. Green, M. L. H. Green, P. M. Hare, M. P. Payne, D. W. H. Rankin, H. E. Robertson, *J.Chem.Soc., Chem.Commun.* **1986,** 520.

[137.] W. Scherer, T. Priermeier, A. Haaland, H. V. Volden, G. S. McGrady, A. J. Downs, R. Boese, D. Bläser, *Organometallics* **1998,** *17*, 4406.

[138.] Z. Dawoodi, M. L. H. Green, V. S. B. Mtetwa, K. Prout, A. J. Schultz, J. M. Williams, T. F. Koetzle, *J.Chem.Soc., Dalton Trans.* **1986,** 1629.

[139.] O. Eisenstein, Y. Jean, *J.Am.Chem.Soc.* **1985,** *107*, 1177.

[140.] Z. Dawoodi, M. L. H. Green, V. S. B. Mtetwa, K. Prout, *J.Chem.Soc., Chem.Commun.* **1982,** 802.

[141.] A. Demolliens, Y. Jean, O. Eisenstein, *Organometallics* **1986,** *5*, 1457.

[142.] G. S. McGrady, A. J. Downs, D. C. McKean, A. Haaland, W. Scherer, H. P. Verne, H. V. Volden, *Inorg.Chem.* **1996,** *35*, 4713.

[143.] G. S. McGrady, A. J. Downs, A. Haaland, W. Scherer, H. P. Verne, and H. V. Volden, **2005**. Unpublished Work

[144.] G. Vacek, V. S. Mastryukov, H. F. Schafer, *J.Phys.Chem.* **1994,** *98*, 11337.

[145.] R. F. W. Bader, R. J. Gillespie, P. J. MacDougall, *J.Am.Chem.Soc.* **1988,** *110*, 7329.

[146.] Bader, R. F. W. http://www.chemistry.mcmaster.ca/aim/aim_0.html *Theory of Atoms in Molecules*. **1995.**

[147.] I. Bytheway, R. J. Gillespie, T.-H. Tang, R. F. W. Bader, *Inorg.Chem.* **1995,** *34*, 2407.

[148.] R. J. Gillespie, P. L. A. Popelier, *Chemical Bonding and Molecular Geometry: From Lewis to Electron Densities*, 1st ed. Oxford University Press, New York **2001.**

[149.] U. Giannini, U. Zucchini, *Chem.Commun. (London)* **1968,** 940.

[150.] K. S. Boustany, K. Bernauer, A. Jacot-Guillarmod, *Helv.Chim.Acta* **1967,** *50*, 1080.

[151.] A. Jacot-Guillarmod, D. Roulet, *Chimia* **1974,** *28*, 15.

[152.] R. F. W. Bader, *Chem.Rev.* **1991,** *91*, 893.

[153.] P. Popelier, *Atoms in Molecules:An Introduction*, 1st ed. Pearson Education, **1999.**

[154.] T. S. Koritsanszky, P. Coppens, *Chem.Rev.* **2001,** *101*, 1583.

[155.] A. Haaland, D. J. Shorokhov, N. V. Tverdova, *Chem.Eur.J.* **2004,** *10*, 4416.

[156.] N. P. Chatterton, Ph.D. Thesis, King's College, London, **2003.**

[157.] R. F. W. Bader, *Chem.Rev.* **1991,** *91*, 893.

[158.] H. Stoeckli-Evans, *Helv.Chim.Acta* **1974,** *57*, 684.

[159.] P. Jeske, K. Wieghardt, B. Nuber, *Inorg.Chem.* **1994,** *33*, 53.

[160.] S. P. Varkey, M. Schormann, T. Pape, H. W. Roesky, M. Noltemeyer, R. Herbst-Irmer, H.-G. Schmidt, *Inorg.Chem.* **2001,** *40*, 2427.

[161.] U. Thewalt, D. Schomburg, *J.Organomet.Chem.* **1977,** *127* 169.

[162.] P. Gowik, T. Klapötke, J. Pickardt, *J.Organomet.Chem.* **1990,** *393*, 343.

For Example: [163.] H. Bürger, H. J. Neese, *J.Organomet.Chem.* **1969,** *20*, 129.

[164.] H. Bürger, H. J. Neese, *Chimia* **1970,** *24*, 209.

[165.] H. Bürger, H. J. Neese, *Z.Anorg.Allg.Chem.* **1969,** *370*, 275.

[166.] D. G. Dick, R. Rousseau, D. W. Stephan, *Can. J. Chem.* **1991,** *69*, 357.

[167.] C. Airoldi, D. C. Bradley, H. Chudzynska, M. B. Hursthouse, K. M. A. Malik, P. R. Raithby, *J.Chem.Soc., Dalton Trans.* **1980,** 2010.

[168.] M. Schubart, L. O'Dwyer, L. H. Gade, W.-S. Li, M. McPartlin, *Inorg.Chem.* **1994,** *33*, 3893.

[169.] Z. Duan, L. M. Thomas, J. G. Verkade, *Polyhedron* **1997,** *16*, 635.

[170.] A. Mommertz, R. Leo, W. Massa, K. Harms, K. Dehnicke, *Z.Anorg.Allg.Chem.* **1998,** *624*, 1647.

[171.] T. J. Boyle, T. M. Alam, E. R. Mechenbier, B. L. Scott, J. W. Ziller, *Inorg.Chem.* **1997,** *36*, 3293.

[172.] M. Schormann, S. P. Varkey, H. W. Roesky, M. Noltemeyer, *J.Organomet.Chem.* **2001,** *621*, 310.

[173.] C. Santamaría, R. Beckhaus, D. Haase, W. Saak, R. Koch, *Chem.Eur.J.* **2001,** 622.

[174.] M. E. Gross, T. Siegrist, *Inorg.Chem.* **1992,** *31*, 4898.

[175.] Z. Wu, J. B. Diminnie, Z. Xue, *Inorg.Chem.* **1998,** *37*, 2570.

[176.] P. Briant, J. Green, A. Haaland, H. Møllendal, K. Rypdal, J. Tremmel, *J.Am.Chem.Soc.* **1989,** *111*, 3434.

[177.] D. C. Bradley, H. Chudzynska, J. D. J. Backer-Dirks, M. B. Hursthouse, A. A. Ibrahim, M. Motevalli, A. C. Sullivan, *Polyhedron* **1990,** *9*, 1423.

[178.] G. R. Davies, J. A. J. Jarvis, B. T. Kilbourn, *J.Chem.Soc., Chem.Commun.* **1971,** 1511.

For Example: [179.] A. E. Shilov, G. B. Shul'pin, *Chem.Rev.* **1997,** *97*, 2879.

[180.] A. Chernaga, J. Cook, M. L. H. Green, L. Labella, S. J. Simpson, J. Souter, A. H. H. Stephens, *J.Chem.Soc., Dalton Trans.* **1997,** 3225.

[181.] D. C. McKean, *Int.J.Chem.Kinet.* **1989,** *21*, 445.

[182.] B. A. Arndtsen, R. G. Bergman, T. A. Mobley, T. H. Peterson, *Acc.Chem.Res.* **1995,** *28*, 154.

[183.] M. D. Rausch, H. B. Gordon, *J.Organomet.Chem.* **1974,** *74*, 85.

[184.] G. S. McGrady, Ph.D. thesis, University of Oxford, **1989.**

[185.] G. S. McGrady, A. J. Downs, J. M. Hamblin, D. C. McKean, *Organometallics* **1995,** *14*, 3783.

[186.] S. F. Parker, U. A. Jayasooriya, *Surf.Sci.* **1996,** *368*, 275.

[187.] A. H. J. Robertson, G. P. McQuillan, D. C. McKean, *J.Chem.Soc., Dalton Trans.* **1995,** 3963.

[188.] D. C. McKean, *Croat.Chem.Acta* **1988,** *61*, 447.

[189.] D. C. McKean, G. P. McQuillan, W. F. Murphy, F. Zerbetto, *J.Phys.Chem.* **1990,** *94*, 4820.

[190.] J. C. Lavalley, N. Sheppard, *Spectrochim.Acta, Part A* **1972,** *28*, 2091.

[191.] A. Einstein, *Ann.Physik* **1905,** *17*, 132.

[192.] J. M. Brown, *Molecular Spectroscopy*, 1st ed. Oxford University Press, Oxford **1998.**

[193.] T. C. Koopmans, *Physica 1* **1934,** *2*, 104.

[194.] P. W. Atkins, *Physical Chemistry*, 5th ed. Oxford University Press, Oxford **1994**.

[195.] R. L. DeKock, H. B. Gray, *Chemical Structure and Bonding*, 1st ed. (Eds.: M. Forkner, D. Palmer) The Benjamin/Cummings Publishing Company, Inc., Menlo Park **1980**.

[196.] D. W. Turner, M. I. Al-Joboury, *J.Chem.Phys.* **1962,** *37*, 3007.

[197.] K. Siegbahn, C. Nordling, A. Fahlman, R. Nordberg, K. Hamrin, J. Hedman, G. Johansson, T. Bergmark, S. E. Karlsson, I. Lindgren, and B. J. Lindberg, *Atomic, Molecular and Solid State Structure Studies by Means of Electron Spectroscopy*. [20]. **1967**. Nova Acta Regiae Soc. Sci. Upsaliensis, Ser. IV: Upsala.

[198.] A. L. Lienard, *L'Eclairage Electr.* **1898,** *16*, 5.

[199.] G. A. Schott, *Electromagnetic Radiation*, Cambridge University Press, Cambridge **1912**.

[200.] D. Iwanenko, Pomeranchuk J., *Phys.Rev.Lett.* **1944,** *65*, 343.

[201.] G. Margaritondo, *Introduction to Synchrotron Radiation*, 1st ed. Oxford University Press, New York **1988**.

[202.] D. H. Tomboulian, P. L. Hartman, *Phys.Rev.* **1955,** *102*, 1423.

[203.] *Synchrotron Radiation - techniques and applications*, (Ed.: C. Kunz) Springer, **1979**.

[204.] J. C. Green, *Acc.Chem.Res.* **1994,** *27*, 131.

[205.] J. C. Green, P. Decleva, *Coord.Chem.Rev.* **2005,** *249*, 209.

[206.] B. E. Bursten, J. C. Green, N. Kaltsoyannis, *Inorg.Chem.* **1994,** *33*, 2315.

[207.] J. C. Green, M. F. Guest, I. H. Hillier, S. A. Jarrettsprague, N. Kaltsoyannis, M. A. Macdonald, K. H. Sze, *Inorg.Chem.* **1992,** *31*, 1588.

[208.] K. C. Prince, R. R. Blyth, R. Delaunay, M. Zitnik, J. Krempasky, R. Krempaska, J. Slezak, R. Richter, M. Vondracek, R. Camilloni, L. Avaldi, M. Coreno, G. Stefani, C. Furlani, M. de Simone, S. Stranges, M.-Y. Adam, *J.Electron Spectrosc.Relat.Phenom.* **1999,** *101-103*, 959.

[209.] K. C. Prince, R. R. Blyth, R. Delaunay, M. Zitnik, J. Krempasky, J. Slezak, R. Camilloni, L. Avaldi, M. Coreno, G. Stefani, C. Furlani, M. de Simone, S. Stranges, *J. Synch. Rad.* **1998,** *5*, 565.

[210.] G. Fronzoni, M. de Simone, M. Coreno, K. C. Prince, S. Furlan, P. Franceschi, P. Decleva, *Phys.Chem.Chem.Phys.* **2003,** *5*, 2758.

[211.] M. de Simone, GAP calculator. **2001**.

[212.] J.-J. Yeh, *Atomic calculation of photoionization cross-sections and asymmetry parameters*, 1st ed. Gordon and Breach Science Publishers: Langhorne, PA, **1993**.

[213.] U. Gelius, K. Siegbahn, *Faraday Discussions* **1972,** *54*, 257.

[214.] U. Fano, J. W. Cooper, *Rev. Mod. Phys.* **1968,** *40* 441.

[215.] U. Fano, J. W. Cooper, *Rev. Mod. Phys.* **1969,** *41*, 724.

[216.] V. Brems, http://www.thch.uni-bonn.de/tc/people/brems.vincent/vincent/home.html **2005.**

[217.] B. H. Bransden, C. J. Joachain, *Physics and Atoms of Molecules*, 2nd ed. Prentice Hall, **2003.**

[218.] N. Kaltsoyannis, *J.Chem.Soc., Dalton Trans.* **1997,** 1.

[219.] P. Pyykkö, J. P. Desclaux, *Acc.Chem.Res.* **1979,** *12*, 276.

[220.] I. R. Beattie, P. J. Jones, *Inorg.Chem.* **1979,** *18*, 2318.

[221.] W. A. Herrmann, J. G. Kuchler, J. K. Felixberger, E. Herdtweck, W. Wagner, *Angew. Chem.Int. Ed. Engl.* **1988,** *27*, 394.

[222.] W.A.Herrmann, F.E.Kuhn, R.W.Fischer, W. R. Thiel, C.C.Romao, *Inorg.Chem.* **1992,** *31*, 4431.

[223.] U. N. Flessner, Ph.D. thesis, Technischen Universität München, **1992.**

[224.] W. A. Herrmann, R. W. Fischer, W. Scherer, M. U. Rauch, *Angew. Chem. Int. Ed. Engl.* **1993,** *32*, 1157.

[225.] W. A. Herrmann, W. Wagner, U. N. Flessner, U. Volkhardt, H. Komber, *Angew. Chem. Int. Ed. Engl.* **1991,** *30*, 1636.

[226.] A. J. Anderson, and N. G. Merckling, U.S.Pat. [2.721.189]. **1955.**

[227.] J. L. Herrison, Y. Chauvin, *Makromol.Chem.* **1971,** *141*, 161.

[228.] W. B. Hughes, *J.Am.Chem.Soc.* **1970,** *92*, 532.

[229.] C. P. Casey, T. J. Burkhard, *J.Am.Chem.Soc.* **1974,** *96*, 7808.

[230.] B. Krebs, K. D. Hasse, *Acta Crystallogr., Sect.B: Struct.Sci.* **1976,** *B32*, 1334.

[231.] R. Buffon, A. Auroux, F. Lefebvre, M. Leconte, A. Choplin, J. M. Basset, W. A. Herrmann, *J.Mol.Catal.* **1992,** *76*, 287.

[232.] W. A. Herrmann, J. G. Kuchler, G. Weichselbaumer, E. Herdtweck, P. Kiprof, *J.Organomet.Chem.* **1989,** *272*, 351.

[233.] R. Buffon, A. Choplin, M. Leconte, J. M. Basset, R. Tourouder, W. A. Herrmann, *J.Mol.Catal.* **1992,** *72*, L7.

[234.] L. J. Morris, A. J. Downs, T. M. Greene, S. G. McGrady, W. A. Herrmann, P. Sirsch, W. Scherer, O. Gropen, *Organometallics* **2001,** *20*, 2344.

[235.] L. J. Morris, A. J. Downs, T. M. Greene, G. S. McGrady, W. A. Herrmann, P. Sirsch, O. Gropen, W. Scherer, *Chem. Commun.* **2000,** 67.

[236.] C. C. Romao, F. E. Kuhn, W. A. Herrmann, *Chem. Rev.* **1997,** *97*, 3197.

[237.] H. Kunkely, T. Türk, C. Teixeira, C. de Meric de Bellefon, W. A. Herrmann, A. Volger, *Organometallics* **1991,** *10*, 2090.

[238.] W. A. Herrmann, F. E. Kühn, P. W. Roesky, *J.Organomet.Chem.* **1995,** *485*, 243.

[239.] W. A. Herrmann, P. Kiprof, K. Rypdal, J. Tremmel, R. Blom, R. Alberto, J. Behm, R. W. Albach, H. Bock, B. Solouki, J. Mink, D. Lichtenberger, N. E. Gruhn, *J.Am.Chem.Soc.* **1991,** *113*, 6527.

[240.] P. Wikrent, B. J. Drouin, S. G. Kukolich, J. C. Lilly, M. T. Ashby, W. A. Herrmann, W. Scherer, *J.Chem.Phys.* **1997,** *107*, 2187.

[241.] S. Köstlmeier, O. D. Häberlen, N. Rösch, W. A. Herrmann, B. Solouki, H. Bock, *Organometallics* **1996,** *15*, 1872.

[242.] C. Mealli, J. A. Lopez, M. J. Calhorda, C. C. Romao, W. A. Herrmann, *Inorg.Chem.* **1994,** *33*, 1139.

[243.] J. C. Green, M. F. Guest, I. H. Hillier, S. A. Jarrettsprague, N. Kaltsoyannis, M. A. Macdonald, K. H. Sze, *Inorg.Chem.* **1992,** *31*, 1588.

[244.] B. E. Bursten, J. C. Green, N. Kaltsoyannis, M. A. Macdonald, K. H. Sze, J. S. Tse, *Inorg.Chem.* **1994,** *33* 5086-50.

[245.] Y. F. Hu, G. M. Bancroft, K. H. Tan, *Inorg.Chem.* **2000,** *39*, 1255.

[246.] *Handbook of X-ray and ultraviolet photoelectron spectroscopy*, (Ed.: D.Briggs) Heyden, London **1977**.

[247.] J. A. Bearden, A. F. Burr, *Rev.Mod.Phys.* **1967,** *39*, 125.

[248.] C. N. Field, J. C. Green, N. Kaltsoyannis, G. S. McGrady, A. N. Moody, M. Siggel, M. de Simone, *J.Chem.Soc. Dalton Trans.* **1997,** 213.

[249.] C. Beermann, H. Bestian, *Angew. Chem., Int. Ed. Engl.* **1959,** *71*, 618.

[250.] E. H. Ademan, *J.Polym.Sci., Polym.Symp.* **1968,** *16*, 3643.

[251.] H. H. Brintzinger, D. Fischer, R. Mulhaupt, B. Rieger, R. M. Waymouth, *Angew.Chem., Int.Ed.Engl.* **1995,** *34*, 1143.

[252.] E. J. Arlman, P. Cossee, *J.Catal.* **1964,** *3*, 99.

[253.] R. W. Broach, I.-S. Chuang, T. J. Marks, J. M. Williams, *Inorg.Chem.* **1983,** *22*, 1081.

[254.] E. R. Bernstein, W. C. Hamilton, T. A. Keiderling, S. J. La Placa, S. J. Lippard, J. J. Mayerle, *Inorg.Chem.* **1972,** *11*, 3009.

[255.] D. B. Beach, K. D. Bomben, N. Edelstein, D. C. Eisenberg, W. L. Jolly, R. Shinomoto, A. Streitwieser, *Inorg.Chem.* **1986,** *25*, 1735.

[256.] A. P. Hitchcock, N. Hao, N. H. Werstiuk, M. J. McGlinchey, T. Ziegler, *Inorg.Chem.* **1982,** *21*, 793.

[257.] R. G. Denning, J. C. Green, T. E. Hutchings, C. Dallera, A. Tagliaferri, K. Giarda, N. B. Brookes, L. Braicovich, *J.Chem.Phys.* **2002,** *117*, 8008.

[258.] R. G. Denning, *Struct.Bonding (Berlin)* **1992,** *79*, 215.

[259.] J. Li, B. E. Bursten, *J.Am.Chem.Soc.* **1997,** *119*, 9021.

[260.] J. G. Brennan, J. C. Green, C. M. Redfern, *J.Am.Chem.Soc.* **1989,** *111*, 2373.

[261.] R. H. Banks, N. Edelstein, B. Spencer, D. H. Templeton, A. Zalkin, *J.Am.Chem.Soc.* **1980,** *102*, 620.

[262.] B. G. Sayer, J. I. A. Thompson, H. Nguyen, T. Birchall, *Inorg.Chem.* **1981,** *20*, 3748.

[263.] P. H. Bird, M. R. Churchill, *J.Chem.Soc., Chem.Commun.* **1967,** 403.

[264.] E. R. Bernstein, T. A. Keiderling, S. J. Lippard, J. J. Mayerle, *J.Am.Chem.Soc.* **2004,** *94*, 2552.

[265.] P. Charpin, M. Nierlich, D. Vigner, M. Lance, D. Baudry, *Acta Crystallogr., Sect.C: Cryst.Struct.Commun.* **1987,** *C43*, 1465.

[266.] A. Haaland, D. J. Shorokhov, A. V. Tutukin, H. V. Volden, O. Swang, G. S. McGrady, N. Kaltsoyannis, A. J. Downs, C. Y. Tang, J. F. C. Turner, *Inorg.Chem.* **2002,** *41*, 6646.

[267.] V. Plato, K. Hedberg, *Inorg.Chem.* **1971,** *10*, 590.

[268.] B. N. Cyvin, S. J. Cyvin, J. C. Whitmer, *J.Mol.Struct.* **1979,** *53*, 281.

[269.] B. D. James, B. E. Smith, H. F. Shurvell, *J.Mol.Struct.* **1976,** *33*, 91.

[270.] J. O. Jensen, *Vib.Spectrosc.* **2003,** *31*, 227.

[271.] A. J. Downs, R. G. Egdell, A. F. Orchard, P. D. P. Thomas, *J.Chem.Soc., Dalton Trans.* **1978,** 1755.

[272.] J. C. Green, R. Shinomoto, N. Edelstein, *Inorg.Chem.* **1986,** *25*, 2718.

[273.] D. Hohl, N. Rösch, *Inorg.Chem.* **1986,** *25*, 2711.

[274.] J.-J. Yeh, I. Lindau, *At.Data Nucl.Data Tables* **1985,** *32*, 1.

[275.] E. R. Bernstein, T. A. Keiderling, *J.Chem.Phys.* **1973,** *59*, 2105.

[276.] K. Rajnak, E. Gamp, R. Shinomoto, N. Edelstein, *J.Chem.Phys.* **1984,** *80*, 5942.

[277.] R. J. Erington, *Advanced Practical Inorganic and Metallorganic Chemistry*, Nelson Thornes, New York **1997**.

[278.] Hooft, R. COLLECT Data Collection Software. Nonius B. V. **1998**. Delft.

[279.] Z. Otwinowski, W. Minor, *Macromolecular Crystallography, Part A*, (Eds.: Jr. C. W. Carter, R. M. Sweet) Academic Press, New York **1997,** pp. 307-326.

[280.] G. M. Sheldrick, SHELXL-97, Program for Crystal Structure Refinement. **1997**. University of Göttingen, Germany.

[281.] L. J. Barbour, Xseed, A Programme of the Manipulation and Display of Crystallographic Models. **1999**.

[282.] C. Cason, POV-Ray, The Persistence of Vision Raytracer. **2001**.

[283.] A. Altomare, G. Cascarano, C. Giacovazzo, A. Guagliardi, *J.Appl.Crystallogr.* **1993,** *26*, 343.

[284.] G. Fronzoni, M. de Simone, M. Coreno, K. C. Prince, S. Furlan, P. Franceschi, P. Decleva, *Phys.Chem.Chem.Phys.* **2003,** *5*, 2758.

[285.] R. H. Blessing, *Acta Crystallogr., Sect.A: Found.Crystallogr.* **1995,** *A51*, 33.

[286.] R. F .Stewart, *Acta Crystallogr., Sect.A: Found.Crystallogr.* **1976,** *A32*, 565.

[287.] H. K. Hansen, P. Coppens, *Acta Crystallogr., Sect.A: Found.Crystallogr.* **1978,** *A34*, 909.

[288.] T. Koritsanszky, S. T. Howard, Z. Su, P. R. Mallinson, T. Richter, and N. K. Hansen, XD. Computer Program Package for Multipole Refinement and Analysis of Electron Densities from Diffraction Data. **1997**. Free University of Berlin, Germany.

[289.] E.Clementi, C.Roetti, *At.Data Nucl.Data Tables* **1974,** *14*, 177.

[290.] E. Clementi, D. L. Raimondi, *J.Chem.Phys.* **1963,** *38*, 2686.

[291.] F. Hirshfeld, *Acta Crystallogr., Sect.A: Found.Crystallogr.* **1976,** *A32*, 239.

[292.] J. D. Duntiz, V. Schomaker, K. N. Trueblood, *J.Phys.Chem.* **1988,** *92*, 856.

[293.] J. D. Duntiz, E. F. Maverick, K. N. Trueblood, *Angew.Chem., Int.Ed.Engl.* **1988,** *27*, 880.

[294.] A. D. Becke, *J.Chem.Phys.* **1993,** *98*, 5648.

[295.] C. Lee, W. Yang, R. G. Parr, *Phys.Rev.* **1988,** *B37*, 785.

[296.] M. J. Frisch, G. W. Trucks, H. B. Schlegel, G. E. Scuseria, M. A. Robb, J. R. Cheeseman, V. G. Zakrzewski, J. A. Montgomery Jr, R. E. Stratmann, J. C. Burant, S. Dapprich, J. M. Millam, A. D. Daniels, K. N. Kudin, M. C. Strain, O. Farkas, J. Tomasi, V. Barone, M. Cossi, R. Cammi, B. Mennucci, C. Pomelli, C. Adamo, S. Clifford, J. Ochterski, G. A. Petersson, P. Y. Ayala, Q. Cui, K. Morokuma, D. K. Malick, A. D. Rabuck, K. Raghavachari, J. B. Foresman, J. Cioslowski, J. V. Ortiz, B. B. Stefanov, G. Liu, A. Liashenko, P. Piskorz, I. Komaromi, R. Gomperts, R. L. Martin, D. J. Fox, T. Keith, M. A. Al-Laham, C. Y. Peng, A. Nanayakkara, C. Gonzalez, M. Head-Gordon, E. S. Replogle and J. A. Pople, Gaussian 98 [A.3]. **1998**. Pittsburgh PA, Gaussian Inc.

[297.] F. W. Biegler-König, R. F. W. Bader, T. J. Tang, *J.Comput.Chem.* **1982,** *3*, 317.

[298.] Baerends, E. J. ADF2000.02. 2000.

[299.] E. van Lenthe, J. G. Snijders, E. J. Baerends, *J.Chem.Phys.* **1996,** *105*, 6505.

[300.] E. van Lenthe, R. van Leeuwen, E. J. Baerends, J. G. Snijders, *Int.J.Quantum Chem.* **1996,** *57*, 281.

[301.] S. H. Vosko, L. Wilk, M. Nusair, *Can.J.Phys.* **1980,** *58*, 1200.

[302.] A. D. Becke, *Phys.Rev.* **1988,** *A38*, 2398.

[303.] J. P. Perdew, *Physical Review B* **1986,** *33*, 8822.

[304.] I. W. Bassi, G. Allegra, R. Scordamaglia, G. Chioccola, *J.Am.Chem.Soc.* **1971,** *93*, 15.

[305.] M. T. Reetz, J. Westermann, R. Steinbach, B. Wenderoth, R. Peter, R. Ostarek, S. Maus, *Chem.Ber.* **1985,** *118*, 1421.

Appendix 2

Safety Protocol

Procedure for conducting PES of $U(BH_4)_4$ to avoid residues

1. Pump chamber with Turbo pump to achieve initial vacuum.
2. Change to cryostat pump only.
3. Open sample valve
4. Run experiment
5. Close sample valve
6. Wait until the pressure has dropped to indicate no more sample present in the chamber
7. Close valve to cryostat pump, trapping sample residue
8. Repeat until the end of the sample run

Disposal of trapped residue:

Backfill cryostat pump with N_2, remove trap and transfer to a fume hood.

Partially open to the air allowing slow decomposition to the oxide.

In the event of compressor failure, press RESET

If this does not succeed, close the sample valve.

Appendix 3

Data

A3.1 X-ray Diffraction Studies

[$Tp^{Me2}NbMe(OEt_2)(MeCCMe)][BAr^f_4]$ (2)

Crystal data and structure refinement for $[Tp^{Me2}NbMe(OEt_2)(MeCCMe)][BAr^f_4]$.

Chemical formula	$C_{56}H_{55}B_2F_{24}NbO$	
Formula weight	1398.59	
Temperature	180(2) K	
Radiation, wavelength	MoKα, 0.70930 Å	
Crystal system, space group	Triclinic,	
Unit cell parameters	a = 12.7185(6) Å	α = 91.249(4) °
	b = 13.0870(7) Å	β = 94.824(4) °
	c = 18.5693(10) Å	γ = 99.599(4) °
Cell volume	3034.7(3) $Å^3$	
Z	2	
Calculated density	1.531 g/cm^3	
Absorption coefficient μ	0.317 mm^{-1}	
F(000)	1416	
Data collection method	Bruker SMART 1K CCD diffractometer	
	ω rotation with narrow frames	
θ range for data collection	3.15 to 23.21°	
Index ranges	h −14 to 14, k −12 to 14, l −20 to 19	
Completeness to θ = 23.21°	99.7 %	
Intensity decay	none%	
Reflections collected	17779	
Independent reflections	8700 (R_{int} = 0.0437)	
Reflections with $F^2>2\sigma$	6918	
Absorption correction	empirical (DIFABS)	
Min. and max. transmission	0.963 and 0.886	
Structure solution	direct methods	
Refinement method	Full-matrix least-squares on F^2	
Data / restraints / parameters	8700/ 48 / 820	
Final R indices [$F^2>2\sigma$]	R1 = 0.0793, wR2 = 0.2155	
R indices (all data)	R1 = 0.0935, wR2 = 0.2274	
Goodness-of-fit on F^2	1.057	
Largest diff. peak and hole	1.482 and −1.530 $eÅ^{-3}$	

Atomic coordinates and equivalent isotropic displacement parameters ($Å^2$) for **2**.

U_{eq} is defined as one third of the trace of the orthogonalized U^{ij} tensor.

	x	y	z	U_{eq}
C(1)	6672(6)	11511(6)	8485(4)	52(2)
C(2)	7243(6)	10723(6)	8559(4)	61(2)
C(3)	6882(6)	10012(5)	7995(4)	54(2)
C(4)	6822(7)	12504(7)	8932(4)	72(2)
C(5)	7271(8)	9040(6)	7790(6)	93(3)
C(6)	5658(5)	12253(5)	5781(3)	45(2)
C(7)	6155(5)	11635(5)	5340(4)	48(2)
C(8)	6152(5)	10711(5)	5683(3)	44(2)
C(9)	5514(7)	13343(6)	5653(4)	63(2)
C(10)	6593(6)	9788(6)	5454(4)	63(2)
C(11)	2701(5)	10099(5)	7184(4)	54(2)
C(12)	2576(5)	9049(5)	7059(4)	53(2)
C(13)	3559(5)	8825(5)	6926(3)	42(2)
C(14)	1839(6)	10734(7)	7331(6)	81(3)
C(15)	3869(6)	7823(5)	6742(4)	53(2)
C(16)	3871(7)	11008(7)	8794(5)	72(2)
C(17)	4277(9)	11090(9)	9535(5)	96(3)
O(1)	4041(4)	11997(4)	8432(3)	63(1)
C(18A)	3317(16)	12651(13)	8717(10)	94(4)
C(19A)	3995(15)	13636(13)	9036(9)	94(4)
C(18B)	3980(20)	12990(20)	8812(19)	116(8)
C(19B)	2790(20)	12980(20)	8844(18)	116(8)
C(20)	3709(6)	13310(6)	7115(4)	59(2)
C(21)	3479(5)	12585(5)	6663(4)	46(2)
C(22)	3409(8)	14336(6)	7271(5)	76(2)
C(23)	2786(7)	12303(7)	5935(5)	77(2)
C(30)	10233(4)	6300(4)	6709(3)	28(1)
C(31)	10806(4)	5714(4)	6300(3)	30(1)
C(32)	11179(4)	6046(4)	5648(3)	33(1)
C(33)	11019(5)	6989(5)	5383(3)	37(1)
C(34)	10462(5)	7590(4)	5782(3)	39(1)
C(35)	10076(4)	7247(4)	6428(3)	31(1)
C(36)	11805(5)	5388(5)	5247(3)	42(2)
C(37)	10249(6)	8615(5)	5503(4)	51(2)
C(40)	9848(4)	4807(4)	7734(3)	29(1)
C(41)	10136(5)	4577(5)	8458(3)	36(1)
C(42)	10054(5)	3556(5)	8675(3)	45(2)
C(43)	9719(5)	2731(5)	8185(4)	46(2)
C(44)	9445(5)	2946(5)	7473(3)	38(1)
C(45)	9500(4)	3961(4)	7264(3)	31(1)
C(46)	9083(6)	2079(5)	6932(4)	50(2)
C(50)	10597(4)	6840(4)	8068(3)	28(1)
C(51)	10297(5)	7711(4)	8377(3)	34(1)
C(52)	11017(5)	8420(4)	8818(3)	37(1)
C(53)	12067(5)	8285(5)	8963(3)	40(1)
C(54)	12392(5)	7441(5)	8649(3)	38(1)
C(55)	11671(4)	6728(4)	8215(3)	33(1)
C(57)	13525(5)	7261(6)	8797(4)	52(2)
C(60)	8549(4)	6115(4)	7523(3)	29(1)
C(61)	7862(4)	6170(4)	6909(3)	30(1)
C(62)	6790(4)	6229(4)	6935(3)	35(1)
C(63)	6352(5)	6220(4)	7594(3)	39(1)

Atomic coordinates and equivalent isotropic displacement parameters ($Å^2$) for **2** continued.

C(64)	7013(5)	6139(5)	8217(3)	38(1)
C(65)	8080(4)	6087(4)	8175(3)	34(1)
C(67)	6113(5)	6328(5)	6245(4)	46(2)
C(24)	5979(6)	13458(5)	7419(4)	59(2)
B(1)	5462(5)	9954(5)	6878(4)	37(2)
B(2)	9814(5)	6006(5)	7503(3)	28(1)
N(1)	5944(4)	11309(4)	7895(3)	42(1)
N(2)	6091(4)	10377(4)	7594(3)	41(1)
N(3)	5657(4)	10770(4)	6302(2)	35(1)
N(4)	5353(4)	11731(4)	6364(3)	38(1)
N(5)	4270(4)	9730(3)	6988(3)	35(1)
N(6)	3749(4)	10521(4)	7146(3)	47(1)
F(1)	11848(4)	5614(4)	4551(2)	67(1)
F(2)	12805(3)	5463(4)	5523(2)	61(1)
F(3)	11381(4)	4374(3)	5245(3)	70(1)
F(4)	11043(5)	9081(4)	5156(4)	120(2)
F(5)	9439(5)	8521(4)	5018(3)	114(2)
F(6)	10114(6)	9262(4)	6009(3)	105(2)
F(7)	9718(6)	2134(4)	6395(3)	113(2)
F(8)	9149(5)	1153(3)	7176(3)	96(2)
F(9)	8158(5)	2071(5)	6630(5)	160(4)
C(47)	10292(7)	3359(5)	9455(5)	76(3)
F(10A)	10994(9)	2661(8)	9502(5)	102(2)
F(11A)	10746(10)	4136(9)	9888(5)	102(2)
F(12A)	9486(9)	2989(8)	9805(5)	102(2)
F(10B)	10434(15)	2429(11)	9645(8)	102(2)
F(11B)	11100(14)	4107(14)	9735(8)	102(2)
F(12B)	9429(13)	3542(13)	9828(7)	102(2)
C(56)	10648(5)	9298(5)	9151(4)	50(2)
F(13A)	11390(6)	9990(6)	9519(5)	96(2)
F(14A)	10199(7)	9895(6)	8650(5)	96(2)
F(15A)	9746(7)	9065(7)	9454(5)	96(2)
F(13B)	11023(17)	10228(10)	8904(11)	96(2)
F(14B)	9583(12)	9276(16)	9126(12)	96(2)
F(15B)	10725(16)	9228(13)	9887(7)	96(2)
F(16)	13838(3)	6685(4)	8303(2)	74(1)
F(17)	14218(4)	8148(5)	8819(4)	118(2)
F(18)	13694(4)	6838(6)	9418(3)	103(2)
C(66)	6577(5)	6115(5)	8927(4)	55(2)
F(19A)	6873(11)	5303(8)	9302(5)	77(1)
F(20A)	7083(8)	6956(8)	9369(4)	77(1)
F(21A)	5554(7)	6128(10)	8959(5)	77(1)
F(19B)	7020(11)	5652(10)	9460(5)	77(1)
F(20B)	6275(9)	6979(8)	9128(5)	77(1)
F(21B)	5537(7)	5504(9)	8860(5)	77(1)
F(22)	6428(3)	5859(3)	5679(2)	64(1)
F(23)	5088(3)	5927(3)	6283(2)	65(1)
F(24)	6152(3)	7318(3)	6075(2)	62(1)
Nb(1)	4647(1)	12163(1)	7366(1)	44(1)

Bond lengths [Å] and torsion angles [°] for **2**.

C(1)–C(2)	1.359(11)	C(19A)–H(19A)	0.9800
C(1)–N(1)	1.366(8)	C(19A)–H(19B)	0.9800
C(1)–C(4)	1.502(10)	C(19A)–H(19C)	0.9800
C(2)–C(3)	1.381(10)	C(18B)–C(19B)	1.52(2)
C(2)–H(2)	0.9500	C(18B)–H(18C)	0.9900
C(3)–N(2)	1.357(8)	C(18B)–H(18D)	0.9900
C(3)–C(5)	1.494(11)	C(19B)–H(19D)	0.9800
C(4)–H(4A)	0.9800	C(19B)–H(19E)	0.9800
C(4)–H(4B)	0.9800	C(19B)–H(19F)	0.9800
C(4)–H(4C)	0.9800	C(20)–C(21)	1.234(10)
C(5)–H(5A)	0.9800	C(20)–C(22)	1.484(11)
C(5)–H(5B)	0.9800	C(20)–Nb(1)	2.047(7)
C(5)–H(5C)	0.9800	C(21)–H(21)	1.0000
C(6)–N(4)	1.343(8)	C(22)–H(22A)	0.9800
C(6)–C(7)	1.397(10)	C(22)–H(22B)	0.9800
C(6)–C(9)	1.491(9)	C(22)–H(22C)	0.9800
C(7)–C(8)	1.379(9)	C(23)–H(23A)	0.9802
C(7)–H(7)	0.9500	C(23)–H(23B)	0.9802
C(8)–N(3)	1.362(8)	C(23)–H(23C)	0.9802
C(8)–C(10)	1.483(10)	C(30)–C(35)	1.394(8)
C(9)–H(9A)	0.9800	C(30)–C(31)	1.395(8)
C(7)–H(9B)	0.9800	C(30)–B(2)	1.642(8)
C(7)–H(9C)	0.9800	C(31)–C(32)	1.390(8)
C(7)–H(10A)	0.9800	C(31)–H(31)	0.9500
C(7)–H(10B)	0.9800	C(32)–C(33)	1.378(8)
C(7)–H(10C)	0.9800	C(32)–C(36)	1.493(8)
C(8)–N(6)	1.364(8)	C(33)–C(34)	1.386(9)
C(7)–C(12)	1.370(10)	C(33)–H(33)	0.9500
C(7)–C(14)	1.519(10)	C(34)–C(35)	1.389(8)
C(7)–C(13)	1.371(10)	C(34)–C(37)	1.506(9)
C(7)–H(12)	0.9500	C(35)–H(35)	0.9500
C(8)–N(5)	1.361(8)	C(36)–F(2)	1.318(7)
C(13)–C(15)	1.474(9)	C(36)–F(1)	1.336(7)
C(14)–H(14A)	0.9800	C(36)–F(3)	1.346(8)
C(14)–H(14B)	0.9800	C(36)–F(6)	1.293(8)
C(14)–H(14C)	0.9800	C(36)–F(5)	1.298(8)
C(15)–H(15A)	0.9800	C(36)–F(4)	1.315(9)
C(15)–H(15B)	0.9800	C(40)–C(45)	1.383(8)
C(15)–H(15C)	0.9800	C(40)–C(41)	1.414(8)
C(16)–C(17)	1.424(12)	C(40)–B(2)	1.644(8)
C(16)–O(1)	1.464(9)	C(41)–C(42)	1.394(9)
C(16)–H(16A)	0.9900	C(41)–H(41)	0.9500
C(16)–H(16B)	0.9900	C(42)–C(43)	1.383(9)
C(17)–H(17A)	0.9800	C(42)–C(47)	1.492(10)
C(17)–H(17B)	0.9800	C(43)–C(44)	1.385(9)
C(17)–H(17C)	0.9800	C(43)–H(43)	0.9500
O(1)–C(18A)	1.478(15)	C(44)–C(45)	1.384(8)
O(1)–C(18B)	1.48(2)	C(44)–C(46)	1.486(9)
O(1)–Nb(1)	2.186(5)	C(45)–H(45)	0.9500
C(18A)–C(19A)	1.51(2)	C(46)–F(9)	1.258(9)
C(18A)–H(18A)	0.9900	C(46)–F(8)	1.316(8)
C(18A)–H(18B)	0.9900	C(46)–F(7)	1.331(9)

Bond lengths [Å] and torsion angles [°] for **2** continued.

C(50)–C(51)	1.389(8)	C(24)–H(24A)	0.9800
C(50)–C(55)	1.403(8)	C(24)–H(24B)	0.9800
C(50)–B(2)	1.642(8)	C(24)–H(24C)	0.9800
C(51)–C(52)	1.388(8)	B(1)–N(5)	1.527(8)
C(51)–H(51)	0.9500	B(1)–N(3)	1.533(8)
C(52)–C(53)	1.382(9)	B(1)–N(2)	1.535(8)
C(52)–C(56)	1.456(9)	B(1)–H(1)	1.0000
C(53)–C(54)	1.376(9)	N(1)–N(2)	1.379(7)
C(53)–H(53)	0.9500	N(1)–Nb(1)	2.307(5)
C(54)–C(55)	1.386(8)	N(3)–N(4)	1.381(7)
C(54)–C(57)	1.502(9)	N(4)–Nb(1)	2.233(5)
C(55)–H(55)	0.9500	N(5)–N(6)	1.358(7)
C(57)–F(16)	1.305(8)	N(6)–Nb(1)	2.270(5)
C(57)–F(18)	1.307(8)	C(47)–F(12A)	1.293(11)
C(57)–F(17)	1.333(9)	C(47)–F(11A)	1.306(11)
C(60)–C(61)	1.391(8)	C(47)–F(10B)	1.312(12)
C(60)–C(65)	1.394(8)	C(47)–F(11B)	1.354(14)
C(60)–B(2)	1.642(8)	C(47)–F(10A)	1.379(11)
C(61)–C(62)	1.384(8)	C(47)–F(12B)	1.396(13)
C(61)–H(61)	0.9500	C(56)–F(15A)	1.313(9)
C(62)–C(63)	1.387(9)	C(56)–F(13A)	1.325(9)
C(62)–C(67)	1.503(9)	C(56)–F(13B)	1.337(13)
C(63)–C(64)	1.388(9)	C(56)–F(14B)	1.347(14)
C(63)–H(63)	0.9500	C(56)–F(15B)	1.368(13)
C(64)–C(65)	1.379(8)	C(56)–F(14A)	1.376(9)
C(64)–C(66)	1.470(9)	C(66)–F(20B)	1.310(10)
C(65)–H(65)	0.9500	C(66)–F(21A)	1.310(10)
C(67)–F(23)	1.331(8)	C(66)–F(19B)	1.315(11)
C(67)–F(22)	1.330(8)	C(66)–F(19A)	1.371(11)
C(67)–F(24)	1.334(7)	C(66)–F(20A)	1.392(10)
C(24)–Nb(1)	2.182(7)	C(66)–F(21B)	1.422(10)
C(2)–C(1)–N(1)	109.7(6)	C(6)–C(7)–H(7)	126.9
C(2)–C(1)–C(4)	127.7(7)	N(3)–C(8)–C(7)	107.9(6)
N(1)–C(1)–C(4)	122.5(7)	N(3)–C(8)–C(10)	123.5(6)
C(1)–C(2)–C(3)	107.5(6)	C(7)–C(8)–C(10)	128.6(6)
C(1)–C(2)–H(2)	126.3	C(6)–C(9)–H(9A)	109.5
C(3)–C(2)–H(2)	126.3	C(6)–C(9)–H(9B)	109.5
N(2)–C(3)–C(2)	107.3(6)	H(9A)–C(9)–H(9B)	109.5
N(2)–C(3)–C(5)	122.6(6)	C(6)–C(9)–H(9C)	109.5
C(2)–C(3)–C(5)	130.0(7)	H(9A)–C(9)–H(9C)	109.5
C(1)–C(4)–H(4A)	109.5	H(9B)–C(9)–H(9C)	109.5
C(1)–C(4)–H(4B)	109.5	C(8)–C(10)–H(10A)	109.5
H(4A)–C(4)–H(4B)	109.5	C(8)–C(10)–H(10B)	109.5
C(1)–C(4)–H(4C)	109.5	H(10A)–C(10)–H(10B)	109.5
H(4A)–C(4)–H(4C)	109.5	C(8)–C(10)–H(10C)	109.5
H(4A)–C(4)–H(4C)	109.5	H(10A)–C(10)–H(10C)	109.5
C(3)–C(4)–H(4B)	109.5	H(10B)–C(10)–H(10C)	109.5
C(3)–C(4)–H(4B)	109.5	N(6)–C(11)–C(12)	109.0(6)
H(5A)–C(4)–H(4B)	109.5	N(6)–C(11)–C(14)	123.6(6)
C(3)–C(4)–H(4B)	109.5	C(12)–C(11)–C(14)	127.5(7)
H(5A)–C(4)–H(4B)	109.5	C(11)–C(12)–C(13)	107.1(6)
H(5B)–C(4)–H(4B)	109.5	C(11)–C(9)–H(12)	126.5
N(4)–C(6)–C(7)	109.8(6)	C(13)–C(9)–H(12)	126.5
N(4)–C(6)–C(9)	124.0(6)	N(5)–C(13)–C(12)	107.7(6)
C(7)–C(6)–C(9)	126.1(6)	N(5)–C(13)–C(15)	122.6(6)

Torsion angles [°] for **2** continued.

C(8)–C(7)–C(6)	106.2(6)	C(12)–C(13)–C(15)	129.7(6)
C(8)–C(7)–H(7)	126.9	C(11)–C(14)–H(14A)	109.5
C(11)–C(14)–H(14B)	109.5	C(20)–C(22)–H(22A)	109.5
H(14A)–C(14)–H(14B)	109.5	C(20)–C(22)–H(22B)	109.5
C(11)–C(14)–H(14C)	109.5	H(22A)–C(22)–H(22B)	109.5
H(14A)–C(14)–H(14C)	109.5	C(20)–C(22)–H(22C)	109.5
H(14B)–C(14)–H(14C)	109.5	H(22A)–C(22)–H(22C)	109.5
C(13)–C(15)–H(14C)	109.5	H(22B)–C(22)–H(22C)	109.5
C(13)–C(15)–H(15A)	109.5	C(21)–C(23)–H(23A)	109.5
H(15A)–C(15)–H(15B)	109.5	C(21)–C(23)–H(23B)	109.5
C(13)–C(15)–H(15C)	109.5	H(23A)–C(23)–H(23B)	109.5
H(15A)–C(15)–H(15C)	109.5	C(21)–C(23)–H(23C)	109.5
H(15B)–C(15)–H(15C)	109.5	H(23A)–C(23)–H(23C)	109.5
C(17)–C(16)–O(1)	113.3(8)	H(23B)–C(23)–H(23C)	109.5
C(17)–C(16)–H(16A)	108.9	C(35)–C(30)–C(31)	115.8(5)
O(1)–C(16)–H(16A)	108.9	C(35)–C(30)–B(2)	118.3(5)
C(17)–C(16)–H(16B)	108.9	C(31)–C(30)–B(2)	125.8(5)
O(1)–C(16)–H(16B)	108.9	C(32)–C(31)–C(30)	122.1(5)
H(16A)–C(16)–H(16B)	107.7	C(32)–C(31)–H(31)	118.9
C(16)–C(17)–H(17A)	109.5	C(30)–C(31)–H(31)	118.9
C(15)–C(17)–H(17B)	109.5	C(33)–C(32)–C(31)	121.0(5)
H(17A)–C(17)–H(17B)	109.5	C(33)–C(32)–C(36)	119.7(5)
C(16)–C(17)–H(17C)	109.5	C(31)–C(32)–C(36)	119.2(5)
H(17A)–C(17)–H(17C)	109.5	C(32)–C(33)–C(34)	118.0(5)
H(17B)–C(17)–H(17C)	109.5	C(32)–C(33)–H(33)	121.0
C(16)–O(1)–C(18A)	107.6(9)	C(34)–C(33)–H(33)	121.0
C(16)–O(1)–C(18B)	121.7(16)	C(33)–C(34)–C(35)	120.7(5)
C(18A)–O(1)–C(18B)	35.0(13)	C(33)–C(34)–C(37)	119.6(5)
C(16)–O(1)–Nb(1)	123.0(5)	C(35)–C(34)–C(37)	119.7(6)
C(18A)–O(1)–Nb(1)	123.9(8)	C(34)–C(34)–C(30)	122.4(5)
C(18B)–O(1)–Nb(1)	114.6(15)	C(34)–C(35)–H(35)	118.8
O(1)–C(18A)–C(19A)	107.8(13)	C(30)–C(35)–H(35)	118.8
O(1)–C(18A)–H(18A)	110.2	F(2)–C(36)–F(1)	106.2(5)
C(19A)–C(18A)–H(18A)	110.2	F(2)–C(36)–F(3)	106.0(5)
O(1)–C(18A)–H(18B)	110.1	F(1)–C(36)–F(3)	105.2(5)
C(19A)–C(18A)–H(18B)	110.1	F(2)–C(36)–C(32)	113.1(5)
H(18A)–C(18A)–H(18B)	108.5	F(1)–C(36)–C(32)	113.4(5)
O(1)–C(18B)–C(19B)	104.6(17)	F(3)–C(36)–C(32)	112.3(5)
O(1)–C(18B)–H(18C)	110.9	F(6)–C(37)–F(5)	108.9(7)
C(19B)–C(18B)–H(18C)	110.8	F(6)–C(37)–F(4)	106.3(7)
O(1)–C(18B)–H(18D)	110.8	F(5)–C(37)–F(4)	102.9(7)
C(19B)–C(18B)–H(18C)	110.8	F(6)–C(37)–C(34)	113.2(6)
H(18C)–C(18B)–H(18D)	108.9	F(5)–C(37)–C(34)	113.0(6)
C(18B)–C(19B)–H(19D)	109.5	F(4)–C(37)–C(34)	111.8(6)
C(18B)–C(19B)–H(19E)	109.5	C(45)–C(40)–C(41)	115.9(5)
H(19D)–C(19B)–H(19E)	109.5	C(45)–C(40)–B(2)	122.9(5)
C(18B)–C(19B)–H(19F)	109.5	C(41)–C(40)–B(2)	120.9(5)
H(19D)–C(19B)–H(19F)	109.5	C(42)–C(41)–C(40)	121.3(6)
H(19E)–C(19B)–H(19F)	109.5	C(42)–C(41)–H(41)	119.4
C(21)–C(20)–C(22)	139.3(8)	C(40)–C(41)–H(41)	119.4
C(21)–C(20)–Nb(1)	70.2(5)	C(43)–C(42)–C(41)	121.1(6)
C(22)–C(20)–Nb(1)	150.5(6)	C(43)–C(42)–C(47)	119.9(6)
C(21)–C(20)–H(20)	90.4	C(41)–C(42)–C(47)	118.9(6)
C(22)–C(20)–H(20)	90.4	C(42)–C(43)–C(44)	118.2(6)
Nb(1)–C(20)–H(20)	90.4	C(42)–C(43)–H(43)	120.9
C(20)–C(21)–C(23)	139.4(7)	C(44)–C(43)–H(43)	120.9

Torsion angles [°] for **2** continued.

C(20)–C(21)–Nb(1)	75.3(5)	C(45)–C(44)–C(43)	120.6(6)
C(23)–C(21)–Nb(1)	144.9(5)	C(45)–C(44)–C(46)	119.8(5)
C(20)–C(21)–H(21)	92.0	C(43)–C(44)–C(46)	119.6(6)
C(23)–C(21)–H(21)	92.0	C(40)–C(45)–C(44)	123.0(5)
Nb(1)–C(21)–H(21)	92.0	C(40)–C(45)–H(45)	118.5
C(44)–C(45)–H(45)	118.5	H(24A)–C(24)–H(24C)	109.5
F(9)–C(46)–F(8)	109.1(7)	H(24B)–C(24)–H(24C)	109.5
F(9)–C(46)–F(7)	105.2(8)	N(5)–B(1)–N(3)	109.4(5)
F(8)–C(46)–F(7)	101.8(6)	N(5)–B(1)–N(2)	109.0(5)
F(9)–C(46)–C(44)	113.9(6)	N(3)–B(1)–N(2)	109.2(5)
F(8)–C(46)–C(44)	114.5(6)	N(5)–B(1)–H(1)	109.8
F(7)–C(46)–C(44)	111.2(6)	N(3)–B(1)–H(1)	109.7
C(51)–C(50)–C(55)	116.3(5)	N(2)–B(1)–H(1)	109.8
C(51)–C(50)–B(2)	124.5(5)	C(60)–B(2)–C(50)	111.9(4)
C(55)–C(50)–B(2)	119.0(5)	C(60)–B(2)–C(30)	111.0(4)
C(52)–C(51)–C(50)	121.8(5)	C(50)–B(2)–C(30)	104.1(4)
C(52)–C(51)–H(51)	119.1	C(60)–B(2)–C(40)	103.8(4)
C(50)–C(51)–H(51)	119.1	C(50)–B(2)–C(40)	111.3(4)
C(53)–C(52)–C(51)	120.9(5)	C(30)–B(2)–C(4)	115.1(4)
C(53)–C(52)–C(56)	119.7(6)	C(1)–N(1)–N(2)	106.1(5)
C(51)–C(52)–C(56)	119.4(6)	C(1)–N(1)–Nb(1)	134.4(5)
C(54)–C(53)–C(52)	118.6(5)	N(2)–N(1)–Nb(1)	119.6(4)
C(54)–C(53)–H(53)	120.7	C(3)–N(2)–N(1)	109.5(5)
C(52)–C(53)–H(53)	120.7	C(3)–N(2)–B(1)	130.2(6)
C(53)–C(54)–C(55)	120.5(6)	N(1)–N(2)–B(1)	120.2(5)
C(53)–C(54)–C(57)	120.2(5)	C(8)–N(3)–N(4)	109.3(5)
C(55)–C(54)–C(57)	119.2(5)	C(8)–N(3)–B(1)	128.5(5)
C(54)–C(55)–C(50)	121.9(5)	N(4)–N(3)–B(1)	122.2(5)
C(54)–C(55)–H(55)	119.0	C(6)–N(4)–N(3)	106.8(5)
C(50)–C(55)–H(55)	119.0	C(6)–N(4)–Nb(1)	133.5(4)
F(16)–C(57)–F(18)	107.3(6)	N(3)–N(4)–Nb(1)	119.4(3)
F(16)–C(57)–F(17)	104.6(6)	N(6)–N(5)–C(13)	109.3(5)
F(18)–C(57)–F(17)	106.0(6)	N(6)–N(5)–B(1)	119.9(5)
F(16)–C(57)–C(54)	114.0(5)	C(13)–N(5)–B(1)	130.7(5)
F(18)–C(57)–C(54)	112.9(6)	N(5)–N(6)–C(11)	107.0(5)
F(17)–C(57)–C(54)	111.4(6)	N(5)–N(6)–Nb(1)	121.3(4)
C(61)–C(60)–C(65)	115.7(5)	C(11)–N(6)–Nb(1)	131.6(4)
C(61)–C(60)–B(2)	123.6(5)	F(12A)–C(47)–F(11A)	100.5(10)
C(65)–C(60)–B(2)	120.6(5)	F(12A)–C(47)–F(10B)	73.5(10)
C(62)–C(61)–C(60)	122.5(5)	F(11A)–C(47)–F(10B)	117.0(12)
C(62)–C(61)–H(61)	118.7	F(12A)–C(47)–F(11B)	123.2(12)
C(60)–C(61)–H(61)	118.7	F(11A)–C(47)–F(11B)	24.1(11)
C(61)–C(62)–C(63)	120.4(5)	F(10B)–C(47)–F(11B)	112.4(12)
C(61)–C(62)–C(67)	119.2(5)	F(12A)–C(47)–F(10A)	107.2(8)
C(63)–C(62)–C(67)	120.4(5)	F(11A)–C(47)–F(10A)	104.7(9)
C(62)–C(63)–C(64)	118.2(5)	F(10B)–C(47)–F(10A)	34.3(8)
C(62)–C(63)–H(63)	120.9	F(11B)–C(47)–F(10A)	88.8(11)
C(64)–C(63)–H(63)	120.9	F(12A)–C(47)–F(12B)	31.6(8)
C(65)–C(64)–C(63)	120.4(5)	F(11A)–C(47)–F(12B)	78.9(10)
C(65)–C(64)–C(66)	119.6(5)	F(10B)–C(47)–F(12B)	103.8(12)
C(63)–C(64)–C(66)	120.0(5)	F(11B)–C(47)–F(12B)	103.0(13)
C(64)–C(65)–C(60)	122.7(5)	F(10A)–C(47)–F(12B)	135.4(9)
C(64)–C(65)–H(65)	118.6	F(12A)–C(47)–C(42)	116.6(7)
C(60)–C(65)–H(65)	118.6	F(11A)–C(47)–C(42)	118.7(7)
F(23)–C(67)–F(22)	106.5(5)	F(10B)–C(47)–C(42)	119.3(9)
F(23)–C(67)–F(24)	107.1(5)	F(11B)–C(47)–C(42)	108.5(9)

Torsion angles [°] for **2** continued.

F(22)–C(67)–F(24)	105.8(5)	F(10A)–C(47)–C(42)	108.0(8)
F(23)–C(67)–C(62)	112.5(5)	F(12B)–C(47)–C(42)	108.5(8)
F(22)–C(67)–C(62)	112.9(5)	F(15A)–C(56)–F(13A)	115.1(7)
F(24)–C(67)–C(62)	111.5(5)	F(15A)–C(56)–F(13B)	124.9(10)
Nb(1)–C(24)–H(24A)	109.5	F(13A)–C(56)–F(13B)	56.6(10)
Nb(1)–C(24)–H(24B)	109.5	F(15A)–C(56)–F(14B)	30.6(10)
H(24A)–C(24)–H(24B)	109.5	F(13A)–C(56)–F(14B)	125.9(10)
Nb(1)–C(24)–H(24C)	109.5	F(13B)–C(56)–F(14B)	103.9(13)
F(15A)–C(56)–F(15B)	63.2(9)	F(20B)–C(66)–C(64)	114.6(6)
F(13A)–C(56)–F(15B)	63.7(9)	F(21A)–C(66)–C(64)	119.2(6)
F(13B)–C(56)–F(15B)	115.7(12)	F(19B)–C(66)–C(64)	119.8(7)
F(14B)–C(56)–F(15B)	91.8(13)	F(19A)–C(66)–C(64)	109.4(7)
F(15A)–C(56)–F(14A)	92.0(7)	F(20A)–C(66)–C(64)	111.0(6)
F(13A)–C(56)–F(14A)	102.4(7)	F(21B)–C(66)–C(64)	108.9(6)
F(13B)–C(56)–F(14A)	49.0(10)	C(21)–Nb(1)–C(20)	34.5(3)
F(14B)–C(56)–F(14A)	62.4(11)	C(21)–Nb(1)–C(24)	105.6(3)
F(15B)–C(56)–F(14A)	136.8(9)	C(20)–Nb()–C(24)	84.0(3)
F(15A)–C(56)–C(52)	114.8(6)	C(21)–Nb(1)–O(1)	108.3(2)
F(13A)–C(56)–C(52)	116.4(6)	C(20)–Nb(1)–O(1)	90.9(2)
F(13B)–C(56)–C(52)	115.8(8)	C(24)–Nb()1–O(1)	108.9(2)
F(14B)–C(56)–C(52)	117.3(10)	C(21)–Nb(1)–N(4)	84.6(2)
F(15B)–C(56)–C(52)	110.0(8)	C(20)–Nb(1)–N(4)	108.5(2)
F(14A)–C(56)–C(52)	112.5(6)	C(24)–Nb(1)–N(4)	82.8(2)
F(20B)–C(66)–F(21A)	61.1(7)	O(1)–Nb(1)–N(4)	158.55(19)
F(20B)–C(66)–F(19B)	113.8(8)	C(21)–Nb(1)–N(6)	85.3(2)
F(21A)–C(66)–F(19B)	114.5(10)	C(20)–Nb(1)–N(6)	113.6(3)
F(20B)–C(66)–F(19A)	132.8(8)	C(24)–Nb(1)–N(6)	158.3(2)
F(21A)–C(66)–F(19A)	110.2(8)	O(1)–Nb(1)–N(6)	84.5(2)
F(19B)–C(66)–F(19A)	22.3(8)	N(4)–Nb(1)–N(6)	79.53(19)
F(20B)–C(66)–F(20A)	47.5(6)	C(21)–Nb(1)–N(1)	163.0(2)
F(21A)–C(66)–F(20A)	104.2(8)	C(20)–Nb(1)–N(1)	162.0(3)
F(19B)–C(66)–F(20A)	78.9(8)	C(24)–Nb(1)–N(1)	82.5(3)
F(19A)–C(66)–F(20A)	101.2(8)	O(1)–Nb(1)–N(1)	82.31(19)
F(20B)–C(66)–F(21B)	96.1(7)	N(4)–Nb(1)–N(1)	81.51(18)
F(21A)–C(66)–F(21B)	35.0(6)	N(6)–Nb(1)–N(1)	82.5(19)
F(19B)–C(66)–F(21B)	99.3(9)		
F(19A)–C(66)–F(21B)	84.9(8)		
F(20A)–C(66)–F(21B)	134.6(7)		

Anisotropic displacement parameters ($Å^2$) for **2**.
The anisotropic displacement factor exponent takes the form: $-2\pi^2[h^2a^{*2}U^{11} + ...+ 2hka^*b^*U^{12}]$

	U^{11}	U^{22}	U^{33}	U^{23}	U^{13}	U^{12}
C(1)	51(4)	65(5)	36(4)	–4(3)	–2(3)	–1(4)
C(2)	58(4)	66(5)	52(4)	10(4)	–18(4)	2(4)
C(3)	51(4)	47(4)	62(5)	11(3)	–15(4)	7(3)
C(4)	67(5)	94(6)	48(4)	–24(4)	–11(4)	6(5)
C(5)	93(7)	48(5)	130(8)	–2(5)	–59(6)	28(5)
C(6)	43(4)	48(4)	42(4)	10(3)	2(3)	5(3)
C(7)	41(4)	61(4)	40(4)	10(3)	5(3)	–2(3)
C(8)	34(3)	51(4)	42(4)	–11(3)	4(3)	–5(3)
C(9)	74(5)	59(5)	66(5)	27(4)	14(4)	17(4)
C(10)	59(5)	60(5)	71(5)	–15(4)	28(4)	2(4)
C(11)	43(4)	52(4)	67(5)	6(3)	11(3)	7(3)
C(12)	39(4)	58(4)	57(4)	7(3)	1(3)	–6(3)
C(13)	43(4)	40(3)	39(3)	7(3)	–3(3)	1(3)
C(14)	46(4)	72(6)	125(8)	0(5)	27(5)	7(4)
C(15)	62(4)	40(4)	53(4)	0(3)	–7(3)	–2(3)
C(16)	75(6)	72(5)	70(6)	21(4)	16(4)	7(4)
C(17)	112(8)	100(7)	73(6)	3(5)	8(6)	3(6)
O(1)	82(4)	64(3)	48(3)	5(2)	23(3)	21(3)
C(18A)	138(12)	78(8)	78(8)	–2(6)	25(8)	48(8)
C(19A)	138(12)	78(8)	78(8)	–2(6)	25(8)	48(8)
C(18B)	120(17)	81(14)	130(20)	–16(13)	–51(16)	8(14)
C(19B)	120(17)	81(14)	130(20)	–16(13)	–51(16)	8(14)
C(20)	55(4)	72(5)	50(4)	9(4)	16(4)	5(4)
C(21)	39(3)	39(4)	64(4)	10(3)	17(3)	7(3)
C(22)	98(7)	65(5)	74(6)	13(4)	12(5)	39(5)
C(23)	69(5)	85(6)	76(6)	–13(5)	–9(4)	18(5)
C(30)	22(3)	35(3)	24(3)	–1(2)	–5(2)	3(2)
C(31)	28(3)	31(3)	30(3)	3(2)	1(2)	2(2)
C(32)	25(3)	44(3)	27(3)	–2(2)	1(2)	0(2)
C(33)	34(3)	50(4)	23(3)	5(3)	5(2)	–2(3)
C(34)	42(3)	36(3)	33(3)	9(3)	–5(3)	–1(3)
C(35)	35(3)	33(3)	27(3)	1(2)	–1(2)	8(2)
C(36)	37(4)	58(4)	29(3)	1(3)	3(3)	5(3)
C(37)	66(5)	43(4)	41(4)	11(3)	2(3)	5(3)
C(40)	26(3)	37(3)	25(3)	4(2)	2(2)	8(2)
C(41)	36(3)	44(3)	28(3)	4(3)	–3(2)	8(3)
C(42)	51(4)	45(4)	39(4)	13(3)	–5(3)	11(3)
C(43)	45(4)	39(3)	53(4)	14(3)	–4(3)	8(3)
C(44)	35(3)	40(3)	39(3)	2(3)	2(3)	8(3)
C(45)	25(3)	43(3)	26(3)	6(2)	0(2)	9(2)
C(46)	59(4)	39(4)	51(4)	0(3)	–2(4)	5(3)
C(50)	32(3)	31(3)	22(3)	4(2)	5(2)	9(2)
C(51)	33(3)	38(3)	33(3)	4(2)	11(2)	9(3)
C(52)	45(4)	36(3)	30(3)	–1(2)	7(3)	5(3)
C(53)	44(4)	43(3)	30(3)	–5(3)	1(3)	–1(3)
C(54)	32(3)	48(4)	30(3)	–2(3)	–1(2)	2(3)
C(55)	35(3)	35(3)	27(3)	–3(2)	3(2)	7(2)
C(57)	39(4)	67(5)	48(4)	–10(3)	–6(3)	13(3)
C(60)	29(3)	31(3)	28(3)	1(2)	–1(2)	7(2)
C(61)	34(3)	32(3)	25(3)	0(2)	–2(2)	8(2)
C(62)	32(3)	32(3)	40(3)	3(2)	–7(3)	10(2)
C(63)	27(3)	40(3)	51(4)	1(3)	2(3)	14(3)
C(64)	34(3)	45(3)	38(3)	4(3)	6(3)	12(3)
C(65)	30(3)	43(3)	31(3)	5(2)	0(2)	10(3)

Anisotropic displacement parameters ($Å^2$) for **2** continued.

C(67)	37(4)	51(4)	50(4)	1(3)	–3(3)	14(3)
C(24)	65(5)	42(4)	64(5)	–10(3)	8(4)	–5(3)
B(1)	37(4)	35(4)	36(4)	0(3)	–3(3)	14(3)
B(2)	25(3)	35(3)	24(3)	0(3)	–1(3)	8(3)
N(1)	44(3)	46(3)	34(3)	0(2)	2(2)	3(2)
N(2)	40(3)	37(3)	44(3)	5(2)	–5(2)	5(2)
N(3)	35(3)	34(3)	33(3)	0(2)	1(2)	4(2)
N(4)	37(3)	40(3)	35(3)	5(2)	4(2)	4(2)
N(5)	34(3)	29(2)	38(3)	2(2)	–1(2)	2(2)
N(6)	38(3)	40(3)	60(4)	3(2)	7(3)	2(2)
F(1)	74(3)	108(3)	28(2)	1(2)	12(2)	40(3)
F(2)	36(2)	103(3)	46(2)	–11(2)	1(2)	21(2)
F(3)	71(3)	56(3)	86(3)	–17(2)	33(2)	7(2)
F(4)	134(5)	73(3)	167(6)	73(4)	69(5)	23(3)
F(5)	146(5)	67(3)	120(5)	16(3)	–74(4)	31(3)
F(6)	210(7)	52(3)	66(3)	12(2)	14(4)	56(3)
F(7)	178(6)	77(3)	73(3)	–29(3)	37(4)	–14(4)
F(8)	164(6)	40(2)	80(3)	0(2)	–1(3)	8(3)
F(9)	103(5)	122(5)	239(9)	–122(6)	–108(5)	52(4)
C(47)	95(7)	46(4)	76(6)	30(4)	–38(5)	–3(4)
F(10A)	135(5)	119(4)	50(2)	44(3)	–14(3)	19(4)
F(11A)	135(5)	119(4)	50(2)	44(3)	–14(3)	19(4)
F(12A)	135(5)	119(4)	50(2)	44(3)	–14(3)	19(4)
F(10B)	135(5)	119(4)	50(2)	44(3)	–14(3)	19(4)
F(11B)	135(5)	119(4)	50(2)	44(3)	–14(3)	19(4)
F(12B)	135(5)	119(4)	50(2)	44(3)	–14(3)	19(4)
C(56)	59(4)	38(4)	54(4)	–10(3)	20(4)	4(3)
F(13A)	107(3)	71(3)	117(4)	–39(3)	20(3)	35(2)
F(14A)	107(3)	71(3)	117(4)	–39(3)	20(3)	35(2)
F(15A)	107(3)	71(3)	117(4)	–39(3)	20(3)	35(2)
F(13B)	107(3)	71(3)	117(4)	–39(3)	20(3)	35(2)
F(14B)	107(3)	71(3)	117(4)	–39(3)	20(3)	35(2)
F(15B)	107(3)	71(3)	117(4)	–39(3)	20(3)	35(2)
F(16)	42(2)	128(4)	56(3)	–26(3)	–3(2)	35(2)
F(17)	40(3)	91(4)	212(7)	–31(4)	–23(3)	0(3)
F(18)	73(3)	205(4)	51(3)	27(3)	4(2)	76(4)
C(66)	33(3)	86(5)	52(4)	9(4)	9(3)	28(4)
F(19A)	75(3)	118(4)	46(2)	0(3)	22(2)	34(3)
F(20A)	75(3)	118(4)	46(2)	0(3)	22(2)	34(3)
F(21A)	75(3)	118(4)	46(2)	0(3)	22(2)	34(3)
F(19B)	75(3)	118(4)	46(2)	0(3)	22(2)	34(3)
F(20B)	75(3)	118(4)	46(2)	0(3)	22(2)	34(3)
F(21B)	75(3)	118(4)	46(2)	0(3)	22(2)	34(3)
F(22)	69(3)	81(3)	46(2)	–16(2)	–20(2)	35(2)
F(23)	41(2)	79(3)	69(3)	4(2)	–18(2)	6(2)
F(24)	75(3)	48(2)	63(3)	12(2)	–20(2)	19(2)
Nb(1)	46(1)	37(1)	51(1)	0(1)	12(1)	6(1)

Hydrogen coordinates and isotropic displacement parameters ($Å^2$) for **2**.

	x	y	z	U
H(2)	7789	10670	8931	73
H(4A)	7097	12383	9426	108
H(4B)	6133	12744	8941	108
H(4C)	7333	13031	8719	108
H(5A)	6719	8440	7859	139
H(5B)	7925	8985	8095	139
H(5C)	7424	9056	7281	139
H(7)	6438	11816	4894	58
H(9A)	4846	13466	5839	97
H(9B)	5484	13461	5132	97
H(9C)	6118	13820	5902	97
H(10A)	7166	9669	5813	95
H(10B)	6882	9906	4984	95
H(10C)	6024	9180	5413	95
H(12)	1930	8566	7063	63
H(14A)	2006	11078	7811	121
H(14B)	1144	10275	7314	121
H(14C)	1812	11257	6964	121
H(15A)	4104	7837	6252	80
H(15B)	3254	7266	6763	80
H(15C)	4456	7697	7087	80
H(16A)	3094	10734	8761	87
H(16B)	4222	10505	8537	87
H(17A)	5042	11381	9574	145
H(17B)	4174	10400	9740	145
H(17C)	3893	11544	9801	145
H(18A)	2909	12282	9092	112
H(18B)	2802	12811	8323	112
H(19A)	4466	13474	9448	141
H(19B)	3531	14105	9200	141
H(19C)	4430	13972	8668	141
H(18C)	4312	13584	8542	139
H(18D)	4355	13021	9305	139
H(19D)	2445	12995	8353	174
H(19E)	2685	13599	9123	174
H(19F)	2469	12358	9078	174
H(20)	3147	12969	7419	71
H(21)	2898	12227	6946	56
H(22A)	3796	14857	6975	114
H(22B)	3596	14531	7784	114
H(22C)	2637	14297	7157	114
H(23A)	2217	12725	5891	116
H(23B)	2467	11567	5920	116
H(23C)	3238	12440	5533	116
H(31)	10945	5068	6474	36
H(33)	11284	7219	4941	44
H(35)	9691	7673	6687	38
H(41)	10390	5129	8802	44
H(43)	9678	2036	8332	55
H(45)	9289	4083	6775	37
H(51)	9581	7826	8284	41
H(53)	12555	8763	9273	48
H(55)	11912	6146	8010	39
H(61)	8140	6167	6447	36

Hydrogen coordinates and isotropic displacement parameters ($Å^2$) for **2** continued.

	x	y	z	U
H(63)	5619	6268	7619	41
H(65)	8513	6029	8610	88
H(24A)	5830	13959	7056	88
H(24B)	6637	13201	7324	88
H(24C)	6069	13796	7902	88
H(1)	5703	9302	6720	44

$BrTi(NMe_2)_3$ (9)

Crystal data and structure refinement for $BrTi(NMe_2)_3$.

Chemical formula	$C_6H_{18}BrN_3Ti$	
Formula weight	260.04	
Temperature	120(2) K	
Radiation, wavelength	MoKα, 0.71073 Å	
Crystal system, space group	Trigonal, R3	
Unit cell parameters	a = 11.4614(16) Å	α = 90 °
	b = 11.4614(16) Å	β = 90 °
	c = 7.3885(15) Å	γ = 120 °
Cell volume	840.5(2) $Å^3$	
Z	3	
Calculated density	1.541 g/cm^3	
Absorption coefficient μ	4.283 mm^{-1}	
F(000)	396	
Data collection method	Bruker SMART 1K CCD diffractometer	
	ω rotation with narrow frames	
θ range for data collection	3.44 to 27.36°	
Index ranges	h −11 to 14, k −14 to 12, l −7 to 9	
Completeness to θ = 27.36°	96.0 %	
Intensity decay	none%	
Reflections collected	1295	
Independent reflections	618 (R_{int} = 0.0831)	
Reflections with $F^2>2\sigma$	610	
Absorption correction	semi-empirical from equivalents	
Min. and max. transmission	0.6740 and 0.6740	
Structure solution	direct methods	
Refinement method	Full-matrix least-squares on F^2	
Weighting parameters a, b	0.0000, 0.0000	
Data / restraints / parameters	618 / 1 / 65	
Final R indices [$F^2>2\sigma$]	R1 = 0.0299, wR2 = 0.0671	
R indices (all data)	R1 = 0.0313, wR2 = 0.0679	
Goodness-of-fit on F^2	0.917	
Absolute structure parameter	0.026(16)	
Largest and mean shift/su	0.011 and 0.001	
Largest diff. peak and hole	0.405 and −0.428 $eÅ^{-3}$	

Atomic coordinates and equivalent isotropic displacement parameters ($Å^2$) for **9**.

U_{eq} is defined as one third of the trace of the orthogonalized U^{ij} tensor.

	x	y	z	U_{eq}
Br1	1.0000	1.0000	0.49906(9)	0.0233(3)
Ti1	1.0000	1.0000	0.83361(11)	0.0135(5)
C1	1.2811(15)	1.1653(15)	0.872(2)	0.021(3)
N1	1.1504(7)	1.1483(7)	0.9342(9)	0.0152(15)
C2	1.1685(11)	1.2485(9)	1.0722(14)	0.025(2)
C1'	1.1678(10)	0.9219(10)	1.0704(15)	0.025(2)
N1'	1.1513(7)	1.0035(7)	0.9347(8)	0.0149(15)
C2'	1.2812(17)	1.1139(14)	0.875(2)	0.025(4)

Bond lengths [Å] and angles [°] for **9**.

Br1–Ti1	2.4718(12)	Ti1–N1	1.866(7)
Ti1–N1a	1.866(7)	Ti1–N1b	1.866(7)
Ti1–N1'a	1.870(7)	Ti1–N1'	1.870(7)
Ti1–N1'b	1.870(7)	C1–N1	1.484(17)
C1–H1A	0.9800	C1–H1B	0.9800
C1–H1C	0.9800	N1–C2	1.471(11)
C2–H2A	0.9800	C2–H2B	0.9800
C2–H2C	0.9800	C1'–N1'	1.447(12)
C1'–H1'1	0.9800	C1'–H1'2	0.9800
C1'–H1'3	0.9800	N1'–C2'	1.458(18)
C2'–H2'1	0.9800	C2'–H2'2	0.9800
C2'–H2'3	0.9800		
N1–Ti1–N1a	105.2(2)	N1–Ti1–N1b	105.2(2)
N1a–Ti1–N1b	105.2(2)	N1–Ti1–N1'a	133.0(3)
N1a–Ti1–N1'a	52.9(3)	N1b–Ti1–N1'a	56.3(3)
N1–Ti1–N1'	52.9(3)	N1a–Ti1–N1'	56.3(3)
N1b–Ti1–N1'	133.0(3)	N1'a–Ti1–N1'	105.1(2)
N1–Ti1–N1'b	56.3(3)	N1a–Ti1–N1'b	133.0(3)
N1b–Ti1–N1'b	52.9(3)	N1'a–Ti1–N1'b	105.1(2)
N1'–Ti1–N1'b	105.1(2)	N1–Ti1–Br1	113.5(2)
N1a–Ti1–Br1	113.5(2)	N1b–Ti1–Br1	113.5(2)
N1'a–Ti1–Br1	113.53(19)	N1'–Ti1–Br1	113.53(19)
N1'b–Ti1–Br1	113.53(19)	C2–N1–C1	112.0(9)
C2–N1–Ti1	133.8(6)	C1–N1–Ti1	114.1(7)
N1'–C1'–H1'1	109.5	N1'–C1'–H1'2	109.5
H1'1–C1'–H1'2	109.5	N1'–C1'–H1'3	109.5
H1'1–C1'–H1'3	109.5	H1'2–C1'–H1'3	109.5
C1'–N1'–C2'	111.3(8)	C1'–N1'–Ti1	133.0(6)
C2'–N1'–Ti1	115.6(7)	N1'–C2'–H2'1	109.5
N1'–C2'–H2'2	109.5	H2'1–C2'–H2'2	109.5
N1'–C2'–H2'3	109.5	H2'1–C2'–H2'3	109.5
H2'2–C2'–H2'3	109.5		

Symmetry operations for equivalent atoms

a –x+y+1,–x+2,z b –y+2,x–y+1,z

Anisotropic displacement parameters ($Å^2$) for **9**.
The anisotropic displacement factor exponent takes the form: $-2\pi^2[h^2a^{*2}U^{11} + ...+ 2hka^*b^*U^{12}]$

	U^{11}	U^{22}	U^{33}	U^{23}	U^{13}	U^{12}
Br1	0.0263(4)	0.0263(4)	0.0174(4)	0.000	0.000	0.01313(18)
Ti1	0.0127(7)	0.0127(7)	0.0150(11)	0.000	0.000	0.0064(3)
C1	0.008(5)	0.024(8)	0.027(7)	0.007(7)	0.001(4)	0.005(6)
N1	0.014(3)	0.017(3)	0.015(4)	−0.001(3)	−0.002(3)	0.008(3)
C2	0.029(6)	0.019(5)	0.022(5)	−0.010(4)	−0.006(4)	0.009(4)
C1'	0.019(5)	0.021(5)	0.030(6)	0.002(4)	−0.004(4)	0.007(4)
N1'	0.016(3)	0.015(3)	0.010(3)	−0.001(3)	0.004(3)	0.006(3)
C2'	0.020(7)	0.025(8)	0.028(7)	0.007(8)	−0.005(5)	0.010(7)

Hydrogen coordinates and isotropic displacement parameters ($Å^2$) for **9**.

	x	y	z	U
H1A	1.3339	1.2534	0.8135	0.032
H1B	1.2647	1.0941	0.7848	0.032
H1C	1.3311	1.1595	0.9757	0.032
H2A	1.2133	1.2375	1.1784	0.037
H2B	1.0803	1.2354	1.1075	0.037
H2C	1.2239	1.3393	1.0225	0.037
H1'1	1.2185	0.8819	1.0190	0.037
H1'2	1.0790	0.8501	1.1100	0.037
H1'3	1.2169	0.9784	1.1743	0.037
H2'1	1.3298	1.1704	0.9791	0.037
H2'2	1.2668	1.1682	0.7850	0.037
H2'3	1.3341	1.0771	0.8211	0.037

Torsion angles [°] for **9**.

N1a–Ti1–N1–C2	−106.3(7)	N1b–Ti1–N1–C2	4.5(9)
N1'a–Ti1–N1–C2	−53.3(10)	N1'–Ti1–N1–C2	−128.4(9)
N1'b–Ti1–N1–C2	25.6(8)	Br1–Ti1–N1–C2	129.1(8)
N1a–Ti1–N1–C1	69.0(9)	N1b–Ti1–N1–C1	179.8(7)
N1'a–Ti1–N1–C1	122.1(8)	N1'–Ti1–N1–C1	47.0(8)
N1'b–Ti1–N1–C1	−159.1(9)	Br1–Ti1–N1–C1	−55.6(8)
N1–Ti1–N1'–C1'	128.7(9)	N1a–Ti1–N1'–C1'	−25.5(7)
N1b–Ti1–N1'–C1'	53.5(9)	N1'a–Ti1–N1'–C1'	−4.2(9)
N1'b–Ti1–N1'–C1'	106.4(7)	Br1–Ti1–N1'–C1'	−128.9(7)
N1–Ti1–N1'–C2'	−47.4(9)	N1a–Ti1–N1'–C2'	158.4(9)
N1b–Ti1–N1'–C2'	−122.6(9)	N1'a–Ti1–N1'–C2'	179.7(8)
N1'b–Ti1–N1'–C2'	−69.7(10)	Br1–Ti1–N1'–C2'	55.0(9)

Symmetry operations for equivalent atoms
a −x+y+1,−x+2,z b −y+2,x−y+1,z

$[\{Ti(NMe_2)_3O\}_2Ti_3(NMe_2)_6OBr_2]$ (10)

Crystal data and structure refinement for **10**.

Empirical formula	$C_{24}H_{72}Br_2N_{12}O_3Ti_5$	
Formula weight	976.26	
Temperature	130(2) K	
Wavelength	0.71073 Å	
Crystal system	Monoclinic	
Space group	P21/m	
Unit cell dimensions	a = 8.5908(2) Å	α= 90 °
	b = 23.6320(10) Å	β= 103.465(2) °
	c = 11.2843(4) Å	γ = 90 °
Volume	2227.94(13) $Å^3$	
Z	2	
Density (calculated)	1.455 Mg/m^3	
Absorption coefficient	2.689 mm^{-1}	
F(000)	1008	
Crystal size	0.40 x 0.30 x 0.10 mm^3	
Theta range for data collection	2.05 to 27.50°.	
Index ranges	-9<=h<=11, -30<=k<=29, -14<=l<=14	
Reflections collected	14421	
Independent reflections	5202 [R(int) = 0.0603]	
Completeness to theta = 27.50°	99.1 %	
Absorption correction	Scalepack	
Max. and min. transmission	0.7748 and 0.4127	
Refinement method	Full-matrix least-squares on F^2	
Data / restraints / parameters	5202 / 0 / 234	
Goodness-of-fit on F^2	1.090	
Final R indices [I>2sigma(I)]	R1 = 0.0434, wR2 = 0.0835	
R indices (all data)	R1 = 0.0605, wR2 = 0.0883	
Extinction coefficient	0.0017(4)	
Largest diff. peak and hole	0.662 and -0.753 $e.Å^{-3}$	

Atomic coordinates (x 10^4) and equivalent isotropic displacement parameters ($Å^2$x 10^3) for **10**. U(eq) is defined as one third of the trace of the orthogonalized U^{ij} tensor.

	x	y	z	U(eq)
Br(1)	4175(1)	7500	5919(1)	19(1)
Ti(1)	3652(1)	5856(1)	8064(1)	20(1)
O(1)	2572(2)	6340(1)	6842(2)	22(1)
N(1)	4644(3)	5259(1)	7398(2)	26(1)
C(1)	3620(4)	4925(2)	6447(3)	38(1)
Br(2)	4404(1)	7500	2768(1)	34(1)
Ti(2)	1364(1)	6830(1)	5813(1)	17(1)
O(2)	577(3)	7500	4691(2)	17(1)
N(2)	2151(3)	5523(1)	8847(2)	29(1)
C(2)	6286(4)	5061(2)	7674(3)	36(1)
Ti(3)	1940(1)	7500	3636(1)	19(1)
N(3)	5222(3)	6241(1)	9227(2)	26(1)
C(3)	1585(5)	4944(2)	8843(4)	45(1)
N(4)	2062(3)	6614(1)	4137(2)	22(1)
C(4)	1201(5)	5904(2)	9403(4)	42(1)
N(5)	-625(3)	6451(1)	5605(2)	25(1)
C(5)	6347(4)	6578(2)	8745(4)	40(1)
N(6)	1154(4)	7500	7078(3)	19(1)
C(6)	5398(5)	6332(2)	10531(3)	49(1)
N(7)	393(5)	7500	2131(3)	30(1)
C(7)	810(4)	6279(2)	3298(3)	32(1)
C(8)	3568(4)	6288(2)	4301(3)	29(1)
C(9)	-2138(4)	6662(2)	4864(3)	35(1)
C(10)	-885(4)	5912(2)	6153(4)	44(1)
C(11)	-439(5)	7500	7380(4)	27(1)
C(12)	2363(5)	7500	8248(4)	23(1)
C(13)	673(7)	7500	907(5)	65(2)
C(14)	-1333(6)	7500	2030(5)	44(1)

Bond lengths [Å] and angles [°] for **10.**

Br(1)-Ti(3)	2.8322(8)	O(2)-Ti(2)#1	2.0416(17)
Br(1)-Ti(2)#1	2.8667(6)	N(2)-C(3)	1.451(5)
Br(1)-Ti(2)	2.8667(6)	N(2)-C(4)	1.452(4)
Ti(1)-O(1)	1.865(2)	Ti(3)-N(7)	1.897(4)
Ti(1)-N(3)	1.883(3)	Ti(3)-N(4)#1	2.165(3)
Ti(1)-N(1)	1.891(3)	Ti(3)-N(4)	2.165(3)
Ti(1)-N(2)	1.895(3)	Ti(3)-Ti(2)#1	3.0583(8)
O(1)-Ti(2)	1.790(2)	N(3)-C(5)	1.453(4)
N(1)-C(2)	1.450(4)	N(3)-C(6)	1.460(4)
N(1)-C(1)	1.451(4)	N(4)-C(8)	1.479(4)
Br(2)-Ti(3)	2.5302(8)	N(4)-C(7)	1.486(4)
Ti(2)-N(5)	1.895(3)	N(5)-C(10)	1.455(4)
Ti(2)-O(2)	2.0417(17)	N(5)-C(9)	1.460(4)
Ti(2)-N(6)	2.168(2)	N(6)-C(12)	1.478(5)
Ti(2)-N(4)	2.173(2)	N(6)-C(11)	1.486(5)
Ti(2)-Ti(3)	3.0583(8)	N(6)-Ti(2)#1	2.168(2)
Ti(2)-Ti(2)#1	3.1676(11)	N(7)-C(13)	1.457(6)
O(2)-Ti(3)	1.855(3)	N(7)-C(14)	1.460(6)
Ti(3)-Br(1)-Ti(2)#1	64.908(17)	N(5)-Ti(2)-N(6)	102.47(12)
Ti(3)-Br(1)-Ti(2)	64.908(17)	O(2)-Ti(2)-N(6)	76.99(9)
Ti(2)#1-Br(1)-Ti(2)	67.07(2)	O(1)-Ti(2)-N(4)	100.23(10)
O(1)-Ti(1)-N(3)	111.74(11)	N(5)-Ti(2)-N(4)	101.83(10)
O(1)-Ti(1)-N(1)	110.92(10)	O(2)-Ti(2)-N(4)	76.21(10)
N(3)-Ti(1)-N(1)	108.77(12)	N(6)-Ti(2)-N(4)	145.75(10)
O(1)-Ti(1)-N(2)	108.92(11)	O(1)-Ti(2)-Br(1)	88.55(7)
N(3)-Ti(1)-N(2)	109.28(12)	N(5)-Ti(2)-Br(1)	173.15(9)
N(1)-Ti(1)-N(2)	107.09(12)	O(2)-Ti(2)-Br(1)	75.63(7)
Ti(2)-O(1)-Ti(1)	172.03(13)	N(6)-Ti(2)-Br(1)	76.55(8)
C(2)-N(1)-C(1)	112.0(3)	N(4)-Ti(2)-Br(1)	76.45(7)
C(2)-N(1)-Ti(1)	131.4(2)	O(1)-Ti(2)-Ti(3)	132.73(7)
C(1)-N(1)-Ti(1)	116.6(2)	N(5)-Ti(2)-Ti(3)	117.09(8)
O(1)-Ti(2)-N(5)	98.29(11)	O(2)-Ti(2)-Ti(3)	36.18(7)
O(1)-Ti(2)-O(2)	164.18(10)	N(6)-Ti(2)-Ti(3)	101.80(7)
N(5)-Ti(2)-O(2)	97.52(11)	N(4)-Ti(2)-Ti(3)	45.05(7)
O(1)-Ti(2)-N(6)	99.75(10)	Br(1)-Ti(2)-Ti(3)	57.000(18)

Bond lengths [Å] and angles [°] for **10** (continued)

O(1)-Ti(2)-Ti(2)#1	130.27(7)	N(4)-Ti(3)-Ti(2)#1	107.33(7)
N(5)-Ti(2)-Ti(2)#1	118.22(8)	Br(2)-Ti(3)-Ti(2)#1	128.10(3)
O(2)-Ti(2)-Ti(2)#1	39.13(6)	Br(1)-Ti(3)-Ti(2)#1	58.092(17)
N(6)-Ti(2)-Ti(2)#1	43.06(6)	O(2)-Ti(3)-Ti(2)	40.52(5)
N(4)-Ti(2)-Ti(2)#1	103.56(7)	N(7)-Ti(3)-Ti(2)	120.53(10)
Br(1)-Ti(2)-Ti(2)#1	56.463(11)	N(4)#1-Ti(3)-Ti(2)	107.33(7)
Ti(3)-Ti(2)-Ti(2)#1	58.811(12)	N(4)-Ti(3)-Ti(2)	45.27(7)
Ti(3)-O(2)-Ti(2)#1	103.30(9)	Br(2)-Ti(3)-Ti(2)	128.10(3)
Ti(3)-O(2)-Ti(2)	103.30(9)	Br(1)-Ti(3)-Ti(2)	58.092(17)
Ti(2)#1-O(2)-Ti(2)	101.74(12)	Ti(2)#1-Ti(3)-Ti(2)	62.38(2)
C(3)-N(2)-C(4)	111.3(3)	C(5)-N(3)-C(6)	112.0(3)
C(3)-N(2)-Ti(1)	130.8(2)	C(5)-N(3)-Ti(1)	115.8(2)
C(4)-N(2)-Ti(1)	117.1(2)	C(6)-N(3)-Ti(1)	131.6(2)
O(2)-Ti(3)-N(7)	99.13(15)	C(8)-N(4)-C(7)	106.5(2)
O(2)-Ti(3)-N(4)#1	80.30(7)	C(8)-N(4)-Ti(3)	121.6(2)
N(7)-Ti(3)-N(4)#1	102.42(7)	C(7)-N(4)-Ti(3)	111.4(2)
O(2)-Ti(3)-N(4)	80.30(7)	C(8)-N(4)-Ti(2)	115.05(19)
N(7)-Ti(3)-N(4)	102.42(7)	C(7)-N(4)-Ti(2)	111.94(19)
N(4)#1-Ti(3)-N(4)	150.51(13)	Ti(3)-N(4)-Ti(2)	89.67(10)
O(2)-Ti(3)-Br(2)	163.45(9)	C(10)-N(5)-C(9)	109.8(3)
N(7)-Ti(3)-Br(2)	97.42(12)	C(10)-N(5)-Ti(2)	125.7(2)
N(4)#1-Ti(3)-Br(2)	96.15(7)	C(9)-N(5)-Ti(2)	124.5(2)
N(4)-Ti(3)-Br(2)	96.15(7)	C(12)-N(6)-C(11)	106.8(3)
O(2)-Ti(3)-Br(1)	79.13(8)	C(12)-N(6)-Ti(2)	116.07(16)
N(7)-Ti(3)-Br(1)	178.27(12)	C(11)-N(6)-Ti(2)	111.94(17)
N(4)#1-Ti(3)-Br(1)	77.34(7)	C(12)-N(6)-Ti(2)#1	116.07(16)
N(4)-Ti(3)-Br(1)	77.34(7)	C(11)-N(6)-Ti(2)#1	111.94(17)
Br(2)-Ti(3)-Br(1)	84.32(3)	Ti(2)-N(6)-Ti(2)#1	93.87(13)
O(2)-Ti(3)-Ti(2)#1	40.52(5)	C(13)-N(7)-C(14)	108.3(4)
N(7)-Ti(3)-Ti(2)#1	120.53(10)	C(13)-N(7)-Ti(3)	127.8(4)
N(4)#1-Ti(3)-Ti(2)#1	45.27(7)	C(14)-N(7)-Ti(3)	123.9(3)

Symmetry transformations used to generate equivalent atoms:

#1 x,-y+3/2,z

Anisotropic displacement parameters ($Å^2 x\ 10^3$) for **10**. The anisotropic displacement factor exponent takes the form: $-2\pi^2[\ h^2\ a^{*2}U^{11} + ... + 2\ h\ k\ a^*\ b^*\ U^{12}\ ]$

	U^{11}	U^{22}	U^{33}	U^{23}	U^{13}	U^{12}
Br(1)	15(1)	21(1)	21(1)	0	5(1)	0
Ti(1)	23(1)	17(1)	20(1)	1(1)	5(1)	0(1)
O(1)	25(1)	19(1)	22(1)	3(1)	4(1)	1(1)
N(1)	31(1)	21(1)	23(1)	0(1)	4(1)	1(1)
C(1)	50(2)	28(2)	35(2)	-10(2)	7(2)	-2(2)
Br(2)	33(1)	46(1)	30(1)	0	19(1)	0
Ti(2)	17(1)	17(1)	17(1)	0(1)	5(1)	-1(1)
O(2)	14(1)	21(2)	16(1)	0	2(1)	0
N(2)	33(2)	27(2)	28(2)	4(1)	9(1)	-3(1)
C(2)	36(2)	28(2)	45(2)	0(2)	12(2)	5(2)
Ti(3)	20(1)	24(1)	15(1)	0	7(1)	0
N(3)	30(1)	22(1)	23(1)	-1(1)	2(1)	-2(1)
C(3)	59(2)	36(2)	42(2)	7(2)	17(2)	-12(2)
N(4)	22(1)	23(1)	21(1)	-5(1)	5(1)	0(1)
C(4)	48(2)	41(2)	45(2)	6(2)	25(2)	3(2)
N(5)	21(1)	27(2)	28(1)	-1(1)	7(1)	-6(1)
C(5)	31(2)	39(2)	45(2)	4(2)	3(2)	-9(2)
N(6)	17(2)	23(2)	17(2)	0	6(1)	0
C(6)	58(3)	59(3)	27(2)	-10(2)	2(2)	-16(2)
N(7)	35(2)	39(2)	15(2)	0	4(2)	0
C(7)	38(2)	30(2)	27(2)	-12(2)	6(1)	-6(2)
C(8)	32(2)	26(2)	34(2)	-6(2)	16(1)	5(1)
C(9)	21(2)	37(2)	46(2)	-5(2)	5(1)	-6(1)
C(10)	39(2)	40(2)	48(2)	12(2)	1(2)	-19(2)
C(11)	28(2)	31(3)	27(2)	0	17(2)	0
C(12)	30(2)	23(2)	17(2)	0	7(2)	0
C(13)	53(4)	124(7)	17(3)	0	8(2)	0
C(14)	33(3)	65(4)	27(3)	0	-7(2)	0

Hydrogen coordinates (x 10^4) and isotropic displacement parameters ($Å^2$x 10^3) for **10**.

	x	y	z	U(eq)
H(1A)	4050	4931	5715	57
H(1B)	2538	5085	6256	57
H(1C)	3582	4534	6728	57
H(2A)	6331	4674	7992	54
H(2B)	6947	5309	8286	54
H(2C)	6690	5066	6930	54
H(3A)	1583	4829	9677	67
H(3B)	2293	4694	8516	67
H(3C)	495	4919	8332	67
H(4A)	83	5892	8942	63
H(4B)	1613	6290	9396	63
H(4C)	1264	5786	10245	63
H(5A)	6202	6979	8911	59
H(5B)	6155	6519	7863	59
H(5C)	7443	6463	9135	59
H(6A)	6495	6240	10966	74
H(6B)	4645	6088	10826	74
H(6C)	5172	6729	10678	74
H(7A)	1093	6239	2510	48
H(7B)	-223	6473	3184	48
H(7C)	733	5903	3649	48
H(8A)	3424	5914	4634	44
H(8B)	4428	6490	4866	44
H(8C)	3848	6245	3513	44
H(9A)	-2599	6380	4246	53
H(9B)	-1948	7015	4464	53
H(9C)	-2882	6733	5387	53
H(10A)	-1728	5955	6601	66
H(10B)	109	5791	6716	66
H(10C)	-1210	5627	5513	66
H(11A)	-555	7157	7840	40
H(11B)	-1279	7500	6625	40
H(12B)	3437	7500	8090	35
H(12A)	2240	7158	8708	35
H(13A)	200	7160	472	97
H(13B)	1828	7500	959	97
H(14A)	-1805	7160	1593	66
H(14B)	-1544	7500	2847	66

Torsion angles [°] for **10**.

N(3)-Ti(1)-O(1)-Ti(2)	-83.7(10)	N(6)-Ti(2)-O(2)-Ti(2)#1	25.28(11)
N(1)-Ti(1)-O(1)-Ti(2)	154.8(9)	N(4)-Ti(2)-O(2)-Ti(2)#1	-133.19(12)
N(2)-Ti(1)-O(1)-Ti(2)	37.2(10)	Br(1)-Ti(2)-O(2)-Ti(2)#1	-53.92(8)
O(1)-Ti(1)-N(1)-C(2)	126.0(3)	Ti(3)-Ti(2)-O(2)-Ti(2)#1	-106.90(14)
N(3)-Ti(1)-N(1)-C(2)	2.8(3)	O(1)-Ti(1)-N(2)-C(3)	110.9(3)
N(2)-Ti(1)-N(1)-C(2)	-115.2(3)	N(3)-Ti(1)-N(2)-C(3)	-126.8(3)
O(1)-Ti(1)-N(1)-C(1)	-54.6(3)	N(1)-Ti(1)-N(2)-C(3)	-9.1(3)
N(3)-Ti(1)-N(1)-C(1)	-177.8(2)	O(1)-Ti(1)-N(2)-C(4)	-58.3(3)
N(2)-Ti(1)-N(1)-C(1)	64.2(3)	N(3)-Ti(1)-N(2)-C(4)	64.0(3)
Ti(1)-O(1)-Ti(2)-N(5)	-62.7(10)	N(1)-Ti(1)-N(2)-C(4)	-178.3(2)
Ti(1)-O(1)-Ti(2)-O(2)	118.1(9)	Ti(2)#1-O(2)-Ti(3)-N(7)	-127.14(8)
Ti(1)-O(1)-Ti(2)-N(6)	41.5(10)	Ti(2)-O(2)-Ti(3)-N(7)	127.14(8)
Ti(1)-O(1)-Ti(2)-N(4)	-166.4(9)	Ti(2)#1-O(2)-Ti(3)-N(4)#1	-25.98(9)
Ti(1)-O(1)-Ti(2)-Br(1)	117.6(10)	Ti(2)-O(2)-Ti(3)-N(4)#1	-131.69(11)
Ti(1)-O(1)-Ti(2)-Ti(3)	157.7(9)	Ti(2)#1-O(2)-Ti(3)-N(4)	131.69(11)
Ti(1)-O(1)-Ti(2)-Ti(2)#1	75.8(10)	Ti(2)-O(2)-Ti(3)-N(4)	25.98(9)
Ti(3)-Br(1)-Ti(2)-O(1)	145.66(7)	Ti(2)#1-O(2)-Ti(3)-Br(2)	52.86(8)
Ti(2)#1-Br(1)-Ti(2)-O(1)	-142.42(7)	Ti(2)-O(2)-Ti(3)-Br(2)	-52.86(8)
Ti(3)-Br(1)-Ti(2)-N(5)	-31.4(7)	Ti(2)#1-O(2)-Ti(3)-Br(1)	52.86(8)
Ti(2)#1-Br(1)-Ti(2)-N(5)	40.5(7)	Ti(2)-O(2)-Ti(3)-Br(1)	-52.86(8)
Ti(3)-Br(1)-Ti(2)-O(2)	-34.19(7)	Ti(2)-O(2)-Ti(3)-Ti(2)#1	-105.71(15)
Ti(2)#1-Br(1)-Ti(2)-O(2)	37.73(7)	Ti(2)#1-O(2)-Ti(3)-Ti(2)	105.71(15)
Ti(3)-Br(1)-Ti(2)-N(6)	-113.96(8)	Ti(2)#1-Br(1)-Ti(3)-O(2)	-37.593(12)
Ti(2)#1-Br(1)-Ti(2)-N(6)	-42.04(8)	Ti(2)-Br(1)-Ti(3)-O(2)	37.593(12)
Ti(3)-Br(1)-Ti(2)-N(4)	44.77(7)	Ti(2)#1-Br(1)-Ti(3)-N(7)	-37.59(3)
Ti(2)#1-Br(1)-Ti(2)-N(4)	116.69(7)	Ti(2)-Br(1)-Ti(3)-N(7)	37.59(3)
Ti(2)#1-Br(1)-Ti(2)-Ti(3)	71.918(14)	Ti(2)#1-Br(1)-Ti(3)-N(4)#1	44.78(7)
Ti(3)-Br(1)-Ti(2)-Ti(2)#1	-71.918(14)	Ti(2)-Br(1)-Ti(3)-N(4)#1	119.97(7)
O(1)-Ti(2)-O(2)-Ti(3)	52.4(4)	Ti(2)#1-Br(1)-Ti(3)-N(4)	-119.97(7)
N(5)-Ti(2)-O(2)-Ti(3)	-126.69(11)	Ti(2)-Br(1)-Ti(3)-N(4)	-44.78(7)
N(6)-Ti(2)-O(2)-Ti(3)	132.18(12)	Ti(2)#1-Br(1)-Ti(3)-Br(2)	142.407(12)
N(4)-Ti(2)-O(2)-Ti(3)	-26.29(10)	Ti(2)-Br(1)-Ti(3)-Br(2)	-142.407(12)
Br(1)-Ti(2)-O(2)-Ti(3)	52.98(8)	Ti(2)-Br(1)-Ti(3)-Ti(2)#1	75.19(2)
Ti(2)#1-Ti(2)-O(2)-Ti(3)	106.90(14)	Ti(2)#1-Br(1)-Ti(3)-Ti(2)	-75.19(2)
O(1)-Ti(2)-O(2)-Ti(2)#1	-54.5(4)	O(1)-Ti(2)-Ti(3)-O(2)	-162.90(14)
N(5)-Ti(2)-O(2)-Ti(2)#1	126.41(11)	N(5)-Ti(2)-Ti(3)-O(2)	63.24(14)

Torsion angles [°] for **10** (continued).

N(6)-Ti(2)-Ti(3)-O(2)	-47.53(13)	Ti(2)#1-Ti(2)-Ti(3)-Br(1)	67.857(13)
N(4)-Ti(2)-Ti(3)-O(2)	142.57(14)	O(1)-Ti(2)-Ti(3)-Ti(2)#1	-118.00(10)
Br(1)-Ti(2)-Ti(3)-O(2)	-112.75(10)	N(5)-Ti(2)-Ti(3)-Ti(2)#1	108.14(10)
Ti(2)#1-Ti(2)-Ti(3)-O(2)	-44.90(10)	O(2)-Ti(2)-Ti(3)-Ti(2)#1	44.90(10)
O(1)-Ti(2)-Ti(3)-N(7)	131.08(13)	N(6)-Ti(2)-Ti(3)-Ti(2)#1	-2.63(9)
N(5)-Ti(2)-Ti(3)-N(7)	-2.78(13)	N(4)-Ti(2)-Ti(3)-Ti(2)#1	-172.53(9)
O(2)-Ti(2)-Ti(3)-N(7)	-66.02(13)	Br(1)-Ti(2)-Ti(3)-Ti(2)#1	-67.857(13)
N(6)-Ti(2)-Ti(3)-N(7)	-113.55(12)	O(1)-Ti(1)-N(3)-C(5)	-52.0(3)
N(4)-Ti(2)-Ti(3)-N(7)	76.55(12)	N(1)-Ti(1)-N(3)-C(5)	70.8(3)
Br(1)-Ti(2)-Ti(3)-N(7)	-178.77(8)	N(2)-Ti(1)-N(3)-C(5)	-172.6(2)
Ti(2)#1-Ti(2)-Ti(3)-N(7)	-110.92(8)	O(1)-Ti(1)-N(3)-C(6)	117.9(3)
O(1)-Ti(2)-Ti(3)-N(4)#1	-112.45(12)	N(1)-Ti(1)-N(3)-C(6)	-119.3(3)
N(5)-Ti(2)-Ti(3)-N(4)#1	113.69(12)	N(2)-Ti(1)-N(3)-C(6)	-2.7(4)
O(2)-Ti(2)-Ti(3)-N(4)#1	50.45(12)	O(2)-Ti(3)-N(4)-C(8)	-143.2(2)
N(6)-Ti(2)-Ti(3)-N(4)#1	2.92(11)	N(7)-Ti(3)-N(4)-C(8)	119.5(2)
N(4)-Ti(2)-Ti(3)-N(4)#1	-166.98(16)	N(4)#1-Ti(3)-N(4)-C(8)	-93.7(3)
Br(1)-Ti(2)-Ti(3)-N(4)#1	-62.31(7)	Br(2)-Ti(3)-N(4)-C(8)	20.5(2)
Ti(2)#1-Ti(2)-Ti(3)-N(4)#1	5.55(7)	Br(1)-Ti(3)-N(4)-C(8)	-62.3(2)
O(1)-Ti(2)-Ti(3)-N(4)	54.53(13)	Ti(2)#1-Ti(3)-N(4)-C(8)	-112.7(2)
N(5)-Ti(2)-Ti(3)-N(4)	-79.33(13)	Ti(2)-Ti(3)-N(4)-C(8)	-119.6(2)
O(2)-Ti(2)-Ti(3)-N(4)	-142.57(14)	O(2)-Ti(3)-N(4)-C(7)	89.9(2)
N(6)-Ti(2)-Ti(3)-N(4)	169.90(13)	N(7)-Ti(3)-N(4)-C(7)	-7.4(2)
Br(1)-Ti(2)-Ti(3)-N(4)	104.68(9)	N(4)#1-Ti(3)-N(4)-C(7)	139.4(2)
Ti(2)#1-Ti(2)-Ti(3)-N(4)	172.53(9)	Br(2)-Ti(3)-N(4)-C(7)	-106.42(19)
O(1)-Ti(2)-Ti(3)-Br(2)	0.33(10)	Br(1)-Ti(3)-N(4)-C(7)	170.8(2)
N(5)-Ti(2)-Ti(3)-Br(2)	-133.53(10)	Ti(2)#1-Ti(3)-N(4)-C(7)	120.45(18)
O(2)-Ti(2)-Ti(3)-Br(2)	163.23(10)	Ti(2)-Ti(3)-N(4)-C(7)	113.5(2)
N(6)-Ti(2)-Ti(3)-Br(2)	115.70(9)	O(2)-Ti(3)-N(4)-Ti(2)	-23.61(10)
N(4)-Ti(2)-Ti(3)-Br(2)	-54.20(9)	N(7)-Ti(3)-N(4)-Ti(2)	-120.93(13)
Br(1)-Ti(2)-Ti(3)-Br(2)	50.48(3)	N(4)#1-Ti(3)-N(4)-Ti(2)	25.9(3)
Ti(2)#1-Ti(2)-Ti(3)-Br(2)	118.33(3)	Br(2)-Ti(3)-N(4)-Ti(2)	140.06(6)
O(1)-Ti(2)-Ti(3)-Br(1)	-50.14(10)	Br(1)-Ti(3)-N(4)-Ti(2)	57.32(6)
N(5)-Ti(2)-Ti(3)-Br(1)	176.00(10)	Ti(2)#1-Ti(3)-N(4)-Ti(2)	6.93(9)
O(2)-Ti(2)-Ti(3)-Br(1)	112.75(10)	O(1)-Ti(2)-N(4)-C(8)	-17.4(2)
N(6)-Ti(2)-Ti(3)-Br(1)	65.22(9)	N(5)-Ti(2)-N(4)-C(8)	-118.2(2)
N(4)-Ti(2)-Ti(3)-Br(1)	-104.68(9)	O(2)-Ti(2)-N(4)-C(8)	146.8(2)

Torsion angles [°] for **10** (continued).

N(6)-Ti(2)-N(4)-C(8)	107.4(3)	N(5)-Ti(2)-N(6)-C(12)	120.2(2)
Br(1)-Ti(2)-N(4)-C(8)	68.6(2)	O(2)-Ti(2)-N(6)-C(12)	-144.8(2)
Ti(3)-Ti(2)-N(4)-C(8)	125.1(2)	N(4)-Ti(2)-N(6)-C(12)	-105.5(2)
Ti(2)#1-Ti(2)-N(4)-C(8)	118.6(2)	Br(1)-Ti(2)-N(6)-C(12)	-66.7(2)
O(1)-Ti(2)-N(4)-C(7)	104.4(2)	Ti(3)-Ti(2)-N(6)-C(12)	-118.3(2)
N(5)-Ti(2)-N(4)-C(7)	3.6(2)	Ti(2)#1-Ti(2)-N(6)-C(12)	-121.6(3)
O(2)-Ti(2)-N(4)-C(7)	-91.4(2)	O(1)-Ti(2)-N(6)-C(11)	-103.5(2)
N(6)-Ti(2)-N(4)-C(7)	-130.8(2)	N(5)-Ti(2)-N(6)-C(11)	-2.7(2)
Br(1)-Ti(2)-N(4)-C(7)	-169.6(2)	O(2)-Ti(2)-N(6)-C(11)	92.3(2)
Ti(3)-Ti(2)-N(4)-C(7)	-113.1(2)	N(4)-Ti(2)-N(6)-C(11)	131.6(2)
Ti(2)#1-Ti(2)-N(4)-C(7)	-119.6(2)	Br(1)-Ti(2)-N(6)-C(11)	170.4(2)
O(1)-Ti(2)-N(4)-Ti(3)	-142.56(9)	Ti(3)-Ti(2)-N(6)-C(11)	118.8(2)
N(5)-Ti(2)-N(4)-Ti(3)	116.63(11)	Ti(2)#1-Ti(2)-N(6)-C(11)	115.5(3)
O(2)-Ti(2)-N(4)-Ti(3)	21.68(8)	O(1)-Ti(2)-N(6)-Ti(2)#1	140.96(10)
N(6)-Ti(2)-N(4)-Ti(3)	-17.8(2)	N(5)-Ti(2)-N(6)-Ti(2)#1	-118.21(12)
Br(1)-Ti(2)-N(4)-Ti(3)	-56.57(6)	O(2)-Ti(2)-N(6)-Ti(2)#1	-23.24(10)
Ti(2)#1-Ti(2)-N(4)-Ti(3)	-6.57(8)	N(4)-Ti(2)-N(6)-Ti(2)#1	16.0(3)
O(1)-Ti(2)-N(5)-C(10)	-1.8(3)	Br(1)-Ti(2)-N(6)-Ti(2)#1	54.83(8)
O(2)-Ti(2)-N(5)-C(10)	178.0(3)	Ti(3)-Ti(2)-N(6)-Ti(2)#1	3.30(11)
N(6)-Ti(2)-N(5)-C(10)	-103.7(3)	O(2)-Ti(3)-N(7)-C(13)	180.000(2)
N(4)-Ti(2)-N(5)-C(10)	100.6(3)	N(4)#1-Ti(3)-N(7)-C(13)	98.01(7)
Br(1)-Ti(2)-N(5)-C(10)	175.3(6)	N(4)-Ti(3)-N(7)-C(13)	-98.01(7)
Ti(3)-Ti(2)-N(5)-C(10)	145.9(3)	Br(2)-Ti(3)-N(7)-C(13)	0.000(3)
Ti(2)#1-Ti(2)-N(5)-C(10)	-146.8(3)	Br(1)-Ti(3)-N(7)-C(13)	180.00(3)
O(1)-Ti(2)-N(5)-C(9)	178.0(3)	Ti(2)#1-Ti(3)-N(7)-C(13)	143.04(5)
O(2)-Ti(2)-N(5)-C(9)	-2.3(3)	Ti(2)-Ti(3)-N(7)-C(13)	-143.04(5)
N(6)-Ti(2)-N(5)-C(9)	76.0(3)	O(2)-Ti(3)-N(7)-C(14)	0.000(1)
N(4)-Ti(2)-N(5)-C(9)	-79.7(3)	N(4)#1-Ti(3)-N(7)-C(14)	-81.99(7)
Br(1)-Ti(2)-N(5)-C(9)	-5.0(9)	N(4)-Ti(3)-N(7)-C(14)	81.99(7)
Ti(3)-Ti(2)-N(5)-C(9)	-34.4(3)	Br(2)-Ti(3)-N(7)-C(14)	180.0
Ti(2)#1-Ti(2)-N(5)-C(9)	32.9(3)	Br(1)-Ti(3)-N(7)-C(14)	0.00(3)
O(1)-Ti(2)-N(6)-C(12)	19.4(2)	Ti(2)#1-Ti(3)-N(7)-C(14)	-36.96(5)
		Ti(2)-Ti(3)-N(7)-C(14)	36.96(5)

Symmetry transformations used to generate equivalent atoms:

#1 x,-y+3/2,z

A3.2 Charge Density Analysis of $[(Bz_3)Ti]_2O$ (8)

Topological analysis and geometrical parameters of 8.

Unit	Method	Distance [Å]	$\rho(r_c)$ [e/Å^3]	$\nabla^2\rho(r_c)$ [e/Å^5]	Ellipticity ε
Ti-O	Exp.[a]	1.8009(1)	0.782(5)	19.620(11)	0.01
	Calc.[b]	1.8010	0.969	16.802	0.00
	Opt.[c]	1.8038	0.978	16.836	0.00
Ti-C1	Exp.	2.0875(3)	0.692(3)	6.004(4)	0.05
	Calc.	2.0874	0.629	2.763	0.13
	Opt.	2.1060	0.708	2.278	0.02
C1-C2	Exp.	1.4806(4)	1.745(16)	-15.117(38)	0.09
	Calc.	1.4809	1.612	-11.824	0.09
	Opt.	1.4909	1.738	-14.360	0.11
C2-C3	Exp.	1.4006(4)	2.127(22)	-20.687(76)	0.25
	Calc.	1.4003	1.838	-15.574	0.16
	Opt.	1.4082	2.064	-19.626	0.20
C2-C7	Exp.	1.4018(4)	2.134(23)	-19.809(81)	0.06
	Calc.	1.4018	2.000	-18.775	0.20
	Opt.	1.4092	2.060	-19.598	0.19
C3-C4	Exp.	1.3901(4)	2.196(24)	-24.148(86)	0.13
	Calc.	1.3902	1.916	-16.800	0.22
	Opt.	1.3947	2.104	-20.411	0.22
C4-C5	Exp.	1.3876(5)	2.156(22)	-20.064(82)	0.15
	Calc.	1.3867	2.023	-19.234	0.21
	Opt.	1.3966	2.099	-20.368	0.21
C5-C6	Exp.	1.3905(5)	2.113(23)	-21.033(79)	0.19
	Calc.	1.3903	1.884	-16.337	0.18
	Opt.	1.3978	2.095	-20.302	0.21
C6-C7	Exp.	1.3855(4)	2.184(24)	-24.228(82)	0.17
	Calc.	1.3851	1.924	-17.047	0.21
	Opt.	1.3945	2.107	-20.459	0.21

[a]Experimental values were obtained by a multipole refinement of the experimental charge density (see S13-S16). [b]Single point calculation on the experimental (XD) geometry was carried out at the B3LYP/6-311G(d,p) level. [c]Geometry optimization was carried out at the B3LYP/6-31G* level, symmetry group S_6 was assumed.

Topological analysis and geometrical parameters of 8 (continued).

Unit	Method	Distance [Å]	$\rho(\mathbf{r}_c)$ [e/Å^3]	$\nabla^2\rho(\mathbf{r}_c)$ [e/Å^5]	Ellipticity ε
C1-H1A	Exp.[a]	1.1000[d]	1.534(40)	-12.666(143)	0.04
	Calc.[b]	1.0995	1.760	-19.813	0.07
	Opt.[c]	1.1012	1.750	-19.331	0.05
C1-H1B	Exp.	1.1000[d]	1.542(33)	-11.330(102)	0.06
	Calc.	1.1000	1.714	-17.820	0.08
	Opt.	1.0973	1.778	-20.239	0.05
C3-H3	Exp.	1.1000[d]	1.639(34)	-16.969(135)	0.02
	Calc.	1.1002	1.783	-20.606	0.02
	Opt.	1.0884	1.858	-22.755	0.02
C4-H4	Exp.	1.1000[d]	1.722(35)	-15.893(123)	0.08
	Calc.	1.1001	1.761	-19.885	0.01
	Opt.	1.0873	1.866	-23.115	0.01
C5-H5	Exp.	1.1000[d]	1.683(34)	-16.417(120)	0.01
	Calc.	1.1009	1.750	-19.662	0.02
	Opt.	1.0865	1.867	-23.110	0.02
C6-H6	Exp.	1.1000[d]	1.634(36)	-16.443(142)	0.02
	Calc.	1.1004	1.798	-20.929	0.02
	Opt.	1.0872	1.868	-23.120	0.01
C7-H7	Exp.	1.1000[d]	1.730(34)	-16.445(115)	0.06
	Calc.	1.1004	1.773	-19.929	0.02
	Opt.	1.0872	1.874	-23.430	0.02

[a]Experimental values were obtained by a multipole refinement of the experimental charge density (see S13-S16). [b]Single point calculation on the experimental (XD) geometry was carried out at the B3LYP/6-311G(d,p) level. [c]Geometry optimization was carried out at the B3LYP/6-31G* level, symmetry group S_6 was assumed. [d] Fixed value.

Fractional atomic co-ordinates and mean-square atomic displacement parameters for the asymmetric unit of 8.

Atom	Fractional atomic coordinates *x/a*	*y/b*	*z/c*	U_{iso} [Å^2]
Ti	0.00000[a]	0.00000[a]	0.099609(4)	
O	0.00000[a]	0.00000[a]	0.00000[a]	
C1	0.16846(3)	0.12706(3)	0.14468(2)	
C2	0.22071(2)	0.24679(2)	0.10696(1)	
C3	0.19598(2)	0.33771(3)	0.13069(2)	
C4	0.24620(3)	0.44926(3)	0.09415(2)	
C5	0.32158(3)	0.47260(3)	0.03328(2)	
C6	0.34504(3)	0.38232(3)	0.00823(2)	
C7	0.29490(2)	0.27093(3)	0.04441(2)	
H1A	0.14421[a]	0.12904[a]	0.20289[a]	0.03206[a,b]
H1B	0.22425[a]	0.08328[a]	0.13765[a]	0.03206[a,b]
H3	0.12985[a]	0.31633[a]	0.17576[a]	0.02290[a,b]
H4	0.22612[a]	0.51846[a]	0.11617[a]	0.02482[a,b]
H5	0.36755[a]	0.56507[a]	0.00946[a]	0.02571[a,b]
H6	0.40818[a]	0.40264[a]	-0.03844[a]	0.02631[a,b]
H7	0.31223[a]	0.19857[a]	0.02486[a]	0.02430[a,b]

[a]Fixed value. [b]Isotropic temperature parameters for the hydrogen atoms were derived from those of the parent carbon atoms ($U_H = 1.5U_{C_{sp^3}}$, $U_H = 1.2U_{C_{sp^2}}$), see S13-S16.

Atom	Mean-square atomic displacement parameters [Å^2] *U*11	*U*22	*U*33	*U*12	*U*13	*U*23
Ti	0.01509(3)	0.01509(3)	0.01200(4)	0.00754(2)	0.00000[a]	0.00000[a]
O	0.0231(1)	0.0231(1)	0.0120(2)	0.0116(1)	0.00000[a]	0.00000[a]
C1	0.01935(9)	0.01993(10)	0.02195(10)	0.00681(7)	-0.00369(7)	0.00033(7)
C2	0.01469(8)	0.01755(9)	0.01834(9)	0.00714(6)	-0.00127(6)	-0.00215(7)
C3	0.01939(9)	0.02162(10)	0.01777(9)	0.01074(7)	-0.00049(7)	-0.00414(7)
C4	0.0229(1)	0.0198(1)	0.0219(1)	0.0120(1)	-0.0033(1)	-0.0050(1)
C5	0.0213(1)	0.0178(1)	0.0233(1)	0.0077(1)	-0.0015(1)	-0.0011(1)
C6	0.01907(9)	0.02082(10)	0.02435(11)	0.00808(8)	0.00474(8)	-0.00002(8)
C7	0.01812(9)	0.01940(10)	0.02455(11)	0.00974(7)	0.00394(8)	-0.00152(8)

[a]Fixed value.

Kappa and multipole parameters for 8.

Atom	κ'	κ''	P_v	P_{11+}	P_{11-}	P_{10}
Ti	1.20(3)[a]	1.20(3)[a]	0.249(18)	*[c]	*	-0.005(3)
O	0.953(5)	1.00[b]	1.087(11)	*	*	*
C1	0.892(5)	0.70[b]	5.39(7)	-0.12(3)	-0.19(3)	0.286(19)
C2	0.951(3)	0.934(13)	4.05(5)	0.029(19)	0.015(18)	*
C3	0.951(3)	0.934(13)	4.33(5)	0.042(18)	-0.038(18)	*
C4	0.951(3)	0.934(13)	4.53(5)	-0.05(2)	0.012(19)	*
C5	0.951(3)	0.934(13)	4.35(5)	-0.01(2)	-0.06(2)	*
C6	0.951(3)	0.934(13)	4.23(5)	0.025(19)	-0.057(19)	*
C7	0.951(3)	0.934(13)	4.45(5)	0.074(18)	-0.053(19)	*
H1A	1.20[b]	1.20[b]	0.60(2)	*	*	0.039(15)
H1B	1.20[b]	1.20[b]	0.66(3)	*	*	0.067(14)
H3	1.20[b]	1.20[b]	0.625(19)	*	*	0.062(12)
H4	1.20[b]	1.20[b]	0.74(2)	*	*	0.093(13)
H5	1.20[b]	1.20[b]	0.69(2)	*	*	0.096(13)
H6	1.20[b]	1.20[b]	0.63(2)	*	*	0.073(13)
H7	1.20[b]	1.20[b]	0.710(19)	*	*	0.139(14)

[a] For Ti $\kappa' = \kappa''$ was assumed, see S14. [b] Fixed value. [c] Symmetry forbidden multipoles are denoted by an asterisk (*).

Atom	P_{20}	P_{21+}	P_{21-}	P_{22+}	P_{22-}
Ti	0.009(4)	*[a]	*	*	*
O	0.024(3)	*	*	*	*
C1	0.054(19)	-0.066(16)	0.113(18)	0.04(2)	-0.11(2)
C2	-0.185(14)	*	*	-0.014(16)	-0.004(15)
C3	-0.220(15)	*	*	-0.024(15)	0.055(16)
C4	-0.199(16)	*	*	0.023(16)	0.007(16)
C5	-0.199(15)	*	*	0.001(16)	0.000(17)
C6	-0.251(16)	*	*	-0.016(16)	0.033(16)
C7	-0.222(15)	*	*	0.026(15)	0.031(16)

[a] Symmetry forbidden multipoles are denoted by an asterisk (*).

Kappa and multipole parameters for 8 (continued).

Atom	P_{30}	P_{31+}	P_{31-}	P_{32+}	P_{32-}	P_{33+}	P_{33-}
Ti	-0.064(3)	*[a]	*	*	*	-0.012(3)	0.022(3)
O	*	*	*	*	*	*	*
C1	0.50(2)	-0.04(2)	0.10(2)	0.09(2)	0.09(2)	-0.10(2)	-0.32(3)
C2	*	-0.064(14)	-0.002(15)	*	*	0.249(19)	-0.021(18)
C3	*	-0.015(15)	0.023(14)	*	*	0.31(2)	0.014(18)
C4	*	-0.021(16)	0.029(15)	*	*	0.34(2)	-0.009(18)
C5	*	0.010(17)	0.045(16)	*	*	0.25(2)	0.002(19)
C6	*	0.048(17)	0.000(16)	*	*	0.31(2)	-0.012(19)
C7	*	0.021(16)	-0.002(15)	*	*	0.28(2)	-0.020(17)

[a]Symmetry forbidden multipoles are denoted by an asterisk (*).

Atom	P_{40}	P_{41+}	P_{41-}	P_{42+}	P_{42-}	P_{43+}	P_{43-}	P_{44+}	P_{44-}
Ti	-0.030(4)	*[b]	*	*	*	0.003(4)	0.037(4)	*	*
O	-0.003(4)	*	*	*	*	0.002(4)	0.003(4)	*	*
C1[a]									
C2	-0.017(18)	*	*	-0.018(18)	-0.046(18)	*	*	0.05(2)	0.07(2)
C3	0.081(19)	*	*	0.003(19)	-0.055(19)	*	*	-0.02(2)	-0.02(2)
C4	0.04(2)	*	*	-0.053(19)	0.00(2)	*	*	-0.02(2)	0.02(2)
C5	0.04(2)	*	*	0.053(19)	-0.02(2)	*	*	0.07(2)	-0.06(2)
C6	0.03(2)	*	*	0.00(2)	-0.04(2)	*	*	0.06(2)	-0.03(2)
C7	0.050(19)	*	*	-0.057(19)	0.044(19)	*	*	0.02(2)	0.00(2)

[a]Hexadecapoles on C1 were not refined, see S13-S16. [b]Symmetry forbidden multipoles are denoted by an asterisk (*).

Local co-ordinate systems for 8 before normalisation.[a]

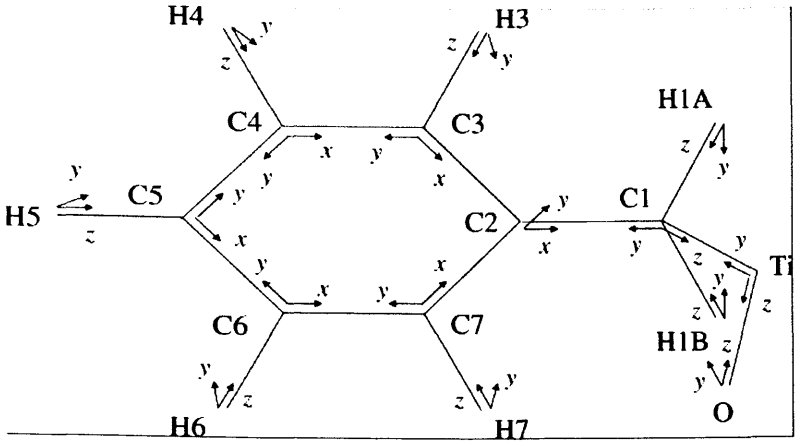

Atom	Atom_1	Axis_1	Atom_2	Atom_3	Axis_2
Ti	O	*Z*	Ti	C1	*y*
O	Ti	*Z*	O	C1	*y*
C1	Ti	*Z*	C1	C2	*y*
C2	C1	*X*	C7	C2	*y*
C3	C2	*X*	C3	C4	*y*
C4	C3	*X*	C4	C5	*y*
C5	C6	*X*	C5	C4	*y*
C6	C7	*X*	C6	C5	*y*
C7	C2	*X*	C7	C6	*y*
H1A	C1	*Z*	H1A	H1B	*y*
H1B	C1	*Z*	H1B	H1A	*y*
H3	C3	*Z*	H3	C2	*y*
H4	C4	*Z*	H4	C3	*y*
H5	C5	*Z*	H5	C4	*y*
H6	C6	*Z*	H6	C5	*y*
H7	C7	*Z*	H7	C2	*y*

[a]The first axis (Axis_1) is given by the internuclear vector from one atom (Atom) to another (Atom_1). This together with the second vector from Atom_2 to Atom_3 defines the (Axis_1, Axis_2) plane. The third vector is assumed to be perpendicular to this plane. The three vectors make a right-handed local coordinate system with (Atom) in the origin.

Residual electron density maps for 8 after mulipole refinement.

Data cut-off at $\sin\Theta/\lambda < 0.8$ Å^{-1}: $\rho_{max} = 0.201$, $\rho_{min} = -0.311$ eÅ^{-3}; contour level: 0.05 eÅ^{-3}.

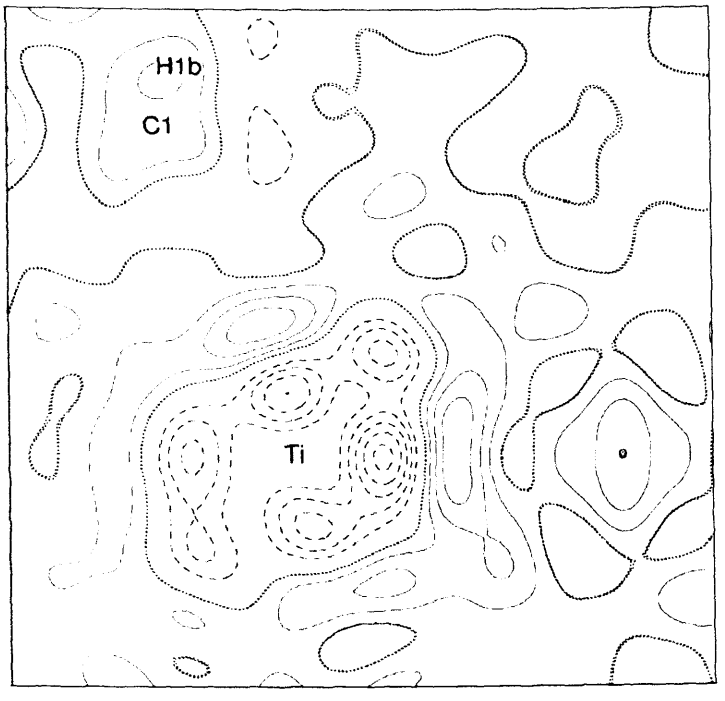

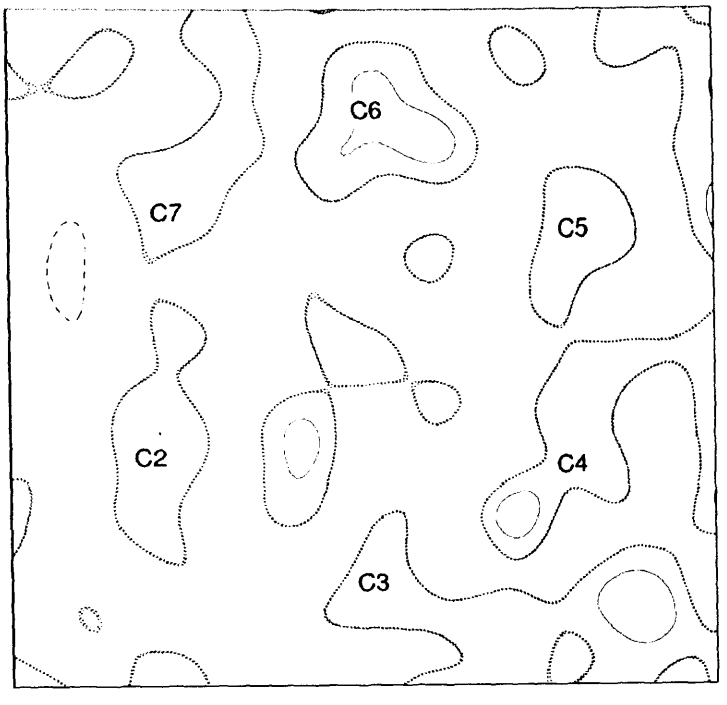

Topological parameters of selected charge concentrations[a] in 8

Parameter	Exp.		6-31G*[b]		6-311G(d,p)[c]
	BUBBLE	TOPXD	HF	B3LYP	B3LYP
Ti LOCC(C)					
$\rho(\mathbf{r})$ [e/Å^3]	9.682[d]	9.855	10.181[d]	10.335[d]	10.220[d]
$\nabla^2\rho(\mathbf{r})$ [e/Å^5]	-345.4[d]	-352.8	-381.1[d]	-382.1[d]	-350.0[d]
Ti LOCC(O)					
$\rho(\mathbf{r})$ [e/Å^3]	8.723[d]	8.928	9.538	9.643	9.639
$\nabla^2\rho(\mathbf{r})$ [e/Å^5]	-249.9[d]	-256.4	-301.8	-296.6	-281.8
C1-Ti CC					
$\rho(\mathbf{r})$ [e/Å^3]	1.768	1.807	1.761	1.742	1.667
$\nabla^2\rho(\mathbf{r})$ [e/Å^5]	-26.6	-26.6	-22.5	-20.2	-17.5
C1-C2 CC					
$\rho(\mathbf{r})$ [e/Å^3]	1.758	1.769	1.868	1.883	1.771
$\nabla^2\rho(\mathbf{r})$ [e/Å^5]	-18.7	-18.6	-23.1	-21.6	-17.4
C1-H1A CC					
$\rho(\mathbf{r})$ [e/Å^3]	1.784	1.796	1.916	1.890	1.851
$\nabla^2\rho(\mathbf{r})$ [e/Å^5]	-24.9	-24.8	-25.5	-23.4	-22.8
C1-H1B CC					
$\rho(\mathbf{r})$ [e/Å^3]	1.713	1.726	1.944	1.930	1.834
$\nabla^2\rho(\mathbf{r})$ [e/Å^5]	-19.3	-19.4	-26.4	-24.5	-21.3

[a](3,-3) critical points in $-\nabla^2\rho(\mathbf{r})$. [b]Geometry optimization. [c]Single point calculation on the experimental (XD) geometry. [d]Mean value.

Topological parameters of selected charge depletions[a] in 8

Parameter	Exp.		6-31G*[b]		6-311G(d,p)[c]
	BUBBLE	TOPXD	HF	B3LYP	B3LYP
Ti CD1[d]					
$\rho(\mathbf{r})$ [e/Å^3]	7.384[e]	7.585	7.674[e]	7.741[e]	7.689[e]
$\nabla^2\rho(\mathbf{r})$ [e/Å^5]	-119.5[e]	-124.8	-128.5[e]	-115.2[e]	-116.9[e]
Ti CD2[f]					
$\rho(\mathbf{r})$ [e/Å^3]	7.256[e]	7.456	7.891[e]	7.920[e]	7.870[e]
$\nabla^2\rho(\mathbf{r})$ [e/Å^5]	-105.3[e]	-110.3	-143.4[e]	-127.7[e]	-127.9[e]
Ti LOCD(O)					
$\rho(\mathbf{r})$ [e/Å^3]	8.842	9.038	-	-	-
$\nabla^2\rho(\mathbf{r})$ [e/Å^5]	-218.0	-224.3	-	-	-
Ti CD(O)					
$\rho(\mathbf{r})$ [e/Å^3]	-	6.397	7.451	7.948	7.891
$\nabla^2\rho(\mathbf{r})$ [e/Å^5]	-	-29.4	-122.1	-149.3	-142.6
C1 LOCD(Ti)					
$\rho(\mathbf{r})$ [e/Å^3]	1.164	1.171	1.262	1.321	1.306
$\nabla^2\rho(\mathbf{r})$ [e/Å^5]	-3.7	-3.7	-1.0	-2.8	-3.2
C1 LOCD(C2)					
$\rho(\mathbf{r})$ [e/Å^3]	1.281	1.305	1.182	1.271	1.289
$\nabla^2\rho(\mathbf{r})$ [e/Å^5]	-5.4	-5.4	1.6	-0.3	-0.6
C1 LOCD(H1A)					
$\rho(\mathbf{r})$ [e/Å^3]	1.399	1.418	1.175	1.257	1.304
$\nabla^2\rho(\mathbf{r})$ [e/Å^5]	-8.0	-7.9	1.6	0.0	-1.2
C1 LOCD(H1B)					
$\rho(\mathbf{r})$ [e/Å^3]	1.179	1.198	1.180	1.270	1.153
$\nabla^2\rho(\mathbf{r})$ [e/Å^5]	-4.3	-4.3	1.5	-0.3	0.4

[a](3,−1) critical points in $-\nabla^2\rho(\mathbf{r})$. [b]Geometry optimization. [c]Single point calculation on the experimental (XD) geometry. [d]Three charge depletions pointing towards O. [e]Mean value. [f]Three charge depletions pointing away from O.

Description of the basis set used for Ti in the calculated model systems.

```
 Ti 0
S    5 1.00
  .2060820000D+06    .1497489231D-02
  .3122680000D+05    .1156061686D-01
  .7199320000D+04    .5918077442D-01
  .2048750000D+04    .2392388796D+00
  .6707900000D+03    .7629408135D+00
S    1 1.00
  .2436500000D+03    .1000000000D+01
S    1 1.00
  .9592500000D+02    .1000000000D+01
S    1 1.00
  .3981010000D+02    .1000000000D+01
S    1 1.00
  .1222050000D+02    .1000000000D+01
S    1 1.00
  .5008820000D+01    .1000000000D+01
S    1 1.00
  .1285690000D+01    .1000000000D+01
S    1 1.00
  .5128060000D+00    .1000000000D+01
S    1 1.00
  .2090000000D+00    .1000000000D+01
S    1 1.00
  .8557600000D-01    .1000000000D+01
P    4 1.00
  .1264700000D+04    .6796738994D-02
  .3012300000D+03    .5478679797D-01
  .9697770000D+02    .2577996748D+00
  .3637270000D+02    .7667928483D+00
P    1 1.00
  .1478140000D+02    .1000000000D+01
P    1 1.00
  .6274650000D+01    .1000000000D+01
P    1 1.00
  .2478780000D+01    .1000000000D+01
P    1 1.00
  .1016180000D+01    .1000000000D+01
P    1 1.00
  .3981620000D+00    .1000000000D+01
P    1 1.00
  .1560000000D+00    .1000000000D+01
P    1 1.00
  .6110000000D-01    .1000000000D+01
D    4 1.00
  .2811000000D+02    .2574652697D-01
  .7630000000D+01    .1412604259D+00
  .2528000000D+01    .4006136061D+00
  .8543000000D+00    .6345262253D+00
D    1 1.00
  .2673000000D+00    .1000000000D+01
D    1 1.00
  .7430000000D-01    .1000000000D+01
F    1 1.00
  .1506000000D+01    .1000000000D+01
 ****
```

A3.3 Calculated Structure of $MeTi(NMe_2)_3$ (14)

Molecular structure of $MeTi(NMe_2)_3$ as obtained from a B3LYP/6-311G* calculation. Symmetry group C_1. Interatomic distances in Å, valence and torsional angles in degrees. Since the optimised structure appears not to have an effective C_3 symmetry, the structure parameters of NMe_2 groups involving N3 and N4 are not listed.

Bond distances

Ti–C	2.127
Ti–N5	1.904
N5–C11	1.456
C1–H[a]	1.098
C11–H[a]	1.098
C14–H[a]	1.098

Valence angles

∠C–Ti–N5	108.2
∠Ti–N5–C11	117.1
∠Ti–N5–C14	130.1
∠C11–N5–C14	112.7
∠N5–Ti–N4	110.7
∠N5–C11–H[a]	111.4
∠N5–C14–H[a]	111.2
∠Ti–C–H[a]	111.8

Torsional angles

∠H7–C–Ti–N5	–177.0
∠C–Ti–N5–C11	53.7
∠C–Ti–N5–C14	–121.6
∠Ti–N5–C11–H22	5.3
∠Ti–N5–C14–H24	–5.4

[a] mean value